The Dissertation Committee for Yingzhe Li
certifies that this is the approved version of the following dissertation:

Modeling and Analyzing the Evolution of Cellular Networks using Stochastic Geometry

Committee:

Jeffrey G. Andrews, Co-Supervisor

François Baccelli, Co-Supervisor

Gustavo de Veciana

Robert W. Heath, Jr.

Thomas D. Novlan

Modeling and Analyzing the Evolution of Cellular Networks using Stochastic Geometry

by

Yingzhe Li, B.S.E.; M.S.E.

DISSERTATION

Presented to the Faculty of the Graduate School of

The University of Texas at Austin

in Partial Fulfillment

of the Requirements

for the Degree of

DOCTOR OF PHILOSOPHY

THE UNIVERSITY OF TEXAS AT AUSTIN

May 2017

Dedicated to my family.

Acknowledgments

The five years of the Ph.D. program at UT Austin has been an incredible journey in my life, and I would like to express my gratitude to many people for their help and supports during this journey.

First and foremost, I would like to thank my advisors Prof. Jeffrey Andrews and Prof. François Baccelli. Thanks to Prof. Andrews' trust, I was fortunate to be admitted into his research group in 2012, which would ultimately change my life and career. His solid engineering knowledge, great senses for research directions, strong writing and presentation skills, have significantly improved my research capabilities. I was also fortunate to be able to work with Prof. François Baccelli since my second year, and I have learned so much from his deep mathematical knowledge, high standards for rigorous works, strong work ethic and dedications to research. I am extremely grateful for all the guidance and help from my advisors, which have really shaped me into an independent researcher and professional engineer.

I also want to thank my dissertation committee members Prof. Gustavo de Veciana, Prof. Robert Heath, and Dr. Thomas Novlan, for providing useful comments to my research and dissertation. Furthermore, I want to thank Prof. de Veciana for his probability and queuing theory coursers, which I really enjoyed and learned a lot. I also want to thank Prof. Heath for the

wireless communications lab and space-time communication courses, which have been very useful for my research and job interviews. I also want to thank Dr. Thomas Novlan for the invaluable comments and discussions, which have inspired me a lot for my research.

During my Ph.D. career, I was fortunate to intern at three companies. I want to thank Dr. Rapeepat Ratasuk and Dr. Amitava Ghosh for hosting me at Nokia Networks in 2013. This is my first ever industry experience, and I have learned so much knowledge such as LTE, machine to machine communications, and link-level simulations. I want to thank Mr. Onur Senel and Mr. Matthew Kwon for recruiting me into Qualcomm research as a summer intern in 2014. As a test engineer, I have learned a lot of details about different layers of LTE, and the LTE-WiFi coexistence feature that I tested at Qualcomm has inspired my second contribution in this dissertation. I also want to thank Dr. Thomas Novlan, Dr. Boon Loong Ng and Dr. Charlie Zhang, for having me in the standards team at Samsung Research America-Dallas to work on the system level simulations development for licensed assisted access LTE networks.

My life at UT has been really wonderful and memorable, thanks to my brilliant colleagues and friends. I thank Ping Xia, Harpreet Dhillon, Sarabjot Singh, Xingqin Lin, Xinchen Zhang and Qiaoyang Ye for their academic guidances during my early Ph.D. years, and Derya Malak, Mandar Kulkarni, Ahmad Alammouri, Junse Lee, Jianhua Mo, and Yuwei Ren for various valuable technical discussions. I would also like to thank my friends for spending a lot of memorable moments with me: Tong Zhao, Daniel Yan Cai, Yicong Wang,

Xinyang Yi, Yajun Chen, Xiyuan Tang, Qiaoyang Ye, Yingxi Liu, Yuhuan Du, Chao Chen, Tianyang Bai, Zheng Lu, Jianhua Mo, Jiaxiao Zheng, Yitao Chen, Yuwei Ren, Junse Lee, and many others. I would also like to thank Ms. Melanie Gulick from ECE graduate office, for having a lot of wonderful conversations with me during the afternoons.

Finally, I woud like to thank my parents, Jinling Su and Zhenjiang Li, for their unconditional love and supports; and my wife, Jiaxin Zhang, for sharing this unbelievable Ph.D. journey with me. Despite the ups and downs, the encouragements from my family have always motivated me to be passionate and confident about my research and life.

Modeling and Analyzing the Evolution of Cellular Networks using Stochastic Geometry

Publication No. _____

Yingzhe Li, Ph.D.
The University of Texas at Austin, 2017

Co-Supervisors: Jeffrey G. Andrews
François Baccelli

The increasing complexity of cellular network due to its continuous evolution has made the conventional system level simulations time consuming and cost prohibitive. By modeling base station (BS) and user locations as spatial point processes, stochastic geometry has recently been recognized as a tractable and efficient analytical tool to quantify key performance metrics. The goal of this dissertation is to leverage stochastic geometry to develop an accurate spatial point process model for the conventional homogeneous macro cellular network, and to address the design and analysis challenges for the emerging cellular networks that will explore new spectrum for cellular communications.

First, this dissertation proposes to use the repulsive determinantal point processes (DPPs) as an accurate model for macro BS locations in a cellular network. Based on three unique computational properties of the DPPs, the exact

expressions of several fundamental performance metrics for cellular networks with DPP configured BSs are analytically derived and numerically evaluated. Using hypothesis testing for various performance metrics of interest, the DPPs are validated to be more accurate than the Poisson point process (PPP) or the deterministic grid model.

Then the focus of this dissertation shifts to emerging networks that exploit new spectrum for cellular communications. One promising option is to allow the centrally scheduled cellular system to also access the unlicensed spectrum, wherein a carrier sensing multiple access with collision avoidance (CSMA/CA) protocol is usually used, as in Wi-Fi. A stochastic geometry-based analytical framework is developed to characterize the performance metrics for neighboring Wi-Fi and cellular networks under various coexistence mechanisms. In order to guarantee fair coexistence with Wi-Fi, it is shown that the cellular network needs to adopt either a discontinuous transmission pattern or its own CSMA/CA like mechanisms.

Next, this dissertation considers cellular networks operating in the millimeter wave (mmWave) band, where directional beamforming is required to establish viable connections. Therefore, a major design challenge is to learn the necessary beamforming directions through the procedures that establish the initial connection between the mobile user and the network. These procedures are referred to as initial access, wherein cell search on the downlink and random access on the uplink are the two major steps. Stochastic geometry is again utilized to develop a unified analytical framework for three directional

initial access protocols under a high mobility scenario where users and random blockers are moving with high speed. The expected delay for a user to succeed in initial access, and the average user-perceived downlink throughput that accounts for the initial access overhead, are derived for all three protocols. In particular, the protocol that has low beam-sweeping overhead during cell search is found to achieve a good trade-off between the initial access delay and user-perceived throughput performance.

Finally, in contrast to the high mobility scenario for initial access, the directional cell search delay in a slow mobile network is analyzed. Specifically, the BS and user locations are fixed for long period of time, and therefore a strong temporal correlation for SINR is experienced. A closed-form expression for the expected cell search delay is derived, indicating that the expected cell search delay is infinite for noise-limited networks (e.g., mmWave) whenever the non-line-of-sight path loss exponent is larger than 2. By contrast, the expected cell search delay for interference-limited networks is proved to be infinite when the number of beams to search at the BS is smaller than a certain threshold, and finite otherwise.

Table of Contents

List of Tables

List of Figures

Chapter 1

Introduction

Comprehensive system level simulation is the conventional approach for the evaluation and design of cellular networks. However, the ever-increasing complexity of cellular networks renders simulation even more time consuming and expensive. By utilizing spatial point processes to model the BS and the user locations, stochastic geometry is recognized as a tractable system-level analytical tool for deriving key performance metrics, providing important insights, as well as guiding and narrowing simulations. Although such mathematical analysis of cellular networks has contributed greatly to our understanding of network behaviors in recent years, some limitations and challenges still exist. Even for conventional macro cellular networks, the most widely used Poisson point process (PPP) is an idealization of the BS locations. As cellular networks evolve to explore new spectrum opportunities in the 5 GHz unlicensed band or the mmWave bands, many challenges exist for stochastic geometry analysis of cellular networks due to the unique characteristics of the new spectrum. The objective of this dissertation is to address these limitations and challenges.

This introductory chapter consists of three parts. Section 1.1 provides

the background on why stochastic geometry is a powerful system level analytical tool for large-scale cellular networks. Section 1.2 identifies several limitations and challenges of stochastic geometry for cellular networks, as it continues to evolve from homogeneous and macro BS-centric to a denser and more heterogeneous network with wider spectrum. Finally, Section 1.3 summaries the key contributions of this dissertation.

1.1 Stochastic Geometry for Analyzing Cellular Networks

The main advantage of the comprehensive system level simulations is that it can investigate any arbitrary network scenario to any detail. This is enabled by implementing the desired network topology, wireless channel model, traffic model, network protocols, and so on. Therefore, many key performance metrics of cellular networks, including the signal-to-interference-plus-noise ratio (SINR) distribution and the data rate, can be accurately determined through simulations. However, a major limitation of simulation is that each desired scenario needs to be simulated separately using distinctive system parameters. As the cellular network continues to evolve with more complicated features and more system parameters to optimize, simulating all the scenarios of interest can be very time-consuming. Due to the limited number of scenarios that can be simulated, the corresponding design insights can also be quite restricted, and hard to infer for the scenarios that are not simulated. An accurate yet efficient analytical tool is very desirable for investigating cellular

network performance.

In recent years, stochastic geometry has become recognized as a very powerful analytical tool for such investigations. Specifically, by modeling BS and user locations as realizations of spatial point processes on the two dimensional plane (i.e., $\mathbb{R}^2$), stochastic geometry provides an analytically tractable approach for the analysis of cellular networks, enabling the characterization of SINR distribution and mean data rate. The analytical expressions can reveal the impact of system parameters on the key performance metrics, therefore providing an efficient tool to extract design insights and optimize the system performance. In addition, stochastic geometry analysis of cellular networks provides a good complement to exhaustive simulations, since a large subset of undesirable deployment parameters can be quickly eliminated through the analytical expressions while the remaining parameters can be investigated through simulations [1].

Due to its simple definition and exceptional analytical tractability, the PPP has become the most popular spatial point process for modeling BS and user locations of cellular networks. For example, the SINR distribution can be derived in closed-form and evaluated very efficiently for a Poisson cellular network [2]. This is in sharp contrast to the conventional deterministic grid network model, under which no closed form expression for SINR distribution is available.

As cellular network continues to evolve with more complicated emerging features, many challenges for the stochastic geometry analysis of cellular

networks have arisen. In the next section, we detail several challenges that will be investigated in this dissertation.

1.2 Challenges in the Stochastic Geometry Analysis for the Evolution Cellular Networks

Traditionally, a cellular system is deployed as a homogeneous, macro BS centric network, where detailed network planning for macro BS deployment is required to control interference and maximize coverage. In order to support the exponentially growing mobile traffic demand [3], cellular networks have been constantly evolved to provide faster and more reliable network connectivity. Three major approaches to achieve such purpose include [4, 5]: (1) increase bandwidth for cellular communications; (2) increase spectral efficiency, such as adopting higher order multiple-input multiple-output (MIMO) or modulation; and (3) increase cell density, such as deploying small BSs underlaid in the conventional macro cells. Fig. 1.1 provides an illustration of these evolution trends. Despite the simplicity of the analysis for single-tier Poisson cellular network [2], we will highlight several major challenges of using stochastic geometry to analyze the cellular network during its evolution, for not only the conventional macro cellular networks, but also when new spectrum opportunities are exploited for cellular communications.

Accurate spatial point process model for macro BSs. As a result of the careful network planning from the operators, the actual macro-cells are irregular, and correlations exist among neighboring macro BS locations [6]. In

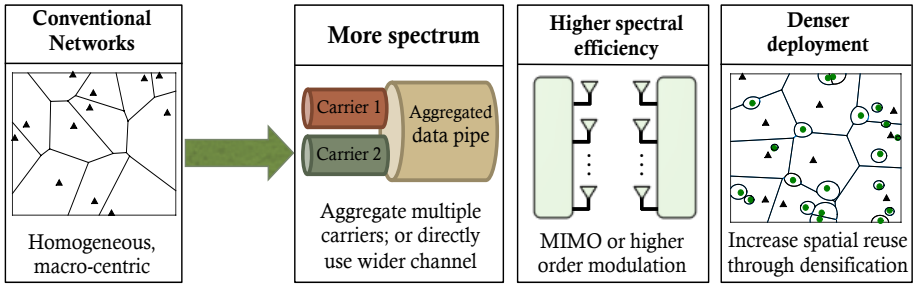

Figure 1.1: Key methods for the evolution of cellular networks to achieve higher capacity.

particular, the macro BSs typically exhibit a repulsive behavior, since no two macro BSs are deployed arbitrarily close to each other. However, the conventional deterministic grid model fails to capture the irregularity of the actual macro BS deployment, and the complete spatial random PPP does not accurately model the repulsiveness among macro BSs. Fig. 1.2 shows an example of the actual macro BS deployment from Houston, and the fitted hexagonal grid model and PPP model. It can be qualitatively observed from Fig. 1.2 that the actual macro BS deployment is less regular than the hexagonal grid model, but more regular than the PPP. Therefore, although PPP is highly tractable and has been widely used for analyzing macro cellular network, its accuracy for modeling actual macro BS deployment is sub-optimal. An accurate yet still tractable point process model for macro BSs is thus necessary to better understand and further optimize the performance of the existing macro-cellular networks.

Analytical model for coexisting cellular and Wi-Fi networks. The conventional cellular systems (e.g., 2G, 3G, and 4G LTE) mainly operate

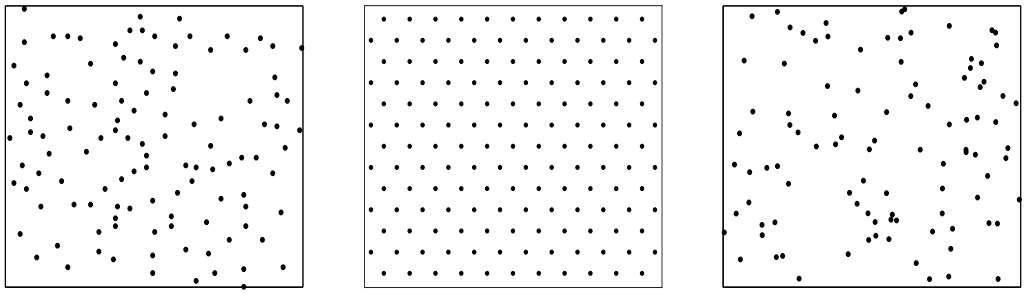

(a) Actual macro BS (b) Fitted grid model (c) Fitted PPP

Figure 1.2: An actual macro BS deployment and the fitted hexagonal grid and PPP models.

in the frequency bands that range from 700 MHz to 2.6 GHz [7], with each component carrier has up to 20 MHz bandwidth [8]. These frequency bands have become saturated in recent years due to the explosive growth of data demanding applications generated by smartphones. Therefore, finding new spectrum opportunities with wider bandwidth for cellular communications is a key method to support the continuously growing mobile traffic demand. One promising option is to allow *small cell* cellular network to simultaneously access both the conventional licensed spectrum and the lightly used 5 GHz unlicensed spectrum, through the carrier aggregation feature of LTE.

The main incumbent system in the 5 GHz unlicensed band is Wi-Fi, which uses carrier sensing multiple access with collision avoidance (CSMA/CA) protocol [9]. In particular, CSMA/CA guarantees a fair sharing of the spectrum by allowing Wi-Fi access points (APs) to transmit only when the channel is sensed idle. However, the cellular network is centrally scheduled without

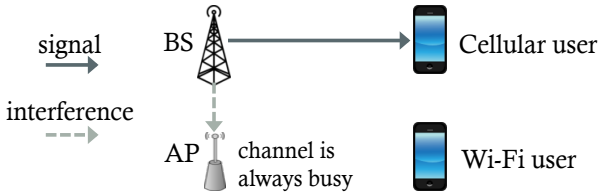

Figure 1.3: An illustration of the how operating cellular in unlicensed band could hurt Wi-Fi.

any carrier sensing mechanism, therefore directly operating cellular in the unlicensed spectrum may significantly degrade Wi-Fi performance. A simple example is shown in Fig. 1.3, where the Wi-Fi AP will never transmit due to a consistently transmitting nearby cellular BS.

Given the above issue, it is important to design certain mechanisms to protect Wi-Fi, and to characterize the corresponding system level performance of the coexisting cellular and Wi-Fi networks. Stochastic geometry is a very suitable tool for this purpose, but the analysis will also be challenging due to the need for an accurate model of the CSMA/CA protocol, and techniques to handle the correlation between both networks created by the carrier sensing mechanism of Wi-Fi and potentially cellular as well.

Analysis and design for directional initial access in mmWave cellular networks. In addition to the 5 GHz unlicensed spectrum, the mmWave bands that range from 30 GHz to 300 GHz also offer tremendous spectrum availability for cellular communications. However, mmWave bands also pose challenges for cellular communications due to the high isotropic pathloss and significant sensitivity to blockage effects. The key method to ad-

dress these challenges is through highly directional beamforming at mmWave BSs and mobile users, such that sufficient signal-to-noise ratio (SNR) can be achieved through large directivity gain. This method is indeed feasible since the small wavelength of mmWave allows large number of antenna arrays to be placed in a compact form factor.

The requirement for high directionality to create viable mmWave links has rendered the initial access, which is the process that allows a mobile user to first connect to the cellular network, a central challenge for mmWave cellular networks. Specifically, the mmWave BSs and users are unaware of which beam directions to use upon initial access, thus they must search over a potentially large beamforming space to find each other, which could be very time consuming. Therefore, it is essential to design initial access protocols for mmWave cellular networks that can achieve small initial access delay and high overall throughput performance. Stochastic geometry can be utilized to design and analyze mmWave initial access protocols, which will require a reasonable analytical model for initial access process, and accurate methods to handle the spatial and temporal correlations of the initial access phases and the data transmission phases.

1.3 Contributions and Organization

As explained above, this dissertation mainly aims to utilize stochastic geometry to model and analyze the evolution of cellular networks, which will advance conventional spatial point process models for macro BS locations,

and tackle the challenges for designing and analyzing the emerging cellular networks that operate in the unlicensed spectrum or mmWave bands. The main technical contributions of this dissertation are covered in Chapter 2 to Chapter 5, which are summarized as follows.

Modeling Macro BS Deployments using Determinantal Point Processes. In Chapter 2, we propose the usage of the soft-core repulsive determinantal point process to take into account the spatial repulsiveness among macro BS locations. By leveraging several unique computational properties of the DPPs, we have demonstrated that the macro cellular networks with DPP configured BSs are analytically tractable. Specifically, we show that the empty space function, the nearest neighbor function, the mean interference and the signal-to-interference ratio (SIR) distribution have explicit analytical representations and can be numerically evaluated for cellular networks with DPP configured BSs. A diagonal approximation approach is shown to provide accurate estimate of the actual SIR distribution in the high SIR regime, which can be evaluated with much higher computational efficiency than the closed-form results. In addition, the modeling accuracy of DPPs is investigated by fitting three DPP models to real BS location data set. Using hypothesis testing for various performance metrics of interest, we show that these fitted DPPs are significantly more accurate than popular choices such as the PPP and the perturbed hexagonal grid model.

Coexistence Analysis of Cellular and Wi-Fi Networks in the Unlicensed Spectrum. A promising approach to meet the ever increasing

data demand for cellular networks is to explore new spectrum opportunities, such as the 5 GHz unlicensed spectrum. Allowing the centrally scheduled cellular system to access the unlicensed spectrum could cause severe performance degradation for the legacy Wi-Fi system, which is built upon the distributed CSMA/CA protocol. In Chapter 3, we leverage stochastic geometry to characterize key performance metrics for neighboring Wi-Fi and cellular networks in the unlicensed spectrum under various cellular coexistence protocols. The locations for *small cell* cellular BSs and Wi-Fi access points are modeled as two independent homogeneous Poisson point processes, and a modified Matern hard-core process is used to model the transmitter locations under the CSMA/CA protocol. Three cellular coexistence mechanisms are investigated: (1) cellular with continuous transmission and no protocol modifications; (2) cellular with discontinuous transmission; and (3) cellular with listen-before-talk (LBT) and random back-off (BO) similar to Wi-Fi. For each scenario, performance metrics including the medium access probability (MAP), the signal-to-interference-plus-noise ratio (SINR) coverage probability, the density of successful transmissions (DST), and the rate coverage probability are analytically derived for both Wi-Fi and cellular networks. Compared to the baseline scenario where one Wi-Fi network coexists with an additional Wi-Fi network, the results show that Wi-Fi performance is severely degraded when cellular BSs transmit continuously. However, the DST and rate coverage probability of Wi-Fi can be improved while the cellular network maintains acceptable data rate performance, if cellular network adopts one or more of the

following coexistence features: a shorter transmission duty cycle, lower channel access priority, or more sensitive clear channel assessment (CCA) thresholds.

Initial Access Analysis in Millimeter Wave Cellular Networks with High Mobility. In Chapter 4, the focus is shifted up from sub-6 GHz communications to the mmWave band (> 30 GHz), which is a key enabling technology for 5G. A central design challenge for mmWave cellular networks is the initial access, which refers to the set of processes that allows a mobile user to first connect to a cellular network. MmWave cellular systems generally rely on directional beamforming in order to create a viable connection. The beamforming direction must therefore be learned – as well as used – in the initial access. Initial access consists of two main steps: cell search (CS) on the downlink and random access (RA) on the uplink. Chapter 4 considers three simple but representative initial access protocols that use various combinations of directional beamforming and omnidirectional transmission and reception at the mobile and the BS, during the CS and RA phases. A high mobility scenario where users and random blockers are moving with relatively high speed is considered. As a result, the BS and user PPPs appear to be independently re-shuffled across different initial access cycles. Stochastic geometry is utilized to provide a system-level analysis of the success probability for CS and RA for each protocol, as well as of the initial access delay and user-perceived downlink throughput (UPT). Of the considered protocols, the best trade-off between initial access delay and UPT is achieved under a fast cell search protocol.

Directional Cell Search Delay in Cellular Networks with Slow

Mobility. In contrast to the high mobility scenario that is investigated in Chapter 4, a slow mobile network where BS and user locations are fixed across a long period of time, is also an important application scenario. Due to the importance of utilizing beam-sweeping to achieve extra directive gain for cell search in the emerging 5G cellular networks, the directional cell search delay performance for slow mobile networks is analyzed in Chapter 5. For a Poisson network with Rayleigh fading channels, a closed-form expression for the expected cell search delay has been derived. Based on this expression, the cell search delay for noise-limited and interference-limited networks are investigated. Specifically, the cell search delay for noise-limited network is proved to have infinite mean value whenever the non-line-of-sight (NLOS) path loss exponent is larger than 2. As the number of BS antennas/beams M increases, the cell search delay for edge users is shown to be significantly reduced. As for the interference-limited network, a phase transition for the expected cell search delay exists in terms of M, such that the mean cell search delay is infinite when M is smaller than a certain threshold and finite otherwise. Overall, Chapter 5 develops a tractable framework to analyze the directional cell search delay in slow mobile networks, based on which beam-sweeping is demonstrated to be essential in decreasing the cell search delay for emerging 5G cellular networks.

Finally, Chapter 6 concludes this dissertation by summarizing the key contributions and discussing potential future research directions.

Chapter 2

Modeling Macro BS Deployments using Determinantal Point Processes[1]

As mentioned in the previous chapter, *macro* base stations have historically been modeled by the deterministic grid-based model, especially the hexagonal grid. However, as a result of detailed network planning, as well as optimization of topological and demographic factors, the actual macro BS deployment is irregular. Therefore, random spatial models become a natural candidate to model BS locations, where BSs form a realization of some random point processes. Due to its simplicity and tractability, the complete spatial random Poisson point process has become the most popular choice. However, as shown in Fig. 1.2, the PPP assumption for the macro BS is idealized since no two macro base stations are deployed arbitrarily close to each other, which means the actual macro BS locations will exhibit repulsive behavior. In order to accurately characterize the fundamental performance metrics, it is of great importance to find alternative tractable point processes that can model the interactions among macro BSs. This chapter proposes the use of

[1]This chapter has been published in [6, 10]. I am the primary author of these works. Coauthor Dr. Harpreet Dhillon has provided many discussions and insightful feedbacks to this work, and Dr. Jeffrey G. Andrews and Dr. François Baccelli are my supervisors.

determinantal point process (DPP) to take into account these correlations; in particular the repulsiveness among macro base station locations.

2.1 Related Works

The PPP has been widely used in prior works to model cellular BS deployments not only because it can describe highly irregular placements, but also because it allows the use of powerful tools from stochastic geometry for tractable analysis. The downlink coverage probability and average downlink Shannon rate for a single tier cellular network were derived in [2]. The analysis of cellular networks with PPP distributed BSs has been extended to several other network scenarios, such as HetNets [11–18], MIMO downlink cellular networks [19–21], MIMO downlink HetNets [19, 21–23], and uplink cellular networks [24, 25].

In fact, real macro BS deployments exhibit repulsion among the BSs, which means that macro BSs are typically distributed more regularly than the realization of a PPP. Therefore, several research efforts have been devoted to investigating more accurate point process models for representing BS deployments. One class of such point processes is the Gibbs point process [26–28]. Gibbs models were validated to be statistically similar to real BS deployments using SIR distribution and Voronoi cell area distribution [26]. The Strauss process, which is an important class of Gibbs processes, can also provide accurate statistical fit to real BS deployments [27, 28]. By contrast, the PPP and the grid models were demonstrated to be less accurate models for real BS

deployments [26,27]. A significant limitation of Gibbs processes is their lack of tractability, since their probability generating functional is generally unknown or difficult to compute [27]. Therefore, point processes that are both tractable and accurate in modeling real BS deployments are desirable.

A promising option is to use the determinantal point processes, which were introduced to model the interactions of fermions in quantum mechanics [29]. For several reasons, DPPs are appealing to model cellular BS deployments. First, DPPs have soft and adaptable repulsiveness [30–32]. Second, there exist quite effective statistical inference tools for DPPs [31, 32]. Third, many stationary DPPs can be easily simulated [32–34]. Fourth, DPPs have many attractive mathematical properties, which can be used for the analysis of cellular network performance [35–37].

The Ginibre point process, which is a type of DPP, has been recently proposed as a possible model for cellular BSs. Closed-form expressions of the coverage probability and the mean data rate were derived for Ginibre single-tier cellular networks in [37, 38], heterogeneous cellular networks in [39], and downlink cellular networks in [40]. In [41], several spatial descriptive statistics and the coverage probability were derived for Ginibre single-tier networks. These results were empirically validated by comparing to real BS deployments. However, the analysis for Ginibre configured cellular networks has been largely facilitated by a specific property of the GPP model [42]. That being said, the modeling accuracy and analytical tractability of using general DPPs to model cellular BS deployments are still largely unexplored.

2.2 Contributions

In this chapter, we will investigate the statistical modeling accuracy and probabilistic properties for DPP configured macro BS networks. The main contributions are summarized as follows:

First, in Chapter 2.4, we provide some backgrounds on stochastic geometry. In particular, we will illustrate the computational properties of PPP that make it tractable for analyzing cellular networks, and explain why PPP is idealized compared to the real macro BS deployment.

Second, in Chapter 2.6, we derive for the first time several key performance metrics in cellular networks with DPP configured BSs. Specifically, we derive the Laplace functional of the DPPs for functions satisfying certain conditions. Based on the Laplace functional of DPPs, we are able to obtain closed-form results for key performance metrics including the empty space function, the nearest neighbor function, the mean total interference and the signal-to-inference ratio (SIR) distribution.

Third, in Chapter 2.7, we propose to use the Quasi-Monte Carlo integration method for efficient evaluation of the derived empty space function, nearest neighbor function, and mean total interference. An approximation for the SIR distribution is proposed, which is shown to be numerically efficient and accurate in the high SIR regime.

Finally, in Chapter 2.8, by fitting three stationary DPP models, namely the Gauss, Cauchy and Generalized Gamma DPP, to real macro BS deploy-

ments, we show DPP models are generally accurate in terms of spatial descriptive statistics and coverage probability. We find that the Gauss DPP model provides a reasonable fit while offering good mathematical tractability. By combining the numerical and simulation results, we show that DPPs outperform PPPs to predict key performance metrics in cellular networks.

2.3 System Model

We focus on a downlink single tier macro cellular network, where BSs are assumed to be distributed according to a stationary point process Φ, while the mobile users are uniformly distributed and independent of the BSs. Each BS $x \in \Phi$ has single transmit antenna with transmit power P, and it is associated with an independent mark h_x which represents the small scale fading effects between the BS and the typical user. Independent Rayleigh fading channels with unit mean are assumed, which means $h_x \sim \exp(1)$ for $\forall x \in \Phi$. The shadowing effects are neglected. Since macro cellular network is typically interference-limited, the thermal noise power is assumed to be 0. In addition, the path loss function for a link with distance r is denoted by $l(r) : \mathbb{R}^+ \mapsto \mathbb{R}^+$, which is non-decreasing with respect to (w.r.t.) r.

2.4 Preliminaries on Poisson Point Process

In this section, the PPP will be defined, and several important computational prosperities that make PPP suitable for cellular network analysis are explained. These preliminaries will be used throughout this dissertation.

A spatial point process Φ is a random collection of points on the d-dimensional Euclidean space, which is a counting measure that can be represented by the sum of Dirac measures on $\mathbb{R}^d$:

$$\Phi = \sum_i \delta_{X_i}, \tag{2.1}$$

where for any $A \in \mathbb{R}^d$, $\delta_X(A) = 1$ if $X \in A$ and $\delta_X(A) = 0$ otherwise. Therefore, $\Phi(A)$ is a discrete random variable which counts the number of points in A that belongs to Φ.

In particular, a PPP with intensity measure Λ is defined as the point process such that for any bounded, mutually disjoint sets $A_i \in \mathbb{R}^d$ $(i = 1, 2, ..., k)$, its finite dimensional distribution is given by [43–45]:

$$\mathbb{P}\bigg(\Phi(A_1) = n_1, ..., \Phi(A_k) = n_k\bigg) = \prod_{i=1}^{k}\bigg(\exp(-\Lambda(A_i))\frac{\Lambda(A_i)^{n_i}}{n_i!}\bigg). \tag{2.2}$$

If the intensity measure Λ admits a density λ (i.e., $\Lambda(\mathrm{d}x) = \lambda \mathrm{d}x$), then Φ is called a homogeneous PPP with intensity λ.

Based on its definition, many unique computational properties of PPP can be derived. Three commonly used properties for analyzing cellular networks are provided as follows.

1. **Complete independence.** An immediate implication of the PPP definition is that for any bounded, mutually disjoint sets A_i $(i = 1, 2, ..., k)$, $(\Phi(A_1), ..., \Phi(A_k))$ is a vector of *independent* Poisson random variables, with mean $(\Lambda(A_1), ..., \Lambda(A_k))$.

2. **Closed-form Laplace functional.** For any non-negative function f on $\mathbb{R}^d$, the Laplace functional of PPP with intensity measure Λ is given by:

$$\mathbb{E}\left[\exp\left(-\int_{\mathbb{R}^d} f(x)\Phi(\mathrm{d}x)\right)\right] = \exp\left(-\int_{\mathbb{R}^d}\left(1-\exp(-f(x))\right)\Lambda(\mathrm{d}x)\right). \tag{2.3}$$

3. **Slivnyak theorem.** For any point $x \in \mathbb{R}^d$ and an event E, define the reduced Palm distribution of a point process Φ as $\mathbb{P}^!_{x_0}(E) = \mathbb{P}(\Phi \setminus \{x_0\} \in E | x_0 \in \Phi)$ [44, 45]. Slivnyak theorem states that PPP preserves its original distribution under the reduced Palm distribution, which means:

$$\mathbb{P}^!_{x_0}(E) = \mathbb{P}(\Phi \in E), \tag{2.4}$$

if Φ is a PPP. An alternative view of the Slivnyak theorem is that the property observed by a typical point x_0 of PPP Φ, is the same as that observed by x_0 in $\Phi \cup \{x_0\}$, which means:

$$\mathbb{P}(\Phi \in E | x_0 \in \Phi) = \mathbb{P}(\Phi + \delta_{x_0} \in E). \tag{2.5}$$

In order to illustrate that PPP is a highly tractable model for analyzing cellular networks, the downlink SIR distribution is derived for the system model defined in Section 2.3. In particular, the BS and user locations are modeled by two independent homogeneous PPPs $\Phi \sim \mathrm{PPP}(\lambda)$ and $\Phi_u \sim \mathrm{PPP}(\lambda_u)$ respectively. The path loss function is assumed to be $l(r) = r^\beta$, where β represents the path loss exponent. Each user is associated with the BS that provides the smallest path loss, which is equivalent to its closest BS.

First, by the Slivnyak theorem (2.5) and the stationarity of PPP, the SIR distribution observed by a typical user of Φ_u is the same as that observed at the origin of $\mathbb{R}^2$, i.e., we can assume the typical user is located in the origin. The serving BS of the typical user is therefore $x^*(0) = \arg\min_{x\in\Phi}\{\|x\|\}$, and the complementary cumulative distribution function (CCDF) of $\|x^*(0)\|$ can be derived as follows:

$$\begin{aligned}\mathbb{P}(\|x^*(0)\| \geq r_0) &\overset{(a)}{=} \mathbb{P}(\Phi(B(0,r_0)) = 0) \\ &\overset{(b)}{=} \exp(-\lambda\pi r_0^2),\end{aligned} \tag{2.6}$$

where (a) holds by noting $x^*(0) = \arg\min_{x\in\Phi}\{\|x\|\}$, and (b) is from the defining property of PPP in (2.2). Based on (2.6), the probability density function (PDF) of $\|x^*(0)\|$ is given by:

$$f_{\|x^*(0)\|}(r_0) = \lambda 2\pi r_0 \exp(-\lambda\pi r_0^2). \tag{2.7}$$

The downlink SIR at the typical user is:

$$SIR(0) = \frac{PF_0/l(\|x^*(0)\|)}{\sum_{X_i\in\Phi\setminus x^*(0)} PF_i/l(\|X_i\|)}, \tag{2.8}$$

where F_0 and $\{F_i\}$ represent independent and identically distributed exponential (i.i.d.) random variables with unit mean. The closed-form CCDF for $SIR(0)$, or equivalently the coverage probability of the typical user, can be derived as follows:

$$\mathbb{P}\left(\frac{PF_0/l(\|x^*(0)\|)}{\sum_{X_i\in\Phi\setminus x^*(0)} PF_i/l(\|X_i\|)} > T\right)$$

$$
\begin{aligned}
&\overset{(a)}{=} \int_0^\infty \mathbb{P}\left(\frac{PF_0/l(r_0)}{\sum_{X_i\in\Phi\setminus x^*(0)} PF_i/l(\|X_i\|)} > T \middle| x^*(0) = (r_0, 0) \right) f_{\|x^*(0)\|}(r_0)\mathrm{d}r_0 \\
&\overset{(b)}{=} \int_0^\infty \mathbb{P}\left(\frac{PF_0/l(r_0)}{\sum_{X_i\in\Phi\setminus x^*(0)} PF_i/l(\|X_i\|)} > T \middle| x^*(0) \in \Phi, \Phi(B(0,r_0)) = 0 \right) f_{\|x^*(0)\|}(r_0)\mathrm{d}r_0 \\
&\overset{(c)}{=} \int_0^\infty \mathbb{P}\left(\frac{PF_0/l(r_0)}{\sum_{X_i\in\Phi} PF_i/l(\|X_i\|)} > T \middle| \Phi(B(0,r_0)) = 0 \right) f_{\|x^*(0)\|}(r_0)\mathrm{d}r_0 \\
&\overset{(d)}{=} \int_0^\infty \mathbb{P}\left(\frac{PF_0/l(r_0)}{\sum_{X_i\in\Phi\setminus B(0,r_0)} PF_i/l(\|X_i\|)} > T \right) f_{\|x^*(0)\|}(r_0)\mathrm{d}r_0 \\
&\overset{(e)}{=} \int_0^\infty \mathbb{E}\left[\sum_{X_i\in\Phi\setminus B(0,r_0)} \exp\left(-TF_i l(r_0)/l(\|X_i\|) \right) \right] f_{\|x^*(0)\|}(r_0)\mathrm{d}r_0 \\
&\overset{(f)}{=} \int_0^\infty \mathbb{E}\left[\prod_{X_i\in\Phi\setminus B(0,r_0)} \frac{1}{1+Tl(r_0)/l(\|X_i\|)} \right] f_{\|x^*(0)\|}(r_0)\mathrm{d}r_0 \\
&\overset{(g)}{=} \int_0^\infty \exp\left(-2\pi\lambda \int_{r_0}^\infty \frac{Tl(r_0)r}{Tl(r_0)+l(r)}\mathrm{d}r \right) \lambda 2\pi r_0 \exp(-\lambda\pi r_0^2)\mathrm{d}r_0 \\
&\overset{(h)}{=} \frac{1}{1+2\int_1^\infty \frac{T\mathrm{d}r}{T+r^\beta}}.
\end{aligned} \tag{2.9}
$$

Step (a) is obtained by conditioning on the location of $x^*(0)$ as $(r_0, 0)$, which is independent of its angle since PPP is isotropic. Step (b) is because the event $\{x^*(0) = (r_0, 0)\}$ is equivalent to $\{x^*(0) \in \Phi\} \cap \{\Phi(B(0, r_0)) = 0\}$, where $B(0, r_0)$ denotes the ball centered around origin with radius r_0. Step (c) and (d) follow from the Slivnyak theorem and complete independence of PPP respectively. Since F_0 and $\{F_i\}$ are i.i.d. exponential random variables with mean 1, step (e) and step (f) are obtained. Step (g) is derived by substituting the nonnegative function $f(x) = \log(1 + Tl(r_0)/l(x))\mathbb{1}_{\|x\|\geq r_0}$ into the Laplace functional (2.3). Finally, step (h) is because the path loss function is $l(r) = r^\beta$.

As shown in (2.9), the coverage probability for Poisson network can be easily evaluated, and many useful design insights can be observed directly

from (2.9). For example, in the interference-limited Poisson cellular network, the coverage probability does not depend on the BS intensity λ, and therefore the area spectral efficiency scales linearly w.r.t. λ [2].

Although PPP has good analytical tractability for modeling macro cellular networks, it neglects the repulsiveness among macro BS locations. By generating 1000 realizations of the PPP fitted to the Houston macro BS deployment in Fig. 1.2a, Fig. 2.1 evaluates the goodness-of-fit of the PPP in terms of the coverage probability. Fig. 2.1 also evaluates the goodness-of-fit for the perturbed hexagonal grid model, which is obtained by independently perturbing each point of a hexagonal grid in the random direction by a distance d [26]. This distance is uniformly distributed between 0 and ηr, with r being the radius of the hexagonal cells and η is chosen as 0.5 in our simulation. Fig. 2.1 shows that the coverage probability of the PPP and of the perturbed hexagonal grid model, correspond to a lower bound and an upper bound of the actual coverage probability respectively. As a result, an accurate yet still tractable point process model for macro BSs is necessary. In the rest of this chapter, we will demonstrate that the determinantal point processes satisfy such purpose.

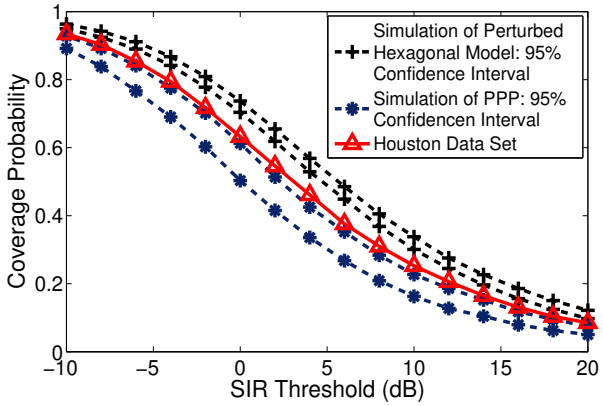

Figure 2.1: Coverage probability of the PPP and the perturbed grid model.

2.5 Mathematical Preliminaries on Determinantal Point Processes

2.5.1 Definition of Determinantal Point Processes

DPPs are defined based on their n-th joint intensity. Consider a spatial point process Φ defined on a locally compact space Λ; then Φ has n-th joint intensity (or n-th order product density) $\rho^{(n)} : \Lambda^n \to [0, \infty)$ if for any Borel function $h : \Lambda^n \to [0, \infty)$:

$$E \sum_{X_1,...,X_n \in \Phi}^{\neq} h(X_1, ..., X_n) = \int_\Lambda \cdots \int_\Lambda \rho^{(n)}(x_1, ..., x_n) \times h(x_1, ..., x_n) \mathrm{d}x_1 \cdots \mathrm{d}x_n, \tag{2.10}$$

where $\neq$ means $X_1, ..., X_n$ are pair-wise different. For all pairwise distinct points $x_1, ..., x_n$, $\rho^{(n)}(x_1, ..., x_n)\mathrm{d}x_1 \cdots \mathrm{d}x_n$ is the probability of finding a point in the region centered around x_i with volume $\mathrm{d}x_i$ $(i = 1, ..., n)$. In particular, $\rho^{(1)}(x)$ is the intensity function of Φ.

Let $\mathbb{C}$ denote the complex plane; then for any function $K : \Lambda \times \Lambda \to \mathbb{C}$, we use $(K(x_i, x_j))_{1 \le i,j \le n}$ to denote the square matrix with $K(x_i, x_j)$ as its (i, j)-th entry. In addition, denote by $\det A$ the determinant of the square matrix A.

Definition 2.5.1. The point process Φ defined on a locally compact space Λ is called a determinantal point process with kernel $K : \Lambda \times \Lambda \to \mathbb{C}$, if its n-th joint intensity has the following form:

$$\rho^{(n)}(x_1, ..., x_n) = \det\left(K(x_i, x_j)\right)_{1 \le i,j \le n}, (x_1, ..., x_n) \in \Lambda^n. \tag{2.11}$$

Note that PPP is a special case of DPP whenever $K(x, y) = 0$ for $x \neq y$. For the rest of this chapter, the kernel function $K(x, y)$ is assumed to be a continuous, Hermitian, locally square integrable and non-negative definite function[2]. We will focus on DPPs defined on the Euclidean plane $\mathbb{R}^2$, and we denote the DPP Φ with kernel K by $\Phi \sim \mathrm{DPP}(K)$.

Remark 2.5.1. The repulsive nature of DPPs can be explained by the fact that if K is continuous, then $\rho^{(n)}(x_1, ..., x_n) \approx 0$ when two points x_i and x_j for $i \neq j$ are close by. In contrast, the joint intensity of a stationary PPP with intensity $\lambda > 0$ is $\rho^{(n)}(x_1, ..., x_n) = \lambda^n$ whenever $x_i \neq x_j$ for $i \neq j$, which means two distinct points on PPP can be arbitrarily close to each other with constant probability.

[2]This is not a sufficient condition to guarantee the existence of the DPP. Readers are referred to [31, 32] for more details.

A DPP Φ is stationary if its n-th order product density is invariant under translations. A natural way to guarantee the stationarity of a DPP is that its kernel K has the form:

$$K(x, y) = K_0(x - y), \qquad x, y \in \mathbb{R}^2.$$

In this case, K_0 is also referred to as the covariance function of the stationary DPP. For stationary DPPs, the intensity measure is constant over $\mathbb{R}^2$. Further if the stationary DPP is isotropic, i.e., invariant under rotations, its kernel only depends on the distance between the node pair.

Definition 2.5.2. (Spectral Density[32]) The spectral density φ of a stationary DPP Φ with covariance function $K_0(t)$ is defined as the Fourier transform of $K_0(t)$, i.e., $\varphi(x) = \int_{\mathbb{R}^2} K_0(t) e^{-2\pi i x \cdot t} \mathrm{d}t$ for $x \in \mathbb{R}^2$.

The spectral density is useful for simulating stationary DPPs. In addition, the spectral density can also be used to assess the existence of the DPP associated with a certain kernel. Specifically, from Proposition 5.1 in [32], the existence of a DPP is equivalent to its spectral density φ belonging to $[0, 1]$.

2.5.2 Computational Properties of DPPs

We now list several important computational properties for the DPPs, which make them suitable to analyze the cellular networks.

1. DPPs have closed-form joint intensities of any order. Specifically, for any $n \in \mathbb{N}$, the n-th joint intensity of $\Phi \sim \mathrm{DPP}(K)$ is given by (2.11).

Therefore, higher order moment measures of shot noise fields such as the mean/variance of interference in cellular networks can be derived.

2. DPPs have a closed-form Laplace functional for any nonnegative measurable function f on $\mathbb{R}^2$ with compact support [35, Theorem 1.2].

Lemma 2.5.1 (Shirai *et al.* [35])**.** *Consider $\Phi \sim DPP(K)$ defined on $\mathbb{R}^2$, where the kernel K guarantees the existence of Φ. Then Φ has the Laplace functional:*

$$\begin{aligned}&\mathbb{E}\left[\exp\left(-\int_{\mathbb{R}^2} f(x)\Phi(\mathrm{d}x)\right)\right]\\ =&\sum_{n=0}^{+\infty}\frac{(-1)^n}{n!}\int_{(\mathbb{R}^2)^n}\det\left(K(x_i,x_j)\right)_{1\le i,j\le n}\\ &\times\prod_{i=1}^{n}\left(1-\exp(-f(x_i))\right)\mathrm{d}x_1...\mathrm{d}x_n,\end{aligned}\tag{2.12}$$

for any nonnegative measurable function f on $\mathbb{R}^2$ with compact support.

In fact, having a compact support is a strong requirement for the function f, and we are able to prove that (2.12) holds for more general functions.

Lemma 2.5.2. *For $\Phi \sim DPP(K)$ with kernel K guarantees the existence of Φ. Then for any nonnegative measurable function f which satisfies the following conditions*[3]*: (a) $\lim_{|x|\to\infty} f(x) = 0$; (b) $\lim_{r\to\infty}\int_{\mathbb{R}^2\setminus B(0,r)} K(x,x)f(x)\mathrm{d}x = 0$; and (c) $\int_{\mathbb{R}^2} K(x,x)(1-\exp(-f(x)))\mathrm{d}x < +\infty$, then the Laplace functional of Φ is given by (2.12).*

[3]For $x \in \mathbb{R}^2$ and $r \ge 0$, $B(x,r)$ ($B^o(x,r)$) denotes the closed (open) ball with center x and radius r. In addition, $B^c(x,r)$ denotes the complement of $B(x,r)$.

Proof. The proof is provided in Appendix 2.10.1. □

Based on Lemma 2.5.2, we can derive the following two lemmas.

Lemma 2.5.3. *If K guarantees the existence of $\Phi \sim DPP(K)$, then the probability generating functional (pgfl) of Φ is:*

$$\begin{aligned} G[v] \triangleq & \mathbb{E}\left(\prod_{x\in\Phi} v(x)\right) \\ = & \sum_{n=0}^{+\infty} \frac{(-1)^n}{n!} \int_{(\mathbb{R}^2)^n} \det\left(K(x_i,x_j)\right)_{1\le i,j\le n} \\ & \times \prod_{i=1}^{n} (1-v(x_i))\,\mathrm{d}x_1 ... \mathrm{d}x_n, \end{aligned} \tag{2.13}$$

for all measurable functions $v : \mathbb{R}^2 \to [0,1]$, such that $-\log v$ satisfies the conditions in Lemma 2.5.2.

Lemma 2.5.4. *Consider a DPP $\Phi = \sum_i \delta_{x_i}$, where Φ is defined on $\mathbb{R}^2$ with kernel K. Each node $x_i \in \Phi$ is associated with an i.i.d. mark p_i, which is independent of x_i with probability law $F(\cdot)$. Then the Laplace functional of the independently marked point process $\tilde{\Phi} = \sum_i \delta_{(x_i,p_i)}$ is given by:*

$$\begin{aligned} L_{\tilde{\Phi}}(f) \triangleq & \mathbb{E}\left[\exp\left(-\sum_i f(x_i,p_i)\right)\right] \\ = & \sum_{n=0}^{+\infty} \frac{(-1)^n}{n!} \int_{(\mathbb{R}^2)^n} \det\left(K(x_i,x_j)\right)_{1\le i,j\le n} \\ & \times \prod_{i=1}^{n} \left(1 - \int_{\mathbb{R}^+} \exp(-f(x_i,p_i))F(\mathrm{d}p_i)\right) \mathrm{d}x_1 ... \mathrm{d}x_n, \end{aligned} \tag{2.14}$$

for any nonnegative measurable function f such that $-\log \int_{\mathbb{R}^+} \exp(-f(x,p))F(\mathrm{d}p)$ satisfies the conditions in Lemma 2.5.2.

Proof. The proof is provided in Appendix 2.10.2. □

The Laplace functional provides a strong tool to analyze the shot noise field of a DPP. In particular, it facilitates the analysis of interference and coverage probability in cellular networks.

3. Under the reduced Palm distribution[4], the DPP has the law of another DPP whose kernel is given in closed-form [35, Theorem 1.7].

Lemma 2.5.5 (Shirai *et al.* [35])**.** *Consider $\Phi \sim DPP(K)$, where the kernel K guarantees the existence of Φ. Then under the reduced Palm distribution at $x_0 \in \mathbb{R}^2$, Φ coincides with another DPP associated with kernel $K^!_{x_0}$ for Lebesgue almost all x_0 with $K(x_0, x_0) > 0$, where:*

$$K^!_{x_0}(x, y) = \frac{1}{K(x_0, x_0)} \det \begin{pmatrix} K(x, y) & K(x, x_0) \\ K(x_0, y) & K(x_0, x_0) \end{pmatrix}. \tag{2.15}$$

This property shows that DPPs are closed under the reduced Palm distribution, which provides a tool similar to Slyvniak's theorem for Poisson processes [44]. In cellular networks, when x_0 is chosen as the serving base station to the typical user, this property shows that all other interferers will form another DPP with the modified kernel provided in (2.15).

[4]For a spatial point process Φ, denote $\mathbb{P}^!_{x_0}(\cdot)$ as the reduced Palm distribution given $x_0 \in \Phi$. For any event A, a heuristic definition of $\mathbb{P}^!_{x_0}(\cdot)$ is: $\mathbb{P}^!_{x_0}(A) = \mathbb{P}(\Phi \backslash \{x_0\} \in A | x_0 \in \Phi)$. The readers are referred to [44, p. 131] for formal definitions.

2.5.3 Examples of Stationary DPPs

In this chapter, we consider three stationary DPP models that are proposed in [32].

Gauss DPP Model: A stationary point process Φ is a Gauss DPP if it has covariance function:

$$K_0(x) = \lambda \exp(-\|x\|^2/\alpha^2), \qquad x \in \mathbb{R}^2. \tag{2.16}$$

In the above definition, λ denotes the spatial intensity of the Gauss DPP, while α is a measure of its repulsiveness. In order to guarantee the existence of the Gauss DPP model, the parameter pair (λ, α) needs to satisfy: $\lambda \leq (\sqrt{\pi}\alpha)^{-2}$.

Cauchy DPP Model: The Cauchy DPP model has a covariance function:

$$K_0(x) = \frac{\lambda}{(1 + \|x\|^2/\alpha^2)^{\nu+1}}, \qquad x \in \mathbb{R}^2. \tag{2.17}$$

In this model, λ describes the intensity, while α is the scale parameter and ν is the shape parameter. Both α and ν affect the repulsiveness of the Cauchy DPP. To guarantee the existence of a Cauchy DPP, the parameters need to satisfy: $\lambda \leq \frac{\nu}{(\sqrt{\pi}\alpha)^2}$.

Generalized Gamma DPP Model: The Generalized Gamma DPP model is defined based on its spectral density:

$$\varphi(x) = \lambda \frac{\nu\alpha^2}{2\pi\Gamma(2/\nu)} \exp(-\|\alpha x\|^\nu), \tag{2.18}$$

where $\Gamma(\cdot)$ denotes the Euler Gamma function. The existence of a Generalized Gamma DPP can be guaranteed when $\lambda \leq \frac{2\pi\Gamma(2/\nu)}{\nu\alpha^2}$.

2.6 Fundamental Analysis for Macro Cellular Networks using DPPs

In this section, based on the three important computational properties discussed in Chapter 2.5.2, we will derive several fundamental performance metrics for the downlink macro cellular networks with DPP configured BSs: (1) the empty space function; (2) the nearest neighbor function; (3) Laplace transform of the total interference; and (4) the downlink SIR distribution.

2.6.1 Empty Space Function

The empty space function is the cumulative distribution function (CDF) of the distance from the origin to its nearest point in the point process. Consider $\Phi \sim \text{DPP}(K)$ and let $d(o,\Phi) = \inf\{\|x\| : x \in \Phi\}$; then the empty space function $F(r)$ is defined as: $F(r) = \mathbb{P}\left(d(o,\Phi) \leq r\right)$ for $r \geq 0$ [44]. In cellular networks, when each user is associated with its nearest BS, the empty space function provides the distribution of the distance from the typical user to its serving BS, which further dictates the statistics of the received signal power at the typical user. Based on the Laplace functional of DPP models provided in Lemma 2.5.1, we have the following lemma:

Lemma 2.6.1. *For any $\Phi \sim$ DPP(K), the empty space function $F(r)$ for $r \geq 0$ is given by:*

$$F(r) = \sum_{n=1}^{+\infty} \frac{(-1)^{n-1}}{n!} \int_{(B(0,r))^n} \det\left(K(x_i,x_j)\right)_{1\leq i,j\leq n} \mathrm{d}x_1 ... \mathrm{d}x_n. \tag{2.19}$$

Proof. The proof is provided in Appendix 2.10.3. □

Based on Lemma 2.6.1, we can also characterize the probability density function (PDF) $f(r)$ of the distance from the origin to its nearest point for all stationary and isotropic DPPs Φ.

Corollary 2.6.2. *Let $F(r)$ denote the empty space function for a stationary and isotropic DPP Φ with covariance function K. Then $f(r) \triangleq \frac{\mathrm{d}F(r)}{\mathrm{d}r}$ is given by:*

$$f(r) = 2\pi r \sum_{n=0}^{+\infty} \frac{(-1)^n}{n!} \int_{(B(0,r))^n} \det(K(x_i, x_j))_{0\leq i,j\leq n} \Big|_{x_0=(r,0)} \mathrm{d}x_1 ... \mathrm{d}x_n. \quad (2.20)$$

Proof. The proof is provided in Appendix 2.10.4. □

2.6.2 Nearest Neighbor Function

The nearest neighbor function gives the distribution of the distance from the typical point of a point process to its nearest neighbor in the same point process. For all stationary DPPs Φ, the nearest neighbor function can be defined based on the reduced Palm distribution of Φ as: $D(r) = \mathbb{P}_o^!(d(o, \Phi) \leq r)$ [44].

In cellular networks, the nearest neighbor function provides the distribution of the distance from a typical BS to its nearest neighboring BS, which can be used as a metric to indicate the clustering/repulsive behavior of the network. Specifically, compared to the PPP, a regularly deployed network corresponds to a smaller nearest neighbor function, while a clustered network corresponds to a larger nearest neighbor function. Therefore, when each user is

associated with its nearest BS, the dominant interferers in regularly deployed networks are farther from the serving BS than a completely random network.

Lemma 2.6.3. *For any $\Phi \sim DPP(K)$ defined on $\mathbb{R}^2$, its nearest neighbor function $D(r)$ is given by:*

$$D(r) = \sum_{n=1}^{+\infty} \frac{(-1)^{n-1}}{n!} \int_{(B(0,r))^n} \det\left(K_o^!(x_i, x_j)\right)_{1\leq i,j\leq n} \mathrm{d}x_1 ... \mathrm{d}x_n, \tag{2.21}$$

where $K_o^!(x, y)$ is:

$$K_o^!(x, y) = \frac{1}{K(0,0)} \det \begin{pmatrix} K(x,y) & K(x,0) \\ K(0,y) & K(0,0) \end{pmatrix}. \tag{2.22}$$

This lemma can be proved noting if $\tilde{\Phi} \sim \mathrm{DPP}(K_o^!(x, y))$, then it follows from Lemma 2.5.5 that: $\mathbb{P}_o^!(d(o, \Phi) \leq r) = \mathbb{P}(d(o, \tilde{\Phi}) \leq r)$.

2.6.3 Interference Distribution

Interference is an important factor that limits the coverage probability and mean data rate in wireless networks. In this section, we analyze the properties of shot noise fields associated with a DPP. Our aim is to evaluate interference in cellular networks under two BS association schemes. First, the BS to which the typical user is associated is assumed to be at an arbitrary but fixed location. We show that in this case, the mean interference is easy to characterize with DPP configured BSs. This simple conditional interference scenario provides a fundamental understanding of interference in wireless networks with DPP configured nodes. The results in this case can be extended to ad-hoc networks as well. Second, each user is assumed to be associated with its nearest BS. In this case, we derive the Laplace transform of interference.

2.6.3.1 Interference with fixed associated BS scheme

Since Φ is invariant under translation and rotation, we assume the typical user located at the origin is served by the base station at $x_0 = (r_0, 0)$, where r_0 denotes the distance from the origin to x_0. Conditionally on $x_0 \in \Phi$ being the serving BS, the interference at the origin is: $I = \sum_{x_i \in \Phi \setminus x_0} P h_{x_i} / l(\|x_i\|)$.

Lemma 2.6.4. *Given $x_0 = (r_0, 0)$ is the serving BS for the typical user located at the origin, the mean interference seen by this typical user is:*

$$\mathbb{E}[I | x_0 = (r_0, 0)] = P \int_{\mathbb{R}^2} K^!_{x_0}(x, x) / l(\|x\|) \mathrm{d}x, \tag{2.23}$$

where $K^!_{x_0}(\cdot, \cdot)$ is given in (2.15)[5].

Proof. This result is proved in Appendix 2.10.5. □

In fact, all the higher order moment measures of the interference can be calculated similarly based on Definition 2.5.1 and Lemma 2.5.5.

2.6.3.2 Interference with nearest BS association scheme

In this part, we consider the BS association scheme where each user is served by its nearest BS. In single tier cellular networks, the nearest BS association scheme provides the highest average received power for each user.

[5]This lemma can be seen as a general property of the shot noise field I created by a DPP, since it holds for all function $l(\cdot)$.

For a user located at $y \in \mathbb{R}^2$, its associated BS is denoted by $x^*(y) = \underset{x\in\Phi}{\operatorname{argmin}}\|x - y\|$. Consider the typical user located at the origin and its associated BS $x^*(0)$. The interference at the typical user is then given by $I = \sum_{x_i\in\Phi\setminus x^*(0)} Ph_{x_i}/l(\|x_i\|)$, where $h_{x_i} \sim \exp(1)$ denotes the Rayleigh fading variable from x_i to the origin. In the next theorem, we provide the general result which characterizes the Laplace transform of interference conditional on the position of the BS nearest to the typical user.

Theorem 2.6.5. *Conditionally on $x^*(0) = x_0$ being the serving BS of the typical user at the origin, if $f(x, h_x) = sPh_x\mathbb{1}_{|x|\geq r_0}/l(\|x\|) - \log \mathbb{1}_{|x|\geq r_0}$ satisfies the conditions in Lemma 2.5.4, then the Laplace transform of the interference at the typical user is:*

$$\begin{aligned}&\mathbb{E}[e^{-sI}|x^*(0) = x_0]\\ =&\frac{\sum_{n=0}^{+\infty}\frac{(-1)^n}{n!}\int_{(\mathbb{R}^2)^n}\det(K^!_{x_0}(x_i,x_j))_{1\leq i,j\leq n}\times\prod_{i=1}^{n}[1-\frac{\mathbb{1}_{|x_j|\geq r_0}}{1+sP/l(\|x_i\|)}]\mathrm{d}x_1...\mathrm{d}x_n}{\sum_{n=0}^{+\infty}\frac{(-1)^n}{n!}\int_{B(0,r_0)^n}\det(K^!_{x_0}(x_i,x_j))_{1\leq i,j\leq n}\mathrm{d}x_1...\mathrm{d}x_n},\end{aligned} \tag{2.24}$$

where $r_0 = |x^*(0)|$ and $K^!_{x_0}(\cdot,\cdot)$ is given in (2.15).

Proof. Please see Appendix 2.10.6. □

Remark 2.6.1. In contrast with what happens in the PPP case, because of the repulsion among DPP points, $\Phi \cap B^c(0, r_0)$ and $\Phi \cap B^o(0, r_0)$ are not independent.

Remark 2.6.2. If Φ is a stationary PPP with intensity λ, then by substituting $\det(K(x_i,x_j))_{1\leq i,j\leq n} = \det(K^!_{x_0}(x_i,x_j))_{1\leq i,j\leq n} = \lambda^n$, Theorem 2.6.5 gives the Laplace transform of the interference at the typical user to be:

$$\mathbb{E}[e^{-sI}|x^*(0)=x_0] = \exp\left(-\lambda\int_{B^c(0,r_0)}(1-\frac{1}{1+sP/l(\|x\|)})\mathrm{d}s\right),$$

which is consistent with (12) in [2].

Since the Laplace transform fully characterizes the probability distribution, many important performance metrics can be derived using Theorem 2.6.5. Specifically, the next lemma gives the mean interference under the nearest BS association scheme.

Lemma 2.6.6. *The mean interference at the typical user conditional on* $x^*(0)=x_0$ *is:*

$$\begin{aligned}&\mathbb{E}[I|x^*(0)=x_0]\\ =&\frac{\sum_{n=0}^{+\infty}\frac{(-1)^n}{n!}\int_{(B(0,r_0))^n}\int_{B^c(0,r_0)}\det(K^!_{x_0}(x_i,x_j))_{1\leq i,j\leq n+1}P/l(\|x_1\|)\mathrm{d}x_1...\mathrm{d}x_{n+1}}{\sum_{n=0}^{+\infty}\frac{(-1)^n}{n!}\int_{(B(0,r_0))^n}\det(K^!_{x_0}(x_i,x_j))_{1\leq i,j\leq n}\mathrm{d}x_1...\mathrm{d}x_n},\end{aligned}$$

where $r_0=|x_0|$.

Proof. The proof is provided in Appendix 2.10.7. □

Since the DPPs are assumed to be stationary and isotropic, thus only the distance from the origin to its nearest BS will affect the mean interference result, which can be observed from Lemma 2.6.6.

2.6.4 SIR Distribution

Based on the same assumptions as in Section 2.6.3, we derive the SIR distribution as the CCDF of the SIR at the typical user under the nearest BS association scheme. Denote by $x^*(0)$ the BS to which the typical user at the origin associates, its received SIR can be expressed as:

$$\mathrm{SIR}(0,\Phi)=\frac{Ph_{x_0}/l(\|x^*(0)\|)}{\sum_{x_i\in\Phi\setminus x^*(0)}Ph_{x_i}/l(\|x_i\|)}. \tag{2.25}$$

In Corollary 2.6.2, the probability density function for the distance from the origin to its nearest BS has been characterized. Therefore, by combining Corollary 2.6.2 and Theorem 2.6.5, we are able to compute the SIR distribution of the typical user under the nearest BS association scheme.

Theorem 2.6.7. *The SIR distribution of the typical user is given by:*

$$\begin{aligned}&\mathbb{P}(SIR(0,\Phi)>T)\\ =&\int_0^{+\infty}\lambda 2\pi\Bigg[\sum_{n=0}^{+\infty}\frac{(-1)^n}{n!}\int_{(\mathbb{R}^2)^n}\det(K^!_{x_0}(x_i,x_j)_{1\le i,j\le n})\\ &\times\prod_{i=1}^{n}[1-\frac{\mathbb{1}_{|x_i|\ge r_0}}{1+Tl(\|x_0\|)/l(\|x_i\|)}]\Big|_{x_0=(r_0,0)}\mathrm{d}x_1...\mathrm{d}x_n\Bigg]r_0\mathrm{d}r_0.\end{aligned} \tag{2.26}$$

Proof. Please see Appendix 2.10.8. □

Remark 2.6.3. If we choose Φ as a stationary PPP with intensity λ, i.e., $\det(K(x_i,x_j))_{1\le i,j\le n}=\det(K^!_{x_0}(x_i,x_j))_{1\le i,j\le n}=\lambda^n$, then Theorem 2.6.7 leads to the same result as [2, Theorem 2].

2.7 Numerical Evaluation

In this section, we provide the numerical method used to evaluate the analytical results derived in Chapter 2.6. Fig. 2.2 shows the BS deployment[6] of 115 BSs in a 16 km $\times$ 16 km area of Houston, which represent sprawling and relatively flat areas where repulsion among BSs is expected. Based on the maximum likelihood (ML) estimate method which is implemented in the software package provided in [32], we have summarized the estimated parameters for different DPPs fitted to the Houston data set in Table 2.1.

In the following, we will focus on the numerical results using the Gauss DPP fitted to the Houston data set. Our simulation results for each metric are based on the average of 1000 realizations of the fitted Gauss DPP. Realizations of the Gauss DPP, Cauchy DPP and Generalized Gamma DPP fitted to the Houston urban area deployment are shown in Fig. 2.3. From these figures, it can be observed that the fitted DPPs are regularly distributed and close to the real BS deployments. In Section 2.8, we will rigorously validate the accuracy of these DPPs based on different summary statistics.

Table 2.1: DPP Parameters for the Houston Data Set

Model	λ	α	ν
Gauss DPP	0.4492	0.8417	–
Cauchy DPP	0.4492	1.558	3.424
Generalized Gamma DPP	0.4492	2.539	2.63

The Laplace functional of DPPs involves a series representation, where

[6]BS location data was provided by Crown Castle.

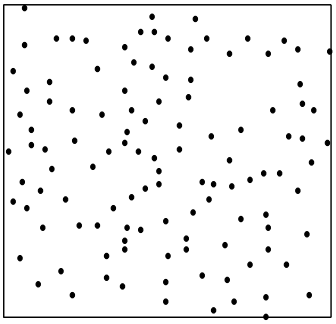

Figure 2.2: Houston data set

each term is a multi-dimensional integration. Therefore, we adopt the Quasi-Monte Carlo (QMC) integration method [46] for efficient numerical integration. The QMC integration method approximates the multi-dimensional integration of function $f : [0,1]^n \to \mathbb{R}$ as:

$$\int_{[0,1]^n} f(\mathbf{x}) d\mathbf{x} \approx \frac{1}{N} \sum_{n=0}^{N-1} f(\mathbf{x}_n).$$

The sample points $\mathbf{x}_0, ..., \mathbf{x}_{N-1} \in [0,1]^n$ are chosen deterministically in the QMC method, and we use the Sobol points generated in MATLAB as the choice for sample points [47]. Compared to the regular Monte Carlo integration method which uses a pseudo-random sequence as the sample points, the QMC integration method converges much faster.

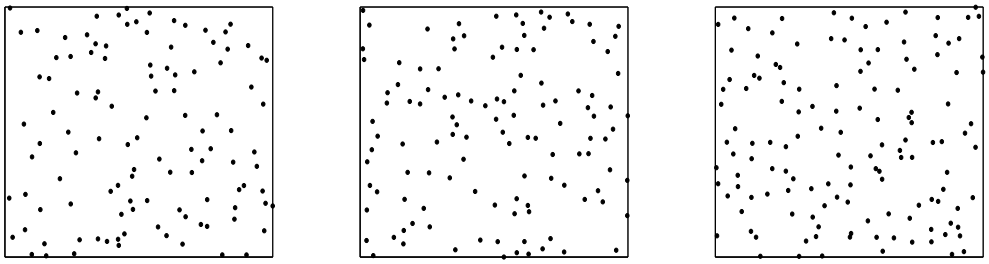

Figure 2.3: Gauss DPP (left), Cauchy DPP (middle) and Generalized Gamma DPP (right) fitted to the Houston BS deployment.

2.7.1 Empty Space Function

Since the QMC integration method requires integration over the unit square, (2.19) can be rewritten as:

$$F(r) = \sum_{n=1}^{+\infty} \frac{(-1)^{n-1}(2r)^{2n}}{n!} \int_{([0,1]\times[0,1])^n} \det(K_0(2r(x_i - x_j)))_{1\le i,j\le n} \prod_i \mathbb{1}_{\{\|x_i-(\frac{1}{2},\frac{1}{2})\|\le\frac{1}{2}\}} \mathrm{d}x_1 ... \mathrm{d}x_n, \tag{2.27}$$

where $K_0(x)$ is the covariance function for the DPP Φ.

The accuracy of (2.27) is verified by computing the empty space function of the Gauss DPP fitted to the Houston data set. Specifically, for the Gauss DPP model, $K_0(x) = \lambda \exp(-\|x/\alpha\|^2)$, where λ and α are chosen according to Table 2.1. Fig. 2.4 shows the QMC integration results of (2.27) with different numbers of Sobol points, as well as the simulation result for the fitted Gauss DPP. We have observed that when the number of Sobol points is 2^{11}, (2.27) can be computed very efficiently (in a few seconds) and the QMC integration results are accurate except for the part where $F(r)$ is over 95%. If

the number of Sobol points is increased to 2^{15}, the QMC integration method is almost 10 times slower while the results are accurate for a much larger range of r. This shows that small number of Sobol points is sufficient to achieve accurate QMC integration results for small r, while more Sobol points are needed to achieve accurate QMC integration result when r grows larger. In contrast, simulating the empty space function involves generating 1000 realizations of the fitted Gauss DPP, which typically takes several minutes due to the complicated algorithm to simulate DPP [32]. Therefore, the numerical method using QMC integration is more efficient than simulation to evaluate the empty space function.

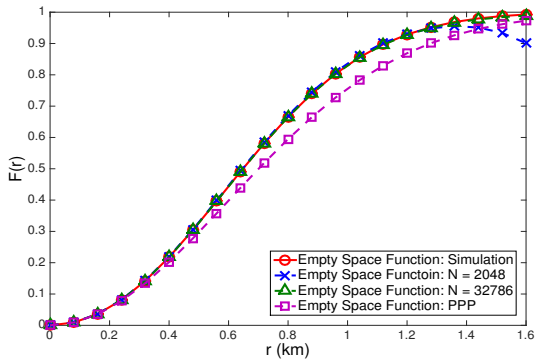

Figure 2.4: Empty space function of the fitted Gauss DPP.

The empty space function of the fitted PPP is also provided in Fig. 2.4. Since the DPPs have more regularly spaced point pattern, they will have larger empty space function than the PPPs. Equivalently, this means the distance from the origin to its closest point on the DPPs is stochastically less than for PPPs, which can be observed from Fig. 2.4 for the Gauss DPP.

Therefore, if each user is associated with its nearest BS, DPPs will lead to a stronger received power at the typical user compared to PPPs in the stochastic dominance sense.

Nearest Neighbor Function: The QMC integration method is also efficient in the numerical evaluation of the nearest neighbor function. Similar to the empty space function, the QMC integration method with $N = 2^{11}$ takes a few seconds to return $D(r)$ in Fig. 2.5, which is accurate up to 95%. By contrast, the QMC integration method is more accurate but almost ten times slower when the number of sample points is increased to $N = 2^{15}$.

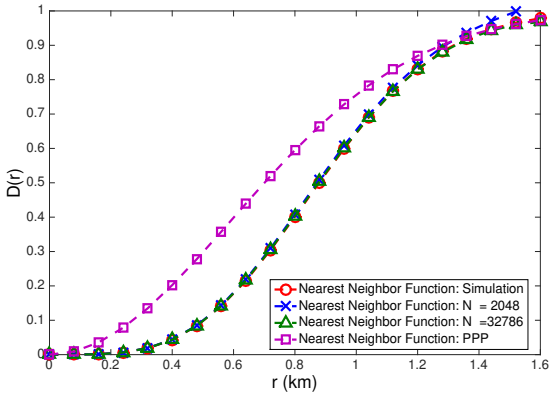

Figure 2.5: Nearest neighbor function of the fitted Gauss DPP.

We can also observe from Fig. 2.5 that the fitted DPPs will have smaller nearest neighbor function than the PPP, especially when r is small. This indicates that the PPP will largely overestimate the nearest neighbor function when r is small, which leads to much closer strong interfering BSs compared to the Gauss DPP.

2.7.2 Mean Interference

In this part, the mean interference of the Gauss DPP is numerically evaluated for the path loss model $l(r) = \max(1, r^{\beta})$, where $\beta > 2$ is the path loss exponent.

2.7.2.1 Mean interference with fixed associated BS scheme

Corollary 2.7.1. *Conditionally on $x_0 = (r_0, 0)$ as the serving BS for the typical user, the mean interference at the typical user when BSs are distributed according to the Gauss DPP with parameters (λ, α) is given by:*

$$\mathbb{E}[I|x_0 = (r_0, 0)] = \frac{P\pi\lambda\beta}{\beta - 2} - 2P\pi\lambda \exp(-\frac{2r_0^2}{\alpha^2})(A_1(r_0) + A_2(r_0)),$$

where $A_1(r_0) = \int_0^1 \exp(-\frac{2r^2}{\alpha^2}) I_0(\frac{4rr_0}{\alpha^2}) r \mathrm{d}r$, $A_2(r_0) = \int_1^{\infty} \exp(-\frac{2r^2}{\alpha^2}) r^{1-\beta} I_0(\frac{4rr_0}{\alpha^2}) \mathrm{d}r$. *Here $I_0(\cdot)$ denotes the modified Bessel function of first kind with parameter $\nu = 0$ [48].*

Based on the fact that $\int_0^{2\pi} \exp(\pm\beta\cos(x))\mathrm{d}x = 2\pi I_0(\beta)$ [48, p. 491], this corollary can be derived by substituting the Gauss DPP kernel into Lemma 2.6.4.

In Fig. 2.7, the mean interference for the Gauss DPP fitted to the Houston data set is provided under different path loss exponents with $P = 1$. From Fig. 2.7, it can be observed that the mean interference increases as r_0 increases; this is because it increases the probability for the existence of a strong interferer close to the typical user. In addition, given r_0, the mean

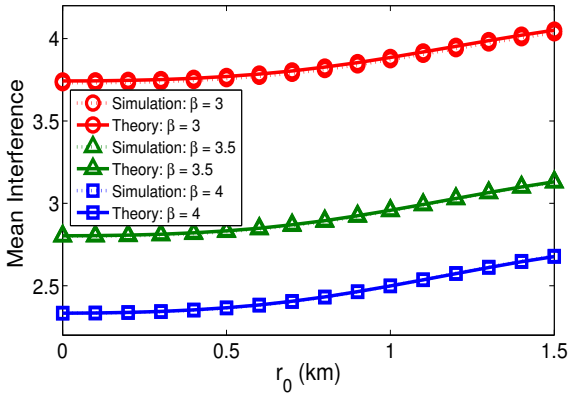

Figure 2.6: Houston data set

Figure 2.7: Mean interference under the fixed associated BS scheme.

interference is decreasing when the path loss exponent β increases; this is because the path loss function is decreasing with respect to β for all interferers.

2.7.2.2 Mean interference with nearest BS association scheme

The Quasi-Monte Carlo integration method is adopted to evaluate the mean interference under the nearest BS association scheme. In Fig. 2.9, the mean interference is evaluated when the path loss exponent β is 3, 3.5, 4. It can be observed from Fig. 2.9 that when r_0 (i.e., the distance from the typical user to its nearest BS) increases, the mean interference decreases. This is because the strong interferers are farther away from the typical user when r_0 increases, which leads to a smaller aggregate interference. This is quite different from the case when the BS associated to the typical user is assumed to be at some fixed location. In addition, since the path loss function $l(r)$ is non-decreasing with respect to β given r, the mean interference decreases when β increases

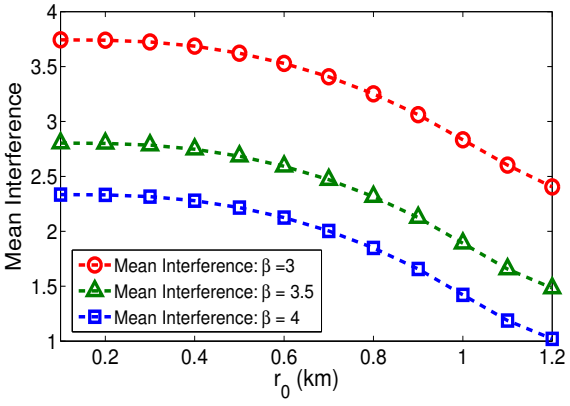

Figure 2.8: Houston data set

Figure 2.9: Mean interference under the nearest BS association scheme.

for a given r_0.

2.7.3 SIR Distribution

The QMC integration method can, in principle, be used to numerically evaluate (2.26). However, it is time consuming due to the need to evaluate multiple integrations over $\mathbb{R}^2$. Therefore, we use the diagonal approximation of the matrix determinant [49] to roughly estimate (2.26). Specifically, the determinant of matrix $(K(x_i, x_j))_{1\leq i,j\leq n}$ is approximated[7] as $\det((K(x_i, x_j))_{1\leq i,j\leq n}) \approx \prod_{i=1}^{n} K(x_i, x_i)$ under the diagonal approximation.

Lemma 2.7.2. *Under the diagonal approximation, the SIR distribution of the typical user is approximated as:*

$$\mathbb{P}(SIR(0,\Phi) > T) \approx \int_0^{+\infty} \lambda 2\pi r_0 \exp\left(- \int_{\mathbb{R}^2} K^!_{x_0}(x,x)\left(1 - \frac{\mathbb{1}_{|x|\geq r_0}}{1 + T\frac{l(\|x_0\|)}{l(\|x\|)}}\right)\Big|_{x_0=(r_0,0)} \mathrm{d}x \right) \mathrm{d}r_0. \tag{2.28}$$

[7]The relative error bound for diagonal approximation is provided in [49, Theorem 1].

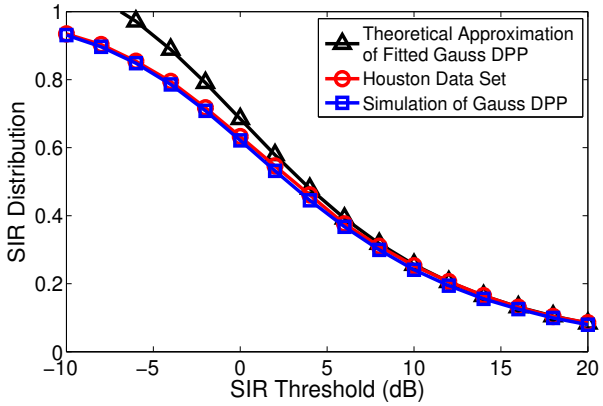

Figure 2.10: Houston data set

Figure 2.11: Diagonal approximation to the SIR distribution of the fitted Gauss DPP.

Lemma 2.7.2 can be proved by applying diagonal approximation to Theorem 2.6.7, thus we omit the proof. Next, the QMC integration method is used to evaluate the accuracy of Lemma 2.7.2 by assuming the BSs are distributed according to the Gauss DPP. The power-law path loss model with path loss exponent $\beta = 4$ is used for simplicity, i.e., $l(r) = r^4$. It can be observed from Fig. 2.11 that for the fitted Gauss DPP model, the diagonal approximation to the SIR distribution is accurate compared to the simulation result in the high SIR regime, i.e., when the SIR threshold is larger than 6 dB. Therefore, we can use the diagonal approximation as an accurate estimate for the SIR distribution in the high SIR regime.

Given the accuracy of the diagonal approximation, the effect of the parameters of the DPP model on the SIR distribution can be easily evaluated

by rewriting (24) as[8]:

$$\mathbb{P}(\mathrm{SIR}(0,\Phi)>T)\approx$$
$$\int_0^{+\infty}\pi\exp\left[-\int_0^{+\infty}\int_0^{2\pi}\left(1-\frac{K_0^2\left(\sqrt{\frac{r_0}{\lambda}(r^2+1-2r\cos\theta)}\right)}{\lambda^2}\right)\right.$$
$$\left.\times\left(1-\frac{\mathbb{1}_{r\geq 1}}{1+Tr^{-\beta}}\right)r_0 r\mathrm{d}\theta\mathrm{d}r\right]\mathrm{d}r_0, \tag{2.29}$$

where the path loss model is $l(r)=r^{\beta}$. Therefore, when the BSs are distributed according to the Gauss DPP model with parameters (λ,α), we can deduce from (2.29) that given α, the SIR distribution will be larger when λ is larger, which means BS densification will improve the SIR performance. This observation is different from [2], which proves that when BSs are modeled as a PPP, the SIR performance does not depend on the BS density. In addition, (2.29) also shows that given λ, larger α will lead to a better SIR distribution. Since larger α corresponds to greater repulsiveness for the Gauss DPP model, this observation is consistent with the intuition that larger repulsiveness among BSs will lead to better SIR performance.

2.8 Goodness-of-fit for Stationary DPPs to Model BS Deployments

DPPs are attractive models for cellular networks not only because they are mathematically tractable, but also because they can accurately model

[8]Since the covariance function $K_0(x)$ of a stationary and isotropic DPP Φ with kernel K only depends on $\|x\|$, so with a slight abuse of notation, we denote $K_0(\|x\|)=K_0(x)$ in (2.29).

macro BS deployments. In this section, we provide rigorous investigation of their modeling accuracy to real BS deployments in this section. Our simulations are based on the publicly available package for DPP models [32] implemented in R, which is used as a supplement to the Spatstat library [50].

2.8.1 Summary Statistics

To test the goodness-of-fit of these DPP models, we have used Ripley's K function and the coverage probability as performance metrics, which are described below:

Ripley's K function: Ripley's K function is a second order spatial summary statistic defined for stationary point processes. It counts the mean number of points within distance r of a given point in the point process excluding the point itself. Formally, the K function $\mathbb{K}(r)$ for a stationary and isotropic point process Φ with intensity λ is defined as:

$$\mathbb{K}(r) = \frac{\mathbb{E}_o^! \left(\Phi(B(0,r))\right)}{\lambda}, \tag{2.30}$$

where $\mathbb{E}_o^!(\cdot)$ is the expectation with respect to the reduced Palm distribution of Φ.

The K-function can also be interpreted in terms of pair correlation function $g_0(r)$, i.e., $\mathbb{K}(r) = 2\pi \int_0^r t g_0(t) dt$. As discussed in the previous section, the pair correlation function can be derived immediately from the kernel of a DPP, so we can have closed form expression for several DPP models. For example, the K-function for Gauss DPP can be derived as $\mathbb{K}(r) = \pi r^2 -$

$\frac{\pi\alpha^2}{2}\left(1-\exp(-\frac{2r^2}{\alpha^2})\right)$.

The K-function is used as a measure of repulsiveness/clustering of spatial point processes. Specifically, compared to the PPP which is completely random, a repulsive point process model will have a smaller K function, while a clustered point process model will have a larger K function. Closed-form expressions of K function can be calculated for Gauss and Cauchy DPP [32], which are strictly smaller than PPP. This explains the repulsiveness of these two DPP models.

Coverage Probability: The coverage probability is defined as the probability that the received SINR at the typical user is larger than the threshold T. When measuring the fitting accuracy of spatial point processes to real BS deployments, metrics related to the wireless system such as the coverage probability are more practical. In particular, the coverage probability also depends on the repulsive/clustering behavior of the underlying point process used to model the BS deployment. Compared to the fitted PPP, due a larger empty space function, the distance from the typical user to its serving BS is stochastically less in a fitted repulsive point process. Similarly, due to a smaller nearest neighbor function, the fitted repulsive point process has stochastically larger distance from the serving BS to its closest interfering BS than the PPP case. Therefore, from (2.25), a larger coverage probability is expected when the BS deployments are modeled by more repulsive spatial point processes. We will use the same parameter assumptions as in Section 2.7.3 for evaluating the coverage probability. Since the thermal noise power is assumed to be 0,

the CCDF of SIR at the typical user, i.e., $\mathbb{P}(\mathrm{SIR}(0,\Phi) > T)$, coincides with its coverage probability with threshold T.

2.8.2 Hypothesis Testing using Summary Statistics

In this part, we evaluate the goodness-of-fit of stationary DPP models using the summary statistics discussed above. Particularly, we fit the real BS deployments in Fig. 2.2 to the Gauss, Cauchy and Generalized Gamma DPPs. To evaluate the goodness-of-fit for these DPP models, we generate 1000 realizations of each DPP model and examine whether the simulated DPPs fit with the behavior of real BS deployments in terms of the summary statistics. Specifically, based on the null hypothesis that real BS deployments can be modeled as realizations of DPPs, we verify whether the K-function of the real data set lies within the envelope of the simulated DPPs. We use similar testing method for the coverage probability; a 95% confidence interval is used for evaluation.

Goodness-of-fit for Gauss DPP Model: The testing results for the K function of the fitted Gauss DPP are given in Fig. 2.12a, which clearly show that the K functions of the real BS deployments lie within the envelope of the fitted Gauss DPP. The coverage probability for the fitted Gauss DPP is provided in Fig. 2.12b, from which it can be observed that the coverage probability of the Houston data sets lies within the 95% confidence interval of the simulated Gauss DPPs. In addition, the average coverage probability of the fitted Gauss DPP is slightly lower than that of real data sets, which means

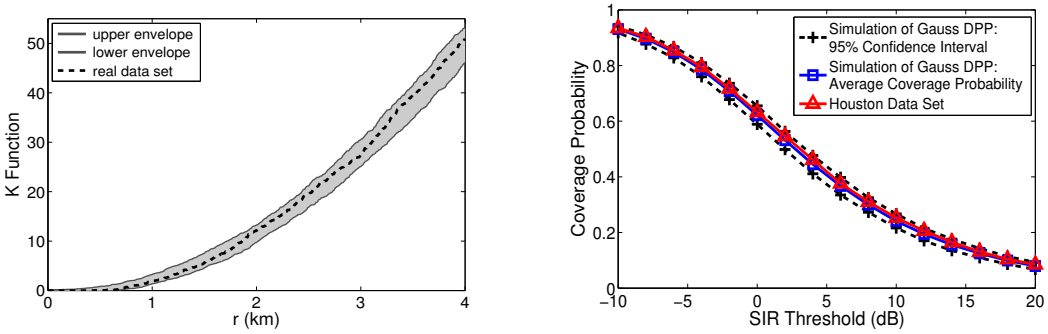

(a) K function (b) Coverage probability

Figure 2.12: Goodness-of-fit for the Gauss DPP.

that the fitted Gauss DPP corresponds to a slightly smaller repulsiveness than the real deployments.

Therefore, in terms of the above summary statistics, the Gauss DPP model can be used as a reasonable point process model for real BS deployments. In addition, due to the concise definition of its kernel, the shot noise analysis of the Gauss DPP is possible, which further motivates the use of Gauss DPPs to model real-world macro BS deployments.

Goodness-of-fit for the Cauchy DPP Model: Based on the same method as for the Gauss DPP model, we tested the goodness-of-fit for the Cauchy DPP model. The fitting results for the K function and coverage probability are shown in Fig. 2.13a and Fig. 2.13b, from which it can be concluded that the Cauchy DPP model is also a reasonable point process model for real BS deployments. Compared to the fitted Gauss DPP, the average coverage probability for the fitted Cauchy DPP in Fig. 2.13b is slightly lower than that in Fig. 2.12b, which means the fitted Cauchy DPP corresponds to a smaller

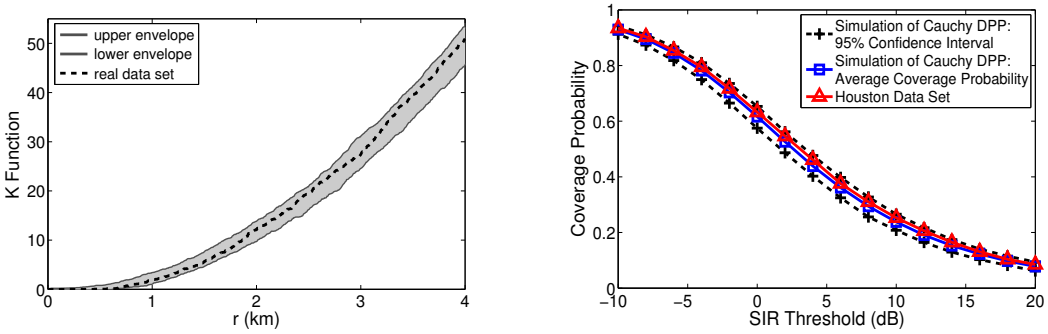

(a) K function (b) Coverage probability

Figure 2.13: Goodness-of-fit for the Cauchy DPP.

repulsiveness than the Gauss DPP.

Goodness-of-fit for the Generalized Gamma DPP Model: The goodness-of-fit for the Generalized Gamma DPP fitted to the Houston data set is evaluated in Fig. 2.14. The Generalized Gamma DPP provides the best fit among all these DPP models, especially in terms of coverage probability. In Fig. 2.14, the average coverage probability of the fitted Generalized Gamma DPP almost exactly matches the real BS deployment, while the average coverage probability of the fitted Gauss DPP and the fitted Cauchy DPP all stay below the real data set. This is because the Generalized Gamma DPP corresponds to a higher repulsiveness, from which a larger coverage probability is expected.

2.8.3 Repulsiveness of Different DPPs

In order to explain why the Generalized Gamma DPP has larger repulsiveness, we use the metric suggested in [32] to measure the repulsive-

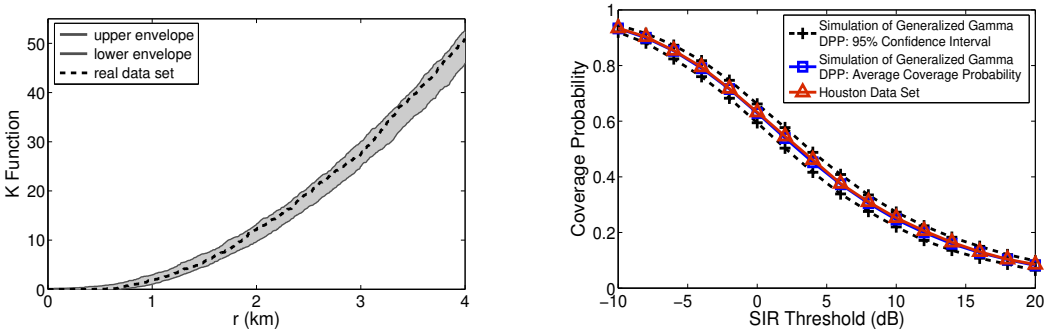

(a) K function (b) Coverage probability

Figure 2.14: Goodness-of-fit for the Generalized Gamma DPP.

ness of different DPPs. Specifically, from Lemma 2.5.5, the intensity measure of a stationary DPP Φ under its reduced Palm distribution is $\rho_o^{(1)}(x) = \rho^{(2)}(0,x)/\rho^{(1)}(x)$, where $\rho^{(2)}$ and $\rho^{(1)}$ are the second and the first joint intensity of Φ. By calculating the difference of the total expected number of points under the probability distribution $\mathbb{P}$ and the reduced Palm distribution $\mathbb{P}_o^!$, the repulsiveness of a stationary DPP Φ with intensity λ can be measured using the following metric [32]:

$$\mu = \int_{\mathbb{R}^2} \left[\lambda - \rho_o^{(1)}(x)\right] \mathrm{d}x = \frac{1}{\lambda}\int_{\mathbb{R}^2} |K_0(x)|^2 \mathrm{d}x = \frac{1}{\lambda}\int_{\mathbb{R}^2} |\varphi(x)|^2 \mathrm{d}x, \qquad (2.31)$$

where $K_0(x)$ and $\varphi(x)$ denote the covariance function and spectral density of Φ respectively.

PPP has $\mu = 0$ due to Slivnyak's theorem, while the grid-based model has $\mu = 1$ since the point at the origin is excluded under reduced Palm distribution. Generally, larger value of μ will correspond to a more repulsive point process. This repulsiveness measure for the Gauss, Cauchy and Generalized

Gamma model can be calculated as: $\mu_{\text{gauss}} = \lambda\pi\alpha^2/2$, $\mu_{\text{cauchy}} = \lambda\pi\alpha^2/(2\nu+1)$, and $\mu_{\text{gengamma}} = \lambda\nu\alpha^2/(2^{1+2/\nu}\pi\Gamma(2/\nu))$. Based on the parameters in Table 2.1, we can calculate the repulsiveness measure of each DPP model fitted to the Houston data set as $\mu_{\text{gauss}} = 0.4999$, $\mu_{\text{cauchy}} = 0.4365$ and $\mu_{\text{gengamma}} = 0.5905$. Similarly, the repulsiveness measure of each DPP model fitted to the LA data set is given by $\mu_{\text{gauss}} = 0.5004$, $\mu_{\text{cauchy}} = 0.4351$, $\mu_{\text{gengamma}} = 0.5479$. Therefore, it can be concluded that the fitted Generalized Gamma DPP has the largest repulsiveness, followed by the fitted Gauss DPP, while the fitted Cauchy DPP is the least repulsive. Since higher repulsiveness will result in more regularity for the point process, a Generalized Gamma DPP generally corresponds to a larger average coverage probability.

2.9 Summary

In this chapter, the analytical tractability and the modeling accuracy of using the determinantal point processes for macro BS locations are validated. The state-of-the-art in DPP prior to this chapter is mainly focused on its mathematical and statistical properties [32, 35, 36]. For example, [35, 36] have derived the reduced Palm distribution of the DPP, and the Laplace functional of DPP when the functions have bounded support. This chapter is the first work to introduce DPP as a feasible macro BS location model, and to provide rigorous analysis for the corresponding network performance. Specifically, this chapter has derived the Laplace functional for DPPs and independently marked DPPs, wherein the functions need to satisfy certain constraints but

can potentially have unbounded support. Based on the reduced Palm distribution of DPP [35] and the derived Laplace functional, the exact expressions for important system performance metrics (e.g., the empty space function, the mean interference, the SIR distribution) can be derived, which are given by series expansion forms. These expressions can be numerically evaluated through the Quasi-Monte Carlo integration method in general, and can also retrieve the results for Poisson cellular networks [2] when the DPP kernel is the degenerated Poisson kernel. By fitting the Gauss DPP model to a real macro BS deployment using the statistical algorithm developed in [32], the determinantal point processes are shown to be accurate in terms of the K function and the coverage probability.

The methodologies for determinantal point processes derived in this chapter provide the basis to investigate more advanced network models, such as the MIMO networks and heterogeneous cellular networks, with determinantal point process configured macro base stations.

2.10 Appendix

2.10.1 Proof of Lemma 2.5.2

For any function f satisfying the conditions in Lemma 2.5.2, define the following function for $k \in \mathbb{N}$:

$$f_k(x) = \begin{cases} f(x), & \text{if } x \in B(0,k), \\ 0, & \text{otherwise.} \end{cases} \tag{2.32}$$

Based on Lemma 2.5.1, since each $f_k(x)$ has finite support, we have:

$$\begin{aligned}&\mathbb{E}\left[\exp\left(-\int_{\mathbb{R}^2} f_k(x)\Phi(\mathrm{d}x)\right)\right]\\&=\sum_{n=0}^{+\infty}\frac{(-1)^n}{n!}\int_{(\mathbb{R}^2)^n}\det\left(K(x_i,x_j)\right)_{1\leq i,j\leq n}\prod_{i=1}^{n}\left(1-\exp(-f_k(x_i))\right)\mathrm{d}x_1...\mathrm{d}x_n.\end{aligned} \tag{2.33}$$

From the monotone convergence theorem, we have:

$$\lim_{k\to\infty}\mathbb{E}\left[\exp\left(-\int_{\mathbb{R}^2} f_k(x)\Phi(\mathrm{d}x)\right)\right]=\mathbb{E}\left[\exp\left(-\int_{\mathbb{R}^2} f(x)\Phi(\mathrm{d}x)\right)\right]. \tag{2.34}$$

Let us now show that:

$$\begin{aligned}&\lim_{k\to\infty}\sum_{n=0}^{+\infty}\frac{(-1)^n}{n!}\int_{(\mathbb{R}^2)^n}\det\left(K(x_i,x_j)\right)_{1\leq i,j\leq n}\prod_{i=1}^{n}\left(1-\exp(-f_k(x_i))\right)\mathrm{d}x_1...\mathrm{d}x_n\\&=\sum_{n=0}^{+\infty}\frac{(-1)^n}{n!}\int_{(\mathbb{R}^2)^n}\det\left(K(x_i,x_j)\right)_{1\leq i,j\leq n}\prod_{i=1}^{n}\left(1-\exp(-f(x_i))\right)\mathrm{d}x_1...\mathrm{d}x_n.\end{aligned} \tag{2.35}$$

To prove this result, we use the following lemma [51, Theorem 7.11]:

Lemma 2.10.1. *Suppose $f_n \to f$ uniformly on a set E in a metric space. Let x be a limit point on E such that $\lim_{t\to x} f_n(t)$ exists for $\forall n \in \mathbb{N}$, then $\lim_{t\to x}\lim_{n\to\infty} f_n(t) = \lim_{n\to\infty}\lim_{t\to x} f_n(t)$.*

Let us denote that:

$$h_n(k)=\sum_{m=0}^{n}\int_{(\mathbb{R}^2)^m}\frac{(-1)^m}{m!}\det\left(K(x_i,x_j)\right)_{1\leq i,j\leq m}\prod_{i=1}^{m}\left(1-\exp(-f_k(x_i))\right)\mathrm{d}x_1...\mathrm{d}x_m.$$

We prove that $\{h_n\}$ converges uniformly $\forall k \in \mathbb{N}$. This is because:

$$\left|\int_{(\mathbb{R}^2)^m}\frac{(-1)^m}{m!}\det\left(K(x_i,x_j)\right)_{1\leq i,j\leq m}\prod_{i=1}^{m}\left(1-\exp(-f_k(x_i))\right)\mathrm{d}x_1...\mathrm{d}x_m\right|$$

$$\overset{(a)}{\leq}\frac{1}{m!}\left(\int_{\mathbb{R}^2}K(x,x)(1-\exp(-f(x)))\mathrm{d}x\right)^m \triangleq M_m,$$

where (a) follows from Hadamard's inequality, i.e., $\det((K(x_i,x_j))_{1\leq i,j\leq n} \leq \prod_{i=1}^n K(x_i,x_i)$ if K is positive semi-definite. Since $\int_{\mathbb{R}^2} K(x,x)(1-\exp(-f(x)))\mathrm{d}x$ is finite by assumption, $\sum_{m=0}^{\infty} M_m$ is also finite. Therefore, by Weierstrass M-test [51, Theorem 7.10], $\{h_n\}$ converges uniformly.

Next, we show $\lim_{k\to\infty} h_n(k)$ exists for $\forall n \in \mathbb{N}$. This is because for $0 \leq m \leq n$, we have:

$$\begin{aligned}
&\lim_{k\to\infty}\int_{(\mathbb{R}^2)^m}\frac{(-1)^m}{m!}\det\left(K(x_i,x_j)\right)_{1\leq i,j\leq m}\prod_{i=1}^m\left(1-\exp(-f_k(x_i))\right)\mathrm{d}x_1...\mathrm{d}x_m\\
\overset{(a)}{=}&\int_{(\mathbb{R}^2)^m}\frac{(-1)^m}{m!}\det\left(K(x_i,x_j)\right)_{1\leq i,j\leq m}\lim_{k\to\infty}\prod_{i=1}^m\left(1-\exp(-f_k(x_i))\right)\mathrm{d}x_1...\mathrm{d}x_m\\
=&\int_{(\mathbb{R}^2)^m}\frac{(-1)^m}{m!}\det\left(K(x_i,x_j)\right)_{1\leq i,j\leq m}\prod_{i=1}^m\left(1-\exp(-f(x_i))\right)\mathrm{d}x_1...\mathrm{d}x_m.
\end{aligned} \tag{2.36}$$

Step (a) follows from the dominated convergence theorem (DCT): given m, denote $\mathbf{x} \triangleq (x_1,...,x_m)$ and $g_k(\mathbf{x}) \triangleq \frac{(-1)^m}{m!}\det\left(K(x_i,x_j)\right)_{1\leq i,j\leq m}\prod_{i=1}^m(1-\exp(-f_k(x_i)))$; then from the definition of $f_k(x)$, $g_k(\mathbf{x})$ converges pointwise to $\frac{(-1)^m}{m!}\det\left(K(x_i,x_j)\right)_{1\leq i,j\leq m}\prod_{i=1}^m(1-\exp(-f(x_i)))$. In addition, observe that $|g_k(\mathbf{x})| \leq \frac{1}{m!}\prod_{i=1}^m K(x_i,x_i)(1-\exp(-f(x_i)))$, we have

$$\begin{aligned}
&\int_{(\mathbb{R}^2)^m}\frac{1}{m!}\prod_{i=1}^m K(x_i,x_i)(1-\exp(-f(x_i)))\mathrm{d}x_1...\mathrm{d}x_m\\
=&\frac{\left(\int_{\mathbb{R}^2}K(x,x)(1-\exp(-f(x)))\mathrm{d}x\right)^m}{m!}<\infty.
\end{aligned}$$

Since each term of $h_n(k)$ has a finite limit when $k\to\infty$, thus $\lim_{k\to\infty} h_n(k)$ also exists.

Now we can apply Lemma 2.10.1 to $h_n(k)$ to derive the desired fact:

$$\begin{aligned}
&\lim_{k\to\infty}\sum_{m=0}^{\infty}\frac{(-1)^m}{m!}\int_{(\mathbb{R}^2)^m}\det\left(K(x_i,x_j)\right)_{1\le i,j\le m}\prod_{i=1}^{m}\left(1-\exp(-f_k(x_i))\right)\mathrm{d}x_1...\mathrm{d}x_m\\
=&\lim_{k\to\infty}\lim_{n\to\infty}\sum_{m=0}^{n}\frac{(-1)^m}{m!}\int_{(\mathbb{R}^2)^m}\det\left(K(x_i,x_j)\right)_{1\le i,j\le m}\prod_{i=1}^{m}\left(1-\exp(-f_k(x_i))\right)\mathrm{d}x_1...\mathrm{d}x_m\\
\overset{(a)}{=}&\lim_{n\to\infty}\lim_{k\to\infty}\sum_{m=0}^{n}\frac{(-1)^m}{m!}\int_{(\mathbb{R}^2)^m}\det\left(K(x_i,x_j)\right)_{1\le i,j\le m}\prod_{i=1}^{m}\left(1-\exp(-f_k(x_i))\right)\mathrm{d}x_1...\mathrm{d}x_m\\
\overset{(b)}{=}&\sum_{m=0}^{\infty}\frac{(-1)^m}{m!}\int_{(\mathbb{R}^2)^m}\det\left(K(x_i,x_j)\right)_{1\le i,j\le m}\prod_{i=1}^{m}\left(1-\exp(-f(x_i))\right)\mathrm{d}x_1...\mathrm{d}x_m,
\end{aligned}\tag{2.37}$$

where (a) is derived using Lemma 2.10.1, and (b) follows from (2.36).

The proof of the lemma follows from (2.33), (2.34), and (2.35).

2.10.2 Proof of Lemma 2.5.4

This can be proved by the following procedure:

$$\begin{aligned}
&\mathbb{E}\left[\exp(-\sum_i f(x_i,p_i))\right]\\
\overset{(a)}{=}&\mathbb{E}\left[\prod_i\int_{\mathbb{R}^+}\exp(-f(x_i,p))F(\mathrm{d}p)\right]\\
\overset{(b)}{=}&\sum_{n=0}^{+\infty}\frac{(-1)^n}{n!}\int_{(\mathbb{R}^2)^n}\det\left(K(x_i,x_j)\right)_{1\le i,j\le n}\prod_{i=1}^{n}\Bigg(1-\int_{\mathbb{R}^+}\exp(-f(x_i,p_i))\\
&\times F(\mathrm{d}p_i)\Bigg)\mathrm{d}x_1...\mathrm{d}x_n,
\end{aligned}$$

where (a) is because all the marks are i.i.d. and independent of DPP Φ, while (b) comes from Corollary 2.5.3.

2.10.3 Proof of Lemma 2.6.1

Choose $f(x) = -\log \mathbb{1}_{\{\|x\|>r\}}$ for $x \in \mathbb{R}^2$, we have:

$$\begin{aligned}\mathbb{E}\left[\exp\left(-\int f(x)\Phi(\mathrm{d}x)\right)\right] &= \mathbb{E}\left[\exp\left(-\sum_{x_i\in\Phi} -\log \mathbb{1}_{\|x_i\|>r}\right)\right] \\ &= \mathbb{P}\left[d(o,\Phi) > r\right].\end{aligned}$$

Therefore, based on Lemma 2.5.2, the empty space function is given by:

$$\begin{aligned}F(r) =& 1 - \mathbb{E}\left[\exp\left(-\int f(x)\Phi(\mathrm{d}x)\right)\right] \\ =& 1 - \sum_{n=0}^{+\infty} \frac{(-1)^n}{n!} \int_{(\mathbb{R}^2)^n} \det\left(K(x_i,x_j)\right)_{1\le i,j\le n} \\ & \times \prod_{i=1}^{n} \left(1 - \exp(\log \mathbb{1}_{\{\|x_i\|>r\}})\right) \mathrm{d}x_1 ... \mathrm{d}x_n \\ =& \sum_{n=1}^{+\infty} \frac{(-1)^{n-1}}{n!} \int_{(B(0,r))^n} \det\left(K(x_i,x_j)\right)_{1\le i,j\le n} \mathrm{d}x_1 ... \mathrm{d}x_n.\end{aligned}$$

2.10.4 Proof of Corollary 2.6.2

We start the proof with the following two lemmas:

Lemma 2.10.2. *Consider two non-negative functions $g(u,v) : \mathbb{R} \times \mathbb{R}^d \to [0,\infty)$, and $p(u) : \mathbb{R} \to [0,+\infty)$, which satisfy the following conditions: (1) $g(u,v)$ is non-decreasing, right continuous w.r.t. u, and $g(u,v) = 0$ for $\forall u \le 0$; (2) $p(u)$ is bounded, right continuous, and $\lim_{u\to+\infty} p(u) = 0$; (3) $p(u)$ and $g(u,v)$ do not have common discontinuities for Lebesgue almost all v. Let $F(u) = \int_{\mathbb{R}^d} g(u,v)\mathrm{d}v$, we also assume that $F(u)$ is continuous, non-decreasing*

and bounded on $\mathbb{R}$*. Then the following equation holds:*

$$\int_{\mathbb{R}} p(u)\mathrm{d}F(u) = \int_{\mathbb{R}^d \times \mathbb{R}} p(u)\mathrm{d}_u g(u,v)\mathrm{d}v, \tag{2.38}$$

where the integrals w.r.t. $\mathrm{d}F(u)$ *and* $\mathrm{d}_u g(u,v)$ *are in the Stieltjes sense.*

Proof. Using Stieltjes integration by parts, we have the following:

$$\begin{aligned}
\int_{\mathbb{R}} p(u)\mathrm{d}F(u) &= \int_{\mathbb{R}} p(u)\mathrm{d}_u \int_{\mathbb{R}^d} g(u,v)\mathrm{d}v \\
&\overset{(a)}{=} -\int_{\mathbb{R}} \int_{\mathbb{R}^d} g(u,v)\mathrm{d}v\mathrm{d}p(u) \\
&\overset{(b)}{=} -\int_{\mathbb{R}^d} \int_{\mathbb{R}} g(u,v)\mathrm{d}p(u)\mathrm{d}v \\
&\overset{(c)}{=} \int_{\mathbb{R}^d} \int_{\mathbb{R}} p(u)\mathrm{d}_u g(u,v)\mathrm{d}v,
\end{aligned} \tag{2.39}$$

where (a) and (c) are derived using integration by parts for the Stieltjes integrals, and (b) follows from Fubini's theorem. □

Lemma 2.10.3 (Rubin [51])**.** *Suppose* $\{f_n\}$ *is a sequence of differentiable functions on* $[a,b]$ *such that* $\{f_n(x_0)\}$ *converges for some point* x_0 *on* $[a,b]$*. If* $\{f_n^{'}\}$ *converges uniformly on* $[a,b]$ *to* f'*, then* $\{f_n\}$ *converges uniformly on* $[a,b]$ *to a function* f*, and* $f^{'}(x) = \lim_{n\to\infty} f_n^{'}(x)$ *for* $a \le x \le b$*.*

We can express the empty space function as $F(r) = \lim_{n\to\infty} F_n(r)$, where:

$$F_n(r) = \sum_{k=1}^{n} \frac{(-1)^{k-1}}{k!} \int_{(B(0,r))^k} \det(K(x_i,x_j))_{1\le i,j\le k}\mathrm{d}x_1 ... \mathrm{d}x_k.$$

From Lemma 2.6.1, we know $F_n(r)$ converges pointwise to $F(r)$ for any $r \ge 0$. Let $u(\cdot)$ denote the unit step function and $\delta(\cdot)$ denote the Dirac measure. Note

that $F_n(r)$ is equal to 0 for $r \leq 0$; then by taking $p(v) = u(v) - u(v-r)$ with $r \in [0, \infty)$, we have:

$$
\begin{aligned}
F_n(r) &= \int_{\mathbb{R}} p(v) \mathrm{d}F_n(v) \\
&\overset{(a)}{=} \sum_{k=1}^{n} \frac{(-1)^{k-1}}{k!} \int_{(\mathbb{R}^2)^k \times [0,r)} \det(K(x_i, x_j))_{1 \leq i,j \leq k} \mathrm{d} \left[\prod_{i=1}^{k} u(v - |x_i|) \right] \mathrm{d}x_1 ... \mathrm{d}x_k \\
&\overset{(b)}{=} \sum_{k=1}^{n} \frac{(-1)^{k-1}}{k!} \int_{(\mathbb{R}^2)^k \times [0,r)} \det(K(x_i, x_j))_{1 \leq i,j \leq k} \sum_{m=1}^{k} \prod_{i=1, i \neq m}^{k} u(v - |x_i|) \\
&\quad \times \delta_{|x_m|}(\mathrm{d}v) \mathrm{d}x_1 ... \mathrm{d}x_k \\
&\overset{(c)}{=} \sum_{k=1}^{n} \frac{(-1)^{k-1}}{k!} \int_{(\mathbb{R}^2)^k \times [0,r)} k \det(K(x_i, x_j))_{1 \leq i,j \leq k} \prod_{i=2}^{k} u(v - |x_i|) \delta_{|x_1|}(\mathrm{d}v) \mathrm{d}x_1 ... \mathrm{d}x_k \\
&= \sum_{k=1}^{n} \frac{(-1)^{k-1}}{(k-1)!} \int_0^{+\infty} \int_0^{2\pi} \int_{(\mathbb{R}^2)^{k-1}} \int_0^{r} \det(K(x_i, x_j))_{1 \leq i,j \leq k} \Big|_{x_1 = (r_1, \theta)} \\
&\quad \times \prod_{i=2}^{k} u(v - |x_i|) r_1 \delta_{r_1}(\mathrm{d}v) \mathrm{d}x_2 ... \mathrm{d}x_k \mathrm{d}\theta \mathrm{d}r_1 \\
&\overset{(d)}{=} \int_0^{r} \sum_{k=1}^{n} \frac{(-1)^{k-1}}{(k-1)!} 2\pi v \int_{(B(0,v))^{k-1}} \det(K(x_i, x_j))_{1 \leq i,j \leq k} \Big|_{x_1 = (v,0)} \mathrm{d}x_2 ... \mathrm{d}x_k \mathrm{d}v
\end{aligned}
\tag{2.40}
$$

Step (a) is derived by applying Lemma 2.10.2 to $F_n(v)$ and $p(v)$. Then (b) follows from the product rule for differentials, and the fact that the Dirac measure is the distributional derivative of the unit step function. Furthermore, (c) is because the determinant $\det(K(x_i, x_j))_{1 \leq i,j \leq n}$ remains the same if we swap the position of x_1 and x_k, which is equivalent to exchanging the first row and the k-th row, and then the first column and the k-th column of $K(x_i, x_j)_{1 \leq i,j \leq n}$. Finally, (d) follows from the the defining property of Dirac measure, and noting that since Φ is stationary and isotropic, the integration is

invariant w.r.t. the angle of x_1. Notice that $F_n(r)$ can be expressed as (2.40), which shows it is differentiable.

Given $r \in [0, \infty)$, we can check $F_n^{'}(v)$ converges uniformly for $v \in [0, r]$ using Hadamard's inequality for positive semi-definite matrices. Then by applying Lemma 2.10.3 to $\{F_n\}$, we have:

$$\begin{aligned} F(r) &= \int_0^r \lim_{n\to\infty} F_n^{'}(v)\mathrm{d}v \\ &= \int_0^r \sum_{n=0}^{+\infty} \frac{(-1)^n}{n!} 2\pi v \int_{(B(0,v))^n} \det(K(x_i, x_j))_{0\le i,j\le n}\Big|_{x_0=(v,0)} \mathrm{d}x_1 ... \mathrm{d}x_n \mathrm{d}v. \end{aligned}$$

2.10.5 Proof of Lemma 2.6.4

From Lemma 2.5.5, the mean interference can be expressed as:

$$\begin{aligned} &\mathbb{E}[\sum_{x_i\in\Phi\setminus x_0} Ph_{x_i}/l(\|x_i\|)|x_0 = (r_0, 0)] \\ =&\mathbb{E}[\sum_{x_i\in\tilde{\Phi}} Ph_{x_i}/l(\|x_i\|)] \\ \overset{(a)}{=}&P\int_{\mathbb{R}^2}\int_{\mathbb{R}^+} hK_{x_0}^{!}(x,x)\exp(-h)/l(\|x\|)\mathrm{d}h\mathrm{d}x \\ =&P\int_{\mathbb{R}^2} K_{x_0}^{!}(x,x)/l(\|x\|)\mathrm{d}x, \end{aligned}$$

where $\tilde{\Phi} \sim \mathrm{DPP}(K_{x_0}^{!})$ follows from Lemma 2.5.5, and (a) follows from Campbell's theorem.

2.10.6 Proof of Theorem 2.6.5

Denote $\tilde{\Phi} \sim \mathrm{DPP}(K_{x_0}^{!})$, we have:

$$\mathbb{E}[\exp(-sI)|x^*(0) = x_0]$$

$$
\begin{aligned}
&= \mathbb{E}[\exp(-sI)|x_0 \in \Phi, \Phi(B^o(0,r_0)) = 0] \\
&\overset{(a)}{=} \mathbb{E}^!_{x_0}[\exp(-s \sum_{x_i \in \Phi \cap B^c(0,r_0)} Ph_{x_i}/l(\|x_i\|))|\Phi(B^o(0,r_0)) = 0] \\
&\overset{(b)}{=} \frac{\mathbb{E}[\exp(-s \sum_{x_i \in \tilde{\Phi} \cap B^c(0,r_0)} Ph_{x_i}/l(\|x_i\|)) \mathbb{1}_{\tilde{\Phi}(B^o(0,r_0))=0}]}{\mathbb{P}[\tilde{\Phi}(B^o(0,r_0)) = 0]}\,, \qquad (2.41)
\end{aligned}
$$

where (a) follows from the Bayes' rule, and the fact that conditionally on $x_0 \in \Phi$, $(\Phi - \delta_{x_0})(B^o(0,r_0)) = 0$ is equivalent to $\Phi(B^o(0,r_0)) = 0$ since x_0 lies on the boundary of the open ball $B^o(0,r_0)$. In addition, (b) follows from the fact that for all random variables X and events A, $\mathbb{E}[X|A] = \frac{\mathbb{E}[X \mathbb{1}_A]}{\mathbb{P}(A)}$.

Next, it is clear that the denominator in (2.41) is given by:

$$
\begin{aligned}
&\mathbb{P}[\tilde{\Phi}(B^o(0,r_0)) = 0] = \mathbb{P}[d(o,\tilde{\Phi}) \geq r_0] \\
&= \sum_{n=0}^{+\infty} \frac{(-1)^n}{n!} \int_{B(0,r_0)^n} \det(K^!_{x_0}(x_i,x_j))_{1 \leq i,j \leq n} \mathrm{d}x_1 ... \mathrm{d}x_n. \qquad (2.42)
\end{aligned}
$$

The numerator in (2.41) is calculated as:

$$
\begin{aligned}
&\mathbb{E}\left[\exp(-s \sum_{x_i \in \tilde{\Phi} \cap B^c(0,r_0)} Ph_{x_i}/l(\|x_i\|)) \mathbb{1}_{\tilde{\Phi}(B^o(0,r_0))=0}\right] \\
&= \mathbb{E}\left[\exp(-s \sum_{x_i \in \tilde{\Phi} \cap B^c(0,r_0)} Ph_{x_i}/l(\|x_i\|)) \prod_{x_i \in \tilde{\Phi}} \mathbb{1}_{|x_i| \geq r_0}\right] \\
&\overset{(a)}{=} \sum_{n=0}^{+\infty} \frac{(-1)^n}{n!} \int_{(\mathbb{R}^2)^n} \int_{(\mathbb{R}^+)^n} \det(K^!_{x_0}(x_i,x_j))_{1 \leq i,j \leq n} \\
&\quad \times \prod_{i=1}^{n} \left[(1 - \exp(-sPh_{x_i} \mathbb{1}_{|x_i| \geq r_0}/l(\|x_i\|) + \log \mathbb{1}_{|x_i| \geq r_0})) \exp(-h_{x_i}) \mathrm{d}h_i\right] \mathrm{d}x_1 ... \mathrm{d}x_n \\
&= \sum_{n=0}^{+\infty} \frac{(-1)^n}{n!} \int_{(\mathbb{R}^2)^n} \det(K^!_{x_0}(x_i,x_j))_{1 \leq i,j \leq n} \prod_{i=1}^{n} \left[1 - \frac{\mathbb{1}_{|x_i| \geq r_0}}{1 + sP/l(\|x_i\|)}\right] \mathrm{d}x_1 ... \mathrm{d}x_n, \\
&\qquad (2.43)
\end{aligned}
$$

where (a) is obtained from Lemma 2.5.4. Finally, substituting (2.42) and (2.43) into (2.41) yields the result.

2.10.7 Proof of Lemma 2.6.6

Denote the empty space function as $F(r)$, then the mean interference is calculated as:

$$
\begin{aligned}
&\mathbb{E}[I|x^*(0)=x_0] \\
&= -\frac{\mathrm{d}}{\mathrm{d}s}\left[\mathbb{E}[\exp(-sI)||x^*(0)=x_0]\right]\Big|_{s=0} \\
&\overset{(a)}{=} -\frac{1}{1-F(r_0)}\sum_{n=0}^{+\infty}\frac{(-1)^n}{n!}\int_{(\mathbb{R}^2)^n}\det(K^!_{x_0}(x_i,x_j))_{1\le i,j\le n}\frac{\mathrm{d}}{\mathrm{d}s}\prod_{i=1}^{n}[1-\frac{\mathbb{1}_{|x_i|\ge r_0}}{1+sP/l(\|x_i\|)}] \\
&\quad\times \mathrm{d}x_1...\mathrm{d}x_n\Big|_{s=0} \\
&\overset{(b)}{=} -\frac{1}{1-F(r_0)}\sum_{n=1}^{+\infty}\frac{(-1)^n}{n!}\int_{(\mathbb{R}^2)^n}\det(K^!_{x_0}(x_i,x_j))_{1\le i,j\le n} \\
&\quad\times\sum_{k=1}^{n}\prod_{i=1,i\ne k}^{n}[1-\frac{\mathbb{1}_{|x_i|\ge r_0}}{1+sP/l(\|x_i\|)}]\frac{P/l(x_k)\mathbb{1}_{|x_k|\ge r_0}}{(1+sP/l(\|x_k\|))^2}\mathrm{d}x_1...\mathrm{d}x_n\Big|_{s=0} \\
&\overset{(c)}{=}\frac{\sum_{n=1}^{+\infty}\frac{(-1)^{n-1}}{n!}\int_{(\mathbb{R}^2)^n}\det(K^!_{x_0}(x_i,x_j))_{1\le i,j\le n}n\prod_{i=2}^{n}\mathbb{1}_{|x_i|<r_0}\mathbb{1}_{|x_1|\ge r_0}P/l(\|x_1\|)\mathrm{d}x_1...\mathrm{d}x_n}{1-F(r_0)} \\
&=\frac{\sum_{n=1}^{+\infty}\frac{(-1)^{n-1}}{(n-1)!}\int_{(B(0,r_0))^{n-1}}\int_{B^c(0,r_0)}\det(K^!_{x_0}(x_i,x_j))_{1\le i,j\le n}P/l(\|x_1\|)\mathrm{d}x_1...\mathrm{d}x_n}{\sum_{n=0}^{+\infty}\frac{(-1)^n}{n!}\int_{B(0,r_0)^n}\det(K^!_{x_0}(x_i,x_j))_{1\le i,j\le n}\mathrm{d}x_1...\mathrm{d}x_n},
\end{aligned}
$$

Interchanging the infinite sum and the differentiation in (a) is guaranteed by Lemma 2.10.3. Then (b) is derived by applying the derivative of product rule. In addition, (c) is true since consider n points $x_1,...,x_n\in\mathbb{R}^2$ such that

$|x_k| \geq r_0$ and the rest are within the open ball $B^o(0, r_0)$, then the determinant $\det(K^!_{x_0}(x_i, x_j))_{1\leq i,j\leq n}$ remains the same if we swap the position of x_1 and x_k.

2.10.8 Proof of Theorem 2.6.7

Without loss of generality, assume $x^*(0) = x_0$, which can be expressed in polar form as $x_0 = (r_0, \theta)$. We know that x_0 admits the probability density $\frac{\mathrm{d}\theta}{2\pi} f(r_0)\mathrm{d}r_0$, where $f(r_0)$ is given in Corollary 2.6.2. Therefore, we have:

$$\begin{aligned}
&\mathbb{P}(\mathrm{SIR}(0,\Phi) > T) \\
=&\int_0^{+\infty}\int_0^{2\pi} \mathbb{P}[\mathrm{SIR}(0,\Phi) > T | x_0 = (r_0,\theta)]\frac{1}{2\pi} f(r_0)\mathrm{d}\theta\mathrm{d}r_0 \\
\overset{(a)}{=}&\int_0^{+\infty} \mathbb{P}[\mathrm{SIR}(0,\Phi) > T | x_0 = (r_0,0)] f(r_0)\mathrm{d}r_0 \\
=&\int_0^{+\infty} \mathbb{E}[\exp(-Tl(x_0)I) | x_0 = (r_0,0)] f(r_0)\mathrm{d}r_0,
\end{aligned}$$

where (a) is because the DPP is stationary and isotropic, so that the angle of x_0 will not affect the result of $\mathbb{P}[\mathrm{SIR}(0,\Phi) > T | x_0 = (r_0,\theta)]$. Since $\det(K^!_{x_0}(x_i, x_j))_{1\leq i,j\leq n} = \frac{1}{K(x_0,x_0)}\det(K(x_i, x_j))_{0\leq i,j\leq n}$, then the proof is completed by applying Corollary 2.6.2 and Theorem 2.6.5.

Chapter 3

Coexistence Analysis of Cellular and Wi-Fi Networks in the Unlicensed Spectrum[1]

The better exploitation of spectrum opportunities is a key component for cellular communications to meet the ever increasing global mobile traffic demand. Given that there is over 400 MHz of generally lightly used unlicensed spectrum in the 5 GHz band, a promising approach is to extend cellular into the unlicensed spectrum, so that the cellular network can aggregate carriers on both licensed and unlicensed bands to provide higher transmission bandwidth [54–61]. The main incumbent system in the unlicensed spectrum is Wi-Fi, which is built on the distributed IEEE 802.11 CSMA/CA protocol [9]. CSMA/CA guarantees fair channel access by allowing Wi-Fi nodes to transmit only when the channel is sensed to be idle for a certain back-off period. By contrast, cellular systems are centrally scheduled, which assumes exclusive usage of the spectrum without any carrier sensing mechanisms. Therefore, this medium access control (MAC) layer difference can potentially lead to very poor Wi-Fi performance when the cellular network operates in the unlicensed spec-

[1]This chapter has been published in [52, 53]. I am the primary author of these works. Coauthors Dr. Thomas Novlan and Dr. Charlie Zhang have provided many valuable discussions and insights to this work, and Dr. Jeffrey G. Andrews and Dr. François Baccelli are my supervisors.

trum without any protocol modifications. In order to protect Wi-Fi, cellular networks can adopt either a discontinuous, duty-cycle transmission pattern, or the listen-before-talk (LBT) with a random backoff mechanism similar to Wi-Fi. Although the coexistence performance of cellular and Wi-Fi can be evaluated through system level simulations, a more fundamental approach would be helpful for transparent comparisons and understanding when and why the various techniques succeed or fail. In particular, the complicated CSMA/CA protocol and the corresponding correlations among the transmitting Wi-Fi APs and cellular BSs render the analysis very challenging. In this chapter, we propose a theoretical framework based on stochastic geometry to model and analyze the coexistence issues that arise when cellular operates in the unlicensed spectrum.

3.1 Related Works

Cellular in unlicensed spectrum operation is mainly designed for the long term evolution (LTE) system [56], and several works have investigated the coexistence of LTE and Wi-Fi through system level simulations [55, 62–72]. When LTE transmits continuously, [62, 63] show that Wi-Fi is most often blocked by the LTE interference, and the throughput performance of Wi-Fi decreases significantly. A simple approach which requires minimal changes to the current LTE protocol is to adopt a discontinuous transmission pattern, also known as LTE-U [73]. By using the almost-blank subframes (ABS) feature to blank a certain fraction of LTE transmissions, Wi-Fi throughput can

be effectively increased for indoor scenarios [63, 65], outdoor scenarios [66], and indoor/outdoor mixed scenarios [66]. However, this discontinuous LTE transmission scheme is infeasible in regions where the LBT feature is mandatory to transmit in the unlicensed spectrum [56, 71, 72]. In addition, through real testing results, [74] shows the frequent on and off switching of LTE-U transmissions will trigger the Wi-Fi rate control algorithm to lower the Wi-Fi transmission rate [74]. Therefore, coexistence methodologies using the LBT feature, also known as licensed-assisted access (LAA), have been considered in [55, 66–68, 70–72]. With the adoption of LBT at each LTE Evolved Node B (eNB), [55, 67, 68] show that LTE can deliver significant throughput while maintaining fair coexistence with Wi-Fi. In [66], a random backoff mechanism with fixed contention window size is proposed in addition to LBT. The LAA operation of LTE in unlicensed spectrum is also investigated in [70], which shows that the load-based LBT protocol of LAA with a backoff defer period can achieve fair coexistence between LAA and Wi-Fi. By leverageing LTE and WiFi antennas available on smartphones, a coexistence approach has been proposed and implemented by USRP in [75], which enables LTE and Wi-Fi to transmit simultaneously and decode the interfering signals successfully.

Despite system level simulation has been widely adopted to study the coexistence issues of cellular (i.e., LTE) and Wi-Fi, it is usually very time-consuming due to the complicated dynamics of the overlaid LTE and Wi-Fi networks. Therefore, a mathematical approach would be helpful for more efficient performance evaluation and transparent comparisons of various tech-

niques. A fluid network model is used in [76] to analyze the coexistence performance when LTE has no protocol modifications. However, the fluid network model is limited to the analysis of deterministic networks, which do not capture the multi-path fading effects and random backoff mechanism of Wi-Fi. A centralized optimization framework is proposed in [77] to optimize the aggregate throughput of LTE and Wi-Fi. However, the analysis of [77] is based on Bianchi's model for CSMA/CA [78], which relies on the idealized assumption that the collision probability of the contending APs is "constant and independent". Game theory has also been utilized to analyze the coexistence performance of LTE and Wi-Fi [79], and multiple operators coexisting in the unlicensed spectrum [80].

Fundamental understandings for the effects of various coexistence methods under dense cellular and Wi-Fi deployment scenarios are relatively rare. Due to its tractability for cellular and Wi-Fi networks, stochastic geometry is a natural candidate for analyzing cellular and Wi-Fi coexistence performance. Specifically, the key performance metrics of cellular/Wi-Fi networks can be derived by modeling the locations of base stations/access points (APs) as a realization of certain spatial random point processes. A modified Matérn hard-core point process, which gives a snapshot view of the simultaneous transmitting CSMA/CA nodes, has been proposed and validated in [81] for dense 802.11 networks. This Matérn CSMA model is also used for analyzing other CSMA/CA based networks, such as ad-hoc CSMA/CA networks with power control [82], ad-hoc networks with channel-aware CSMA/CA protocols [83],

CSMA/CA networks with controlled network topology (i.e., non-Poisson) [84], and cognitive radio networks [85].

Due to its tractability for cellular and Wi-Fi networks, stochastic geometry is a natural candidate for analyzing cellular and Wi-Fi coexistence performance. In [86], the coverage and throughput performance of coexisting cellular and Wi-Fi networks were derived using stochastic geometry. However, the analytical Wi-Fi throughput in [86] does not closely match the simulation results. Also, the effect of possible cellular coexistence methods, including discontinuous transmission and LBT with random backoff, were not investigated in [86].

3.2 Contributions

In this chapter, we develop an analytical framework to model various cellular and Wi-Fi coexistence scenarios using stochastic geometry, based on which key performance metrics for cellular and Wi-Fi networks can be quantified. Specifically, three coexistence scenarios are studied depending on the mechanism adopted by cellular network, including: (1) cellular with continuous transmission and no protocol changes; (2) cellular with fixed duty-cycling discontinuous transmission; and (3) cellular with LBT and random backoff (BO) mechanism. Several key performance metrics, including the medium access probability (MAP), the SINR coverage probability, the density of successful transmission (DST), and the rate coverage probability are derived under each scenario. The accuracy of the analytical results is validated against simula-

tion results using SINR coverage probability. The main design insights of this chapter can be summarized as follows:

- Compared to the baseline scenario where the Wi-Fi network coexists with an additional Wi-Fi network from another operator, the SINR coverage probability, DST, and rate coverage probability of Wi-Fi are severely degraded when cellular BSs transmit persistently. In contrast, cellular network performance is shown to be relatively robust to Wi-Fi's presence.

- When the cellular network transmits discontinuously with a fixed duty cycle, Wi-Fi generally has better DST and rate coverage under a synchronous muting pattern among BSs compared to the asynchronous one; and a short duty cycle for cellular transmission is required to protect Wi-Fi.

- When the cellular network follows the LBT and random BO mechanism, Wi-Fi can achieve better DST and rate coverage performance compared to the baseline scenario if cellular BSs accept either lower channel access priority or more sensitive CCA threshold to protect Wi-Fi. Under both scenarios, cellular network is shown to maintain acceptable rate coverage performance despite using LBT and random BO.

Overall, this chapter provides a flexible stochastic geometry framework for cellular and Wi-Fi coexistence, which validates and complements the system level simulation studies of standardization efforts such as LTE-U forum [87] and 3GPP [56].

3.3 System Model

In this section, we present the spatial location model for Wi-Fi APs and cellular BSs, the radio propagation assumptions, and the channel access model for Wi-Fi and cellular.

3.3.1 Spatial locations

We focus on the scenario where two operators coexist in a single unlicensed frequency band with bandwidth B. Operator 1 uses Wi-Fi, while operator 2 uses cellular (e.g. LTE), which may implement certain coexistence methods to better coexist with operator 1. Both Wi-Fi and cellular are assumed to have full buffer downlink only traffic. Cellular in unlicensed spectrum is mainly designed for femto cellular networks, wherein the small cell BSs are deployed more randomly than the macro BSs [54,56,58,88]. Similarly, most Wi-Fi AP deployments typically have unplanned nature. Therefore, the locations for APs and BSs are modeled as realizations of two independent homogeneous PPPs. Specifically, the AP process $\Phi_W = \{x_i\}_i$ has intensity λ_W[2], while the cellular BS process $\Phi_L = \{y_k\}_k$ has intensity λ_L. As a result, the numbers of APs and BSs in any region with area A are two independent Poisson random variables with mean $\lambda_W A$ and $\lambda_L A$ respectively (resp.).

Both Wi-Fi stations (STAs) and cellular user equipments (UEs)[3] are

[2]Note in any given time slot, not all Wi-Fi APs will be necessarily scheduled by CSMA/CA.

[3]Wi-Fi STA and Wi-Fi users, as well as LTE UE and LTE users, are used interchangeably in this chapter.

also assumed to be distributed according to homogeneous PPPs. Each STA/UE is associated with its closest AP/BS, which provides the strongest average received power. We assume the STA/UE intensity is much larger than the AP/BS intensity, such that each AP/BS has at least one STA/UE to serve. Since both STAs and UEs are homogeneous PPPs, we can analyze the performance of the typical STA/UE, which is assumed to be located at the origin. This is guaranteed by the independence assumption and Slyvniak's theorem [44], which states that for any event A and PPP Φ, $\mathbb{P}(\Phi \in A | o \in \Phi) = \mathbb{P}(\Phi \cup \{o\} \in A)$. Index 0 is used for the serving AP/BS to the typical STA/UE, which will be referred to as the closest or tagged AP/BS for the rest of the chapter. In addition, the link between the typical STA/UE and the tagged AP/BS is referred to as the typical Wi-Fi/cellular link. Since Φ_W is a PPP with intensity λ_W, the probability density function (PDF) of the distance from the typical STA to the tagged AP is $f_W(r) = \lambda_W 2\pi r \exp(-\lambda_W \pi r^2)$. Similarly, the PDF from the typical UE to the tagged BS is $f_L(r) = \lambda_L 2\pi r \exp(-\lambda_L \pi r^2)$.

3.3.2 Propagation Assumptions

The transmit power for each AP and BS is assumed to be P_W and respectively P_L. A common free space path loss model with reference distance of 1 meter is used for both Wi-Fi and cellular links, which is given by $l(d) = 20\log_{10}(\frac{4\pi}{\lambda_c}) + 10\alpha\log_{10}(d)$ dB. Here λ_c denotes the wavelength, α denotes the path loss exponent, and d denotes the link length. The large-scale shadowing effects are neglected for simplicity. All the channels are assumed to be subject

Table 3.1: Notation and Simulation Parameters

Symbol	Definition	Simulation Value
Φ_W, λ_W	Wi-Fi AP PPP and intensity	
Φ_L, λ_L	Cellular BS PPP and intensity	
P_W, P_L	Wi-Fi AP, cellular BS transmit power	23 dBm, 23 dBm
Γ_{cs}, Γ_{ed}	Carrier sensing and energy detection thresholds	-82 dBm, -62 dBm
e_i^W, e_k^L	Medium access indicator for AP x_i, BS y_k	
x_0, y_0	The tagged AP and tagged BS (i.e., the AP and BS closest to the typical STA and UE resp.)	
$f_W(r), f_L(r)$	PDF of the distance from tagged AP/BS to typical STA/UE	
f_c, B	Carrier frequency and bandwidth of the unlicensed band	5 GHz, 20 MHz
α	Path loss exponent	4
σ_N^2	Noise power	0

to i.i.d. Rayleigh fading, with each fading variable exponentially distributed with parameter μ. The thermal noise power is σ_N^2. Notation and system parameters are listed in Table 5.1.

3.3.3 Modeling Channel Access for Wi-Fi

In contrast to cellular which is a centrally-scheduled system, Wi-Fi implements the distributed CSMA/CA protocol for channel access coordination among multiple APs. The CSMA/CA protocol consists of the physical layer clear channel assessment (CCA) process and a random backoff mechanism, such that two nearby nodes will never transmit simultaneously. In particular,

the Wi-Fi device will hold CCA as busy if any valid Wi-Fi signal that exceeds the carrier sense (CS) threshold Γ_{cs} is detected, or if any signal that exceeds the energy detection threshold (ED) Γ_{ed} is received [9]. Similar to [76], we assume Wi-Fi devices detect the BS transmission with the energy detection threshold Γ_{ed} since the cellular signal is not decodable. As soon as a CSMA/CA device observes an idle channel, it needs to follow a random back-off period before transmission. This back-off period is chosen randomly from a set of possible values called the contention window.

To model the locations of Wi-Fi APs which simultaneously access the channel at a given time, we adapt the formulation of [81] to account for the coexisting cellular network. We can define the contender of a Wi-Fi AP x_i as the other Wi-Fi APs and the LTE BSs whose power received by x_i exceeds the threshold Γ_{cs} and Γ_{ed} respectively. Each Wi-Fi AP x_i has an independent mark t_i^W to represent the random back-off period, which is uniformly distributed on $[0, 1]$. Each Wi-Fi AP obtains channel access for packet transmission if it chooses a smaller timer, i.e., back-off period, than all its contenders. A medium access indicator e_i^W is assigned to each AP, which is equal to 1 if the AP is allowed to transmit by the CSMA/CA protocol, and 0 otherwise. Depending on the specific coexistence mechanism of cellular network, the medium access indicator for each AP is determined differently. The Palm probability [44, p.131] that the medium access indicator of a Wi-Fi AP is equal to 1 is referred to as the medium access probability, or MAP for short.

The considered channel access mechanism has some limitations, such as

it has a fixed contention window size which does not capture the exponential backoff, and it is also more suitable for synchronized and slotted version of CSMA/CA. Nevertheless, it is able to model the key feature of CSMA/CA in IEEE 802.11 standard [9], such that each CSMA/CA device transmits if it does not carrier sense any other CSMA/CA device with a smaller back-off timer. In addition, through comparisons with simulation results, [81, 89] show this simplified model provides a reasonable conservative representation of transmitting APs in the actual CSMA/CA networks.

3.3.4 Definition of Performance Metrics

The main performance metrics that are analyzed include the MAP of the tagged AP and BS, as well as the SINR coverage probability for the typical STA and UE. Specifically, given the tagged AP x_0 transmits (i.e., $e_0^W = 1$), the received SINR of the typical Wi-Fi STA is:

$$\mathrm{SINR}_0^W = \frac{P_W F_{0,0}^W / l(\|x_0\|)}{\sum\limits_{x_j \in \Phi_W \setminus \{x_0\}} P_W F_{j,0}^W e_j^W / l(\|x_j\|) + \sum\limits_{y_m \in \Phi_L} P_L F_{m,0}^{LW} e_m^L / l(\|y_m\|) + \sigma_N^2}, \quad (3.1)$$

where e_j^W and e_m^L represent the medium access indicator for AP x_j and BS y_m respectively. The SINR coverage probability of the typical STA with SINR threshold T is defined as $\mathbb{P}(\mathrm{SINR}_0^W > T | e_0^W = 1)$, which gives the instantaneous SINR performance of the typical Wi-Fi link. Equivalently, this can also be interpreted as the fraction of Wi-Fi links that achieve the SINR level T. Similarly, the received SINR of the typical UE given the tagged BS y_0

transmits is:

$$\mathrm{SINR}_0^L = \frac{P_L F_{0,0}^L / l(\|y_0\|)}{\sum\limits_{x_j \in \Phi_W} P_W F_{j,0}^{WL} e_j^W / l(\|x_j\|) + \sum\limits_{y_m \in \Phi_L \setminus \{y_0\}} P_L F_{m,0}^L e_m^L / l(\|y_j\|) + \sigma_N^2}, \quad (3.2)$$

and the SINR coverage probability is $\mathbb{P}(\mathrm{SINR}_0^L > T | e_0^L = 1)$.

Based on the MAP and the SINR distribution, we will compare different cellular coexistence mechanisms using the density of successful transmission and the rate coverage probability, which are defined as follows.

Definition 3.3.1 (Density of Successful Transmissions)**.** For decoding SINR requirement T, the density of successful transmission, or DST for short, is defined as the mean number of successful transmission links per unit area [90]. Since the typical Wi-Fi/cellular link is activated only when the tagged AP/BS accesses the channel, the DST for Wi-Fi and cellular are given by:

$$\begin{aligned} d_{suc}^W(\lambda_W, \lambda_L, T) &= \lambda_W \mathbb{E}[e_0^W] \mathbb{P}(\mathrm{SINR}_0^W > T | e_0^W = 1), \\ d_{suc}^L(\lambda_W, \lambda_L, T) &= \lambda_L \mathbb{E}[e_0^L] \mathbb{P}(\mathrm{SINR}_0^L > T | e_0^L = 1). \end{aligned} \quad (3.3)$$

Definition 3.3.2 (Rate coverage)**.** The rate coverage probability with threshold ρ is defined as the probability for the tagged Wi-Fi AP/cellular BS to support an aggregate data rate of ρ, given by[4]:

$$\begin{aligned} P_{rate}^W(\lambda_W, \lambda_L, \rho) &= \mathbb{P}(B \log(1 + \mathrm{SINR}_0^W) \mathbb{E}[e_0^W] > \rho | e_0^W = 1), \\ P_{rate}^L(\lambda_W, \lambda_L, \rho) &= \mathbb{P}(B \log(1 + \mathrm{SINR}_0^L) \mathbb{E}[e_0^L] > \rho | e_0^L = 1). \end{aligned} \quad (3.4)$$

[4]The user-perceived data rate distribution can be obtained from (3.4) by considering the average fraction of resource that each user achieves.

The terms $\mathbb{E}[e_0^W]$ and $\mathbb{E}[e_0^L]$ in (3.4) account for the fact that the tagged AP and tagged BS have channel access for $\mathbb{E}[e_0^W]$ and $\mathbb{E}[e_0^L]$ fraction of time respectively. Equivalently, the rate coverage probability gives the fraction of Wi-Fi APs/cellular BSs that can support an aggregate data rate of ρ for the rest of the chapter.

Remark 3.3.1. Since both Φ_W and Φ_L are stationary and isotropic, the above performance metrics are invariant with respect to (w.r.t.) the angle of the tagged AP x_0 and tagged BS y_0. Without loss of generality, the angle of x_0 and y_0 are assumed to be 0. In addition, the PDF of $\|x_0\|$ and $\|y_0\|$ are given by $f_W(\cdot)$ and $f_L(\cdot)$ respectively, which are defined in Table 5.1.

Finally, we define several functions that will be used throughout this chapter in Table II. Specifically, $N_0^L(y, r, \Gamma)$ and $N_0^W(y, r, \Gamma)$ represent the expected number of BSs and APs respectively in $\mathbb{R}^2 \setminus B(0, r)$, whose signal power received at $y \in \mathbb{R}^2$ exceeds Γ. In addition, $C_0^L(y_1, \Gamma_1, y_2, \Gamma_2)$ and $C_0^W(y_1, \Gamma_1, y_2, \Gamma_2)$ represent the expected number of BSs and APs respectively in $\mathbb{R}^2 \setminus B(0, \|y_2\|)$, whose signal powers received at $y_1 \in \mathbb{R}^2$ and $y_2 \in \mathbb{R}^2$ exceed Γ_1 and Γ_2 respectively. Moreover, M, V and U are functions helping to calculate the conditional MAP in the following sections.

3.4 Cellular with Continuous Transmission and No Protocol Change

In this section, the MAP and SINR coverage performance for the cellular and Wi-Fi networks are investigated when cellular BSs transmit contin-

Table 3.2: Notations and Definitions of Special Functions

Notation	Definition
$N_0^L(y,r,\Gamma)$	$\lambda_L \int_{\mathbb{R}^2\setminus B(0,r)} \exp(-\mu\frac{\Gamma}{P_L} l(\|x-y\|))\mathrm{d}x$
$N_0^W(y,r,\Gamma)$	$\lambda_W \int_{\mathbb{R}^2\setminus B(0,r)} \exp(-\mu\frac{\Gamma}{P_W} l(\|x-y\|))\mathrm{d}x$
$N_1^L(r,\Gamma)$, $N_1^W(r,\Gamma)$	$N_0^L(y,r,\Gamma)$, $N_0^W(y,r,\Gamma)$ (polar coordinates of $y=(r,0)$)
$N_2^L(r)$, $N_2^W(r)$	$N_0^L(y,r,\Gamma_{ed})$, $N_0^W(y,r,\Gamma_{cs})$ (polar coordinates of $y=(r,0)$)
$N_3^L(\Gamma)$, $N_3^W(\Gamma)$	$N_0^L(o,0,\Gamma)$, $N_0^W(o,0,\Gamma)$
N^L, N^W	$N_0^L(o,0,\Gamma_{ed})$, $N_0^W(o,0,\Gamma_{cs})$
$C_0^L(y_1,\Gamma_1,y_2,\Gamma_2)$	$\lambda_L \int_{\mathbb{R}^2\setminus B(0,\|y_2\|)} \exp(-\mu\frac{\Gamma_1}{P_L} l(\|x-y_1\|) - \mu\frac{\Gamma_2}{P_L} l(\|x-y_2\|))\mathrm{d}x$
$C_0^W(y_1,\Gamma_1,y_2,\Gamma_2)$	$\lambda_W \int_{\mathbb{R}^2\setminus B(0,\|y_2\|)} \exp(-\mu\frac{\Gamma_1}{P_W} l(\|x-y_1\|) - \mu\frac{\Gamma_2}{P_W} l(\|x-y_2\|))\mathrm{d}x$
$C_1^L(y_1,y_2)$, $C_1^W(y_1,y_2)$	$C_0^L(y_1,\Gamma_{ed},y_2,\Gamma_{ed})$, $C_0^W(y_1,\Gamma_{cs},y_2,\Gamma_{cs})$
$C_2^L(y_1)$, $C_2^W(y_1)$	$C_0^L(y_1,\Gamma_{ed},o,\Gamma_{ed})$, $C_0^W(y_1,,\Gamma_{cs},o,\Gamma_{cs})$
$M(N_1,N_2,N_3)$	$(\frac{1-\exp(-N_1)}{N_1} - \frac{1-\exp(-N_1-N_2+N_3)}{N_1+N_2-N_3})/(N_2-N_3)$
$V(x,s_1,s_2,N_1,N_2,N_3)$	$(1-\exp(-\mu s_1 l(\|x\|)))M(N_1,N_2,N_3) + (1-\exp(-\mu s_2 l(\|x\|)))M(N_2,N_1,N_3)$
$U(x,s,N_1)$	$\frac{1-\exp(-N_1)}{N_1} - \exp(-\mu s l(\|x\|))(\frac{1-\exp(-N_1)}{N_1^2} - \frac{\exp(-N_1)}{N_1})$

uously without any protocol modifications.

3.4.1 Medium Access Probability

From the CSMA/CA protocol described in Section II-C, a Wi-Fi AP will not transmit whenever it has an cellular BS as its contender, i.e., the power it receives from any cellular BS exceeds the energy detection threshold Γ_{ed}. Therefore, the medium access indicator e_i^W for AP x_i is:

$$e_i^W = \prod_{y_k\in\Phi_L} \mathbb{1}_{G_{ki}^{LW}/l(\|y_k-x_i\|)\le\frac{\Gamma_{ed}}{P_L}} \prod_{x_j\in\Phi_W\setminus\{x_i\}} \left(\mathbb{1}_{t_j^W\ge t_i^W} + \mathbb{1}_{t_j^W<t_i^W}\mathbb{1}_{G_{ji}^W/l(\|x_j-x_i\|)\le\frac{\Gamma_{cs}}{P_W}}\right). \tag{3.5}$$

The first part of (3.5) means each Wi-Fi AP will not transmit whenever it has any cellular contender, while the second part of (3.5) means each Wi-Fi AP

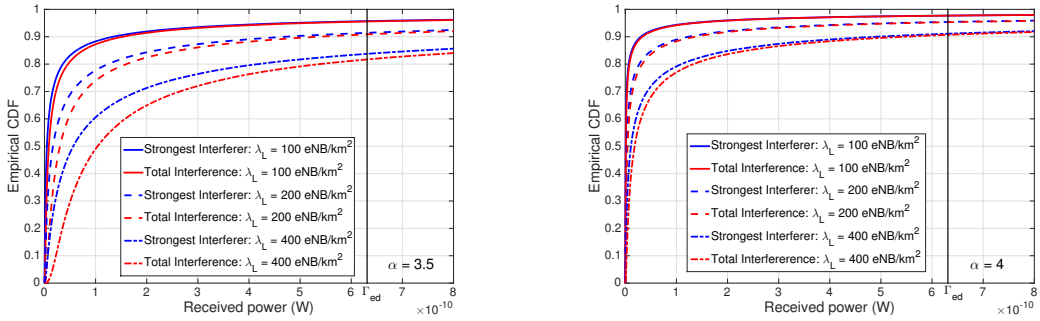

Figure 3.1: Empirical CDF of total cellular interference and strongest cellular interferer at a typical AP.

will not transmit whenever any of its Wi-Fi contenders has a smaller back-off timer.

Remark 3.4.1. Although (3.5) is consistent with IEEE 802.11 specifications [9], energy detection is typically implemented based on total interference [56], i.e., each AP will report channel as busy if the total (non Wi-Fi) interference exceeds the energy detection threshold Γ_{ed}. Nevertheless, under the assumption that BSs/APs have a PPP distribution, (3.5) is a reasonable model for the total interference based energy detection since: (1) the tail distribution of the total interference asymptotically approaches that of the interference from the strongest interferer [91]; (2) ED threshold Γ_{ed} is 20 dB higher than the CS threshold Γ_{cs}, which makes Γ_{ed} a relatively large number; (3) simulation results in Fig. 3.1 show that given $\Gamma_{ed} = -62$dBm and AP x_i, $\mathbb{P}(\sum_{y_k \in \Phi_L} \frac{P_L G_{ki}^{LW}}{l(\|y_k - x_i\|)} \leq \Gamma_{ed}) \approx \mathbb{P}(\max_{y_k \in \Phi_L} \frac{P_L G_{ki}^{LW}}{l(\|y_k - x_i\|)} \leq \Gamma_{ed})$ for various values of α and λ_L; and (4) there is no known closed-form interference distribution with PPP distributed transmitters [91].

Lemma 3.4.1. *When cellular transmits continuously with no protocol modifications, the MAP for a typical Wi-Fi AP is given by:*

$$p^{W}_{0,MAP}(\lambda_W, \lambda_L) = \exp(-N^L)\frac{1-\exp(-N^W)}{N^W}, \tag{3.6}$$

where N^L and N^W are defined in Table 3.2.

Proof. Please see Appendix 3.9.1. □

Remark 3.4.2. By the addition of the cellular network with intensity λ_L, the MAP for a typical AP is degraded by $\exp(-N^L)$ compared to the Wi-Fi only scenario. Note that the decrease is exponential w.r.t. λ_L, the cellular BS intensity.

Based on the system parameters listed in Table 5.1, the MAP for the typical Wi-Fi AP is plotted in Fig. 3.2 w.r.t. different AP and BS intensities. From Fig. 3.2, it can be observed that with low cellular BS intensity (e.g. cellular BS intensity is less than $100/\text{km}^2$), the MAP for the typical Wi-Fi AP is not much affected by the additional cellular network as a result of the high energy detection threshold for cellular signals. However, when the cellular BS intensity increases to over $100/\text{km}^2$, the additional BSs significantly degrade the MAP of the typical Wi-Fi AP.

Since the tagged AP is closer to the typical STA than other APs, the MAP of the tagged AP will be a biased version for the MAP of typical AP:

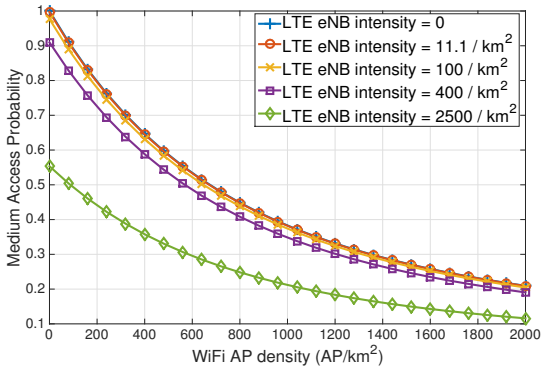

Figure 3.2: Effect of AP and BS intensities on the MAP for the typical Wi-Fi AP.

Corollary 3.4.2. *When cellular transmits continuously with no protocol modifications, the MAP for the tagged Wi-Fi AP is given by:*

$$\hat{p}^{W}_{0,MAP}(\lambda_W, \lambda_L) = \int_0^{\infty} \frac{1-\exp(-N_2^W(r_0))}{N_2^W(r_0)} \exp(-N^L) f_W(r_0) \mathrm{d}r_0, \tag{3.7}$$

where f_W is defined in Table 5.1, while N^L and N_2^W are defined in Table 3.2.

Proof. The proof is provided in Appendix 3.9.2. □

3.4.2 SINR Coverage Probability

3.4.2.1 SINR Coverage Probability of Typical Wi-Fi STA

Since cellular BSs transmit continuously with no protocol modifications, the medium access indicator for each cellular BS is 1 almost surely. The medium access indicator e_j^W in (3.5) depends on both Φ_L and Φ_W. So there exists a correlation between the interference from cellular BSs and that from the Wi-Fi APs. Later we will show that if we substitute Φ_L by another independent PPP $\Phi_L^{'}$ with intensity λ_L in (3.5), the corresponding SINR coverage

is an accurate approximation. This means the correlation between the interference from BSs and APs is mostly captured by the statistical effect of Φ_L on determining the MAP for Wi-Fi APs. Given the tagged AP is located at x_0, we first derive the conditional MAP for another Wi-Fi AP and x_0 to transmit simultaneously.

Corollary 3.4.3. *Conditionally on the fact that the tagged AP $x_0 = (r_0, 0)$ transmits, the probability for another AP $x \in \Phi_W \cap B^c(0, r_0)$ to transmit is:*

$$h_1(r_0, x) = \frac{V(x - x_0, \frac{\Gamma_{cs}}{P_W}, \frac{\Gamma_{cs}}{P_W}, N_2^W(r_0), N_0^W(x, r_0, \Gamma_{cs}), C_1^W(x, x_0))}{U(x - x_0, \frac{\Gamma_{cs}}{P_W}, N_2^W(r_0)) \exp(N^L - C_2^L(x - x_0))}, \quad (3.8)$$

where $B^c(0, r_0)$ is defined in Table 5.1.

Proof. The proof is provided in Appendix 3.9.3. □

Then the SINR coverage performance of the typical STA, denoted by $p_0^W(T, \lambda_W, \lambda_L)$, is obtained as follows:

Lemma 3.4.4. *The SINR coverage probability of the typical Wi-Fi STA with the SINR threshold T can be approximated as:*

$$p_0^W(T, \lambda_W, \lambda_L) \approx \int_0^\infty \exp\left(-\mu T l(r_0) \frac{\sigma_N^2}{P_W}\right) \exp\left(-\int_{\mathbb{R}^2} \frac{T l(r_0) \lambda_L}{\frac{P_W}{P_L} l(\|x\|) + T l(r_0)} \mathrm{d}x\right)$$
$$\times \exp\left(-\int_{\mathbb{R}^2 \setminus B(0, r_0)} \frac{T l(r_0) \lambda_W h_1(r_0, x)}{l(\|x\|) + T l(r_0)} \mathrm{d}x\right) f_W(r_0) \mathrm{d}r_0. \quad (3.9)$$

Proof. The proof is provided in Appendix 3.9.4. □

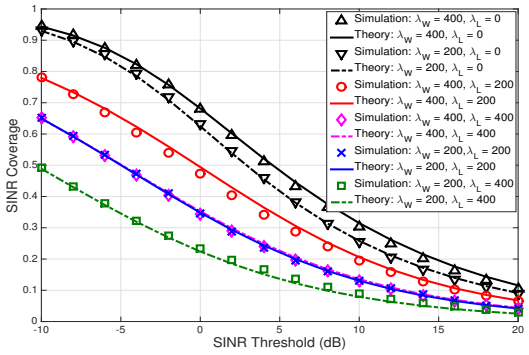

Figure 3.3: SINR coverage for the typical Wi-Fi STA.

Remark 3.4.3. For the rest of this chapter, given the tagged AP or tagged BS located at $(r_0, 0)$ transmits, we use the term "non-homogeneous PPP approximation" to refer to the process of approximating Wi-Fi/cellular interferers as a non-homogeneous PPP with intensity $\lambda_W h(r_0, x)/\lambda_L h(r_0, x)$, where h denotes the conditional MAP of the AP/BS located at x. The non-homogeneous PPP approximation models the dependencies of cellular/Wi-Fi interferers on the tagged BS/AP, but neglects the correlations among the cellular/Wi-Fi interferers. The accuracy of non-homogeneous PPP approximation has been well validated for standalone CSMA/CA networks [81–85, 90], and it will be used in this chapter to derive the SINR distribution for the coexisting cellular and Wi-Fi networks.

Based on the parameters in Table 5.1, Fig. 3.3 gives the SINR coverage performance of the typical Wi-Fi STA. The simulation results are obtained from the following procedure. First, 50 realizations for BS PPP and 50 realizations for AP PPP are generated in an 1 km $\times$ 1 km area, which results in

a total of 2500 combinations of the BS and AP processes. For each combination, we determine the medium access indicator at each AP according to (3.5). In addition, 50 uniformly chosen locations for the typical STA are generated, and we evaluate the received SINR at each STA location if the serving AP transmits. Finally, the SINR coverage probability is obtained as the fraction of STAs whose received SINR exceeds the threshold T.

It can be observed from Fig. 3.3 that Lemma 3.4.4 provides an accurate estimate of the actual SINR coverage. When $\lambda_L = 0$, Wi-Fi achieves good SINR performance due to the carrier sensing for Wi-Fi interferers. However, when coexisting with cellular, the additional interference contributed by the consistently transmitting BSs significantly impacts the SINR coverage of the typical Wi-Fi STA. The smaller the AP intensity λ_W, the more significant the cellular interference, which will lead to worse Wi-Fi SINR coverage performance. In Fig. 3.3, given λ_L, the Wi-Fi SINR coverage for $\lambda_W = 200$ is worse than the case when $\lambda_W = 400$.

3.4.2.2 SINR Coverage Probability of Typical UE

The SINR coverage probability of the typical UE, which is denoted by $p_0^L(T, \lambda_W, \lambda_L)$, is given in the following lemma:

Lemma 3.4.5. *The SINR coverage probability for a typical cellular UE with SINR threshold T can be approximated by:*

$$p_0^L(T, \lambda_W, \lambda_L)$$

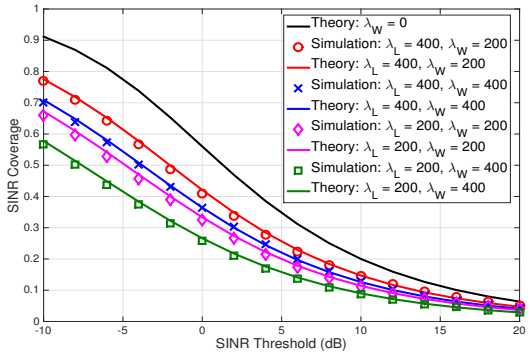

Figure 3.4: SINR coverage for the typical cellular UE.

$$\approx \int_0^\infty \exp\left(-\mu T l(r_0)\frac{\sigma_N^2}{P_L}\right)\exp\left(-\int_{\mathbb{R}^2\setminus B(0,r_0)}\frac{T\lambda_L l(r_0)\mathrm{d}y}{Tl(r_0)+l(\|y\|)}\right)$$
$$\times \exp\left(-\int_{\mathbb{R}^2}\frac{Tl(r_0)\lambda_W h_1^W(r_0,x)}{Tl(r_0)+\frac{P_L}{P_W}l(\|x\|)}\right) f_L(r_0)\mathrm{d}r_0 \tag{3.10}$$

where $h_1^W(r_0,x) = \frac{1-\exp(-N^W)}{N^W}\exp(-N_0^L(x,r_0,\Gamma_{ed}))(1-\exp(-\mu\frac{\Gamma_{ed}}{P_L}l(\|y_0-x\|)))$ *denotes the conditional MAP for AP* x *given the tagged BS* $y_0=(r_0,0)$ *transmits.*

Proof. Please see Appendix 3.9.5. □

Remark 3.4.4. The first two terms in (3.10) come from the thermal noise and the BS interferers respectively, which give the same result as Theorem 2 in [2]. In contrast, the effect of coexisting transmitting Wi-Fi APs is reflected in the third term, which decreases by increasing the Wi-Fi AP intensity λ_W or the energy detection threshold Γ_{ed}.

The SINR coverage for the typical cellular UE is evaluated using both the simulation and analytical results of Lemma 3.4.5. It is given in Fig. 3.4.

The SINR coverage performance when $\lambda_W = 0$ is independent of the BS intensity under Rayleigh fading channels for negligible thermal noise power [2]. From Fig. 3.4, the accuracy of Lemma 3.4.5 can be validated. In addition, it can be observed that the typical cellular UE achieves better SINR coverage when increasing the BS intensity λ_L or decreasing the AP intensity λ_W, with the SINR coverage for $\lambda_W = 0$ as an upper bound. In particular, when $\lambda_L = \lambda_W$, the MAP for each Wi-Fi AP becomes smaller by increasing λ_L, and therefore a better SINR coverage can be achieved by the cellular UE when λ_L is larger. Overall, it can be observed from Fig. 3.4 that unless $\lambda_L \ll \lambda_W$, the typical cellular UE achieves reasonable SINR performance compared to the case when $\lambda_W = 0$, which demonstrates the robustness of the cellular system to the coexisting Wi-Fi system.

Therefore, when cellular coexists with Wi-Fi without any protocol changes, cellular is able to maintain good SINR coverage performance, while Wi-Fi experiences drastically degraded SINR coverage. This imbalanced performance means some fair coexistence methods have to be implemented by cellular in order to guarantee a reasonable performance for Wi-Fi network. The DST and rate coverage performance for cellular and Wi-Fi can be derived directly from Corollary 3.4.2, Lemma 3.4.4 and Lemma 3.4.5. The detailed discussions are provided in Section 3.7.

Finally, although we consider a downlink only scenario for Wi-Fi, similar techniques can be used to derive the MAP and SINR coverage performance when Wi-Fi uplink traffic also exists. Since STAs will apply the same channel

access mechanism as APs, the medium access indicator for each AP and STA will account for both the contending APs and STAs. The detailed performance analysis when Wi-Fi uplink traffic exists is left to future work.

3.5 Cellular with Discontinuous Transmission

A straightforward scheme to guarantee the fair-coexistence between Wi-Fi and cellular is to let cellular adopt a discontinuous, duty-cycle transmission pattern, which is also know as LTE-U [73, 87]. Specifically, within a fixed transmission interval, cellular network transmits for a fraction η of time ($0 \leq \eta \leq 1$), and is muted for the complementary 1-η fraction.

The cellular transmission duy cycle η can be fixed or adaptively adjusted based on Wi-Fi medium utilization [73]. Generally, η needs to be chosen in such a way that cellular shall not impact Wi-Fi more than an additional Wi-Fi network w.r.t. SINR coverage probability, rate coverage, etc. We consider a static muting pattern for cellular, where all the BSs follow the same muting pattern either synchronously or asynchronously. If the BSs are muted synchronously, they transmit and mute at the same time. If the BSs are muted asynchronously, the neighboring BSs could adopt a shifted version of the muting pattern [66]. For simplicity, we assume each BS is transmitting with probability η at a given time under the asynchronous scheme. In the rest of this section, the time-averaged DST and rate coverage performance when cellular transmits discontinuously are derived.

3.5.1 Cellular Network with Synchronous Discontinuous Transmission Pattern

In this case, since all BSs transmit and mute at the same time, the MAP for the tagged Wi-Fi AP during cellular "On" and "Off" period are $\hat{p}^W_{0,MAP}(\lambda_W, \lambda_L)$ and $\hat{p}^W_{0,MAP}(\lambda_W, 0)$ respectively, where $\hat{p}^W_{0,\mathrm{MAP}}$ is given in (3.7). Similarly, the SINR coverage probability of the typical Wi-Fi STA (resp. cellular UE) with threshold T is $p_0^W(T, \lambda_W, \lambda_L)$ (resp. $p_0^L(T, \lambda_W, \lambda_L)$) and $p_0^W(T, \lambda_W, 0)$ (resp. 0) during cellular "On" and "Off" period respectively, where p_0^W and p_0^L are provided in Lemma 3.4.4 and Lemma 3.4.5. Define the time-averaged DST with SINR threshold T as the time-averaged fraction of links that can support SINR level T.

Lemma 3.5.1. *When cellular network adopts a synchronous discontinuous transmission pattern with duty cycle η, the time-averaged DST with threshold T for the Wi-Fi and cellular network are given by:*

$$\begin{aligned} d^W_{1,suc}(\lambda_W, \lambda_L, T, \eta) &= \eta\lambda_W \hat{p}^W_{0,MAP}(\lambda_W, \lambda_L) p_0^W(T, \lambda_W, \lambda_L) \\ &\quad + (1-\eta)\lambda_W \hat{p}^W_{0,MAP}(\lambda_W, 0) p_0^W(T, \lambda_W, 0), \\ d^L_{1,suc}(\lambda_W, \lambda_L, T, \eta) &= \eta\lambda_L p_0^L(T, \lambda_W, \lambda_L), \end{aligned} \tag{3.11}$$

respectively.

Since cellular transmits for η fraction of time and silences for $1-\eta$ fraction time, Lemma 3.5.1 can be obtained directly from Definition 3.3.1.

The time-averaged rate coverage probability with threshold ρ is defined as the time-averaged fraction of BSs/APs that can support an aggregate data

rate of ρ. Since each cellular BS transmits for η fraction of time, we treat the MAP of the tagged BS as η in (3.4).

Lemma 3.5.2. *When cellular network adopts a synchronous discontinuous transmission pattern with duty cycle η, the time-averaged rate coverage probability with rate threshold ρ for Wi-Fi and cellular are given by:*

$$\begin{aligned} P^W_{1,rate}(\lambda_W,\lambda_L,\rho,\eta) =& \eta p_0^W(2^{\frac{\rho}{B\hat{p}^W_{0,MAP}(\lambda_W,\lambda_L)}}-1,\lambda_W,\lambda_L) \\ &+(1-\eta)p_0^W(2^{\frac{\rho}{B\hat{p}^W_{0,MAP}(\lambda_W,0)}}-1,\lambda_W,0), \\ P^L_{1,rate}(\lambda_W,\lambda_L,\rho,\eta) =& p_0^L(2^{\frac{\rho}{B\eta}}-1,\lambda_W,\lambda_L), \end{aligned} \tag{3.12}$$

respectively.

Proof. Please see Appendix 3.9.6. □

It is straightforward from (3.11) and (3.12) that better DST and rate coverage can be achieved by Wi-Fi when η decreases. By contrast, since $p_0^L(T,\lambda_W,\lambda_L)$ is a decreasing function w.r.t. the SINR threshold T, cellular achieves better DST and rate coverage when η increases.

3.5.2 Cellular Network with Asynchronous Discontinuous Transmission Pattern

Since each BS transmits independently with probability η at a given time, the BSs contributing to the interference of Wi-Fi form a PPP with intensity $\eta\lambda_L$. Therefore, the MAP for the tagged AP is $\hat{p}^W_{0,\mathrm{MAP}}(\lambda_W,\eta\lambda_L)$, and the SINR coverage probability with threshold T for the typical Wi-Fi station

is $p_0^W(T, \lambda_W, \eta\lambda_L)$. Correspondingly, the time-averaged DST of Wi-Fi is given by:

$$d_{2,suc}^W(\lambda_W, \lambda_L, T, \eta) = \lambda_W \hat{p}_{0,MAP}^W(\lambda_W, \eta\lambda_L) p_0^W(T, \lambda_W, \eta\lambda_L), \tag{3.13}$$

and the time-averaged rate coverage probability of Wi-Fi is given by:

$$P_{2,rate}^W(\lambda_W, \lambda_L, \rho, \eta) = p_0^W(2^{\frac{\rho}{B\hat{p}_{0,MAP}^W(\lambda_W, \eta\lambda_L)}} - 1, \lambda_W, \eta\lambda_L). \tag{3.14}$$

According to (3.13) and (3.14), Wi-Fi achieves better DST and rate coverage when η decreases.

For cellular network, during the η fraction of time that the tagged BS transmits, the interfering BSs form a PPP with intensity $\eta\lambda_L$. Thus, the time-averaged DST of cellular is given by:

$$d_{2,suc}^L(\lambda_W, \lambda_L, T, \eta) = \lambda_L \eta \int_0^\infty p_0^L(r_0, T, \lambda_W, \eta\lambda_L) 2\pi\lambda_L r_0 \exp(-\lambda_L \pi r_0^2) \mathrm{d}r_0, \tag{3.15}$$

and the time-averaged rate coverage probability is given by:

$$P_{2,rate}^L(\lambda_W, \lambda_L, \rho, \eta) = \int_0^\infty p_0^L(r_0, 2^{\frac{\rho}{B\eta}} - 1, \lambda_W, \eta\lambda_L) 2\pi\lambda_L r_0 \exp(-\lambda_L \pi r_0^2) \mathrm{d}r_0, \tag{3.16}$$

where $p_0^L(r_0, T, \lambda_W, \lambda_L)$ is derived in Lemma 3.4.5.

3.5.3 Comparison of Synchronous and Asynchronous Muting Patterns

Fig. 3.5 and Fig. 3.6 show the analytical time-averaged DST and rate coverage performance when $\lambda_W = 400$ APs/km^2 and $\lambda_L = 400$ BSs/km^2. In

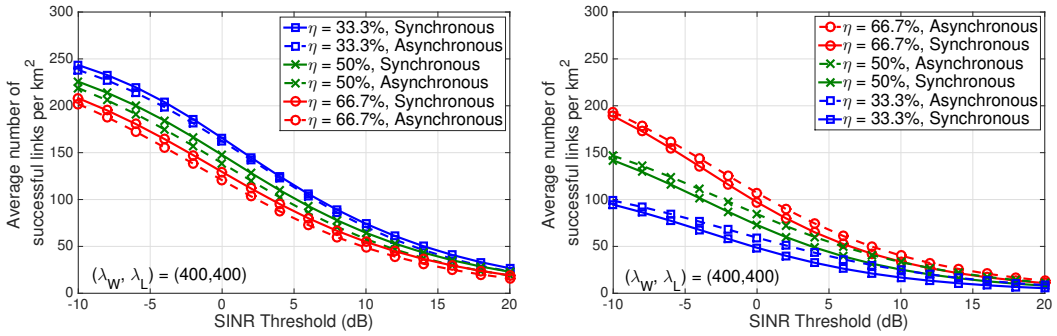

(a) DST for Wi-Fi network (b) DST for cellular network

Figure 3.5: DST comparison.

terms of Wi-Fi DST and rate coverage performance, the synchronous cellular muting pattern generally outperforms the asynchronous one. This is due to fact that when all cellular BSs are muted, Wi-Fi APs observe a much cleaner channel and therefore benefit more compared to the asynchronous scheme. Since cellular interferers form an independent thinning of the BS process under the asynchronous muting pattern, the latter outperforms the synchronous pattern in terms of DST and rate coverage. In addition, Fig. 3.5 and Fig. 3.6 also indicate that cellular needs to adopt a short transmission duty cycle η (e.g., less than 50%) to protect Wi-Fi. However, cellular is also more sensitive to the transmission duty cycle compared to Wi-Fi, which means that a very small η leads to much degraded performance of cellular. Therefore, a synchronous muting pattern with a reasonably short cellular transmission duty cycle (e.g., within 33.3% to 50%) is suggested to best protect Wi-Fi.

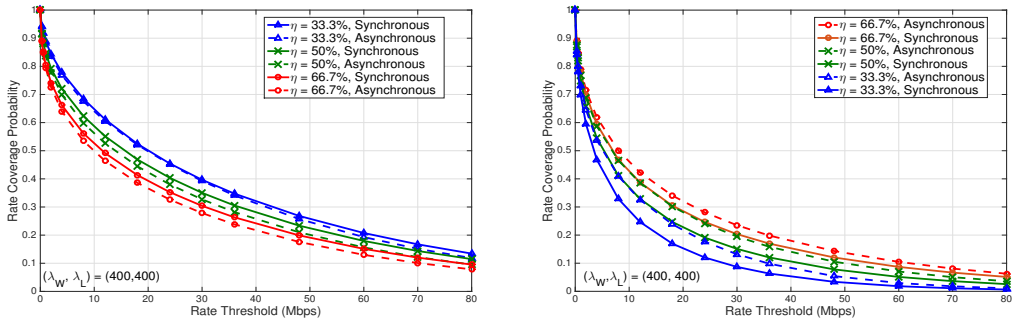

(a) Rate coverage for Wi-Fi network (b) Rate coverage for cellular network

Figure 3.6: Rate coverage comparison.

3.6 Cellular with Listen-before-talk and Random Back-off

Besides cellular with discontinuous transmission, another fair coexistence method is to let cellular implement the listen-before-talk (LBT) and random backoff (BO) mechanism similar to Wi-Fi. This is also known as the licensed assisted access (LAA), which is proposed by 3GPP as a global solution to guarantee fair coexistence between cellular and Wi-Fi. Specifically, we consider each BS implements carrier sense mechanism to detect strong interfering cellular and Wi-Fi neighbors with a common threshold Γ^L. In addition, each BS implements a random back off timer, which is uniformly distributed between a and b. The value of (a, b) determines how aggressively cellular BSs access the channel. The medium access indicators for AP x_i and BS y_k are given as follows:

$$e_i^W = \prod_{x_j \in \Phi_W \setminus \{x_i\}} \left(\mathbb{1}_{t_j^W \geq t_i^W} + \mathbb{1}_{t_j^W < t_i^W} \mathbb{1}_{\frac{G_{ji}^W}{l(\|x_j - x_i\|)} \leq \frac{\Gamma_{cs}}{P_W}} \right) \prod_{y_m \in \Phi_L} \left(\mathbb{1}_{t_m^L \geq t_i^W} + \mathbb{1}_{t_m^L < t_i^W} \mathbb{1}_{\frac{G_{mi}^{LW}}{l(\|y_m - x_i\|)} \leq \frac{\Gamma_{ed}}{P_L}} \right),$$

$$e_k^L = \prod_{x_j \in \Phi_W} \left(\mathbb{1}_{t_j^W \geq t_k^L} + \mathbb{1}_{t_j^W < t_k^L} \mathbb{1}_{\frac{G_{jk}^{WL}}{l(\|y_k - x_j\|)} \leq \frac{\Gamma^L}{P_W}} \right) \prod_{y_m \in \Phi_L \setminus \{y_k\}} \left(\mathbb{1}_{t_m^L \geq t_k^L} + \mathbb{1}_{t_m^L < t_k^L} \mathbb{1}_{\frac{G_{mk}^{L}}{l(\|y_m - y_k\|)} \leq \frac{\Gamma^L}{P_L}} \right). \tag{3.17}$$

The expression for e_i^W means AP x_i does not transmit whenever the power it receives from any AP or BS with a smaller back-off timer exceeds Γ_{cs} or Γ_{ed}; while the expression for e_k^L means BS y_k does not transmit whenever the power it receives from any AP or BS with a smaller back-off timer exceeds Γ^L. By implementing the LBT and random BO scheme, cellular has some flexibility in choosing the sensing threshold (i.e., Γ^L), and the channel access priority (i.e., (a, b)) to better coexist with Wi-Fi. In particular, two channel access priority scenarios of cellular are considered, namely when cellular has the same channel access priority as Wi-Fi, and when cellular has the lower channel access priority than Wi-Fi. These two scenarios correspond to the cases when $(a, b) = (0, 1)$ and $(a, b) = (1, 2)$, which are analyzed in the rest of the section.

3.6.1 Cellular with Same Channel Access Priority as Wi-Fi when $(a, b) = (0, 1)$

In this case, cellular network has the same channel access priority as Wi-Fi in terms of the random backoff procedure. In addition, the sensitivity of cellular to interfering signals is controlled by the threshold Γ^L. A more sensitive Γ^L provides a better protection to Wi-Fi, and vice versa. The MAP for a typical AP and BS can be easily derived from (3.17):

Lemma 3.6.1. *When cellular follows the LBT and random BO mechanism*

with $(a, b) = (0, 1)$*, the MAPs for typical AP and BS, denoted by* $p^W_{3,MAP}$ *and* $p^L_{3,MAP}$ *respectively, are given by:*

$$p^W_{3,MAP}(\lambda_W, \lambda_L) = \frac{1 - \exp(-N^W - N^L)}{N^W + N^L},$$
$$p^L_{3,MAP}(\lambda_W, \lambda_L) = \frac{1 - \exp(-N^W_3(\Gamma^L) - N^L_3(\Gamma^L))}{N^W_3(\Gamma^L) + N^L_3(\Gamma^L)},$$

where N^W*,* N^L*,* $N^W_3(\Gamma^L)$ *and* $N^L_3(\Gamma^L)$ *are defined in Table 3.2.*

Lemma 3.6.1 can be proved similarly to Lemma 3.4.1; thus the detailed proof is omitted.

Remark 3.6.1. Lemma 3.6.1 shows that $\frac{1}{1+N^W+N^L} \leq p^W_{3,\mathrm{MAP}}(\lambda_W, \lambda_L) < \frac{1}{N^W+N^L}$. Therefore, the MAP for the typical Wi-Fi AP is inversely proportional to the total number of its Wi-Fi and cellular contenders. Similarly, the MAP for the typical BS is inversely proportional to the total number of APs and BSs whose power received by the typical BS exceeds Γ^L.

Corollary 3.6.2. *When cellular implements LBT and random BO with contention window size* $[a, b] = [0, 1]$*, the MAPs of the tagged Wi-Fi AP and cellular BS are given by:*

$$\mathbb{E}(e^W_0) = \int_0^\infty \frac{1 - \exp(-N^W_2(r_0) - N^L)}{N^W_2(r_0) + N^L} f_W(r_0)\mathrm{d}r_0,$$
$$\mathbb{E}(e^L_0) = \int_0^\infty \frac{1 - \exp(-N^W_3(\Gamma^L) - N^L_1(r_0, \Gamma^L))}{N^W_3(\Gamma^L) + N^L_1(r_0, \Gamma^L)} f_L(r_0)\mathrm{d}r_0,$$

respectively.

In terms of MAP, the effect of the additional cellular network on Wi-Fi is similar to that of deploying another CSMA/CA network with intensity λ_L

and transmit power P_L. However, since each STA (UE) can only associate with its closest AP (BS), the cellular (Wi-Fi) network becomes a closed access CSMA/CA network to Wi-Fi (cellular), which may have significant impact on SINR performance. Since the transmitting BS/AP process is a dependent thinning of Φ_L/Φ_W, whose Laplace functional is generally unknown in a closed form, the independent non-homogeneous PPP approximation to the transmitting BS and AP point processes is used. First, we derive the following conditional MAP for each AP/BS given the tagged AP transmits.

Corollary 3.6.3. *Conditionally on the fact that tagged AP $x_0 = (r_0, 0)$ transmits, the probability for another AP $x_i \in \Phi_W \cap B^c(0, r_0)$ to transmit is:*

$$h_2^W(r_0, x_i) = \frac{V(x_i - x_0, \frac{\Gamma_{cs}}{P_W}, \frac{\Gamma_{cs}}{P_W}, N_1, N_2, N_3)}{U(x_i - x_0, \frac{\Gamma_{cs}}{P_W}, N_2)}, \tag{3.18}$$

where $N_1 = N_0^W(x_i, r_0, \Gamma_{cs}) + N^L$, $N_2 = N_2^W(r_0) + N^L$ and $N_3 = C_1^W(x_0, x_i) + C_2^L(x_i - x_0)$.

Corollary 3.6.4. *Conditionally on the fact that tagged AP $x_0 = (r_0, 0)$ transmits, the probability for BS $y_k \in \Phi_L$ to transmit is:*

$$h_2^L(r_0, y_k) = \frac{V(y_k - x_0, \frac{\Gamma^L}{P_W}, \frac{\Gamma_{ed}}{P_L}, N_4, N_5, N_6)}{U(y_k - x_0, \frac{\Gamma_{ed}}{P_L}, N_5)}, \tag{3.19}$$

where $N_4 = N_0^W(y_k, r_0, \Gamma^L) + N_3^L(\Gamma^L)$, $N_5 = N_2^W(r_0) + N^L$, $N_6 = C_0^W(y_k, \Gamma^L, x_0, \Gamma_{cs}) + C_0^L(y_k - x_0, \Gamma^L, o, \Gamma_{ed})$.

The proof of Corollary 3.6.3 is provided in the Appendix 3.9.7, while Corollary 3.6.4 can be proved in a similar way to Corollary 3.6.3; thus we omit the detailed proof.

Given the tagged AP x_0 transmits, we resort to approximating the interfering AP and BS process by two independent non-homogeneous PPPs with intensities $\lambda_W h_2^W(r_0, x)$ and $\lambda_L h_2^L(r_0, x)$ respectively, which leads to the following approximate SINR coverage of the typical Wi-Fi STA:

Lemma 3.6.5. *When cellular network implements the listen-before-talk and random backoff mechanism with $(a, b) = (0, 1)$, the approximate SINR coverage probability of the typical STA is given by:*

$$p_3^W(T, \lambda_W, \lambda_L) \approx \int_0^\infty \exp\left(-\mu T l(r_0) \frac{\sigma_N^2}{P_W}\right) \exp\left(-\int_{\mathbb{R}^2} \frac{T l(r_0) \lambda_L h_2^L(r_0, y)}{\frac{P_W}{P_L} l(\|y\|) + T l(r_0)} \mathrm{d}y\right) \times \exp\left(-\int_{\mathbb{R}^2 \setminus B(0, r_0)} \frac{T l(r_0) \lambda_W h_2^W(r_0, x)}{l(\|x\|) + T l(r_0)} \mathrm{d}x\right) f_W(r_0) \mathrm{d}r_0. \tag{3.20}$$

Lemma 3.6.5 can be easily proved using the non-homogeneous PPP approximation; thus we omit the detailed proof.

Remark 3.6.2. The first and second terms in (3.20) stem from thermal noise and interferers respectively, while the third term stems from the transmitting Wi-Fi interferers. The intensity of the Wi-Fi interferers at $x \in \mathbb{R}^2 \cap B^o(0, r_0)$ is described by the function $\lambda_W h_2^W(r_0, x)$. Note that when $\|x\| \to \infty$, we have $N_0^W(x, r_0, \Gamma_{cs}) \to N^W$, $C_1^W(x_0, x) \to 0$ and $C_2^L(x - x_0) \to 0$, which gives the following asymptotic result: $\lim_{\|x\| \to \infty} \lambda_W h_2^W(r_0, x) = \lambda_W p_{3,\mathrm{MAP}}^W(\lambda_W, \lambda_L)$. The intensity of cellular interferers also satisfies the asymptotic result: $\lim_{\|y\| \to \infty} \lambda_L h_2^L(r_0, y) = \lambda_L p_{3,\mathrm{MAP}}^L(\lambda_W, \lambda_L)$.

Similar to Wi-Fi, given the tagged BS is located at $y_0 = (r_0, 0)$, the

modified medium access indicators for each AP and BS are given by:

$$\hat{e}_i^W = \prod_{x_j \in \Phi_W \setminus \{x_i\}} \left(\mathbb{1}_{t_j^W \geq t_i^W} + \mathbb{1}_{t_j^W < t_i^W} \mathbb{1}_{G_{ji}^W / l(\|x_j - x_i\|) \leq \frac{\Gamma_{cs}}{P_W}} \right)$$
$$\times \prod_{y_m \in (\Phi_L \cap B^c(0,r_0) + \delta_{y_0})} \left(\mathbb{1}_{t_m^L \geq t_i^W} + \mathbb{1}_{t_m^L < t_i^W} \mathbb{1}_{G_{mi}^{LW} / l(\|y_m - x_i\|) \leq \frac{\Gamma_{ed}}{P_L}} \right),$$
$$\hat{e}_k^L = \prod_{x_j \in \Phi_W} \left(\mathbb{1}_{t_j^W \geq t_k^L} + \mathbb{1}_{t_j^W < t_k^L} \mathbb{1}_{G_{jk}^{WL} / l(\|y_k - x_j\|) \leq \frac{\Gamma^L}{P_W}} \right)$$
$$\times \prod_{y_m \in (\Phi_L \cap B^c(0,r_0) + \delta_{y_0}) \setminus \{y_k\}} \left(\mathbb{1}_{t_m^L \geq t_k^L} + \mathbb{1}_{t_m^L < t_k^L} \mathbb{1}_{G_{mk}^L / l(\|y_m - y_k\|) \leq \frac{\Gamma^L}{P_L}} \right).$$

By following the same procedure as Corollary 3.6.3 and Corollary 3.6.4, we can calculate the conditional MAP for each AP and BS, given the tagged BS of the typical UE transmits.

Corollary 3.6.6. *Conditionally on the fact that the tagged BS $y_0 = (r_0, 0)$ transmits, the probability for another AP $x_i \in \Phi_W \cap B^c(0, r_0)$ to transmit is:*

$$h_3^W(r_0, x_i) = \frac{V(x_i - y_0, \frac{\Gamma_{ed}}{P_L}, \frac{\Gamma^L}{P_W}, N_1, N_2, N_3)}{U(x_i - y_0, \frac{\Gamma^L}{P_W}, N_1)},$$

where $N_1 = N_3^W(\Gamma^L) + N_1^L(r_0, \Gamma^L)$, $N_2 = N^W + N_0^L(x_i, r_0, \Gamma_{ed})$, and $N_3 = C_0^W(y_0 - x_i, \Gamma^L, o, \Gamma_{cs}) + C_0^L(x_i, \Gamma_{ed}, y_0, \Gamma^L)$.

Corollary 3.6.7. *Conditionally on the fact that the tagged BS $y_0 = (r_0, 0)$ transmits, the probability for another AP $x_i \in \Phi_W \cap B^c(0, r_0)$ to transmit is:*

$$h_3^L(r_0, y_k) = \frac{V(y_k - y_0, \frac{\Gamma^L}{P_L}, \frac{\Gamma^L}{P_L}, N_4, N_5, N_6)}{U(y_k - y_0, \frac{\Gamma^L}{P_L}, N_4)},$$

where $N_4 = N_3^W(\Gamma^L) + N_1^L(r_0, \Gamma^L)$, $N_5 = N_3^W(\Gamma^L) + N_0^L(y_k, r_0, \Gamma^L)$, and $N_6 = C_0^W(y_0 - y_k, \Gamma^L, o, \Gamma^L) + C_0^L(y_k, \Gamma^L, y_0, \Gamma^L)$.

Based on Corollary 3.6.6 and Corollay 3.6.7, the SINR coverage of the typical UE can also be derived using the non-homogeneous PPP approximation of the interfering BSs and APs:

Lemma 3.6.8. *When cellular network implements listen-before-talk and random backoff mechanism with* $(a, b) = (0, 1)$*, the approximate SINR coverage probability of the typical cellular UE is:*

$$p_3^L(T, \lambda_W, \lambda_L) \approx \int_0^\infty \exp\left(-\mu T l(r_0)\frac{\sigma_N^2}{P_W}\right) \exp\left(-\int_{\mathbb{R}^2} \frac{T l(r_0)\lambda_W h_3^W(r_0, x)}{\frac{P_L}{P_W} l(\|x\|) + T l(r_0)} \mathrm{d}x\right) \times \exp\left(-\int_{\mathbb{R}^2 \setminus B(0,r_0)} \frac{T l(r_0)\lambda_L h_3^L(r_0, y)}{l(\|y\|) + T l(r_0)} \mathrm{d}y\right) f_L(r_0)\mathrm{d}r_0.$$

3.6.2 Cellular with Lower Channel Access Priority as Wi-Fi when (a,b) = (1,2)

In this case, since the random backoff timer for each cellular BS is always larger than that of Wi-Fi APs, cellular has a lower channel access priority. Specifically, the medium access indicator for each Wi-Fi AP and cellular BS in (3.17) can be simplified to:

$$e_i^W = \prod_{x_j \in \Phi_W \setminus \{x_i\}} \left(\mathbb{1}_{t_j^W \geq t_i^W} + \mathbb{1}_{t_j^W < t_i^W} \mathbb{1}_{G_{ji}^W / l(\|x_j - x_i\|) \leq \frac{\Gamma_{cs}}{P_W}}\right),$$

$$e_k^L = \prod_{x_j \in \Phi_W} \mathbb{1}_{G_{jk}^{WL} / l(\|x_j - y_k\|) \leq \frac{\Gamma^L}{P_W}} \prod_{y_m \in \Phi_L \setminus \{y_k\}} \left(\mathbb{1}_{t_m^L \geq t_k^L} + \mathbb{1}_{t_m^L < t_k^L} \mathbb{1}_{G_{mk}^L / l(\|y_m - y_k\|) \leq \frac{\Gamma^L}{P_L}}\right). \tag{3.21}$$

The MAP for the typical AP and BS are given in the following lemma.

Lemma 3.6.9. *When cellular network follows a LBT and random BO mechanism with* $(a, b) = (1, 2)$*, the MAPs for typical AP and BS, denoted by* $p_{4,MAP}^W$

and $p^L_{4,MAP}$ *respectively, are given by:*

$$p^W_{4,MAP}(\lambda_W, \lambda_L) = \frac{1-\exp(-N^W)}{N^W},$$
$$p^L_{4,MAP}(\lambda_W, \lambda_L) = \exp(-N^W_3(\Gamma^L))\frac{1-\exp(-N^L_3(\Gamma^L))}{N^L_3(\Gamma^L)},$$

respectively.

Corollary 3.6.10. *When cellular network follows a LBT and random BO mechanism with* $(a, b) = (1, 2)$*, the MAP for the tagged Wi-Fi AP and cellular BS are given by:*

$$\hat{p}^W_{4,MAP}(\lambda_W, \lambda_L) = \int_0^\infty \frac{1-\exp(-N^W_2(r_0))}{N^W_2(r_0)} f_W(r_0)\mathrm{d}r_0,$$
$$\hat{p}^L_{4,MAP}(\lambda_W, \lambda_L) = \int_0^\infty \exp(-N^W_3(\Gamma^L)), \frac{1-\exp(-N^L_1(r_0, \Gamma^L))}{N^L_1(r_0, \Gamma^L)} f_L(r_0)\mathrm{d}r_0,$$

respectively.

In terms of MAP, this scheme is optimal to protect Wi-Fi since each AP has the same MAP as if cellular does not exist. In contrast, since BSs will not transmit whenever a strong interfering AP exists, BSs will have a role similar to APs in the scenario when cellular transmits continuously.

In order to determine the coverage probability for the typical STA and typical UE, procedures similar to that of the previous parts are used. In particular, the conditional MAP $\mathbb{P}^{x_i}_{\Phi_W}(e^W_i = 1 | e^W_0 = 1, x_0 = (r_0, 0))$, denoted by $h^W_4(r_0, x_i)$, can be directly obtained from Corollary 3.4.3 by making $\lambda_L = 0$, which is given by:

$$h^W_4(r_0, x_i) = \frac{V(x - x_0, \frac{\Gamma_{cs}}{P_W}, \frac{\Gamma_{cs}}{P_W}, N^W_2(r_0), N^W_0(x, r_0, \Gamma_{cs}), C^W_2(x, x_0))}{U(x - x_0, \frac{\Gamma_{cs}}{P_W}, N^W_2(r_0))}.$$

In addition, denote the conditional probability $\mathbb{P}^{y_k}_{\Phi_L}(e^L_k = 1|e^W_0 = 1, x_0 = (r_0, 0))$ by $h^L_4(r_0, y_k)$, we get:

$$h^L_4(r_0, y_k) = \frac{\frac{1-\exp(-N^L_3(\Gamma^L))}{N^L_3(\Gamma^L)} \frac{1-\exp(-N^W_2(r_0)+C^W_0(y_k,\Gamma^L,x_0,\Gamma_{cs}))}{N^W_2(r_0)-C^W_0(y_k,\Gamma^L,x_0,\Gamma_{cs})}(1-\exp(-\mu\frac{\Gamma^L}{P_W}l(\|x_0-y_k\|)))}{\frac{1-\exp(-N^W_2(r_0))}{N^W_2(r_0)}\exp(N^W_0(y_k, r_0, \Gamma^L))}.$$

By applying the non-homogeneous PPP approximation to Wi-Fi and cellular interferers, the SINR coverage probability of the typical STA can be derived by the following procedures which are similar to that of Lemma 3.6.5:

Lemma 3.6.11. *When cellular implements the listen-before-talk and random backoff mechanism with $(a, b) = (1, 2)$, the approximate SINR coverage probability of a typical Wi-Fi STA is:*

$$p^W_4(T, \lambda_W, \lambda_L) \approx \int_0^\infty \exp\left(-\mu T l(r_0)\frac{\sigma^2_N}{P_W}\right)\exp\left(-\int_{\mathbb{R}^2}\frac{T l(r_0)\lambda_L h^L_4(r_0, y)}{\frac{P_W}{P_L}l(\|y\|)+T l(r_0)}\mathrm{d}y\right)$$
$$\times \exp\left(-\int_{\mathbb{R}^2\setminus B(0,r_0)}\frac{T l(r_0)\lambda_W h^W_4(r_0, x)}{l(\|x\|)+T l(r_0)}\mathrm{d}x\right) f_W(r_0)\mathrm{d}r_0.$$

Next, given the tagged BS of the typical UE is located at $y_0 = (r_0, 0)$, the two conditional probabilities $\mathbb{P}^{x_i}_{\Phi_W}(e^W_i = 1|e^L_0 = 1, y_0 = (r_0, 0))$ and $\mathbb{P}^{y_k}_{\Phi_L}(e^L_k = 1|e^L_0 = 1, y_0 = (r_0, 0))$, denoted by $h^W_5(r_0, x_i)$ and $h^L_5(r_0, y_k)$ respectively, are given in (3.22) and (3.23):

$$h^W_5(r_0, x_i) = \frac{1-\exp(-N^W + C^W_0(y_0 - x_i, \Gamma^L, o, \Gamma_{cs}))}{N^W - C^W_0(y_0 - x_i, \Gamma^L, o, \Gamma_{cs})}, \tag{3.22}$$

$$h^L_5(r_0, y_k) = \frac{(1-\exp(-\mu\frac{\Gamma^L}{P_L}l(\|y_k - y_0\|)))(M(N_4, N_5, N_6) + M(N_5, N_4, N_6))}{\exp(N^W_3(\Gamma^L) - C^W_0(y_0 - y_k, \Gamma^L, o, \Gamma^L))U(y_k - y_0, \frac{\Gamma^L}{P_L}, N_4)}, \tag{3.23}$$

where $N_4 = N_1^L(r_0, \Gamma^L)$, $N_5 = N_0^L(y_k, r_0, \Gamma^L)$ and $N_6 = C_0^L(y_k, \Gamma^L, y_0, \Gamma^L)$ in (3.23).

Based on h_5^W and h_5^L, the SINR coverage probability of the typical UE can be derived by applying the non-homogeneous PPP approximation:

Lemma 3.6.12. *When cellular network implements the listen-before-talk and random backoff mechanism with $(a, b) = (1, 2)$, the approximate SINR coverage probability of the typical cellular UE is:*

$$p_4^L(T, \lambda_W, \lambda_L) \approx \int_0^\infty \exp\left(-\mu T l(r_0) \frac{\sigma_N^2}{P_W}\right) \exp\left(-\int_{\mathbb{R}^2 \setminus B(0,r_0)} \frac{T l(r_0) \lambda_L h_5^L(r_0, y)}{l(\|y\|) + T l(r_0)} \mathrm{d}y\right) \times \exp\left(-\int_{\mathbb{R}^2} \frac{T l(r_0) \lambda_W h_5^W(r_0, x)}{\frac{P_L}{P_W} l(\|x\|) + T l(r_0)} \mathrm{d}x\right) f_L(r_0) \mathrm{d}r_0.$$

The SINR coverage performance of the typical STA and UE under two cellular channel access priority schemes is plotted in Fig. 3.7 and Fig. 3.8, where the simulation results are obtained from the definition of SINR in (3.1) and (3.2). The accuracy of the approximations can be validated for various cellular sensing thresholds and AP/BS densities. Since both Wi-Fi/cellular adopt the LBT and random backoff mechanism, a good overall SINR coverage probability can be achieved for Wi-Fi and cellular. In addition, given cellular contention window size (a, b), both Wi-Fi STA and cellular UE can achieve better SINR performance with a more sensitive threshold Γ^L, which is due to less cellular interference. It can also be observed that when cellular has lower channel access priority, a less sensitive threshold Γ^L is needed to obtain a similar Wi-Fi SINR performance as in the case when cellular has the same channel access priority as Wi-Fi.

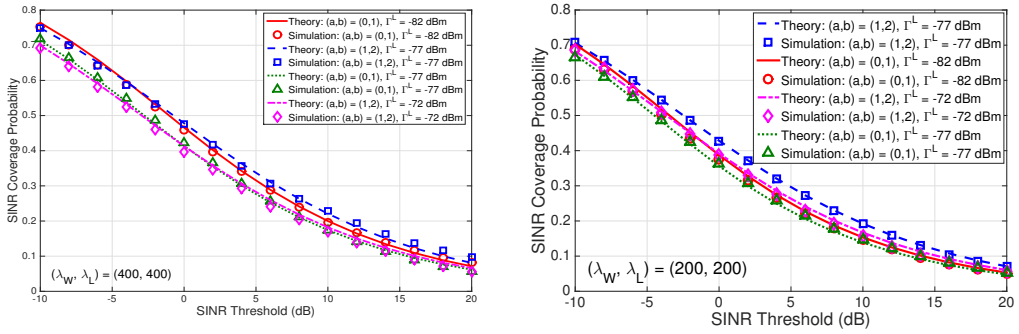

Figure 3.7: Wi-Fi SINR performance under different cellular channel access priorities and Γ^L.

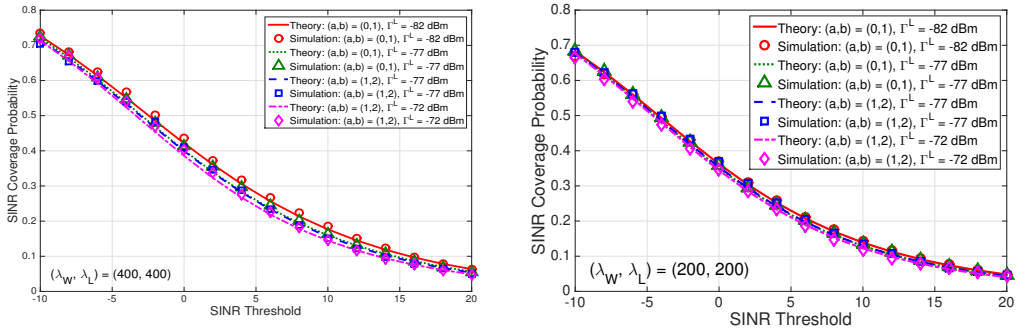

Figure 3.8: Cellular SINR performance under different channel access priorities and Γ^L.

3.7 Performance Comparisons of Different Coexistence Mechanisms

In this section, the DST and rate coverage performance for each coexistence scenario are compared through numerical evaluations. As mentioned earlier, cellular in unlicensed spectrum operation is mainly designed for LTE. In particular, we use Wi-Fi + LTE (Wi-Fi + LTE-U, and Wi-Fi + LAA respectively) to denote the scenario when Wi-Fi operator 1 coexists with another

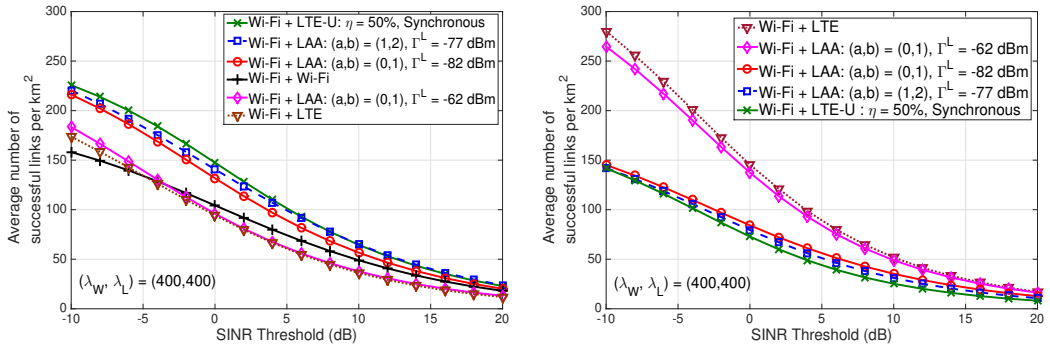

(a) DST for operator 1 (b) DST for operator 2

Figure 3.9: DST comparisons under different coexistence scenarios.

operator 2, which uses cellular with no protocol change (cellular with discontinuous transmission, and cellular with LBT and random BO respectively). The baseline performance of Wi-Fi operator 1 is when operator 2 also uses Wi-Fi (i.e., Wi-Fi + Wi-Fi). The Wi-Fi MAP and SINR coverage of the baseline scenario can be obtained directly from Lemma 3.6.1 and Lemma 3.6.5 by setting all the sensing thresholds to Γ_{cs}. In addition, we focus on a dense network deployment where $\lambda_W = 400$ APs/km^2 and $\lambda_L = 400$ BSs/km^2. Based on the MAP and approximate SINR coverage probability, we have investigated the DST and rate coverage probability of Wi-Fi and cellular under all the coexistence scenarios in Fig. 3.9 and Fig. 3.10.

Fig. 3.9a shows that under Wi-Fi+LTE, Wi-Fi has the worst DST performance since it experiences strong interference from the persistent transmitting cellular BSs. In addition, Wi-Fi achieves similar DST performance when operator 2 implements one of the following mechanisms: (1) LTE-U with a

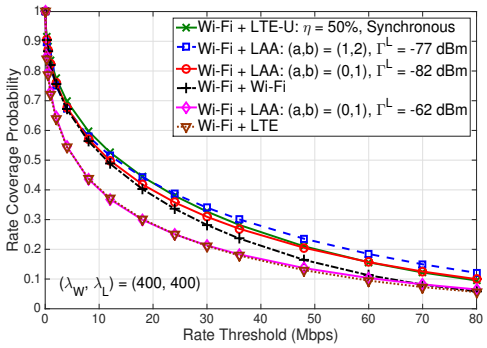

(a) Rate coverage for operator 1

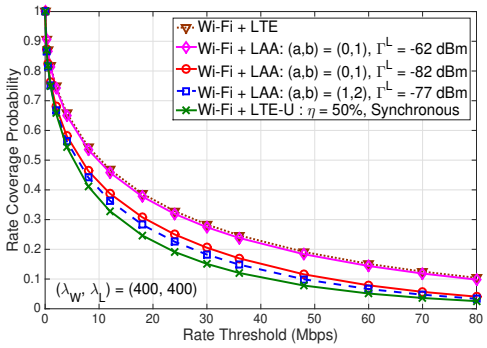

(b) Rate coverage for operator 2

Figure 3.10: Rate coverage comparisons under different coexistence scenarios.

short duty cycle (e.g., 50%); (2) LAA with same channel access priority as Wi-Fi and a more sensitive sensing threshold (e.g., $(a, b) = (0, 1)$, $\Gamma^L = -82$ dBm); and (3) LAA with lower channel access priority than Wi-Fi and a less sensitive sensing threshold (e.g., $(a, b) = (1, 2)$, $\Gamma^L = -77$ dBm). Compared to the baseline scenario, Wi-Fi has better DST under the above scenarios, especially in the low SINR threshold regime. This is because although Wi-Fi has better SINR coverage performance under the baseline scenario, its DST suffers from the much degraded MAP due to the highly sensitive sensing threshold Γ_{cs}. Furthermore, when operator 2 implements LAA with the -62 dBm energy detection threshold, the DST performance of Wi-Fi is not much improved over Wi-Fi + LTE. Therefore, the -62 dBm energy detection threshold is too conservative to protect Wi-Fi, and a more sensitive threshold Γ^L is recommended for LAA. In contrast, Fig. 3.9b shows that operator 2 has significantly lower (around 50%) DST when using LTE-U or LAA with a sensitive sensing threshold (e.g., -82 dBm or -77 dBm), which is mainly due to the decreased MAP

for BSs.

In terms of rate coverage, it can be observed from Fig. 3.10a that when operator 2 adopts LTE-U with a 50% duty cycle or LAA with a sensitive sensing threshold (e.g., -82 dBm or -77 dBm), Wi-Fi has similar performance as the baseline scenario in low rate threshold regime (e.g. less than 5 Mbps), and better performance with medium to high rate threshold (e.g., more than 10 Mbps). If LAA uses the -62 dBm energy detection threshold, the rate coverage of Wi-Fi has negligible improvement over the Wi-Fi + LTE scenario, which means the energy detection threshold does not suffice to protect Wi-Fi. In addition, due to the degraded SINR performance, Wi-Fi has worse rate performance under Wi-Fi + LTE than the baseline scenario. Meanwhile, when the sensing threshold of LAA is -82 dBm or -77 dBm, Fig. 3.10b shows that the rate loss of operator 2 under Wi-Fi + LAA is around 30% to 40% compared to Wi-Fi + LTE. In contrast, the rate loss under Wi-Fi + LTE-U is slightly more than 50% for most rate thresholds.

Overall, under Wi-Fi + LTE, the DST and rate coverage probability of Wi-Fi decreases significantly compared to the baseline performance, which makes it an impractical scenario to operate cellular in unlicensed spectrum. Under Wi-Fi + LTE-U, LTE-U operator 2 has the flexibility to guarantee good DST and rate coverage performance for Wi-Fi operator 1 by choosing a low cellular transmission duty cycle. In addition, LTE-U has low implementation cost due to its simple scheme. However, LTE-U also has the following disadvantages: (1) the LTE-U operator has much degraded DST and rate coverage

performance under low transmission duty cycle; (2) LTE-U is only feasible in certain regions and/or unlicensed bands where LBT feature is not required, such as the 5.725-5.825 GHz band in U.S. [56]; (3) LTE-U transmissions are more likely to collide with Wi-Fi acknowledgment packets due to the lack of a CCA procedure, which means Wi-Fi SINR coverage under Wi-Fi + LTE-U may not as easily translate into the rate performance as Wi-Fi + LAA; and (4) LTE-U has practical cross-layer issues, such that the frequent on and off switching of LTE will trigger the Wi-Fi rate control algorithm to lower the Wi-Fi transmission rate [74]. In contrast, under Wi-Fi + LAA, by choosing an appropriate LAA channel access priority (i.e., contention window size) and sensing threshold, Wi-Fi operator 1 also achieves better DST and rate coverage performance compared to the baseline scenario, while LAA operator 2 can maintain acceptable rate coverage performance. Additionally, LAA also meets the global requirement for operation in the unlicensed spectrum. The main disadvantage of LAA versus LTE-U is that LAA requires more complicated implementation for the LBT and random BO feature. Therefore, in terms of performance comparisons and practical constraints, cellular with LBT and random BO (i.e., LAA) is more promising than cellular with discontinuous transmission (i.e., LTE-U) to provide a global efficient solution to the coexistence issues of cellular and Wi-Fi in unlicensed spectrum.

3.8 Summary

This chapter has proposed a probabilistic framework using stochastic geometry to analyze the MAC protocols for coexisting cellular network and CSMA/CA based Wi-Fi network. The proposed framework has adapted the modified Matérn point process that has been previously used for the standalone CSMA network [81] and cognitive CSMA networks [85], to the new application scenario of coexisting cellular and Wi-Fi networks. Specifically, several coexistence scenarios are analytically investigated, including when cellular BSs always have the medium access, and when cellular BSs adopt the CSMA/CA with tunable random back-off timer and sensing threshold. Based on the retaining indicator for each cellular BS/Wi-Fi AP, the MAP of a typical BS/AP, as well as the conditional MAP of a BS/AP given the tagged BS/AP is retained, can be quantified for each coexistence scenario. By leveraging the derived conditional MAP, we adopt the second order moment matching approach [81,85] to approximate the cellular and Wi-Fi interferers as independent non-homogeneous PPPs, so that the approximate SINR and rate coverage distribution can be derived. This chapter has shown through the proposed methodology that cellular network can be a good neighbor to Wi-Fi by manipulating its transmission duty cycle, sensing threshold, or channel access priority.

The analytical framework proposed in this chapter validates and complements the system level simulation studies of standardization efforts including LTE-U [87] and LAA [56], which can be utilized by both academia and

industry to rigorously study cellular and Wi-Fi coexistence performance under various scenarios, such as when multiple unlicensed bands are available, or when both downlink and uplink traffic exist.

3.9 Appendix

3.9.1 Proof of Lemma 3.4.1

The MAP of Wi-Fi AP x_i is the Palm probability that its medium access indicator is equal to 1. Given its timer $t_i^W = t$, the MAP can be derived as:

$$\mathbb{E}_{\Phi_W}^{x_i}\left[\prod_{y_k\in\Phi_L}\mathbb{1}_{G_{ki}^{LW}/l(\|y_k-x_i\|)\le\frac{\Gamma_{ed}}{P_L}}\prod_{x_j\in\Phi_W\setminus\{x_i\}}\left(\mathbb{1}_{t_j^W\ge t}+\mathbb{1}_{t_j^W<t}\mathbb{1}_{G_{ji}^{W}/l(\|x_j-x_i\|)\le\frac{\Gamma_{cs}}{P_W}}\right)\right]$$
$$\overset{(a)}{=}\mathbb{E}\left[\prod_k\left(1-\exp(-\mu\frac{\Gamma_{ed}}{P_L}l(\|y_k-x_i\|))\right)\right]\mathbb{E}_{\Phi_W}^{!x_i}\left[\prod_j\left(1-t\exp(-\mu\frac{\Gamma_{cs}}{P_W}l(\|x_j-x_i\|))\right)\right]$$
$$\overset{(b)}{=}\exp(-N^L)\exp(-tN^W),$$

where (a) follows from the fact that Φ_L is independent of Φ_W, and (b) follows from Slyvniak's theorem and the PGFL of a homogeneous PPP. Finally noting that $t\sim U(0,1)$ and deconditioning on t gives the desired result.

3.9.2 Proof of Corollary 3.4.2

According to Remark 3.3.1, given the tagged AP is located at $x_0 = (r_0, 0)$, we have:

$$\mathbb{P}(e_0^W = 1|x_0 = (r_0, 0))$$

$$
\begin{aligned}
=&\mathbb{E}^{x_0}_{\Phi_W}\Bigg(\prod_{y_k\in\Phi_L}\mathbb{1}_{\frac{G^{LW}_{ki}}{l(\|y_k-x_0\|)}\le\frac{\Gamma_{ed}}{P_L}}\prod_{x_j\in\Phi_W\setminus\{x_0\}}\Bigg(\mathbb{1}_{t^W_j\ge t^W_0}+\mathbb{1}_{t^W_j<t^W_0}\\
&\times\mathbb{1}_{\frac{G^W_{j0}}{l(\|x_j-x_0\|)}\le\frac{\Gamma_{cs}}{P_W}}\Bigg)\Bigg|\Phi_W(B^o(0,r_0))=0\Bigg)\\
=&\mathbb{E}\left(\prod_{y_k\in\Phi_L}\mathbb{1}_{G^{LW}_{k0}/l(\|y_k-x_0\|)\le\frac{\Gamma_{ed}}{P_L}}\prod_{x_j\in\Phi_W\cap B^c(0,r_0)}\left(\mathbb{1}_{t^W_j\ge t^W_0}+\mathbb{1}_{t^W_j<t^W_0}\mathbb{1}_{G^W_{j0}/l(\|x_j-x_0\|)\le\frac{\Gamma_{cs}}{P_W}}\right)\right)\\
=&\frac{1-\exp(-N^W_2(r_0))}{N^W_2(r_0)}\exp(-N^L),
\end{aligned}
$$

Finally, Corollary 3.4.2 is derived by incorporating the distribution of $\|x_0\|$.

3.9.3 Proof of Corollary 3.4.3

For AP $x_i\in\Phi_W$, the conditional MAP of x_i given the tagged AP $x_0=(r_0,0)$ transmits is:

$$
\begin{aligned}
&\mathbb{P}^{x_i}_{\Phi_W}(e^W_i=1|e^W_0=1,x_0\in\Phi_W,\Phi_W(B^o(0,r_0))=0)\\
\overset{(a)}{=}&\frac{P^{x_i,x_0}_{\Phi_W}(e^W_i=1,e^W_0=1|\Phi_W(B^o(0,r_0))=0)}{P^{x_i,x_0}_{\Phi_W}(e^W_0=1|\Phi_W(B^o(0,\|x_0\|))=0)}\\
\overset{(b)}{=}&\frac{E^{x_i}_{\Phi_W}(\hat{e}^W_i\hat{e}^W_0)}{E^{x_i}_{\Phi_W}(\hat{e}^W_0)},
\end{aligned}
\tag{3.24}
$$

where (a) follows from the Bayes' rule, and (b) is derived by applying the Slyvniak's theorem and de-conditioning. The modified medium access indicators for x_i and x_0 are:

$$
\begin{aligned}
\hat{e}^W_i=&\prod_{x_j\in(\Phi_W\cap B^c(0,r_0)+\delta_{x_0})\setminus\{x_i\}}\left(\mathbb{1}_{t^W_j\ge t^W_i}+\mathbb{1}_{t^W_j<t^W_i}\mathbb{1}_{\frac{G^W_{ji}}{l(\|x_j-x_i\|)}\le\frac{\Gamma_{cs}}{P_W}}\right)\prod_{y_k\in\Phi_L}\mathbb{1}_{\frac{G^{LW}_{ki}}{l(\|y_k-x_i\|)}\le\frac{\Gamma_{ed}}{P_L}},\\
\hat{e}^W_0=&\prod_{x_j\in\Phi_W\cap B^c(0,r_0)}\left(\mathbb{1}_{t^W_j\ge t^W_0}+\mathbb{1}_{t^W_j<t^W_0}\mathbb{1}_{\frac{G^W_{j0}}{l(\|x_j-x_0\|)}\le\frac{\Gamma_{cs}}{P_W}}\right)\prod_{y_k\in\Phi_L}\mathbb{1}_{\frac{G^{LW}_{k0}}{l(\|y_k-x_0\|)}\le\frac{\Gamma_{ed}}{P_L}}.
\end{aligned}
\tag{3.25}
$$

Therefore, the denominator in (3.24) is given by:

$$
\begin{aligned}
&\mathbb{E}^{x_i}_{\Phi_W}\left[\prod_{x_j\in\Phi_W\cap B^c(0,r_0)}\left(\mathbb{1}_{t_j^W\geq t_0^W}+\mathbb{1}_{t_j^W<t_0^W}\mathbb{1}_{\frac{G^W_{j0}}{l(\|x_j-x_0\|)}\leq\frac{\Gamma_{cs}}{P_W}}\right)\prod_{y_k\in\Phi_L}\mathbb{1}_{\frac{G^{LW}_{k0}}{l(\|y_k-x_0\|)}\leq\frac{\Gamma_{ed}}{P_L}}\right]\\
=&\int_0^1\mathbb{E}\left[\prod_{x_j\in(\Phi_W\cap B^c(0,r_0)+\delta_{x_i})}\left(\mathbb{1}_{t_j^W\geq t}+\mathbb{1}_{t_j^W<t}\mathbb{1}_{G^W_{j0}/l(\|x_j-x_0\|)\leq\frac{\Gamma_{cs}}{P_W}}\right)\middle|t_0^W=t\right]\mathrm{d}t\\
&\times\mathbb{E}\left[\prod_{y_k\in\Phi_L}\mathbb{1}_{G^{LW}_{k0}/l(\|y_k-x_0\|)\leq\frac{\Gamma_{ed}}{P_L}}\right]\\
=&U(x_i-x_0,\frac{\Gamma_{cs}}{P_W},N_2^W(r_0))\exp(-N^L).
\end{aligned}
\tag{3.26}
$$

On the other hand, the numerator in (3.24) can be computed as:

$$
\begin{aligned}
&\mathbb{E}^{x_i}_{\Phi_W}(\hat{e}_i^W\hat{e}_0^W)\\
\overset{(a)}{=}&\mathbb{E}\Bigg[\prod_{x_j\in(\Phi_W\cap B^c(0,r_0)+\delta_{x_0})}\left(\mathbb{1}_{t_j^W\geq t_i^W}+\mathbb{1}_{t_j^W<t_i^W}\mathbb{1}_{G^W_{ji}/l(\|x_j-x_i\|)\leq\frac{\Gamma_{cs}}{P_W}}\right)\prod_{y_k\in\Phi_L}\mathbb{1}_{G^{LW}_{ki}/l(\|y_k-x_i\|)\leq\frac{\Gamma_{ed}}{P_L}}\\
&\times\prod_{x_j\in(\Phi_W\cap B^c(0,r_0)+\delta_{x_i})}\left(\mathbb{1}_{t_j^W\geq t_0^W}+\mathbb{1}_{t_j^W<t_0^W}\mathbb{1}_{G^W_{j0}/l(\|x_j-x_0\|)\leq\frac{\Gamma_{cs}}{P_W}}\right)\prod_{y_k\in\Phi_L}\mathbb{1}_{G^{LW}_{k0}/l(\|y_k-x_0\|)\leq\frac{\Gamma_{ed}}{P_L}}\Bigg]\\
=&\int_0^1\int_0^1\mathbb{E}\Bigg[\prod_{x_j\in\Phi_W\cap B^c(0,r_0)}(1-\mathbb{1}_{t_j<t}\mathbb{1}_{G^W_{j0}/l(\|x_j-x_0\|)>\frac{\Gamma_{cs}}{P_W}})(1-\mathbb{1}_{t_j<t'}\mathbb{1}_{G^W_{ji}/l(\|x_j-x_i\|)>\frac{\Gamma_{cs}}{P_W}})\\
&\times\mathbb{1}_{\frac{G^W_{0i}}{l(\|x_0-x_i\|)}\leq\frac{\Gamma_{cs}}{P_W}}\prod_{y_k\in\Phi_L}\mathbb{1}_{G^{LW}_{k0}/l(\|y_k-x_0\|)\leq\frac{\Gamma_{ed}}{P_L}}\mathbb{1}_{G^{LW}_{ki}/l(\|y_k-x_i\|)\leq\frac{\Gamma_{ed}}{P_L}}\Bigg|t_0^W=t,t_i^W=t'\Bigg]\mathrm{d}t'\mathrm{d}t\\
=&\exp\Big(-2N^L+C_2^L(x_i-x_0)\Big)V\Big(x_i-x_0,\frac{\Gamma_{cs}}{P_W},\frac{\Gamma_{cs}}{P_W},N_2^W(r_0),N_0^W(x_i,r_0,\Gamma_{cs})\\
&,C_1^W(x_i,x_0)\Big),
\end{aligned}
\tag{3.27}
$$

where (a) follows from Slyvniak's theorem.

3.9.4 Proof of Lemma 3.4.4

The conditional SINR coverage of the typical STA is derived as follows:

$$
\begin{aligned}
&\mathbb{P}(\mathrm{SINR}_0^W > T | x_0 = (r_0, 0), e_0^W = 1) \\
&\overset{(a)}{=} \mathbb{P}^{x_0}_{\Phi_W}\Big(\frac{F^W_{0,0}/l(\|x_0\|)}{\sum\limits_{x_j \in \Phi_W \setminus \{x_0\}} \frac{F^W_{j,0} e^W_j}{l(\|x_j\|)} + \sum\limits_{y_m \in \Phi_L} \frac{P_L}{P_W} \frac{F^{LW}_{m,0}}{l(\|y_m\|)} + \frac{\sigma_N^2}{P_W}} > T | \Phi_W(B^o(0, r_0)) = 0, e_0^W = 1\Big) \\
&\overset{(b)}{=} \mathbb{P}\Big(\frac{F^W_{0,0}/l(\|x_0\|)}{\sum\limits_{x_j \in \Phi_W \cap B^c(0,r_0)} \frac{F^W_{j,0} \hat{e}^W_j}{l(\|x_j\|)} + \sum\limits_{y_m \in \Phi_L} \frac{P_L}{P_W} \frac{F^{LW}_{m,0}}{l(\|y_m\|)} + \frac{\sigma_N^2}{P_W}} > T | \hat{e}_0^W = 1\Big) \\
&\overset{(c)}{\approx} \exp(-\mu T l(r_0) \frac{\sigma_N^2}{P_W}) \mathbb{E}\Big[-\mu T l(r_0)\Big(\sum_{x_i \in \Phi_W \cap B^c(0,r_0)} \frac{P_W}{P_L} \frac{F^{WL}_{i,0} \hat{e}^W_i}{l(\|x_i\|)}\Big) \Big| \hat{e}_0^W = 1\Big] \\
&\quad \times \mathbb{E}\Big[-\mu T l(r_0)\Big(\sum_{y_m \in \Phi_L} \frac{F^L_{m,0}}{l(\|y_m\|)}\Big)\Big],
\end{aligned}
$$

where (a) follows from Baye's rule by re-writing $x_0 = (r_0, 0)$ as $x_0 \in \Phi_W$ and $\Phi_W(B^o(0, r_0)) = 0$. Here $B^o(0, r_0)$ is defined in Table 5.1. Step (b) is derived from Slyvniak's theorem and by de-conditioning on $\Phi_W(B^o(0, r_0)) = 0$. The modified medium access indicator for AP $x_i \in (\Phi_W \cap B^c(0, r_0) + \delta_{x_0})$ is given by (3.25). The conditional probability for the Wi-Fi AP $x_j \in \Phi_W \cap B^c(0, r_0)$ to transmit given x_0 transmits, i.e., $\mathbb{P}(\hat{e}_i^W = 1 | \hat{e}_0^W = 1)$, is derived in Corollary 3.4.3. Step (c) uses the assumption that the interference from cellular BSs is independent of the Wi-Fi network.

Since the interfering AP process is a non-independent thinning of Φ_W, the Laplace transform of Wi-Fi interference (i.e., the second term in step (c)) is not known in closed-from. Therefore, similar to [81, 90], we approximate

the Wi-Fi interferers as a non-homogeneous PPP with intensity $\lambda_W h_1(r_0, x)$, which gives (3.9).

3.9.5 Proof of Lemma 3.4.5

According to Remark 3.3.1, given the tagged BS is located at $y_0 = (r_0, 0)$, denoting the conditional SINR coverage probability by $p_0^L(r_0, T, \lambda_W, \lambda_L)$, we have:

$$
\begin{aligned}
& p_0^L(r_0, T, \lambda_W, \lambda_L) \\
& \overset{(a)}{=} \mathbb{E}\Bigg[\exp(-\mu T l(r_0))\Big(\frac{\sigma_N^2}{P_L} + \sum_{y_m \in \Phi_L \setminus \{y_0\}} \frac{F_{m,0}^L}{l(\|y_m\|)} \\
& \quad + \sum_{x_j \in \Phi_W} \frac{P_W}{P_L} \frac{F_{j,0}^{WL} e_j^W}{l(\|x_j\|)}\Big) \Big| y_0 \in \Phi_L, \Phi_L(B^0(0, r_0)) = 0\Bigg] \\
& \overset{(b)}{=} \mathbb{E}\Bigg[\exp(-\mu T l(r_0))\Big(\frac{\sigma_N^2}{P_L} + \sum_{y_m^L \in \Phi_L \cap B^c(0,r_0)} \frac{F_{m,0}^L}{l(\|y_m\|)} + \sum_{x_j \in \Phi_W} \frac{P_W}{P_L} \frac{F_{j,0}^{WL} \hat{e}_j^W}{l(\|x_j\|)}\Big)\Bigg] \\
& \overset{(c)}{\approx} \exp(-\mu T l(r_0) \frac{\sigma_N^2}{P_L}) \mathbb{E}\Bigg[\exp\Bigg(-\mu T l(r_0) \sum_{y_m \in \Phi_L \cap B^c(0,r_0)} \frac{F_{m,0}^L}{l(\|y_m\|)}\Bigg)\Bigg] \\
& \quad \times \mathbb{E}\Bigg[\exp\Bigg(-\mu T l(r_0) \sum_{x_j \in \Phi_W} \frac{P_W}{P_L} \frac{F_{j,0}^{WL} \hat{e}_j^W}{l(\|x_j\|)}\Bigg)\Bigg],
\end{aligned}
$$

where (a) is because the channels have Rayleigh fading and y_0^L is the closest BS to the typical user. Step (b) is obtained by using Slyvniak's theorem and de-conditioning on $\Phi_L(B^0(0, r_0)) = 0$. The modified medium access indicator for each AP in step (b) is given by:

$$
\hat{e}_j^W = \prod_{y_k \in \Phi_L \cap B^c(0,r_0)} \Bigg(\mathbb{1}_{G_{kj}^{LW}/l(\|y_k - x_j\|) \leq \frac{\Gamma_{ed}}{P_L}} \mathbb{1}_{G_{0j}^{LW}/l(\|y_0 - x_j\|) \leq \frac{\Gamma_{ed}}{P_L}}\Bigg)
$$

$$\times \prod_{x_i \in \Phi_W \setminus \{x_j\}} \left(\mathbb{1}_{t_i^W \geq t_j^W} + \mathbb{1}_{t_i^W < t_j^W} \mathbb{1}_{G_{ij}^W / l(\|x_i - x_j\|) \leq \frac{\Gamma_{cs}}{P_W}} \right).$$

For each Wi-Fi AP $x_j \in \Phi_W$, its modified MAP given the tagged BS is at $y_0 = (r_0, 0)$ is:

$$\begin{aligned} &\mathbb{P}^{x_j}_{\Phi_W}(\hat{e}_j^W = 1) \\ =&\frac{1 - \exp(-N^W)}{N^W} \exp(-N_0^L(x_j, r_0, \Gamma_{ed}))(1 - \exp(-\mu \frac{\Gamma_{ed}}{P_L} l(\|y_0 - x_j\|)), \quad (3.28) \end{aligned}$$

where N^W and $N_0^L(x_j, r_0, \Gamma_{ed})$ are defined in Table 3.2. In step (c), the correlation between the interference from BSs and APs is neglected for simplicity. Finally, the desired result is obtained by treating $\hat{e}_j^W$ as independent for each AP x_j, and applying the non-homogeneous PPP approximation to Wi-Fi interferers.

3.9.6 Proof of Lemma 3.5.2

The time-averaged Wi-Fi rate coverage can be derived since the fraction of Wi-Fi APs that can support data rate ρ is $p_0^W(2^{\frac{\rho}{B\hat{p}_{0,MAP}^W(\lambda_W, \lambda_L)}} - 1, \lambda_W, \lambda_L)$ and $p_0^W(2^{\frac{\rho}{B\hat{p}_{0,MAP}^W(\lambda_W, 0)}} - 1, \lambda_W, 0)$ during cellular "on" and "off" period respectively. In addition, the time-averaged cellular rate coverage is derived by noting that the typical cellular link is active for η fraction of time.

3.9.7 Proof of Corollary 3.6.3

For every AP x_i, the quantity that needs to be computed is $h_2^W(r_0, x_i) = \mathbb{P}^{x_i}_{\Phi_W}[e_i^W = 1 | e_0^W = 1, x_0 = (r_0, 0)]$. Similar to (3.24), $h_2^W(r_0, x_i)$ can be rewrit-

ten as $\frac{\mathbb{E}^{x_i}_{\Phi_W}(\hat{e}^W_i \hat{e}^W_0)}{\mathbb{E}^{x_i}_{\Phi_W}(\hat{e}^W_0)}$, where:

$$\hat{e}^W_i = \prod_{x_j \in (\Phi_W \cap B^c(0,r_0)+\delta_{x_0}) \setminus \{x_i\}} \left(\mathbb{1}_{t^W_j \geq t^W_i} + \mathbb{1}_{t^W_j < t^W_i} \mathbb{1}_{G^W_{ji}/l(\|x_j - x_i\|) \leq \frac{\Gamma_{cs}}{P_W}} \right)$$
$$\times \prod_{y_m \in \Phi_L} \left(\mathbb{1}_{t^L_m \geq t^W_i} + \mathbb{1}_{t^L_m < t^W_i} \mathbb{1}_{G^{LW}_{mi}/l(\|y_m - x_i\|) \leq \frac{\Gamma_{ed}}{P_L}} \right),$$
$$\hat{e}^W_0 = \prod_{x_j \in \Phi_W \cap B^c(0,r_0)} \left(\mathbb{1}_{t^W_j \geq t^W_0} + \mathbb{1}_{t^W_j < t^W_0} \mathbb{1}_{G^W_{j0}/l(\|x_j - x_0\|) \leq \frac{\Gamma_{cs}}{P_W}} \right)$$
$$\times \prod_{y_m \in \Phi_L} \left(\mathbb{1}_{t^L_m \geq t^W_0} + \mathbb{1}_{t^L_m < t^W_0} \mathbb{1}_{G^{LW}_{m0}/l(\|y_m - x_0\|) \leq \frac{\Gamma_{ed}}{P_L}} \right).$$

Both $\mathbb{E}^{x_i}_{\Phi_W}(\hat{e}^W_0)$ and $\mathbb{E}^{x_i}_{\Phi_W}(\hat{e}^W_i \hat{e}^W_0)$ can be calculated using Slyvniak's theorem and the PGFL of PPP, which will give the result in (3.18).

Chapter 4

Initial Access Analysis in Millimeter Wave Cellular Networks with High Mobility[1]

In the current sub-6GHz cellular systems, the spectral efficiency per link is already approaching theoretical limits [94]. Since mmWave bands cover a wide frequency range from 30 GHz to 300 GHz, they have been considered as the primary frequency bands to support the stringent data rate requirements for future cellular systems [95]. Although mmWave bands offer vast spectrum opportunities, they also pose significant challenges for cellular communications due to the high isotropic pathloss and high sensitivity to blockage effects. In order to combat these issues, one distinctive feature of mmWave communication is to use beamforming (BF) techniques to form narrow beams with high antenna gain for data transmissions [95–98]. This is possible since the small wavelength of mmWave allows large number of antenna arrays to be placed in a compact form factor.

However, the requirement for narrow beam communication renders the design of initial access (IA) a central and novel challenge for mmWave cellular

[1]This chapter has been published in [92, 93]. I am the primary author of these works. Coauthors Dr. Thomas Novlan and Dr. Charlie Zhang have provided many valuable discussions and insights to this work, and Dr. Jeffrey G. Andrews and Dr. François Baccelli are my supervisors.

systems relative to existing cellular systems. Specifically, initial access refers to the procedures that establish an initial connection between a mobile user and the cellular network, which is the critical prerequisite for any subsequent communication. In mmWave cellular networks, the mobile and the BS have no idea what beam directions to use upon initial access, and so cannot communicate at all. Thus, they must search over a potentially quite large beamforming space to find each other, which is potentially time and resource consuming. In addition, because mmWave links are fragile due to their vulnerability to blocking and falling out of beam alignment, initial access will need to be done much more frequently than in conventional systems. For this reason, it may be necessary to constantly perform initial access to identify new candidate BSs, even when connected to another BS.

Despite the importance of initial access design in mmWave cellular systems, fundamental system level analysis for the performance of initial access protocols and the corresponding achievable user throughput is still largely unexplored. In addition, since the mmWave user throughput is highly correlated with the initial access protocol, such analysis is also challenging. In this chapter, we develop an analytical framework and detailed performance analysis for initial access in a mmWave cellular system using tools from stochastic geometry [2, 43, 44, 99].

4.1 Related Works

Initial access for mmWave has been investigated by a few standard organizations in recent years [100–102]. The IEEE 802.11ad standard adopted a two level initial beamforming training protocol for the 60 GHz unlicensed band, where a coarse-grained sector level sweep phase is followed by an optional beam refinement phase [100, 101, 103]. However, IEEE 802.11ad is mainly designed for indoor communications within an ad hoc type network without significant mobility or range. The Verizon 5G forum [102] has created technical specifications for early mmWave cellular systems, where beam sweeping is applied by the BSs during cell search, and the beam reference signal (BRS) is transmitted along with the synchronization signals to enable the users to determine appropriate BS beamforming directions.

Despite the standardization of initial access for mmWave cellular networks is still in its early stages, several recent research efforts have investigated this problem. An exhaustive procedure to sequentially search all the possible transmit-receive beam pairs has been proposed in [104]. A hierarchical search procedure is proposed in [105], where the BS first performs an exhaustive search over wide beams, then refines to search narrow beams. The exhaustive and hierarchical strategies are compared in [106], which shows that hierarchical search generally has smaller initial access delay, but exhaustive search gives better coverage to cell-edge users. A context information based search, wherein the users are informed about the mmWave BS locations through microwave links, is shown to achieve small initial access delay [107]. By adapting

limited feedback-type directional codebooks, a low-complexity beamforming approach for initial user discovery is proposed in [108]. Several initial access options with different modifications to LTE initial access procedures are proposed in [109], which has observed that the initial access delay can be reduced by omni-directional transmission from the BSs during cell search, and digital beamforming can even further reduce the delay. A two step cell search procedure, which leverages an omni-directional synchronization from the macro BSs, followed by sequential spatial search from the mmWave BSs, is shown to enhance the efficiency of initial access [110]. In addition to the initial access design for mmWave cellular networks, the beam alignment problem for the mmWave system has also been investigated in several literatures [111–116]. An efficient beam alignment technique using adaptive subspace sampling and hierarchical beam codebooks is proposed in [111]. An auxiliary beam pair design for mmWave channel estimation is proposed in [112, 113], which can be utilized to reduced the initial access delay. By exploiting the information from the sub-6 GHz channels, [114] has proposed a beam alignment algorithm with low training overhead for mmWave system. Probability of beam misalignment due to thermal noise and antenna gain fluctuations is analyzed in [115] for the IEEE 802.11ad and IEEE 802.15.3c mmWave systems. In [116], a bisection search algorithm for beam alignment in mmWave system is shown to achieve higher overall throughput than the exhaustive and iterative algorithms.

All the aforementioned works are either a point-to-point analysis or only consider one user with a few nearby BSs and, a system-level analysis of

initial access in mmWave networks in terms of not only initial access delay, but also the subsequent coverage and throughput performance for data transmission, has yet to be offered. Stochastic geometry has been recognized as a powerful mathematical tool to analyze key performance metrics in large-scale wireless networks, such as macro cellular networks [2], heterogeneous cellular networks [13], Wi-Fi networks [81], and ad hoc networks [117]. Coverage and rate trends for mmWave cellular networks have also been studied recently using stochastic geometry [118–124]. By incorporating directional beamforming without capturing the blockage effects, [118] shows mmWave network can achieve comparable coverage probability and much higher data rate than conventional microwave networks. Similar performance gains of mmWave networks have been observed when statistical blockage models are used, such as a line-of-sight (LOS) ball blockage model [119–121], an exponential decreasing LOS probability function with respect to (w.r.t.) the link length [121–123], or a blockage model which also incorporates an outage state [124]. In [123], the impact of beam training/alignment on the effective rate for mmWave user is investigated. Given the highly directional antennas used in mmWave networks, [125] has validated the theoretical feasibility of spectrum sharing among mmWave cellular operators. However, [118–125] all assume the association between user and its serving BS has already been established, while in fact the initial access is a key design challenge and performance limiting factor for mmWave networks.

4.2 Contributions

In this chapter, we focus on a high mobility scenario where the users and random blockers are moving with relatively high speeds, such that the initial access needs to performed very frequently (e.g., every 20 ms to 100 ms). We consider three simple but representative initial access protocols that use various combinations of directional beamforming and omnidirectional transmission and reception at the mobile and the BS, during the two key phases of cell search (BS transmits a beacon) and random access (mobile transmits in the other direction). Specifically, the initial access protocols are compliant with the basic initial access procedures of LTE, including a baseline exhaustive search protocol wherein BS and user sweep through all transmit-receive beam pairs during cell search, and two other protocols that require less initial access overhead.

We consider both a single stage beamforming approach where BS beam direction for data transmission is solely determined from the initial access phase; and a two-stage beamforming approach wherein only a coarse beam direction is obtained from initial access, while a beam refinement phase is applied afterwards to refine the BS beams. We derive key metrics including the initial access success probability (what is the chance the protocol succeeds?), the average initial access delay (how long does it take?), and the user-perceived downlink throughput (accounting for the initial access overhead). The main contributions of this chapter are as follows:

Accurate analytical framework for mmWave system-level per-

formance under various initial access protocols. In contrast to the link-level analysis in [104–106, 108, 109], we derive several system-level performance metrics in a large-scale mmWave cellular network for the first time, including the expected initial access delay, and a new metric called average user-perceived downlink throughput which quantifies the effect of the initial access protocol on the user-perceived throughput performance. Our analytical results are validated against detailed system level simulations.

Beam sweeping is shown to be essential for cell search. We find that the mmWave system is subject to significant coverage issues if beam sweeping is not applied during cell search. By contrast, a reasonable cell search success probability can be achieved even with a small (e.g., 4 to 8) number of beamforming directions to search at the BS or user.

Comparison of expected initial access delay and average user-perceived downlink throughput under the single-stage BF approach. The baseline exhaustive search protocol gives the best initial access delay performance when blockage is severe, but it also has the worst user-perceived downlink throughput, due to its high initial access overhead. By contrast, the protocol wherein the BS (user) applies beam sweeping and the user (BS) receives omni-directionally during cell search (random access), generally gives the best user-perceived downlink throughput performance. However, due to a high random access preamble collision probability, this protocol also has high initial access delay. Of the three considered sample protocols, the best trade-off between initial access delay and average user-perceived downlink throughput

is achieved when the BS transmits using relatively wide beams and the user applies beam sweeping during cell search.

Benefits of the two-stage beamforming approach: compares to the single-stage beamforming approach, the two stage beamforming approach significantly increases UPT for baseline protocol, and provides high flexibility to achieve good initial access delay and user-perceived throughput simultaneously by adapting the beam refinement factor.

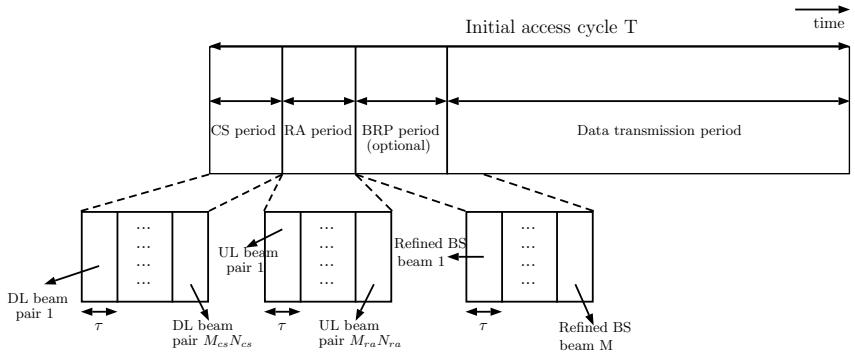

Figure 4.1: Illustration of two cycles for the timing structure.

4.3 System Model and Performance Metrics

In this chapter, a time-division duplex (TDD) mmWave system in Fig. 4.1 is considered, where the system time is divided into different initial access cycles with period T, and τ denotes the duration of an OFDM symbol. Each cycle begins with a cell search phase, followed by the random access phase, an optional beam refinement phase, and finally the data transmission phase. The mmWave cellular system has carrier frequency f_c and

total system bandwidth W. The transmit power of BSs and users are P_b and P_u respectively, and the total thermal noise power is σ^2. In the rest of this section, we present the spatial location models, the propagation and blockage assumptions, and the antenna and beamforming models.

4.3.1 Spatial Locations

Since the mmWave cellular networks are going to be densely deployed with more random nature than the macro cellular network, and currently there is no real mmWave BS location data available to extract a better model, thus the locations for BSs and users are modeled as realizations of two independent homogeneous PPPs. Specifically, the BS process $\Phi = \{x_i\}$ has intensity λ, and the user process $\Phi_u = \{u_i\}$ has intensity λ_u. The PPP assumption for BS locations could lead to many tractable and insightful results. In fact, this assumption is also reasonable since [126] has proved that the SINR trend under the PPP assumption only has a constant SINR gap compared to any other stationary BS location model. In addition, [127] has proved that for any arbitrary spatial BS location pattern with sufficiently large shadowing variance, the statistics of the propagation losses of a user with respect to all BSs will converge to that of a Poisson network. As a result, the PPP assumption for BSs can also be treated by combining the shadowing effects and the BS locations. Thus we do not consider shadowing separately in our analysis, similar to [120–123, 125, 128].

Since the user locations form a realization of a PPP, we can analyze

Table 4.1: Definitions and Values for System Parameters

Symbol	Definition	Simulation Value
Φ, λ	MmWave BS PPP and intensity	100 BS/km^2
Φ_u, λ_u	User PPP and intensity	1000 user/km^2
Φ_L, Φ_N	LOS and NLOS BS tier to the typical user	
f_c, W	Carrier frequency and system bandwidth	28 GHz, 100 MHz
P_b, P_u	BS and user transmit power	30 dBm, 23 dBm
σ^2	Total thermal noise power	-94 dBm
$G(\theta), g(\theta)$	Main lobe and side lobe gain at BS and user with beamwidth θ, defined in (4.2)	$C_0 = 10$ dB for user antennas
M, N	Number of antennas/BF directions at each BS and user	$M = 4, 8, ..., 48$, $N = 4$
M_{cs}, N_{cs}, K_{cs}	M_{cs}/N_{cs}: number of BF directions to search at BS/user in cell search; $K_{cs} = \min(M_{cs}, N_{cs})$	
m_{cs}	Number of wide beams to sweep during cell search for fast CS protocol	4
M_{ra}, N_{ra}	Number of BF directions to search at BS and user during RA	
M_{IA}, m	Number of BS beams to search during IA ($M_{IA} = \max(M_{cs}, M_{ra})$); beam refinement factor	
N_{pa}	Number of random access preamble sequences	64
α_L, α_N	Path loss exponent for LOS and NLOS links	2, 4
β	Path loss at close-in reference distance (i.e., 1m)	61.4 dB
Γ_{cs}, Γ_{ra}	SINR threshold to detect synchronization signal and RA preamble	-4 dB, -4 dB
τ	OFDM symbol duration	14.3 μs
T	Initial access cycle period	20 ms
$h(r)$	Probability for a link with length r to be LOS	
R_c, p	Radius and LOS probability for the LOS region in the LOS ball model	$R_c = 100$m, $p = 1, 0.75, 0.5, 0.25$
μ	LOS region size for the exponential blockage model	$\mu = 100$m, 50m, 25m
$B(x,r)$ ($B^o(x,r)$)	Closed (open) ball with center x and radius r	
$S(u, \theta_1, \theta_2)$	Infinite sector domain $\{x \in \mathbb{R}^2,$ s.t., $\angle(x-u) \in [\theta_1, \theta_2)\}$	
S_j $(1 \le j \le K_{cs})$	The j-th BS locatoin location sector with $S_j \triangleq S(o, \frac{2\pi(j-1)}{K_{cs}}, \frac{2\pi j}{K_{cs}})$	
$V(z,T,\lambda), U(z,T,\lambda)$	Two special functions defined in (4.3)	
$f_{Z_1}(z)$	The PDF for the minimum path loss from the typical user to BSs inside the typical BS sector, which is given by (4.9)	
$P_{M_{cs},N_{cs}}(\Gamma_{cs})$	Probability to detect the BS providing the smallest path loss inside the typical BS sector derived, which is given by (4.11)	
$\tilde{P}_{M_{cs},N_{cs}}(z,\Gamma_{cs})$	$\tilde{P}_{M_{cs},N_{cs}}(z,\Gamma_{cs})$: Conditional detection probability when the minimum path loss inside the typical BS sector is z, which is given by (4.12)	
$P_{M_{cs},N_{cs}}(z_0,\Gamma_{cs})$	$P_{M_{cs},N_{cs}}(z_0,\Gamma_{cs}) = \int_{z_0}^{\infty} \tilde{P}_{M_{cs},N_{cs}}(z,\Gamma_{cs})\mathrm{d}z$	
P_{co}	Probability of no RA preamble collision, given by (4.15)	
$P_{ra}(Z_0,\Gamma_{ra})$	Probability the RA preamble SINR at the tagged BS exceeds Γ_{ra}, given by (4.16)	
η_{IA}	Overall success probability of initial access, given by (4.17)	

the performance of a typical user located at the origin. This is guaranteed by Slivnyak's theorem, which states that the property observed by the typical point of PPP Φ' is the same as that observed by the point at origin in $\Phi' \cup \{o\}$ [43, 44].

4.3.2 Blockage and Propagation Models

The link between a BS and a user is either line-of-sight (LOS) or non-line-of-sight (NLOS). We denote by $h(r)$ the probability for a link of distance

r to be LOS, which is only a function of r and independent of other links. From the typical user's perspective, the BS process Φ is divided into two tiers: the LOS BS tier Φ_L and the NLOS BS tier Φ_N. Since the LOS probability function h only depends on the link length, Φ_L and Φ_N are two independent PPPs. For any $x \in \mathbb{R}^2$, the intensity function for Φ_L is $\lambda_L(x) = \lambda h(\|x\|)$, and the intensity function for Φ_N is $\lambda_N(x) = \lambda(1 - h(\|x\|))$. Incorporating the blockage model to differentiate the LOS and NLOS links is the most distinctive difference for analyzing the mmWave network performance, compared to the analysis in traditional sub-6 GHz networks [2].

Two examples of LOS probability functions $h(r)$ include: (1) the "generalized LOS ball model" [119, 121] with $h(r) = p\mathbb{1}_{r \leq R_c}$, where R_c represents the radius for the LOS region ($R_c > 1$m), and p represents the LOS probability within the LOS region; (2) the "exponential blockage model" [121] with $h(r) = \exp(-r/\mu)$, where μ represents the average LOS region length. Compared to the 3GPP blockage model which has accurate fit to the empirical LOS probability, [128, 129] show that the LOS ball model and exponential blockage model better estimate the SINR and are simpler.

The path loss for a link with distance r in dB is given by:

$$l(r) = \begin{cases} 10\log(\beta) + 10\alpha_L \log_{10}(r) \text{ dB}, & \text{if LOS}, \\ 10\log(\beta) + 10\alpha_N \log_{10}(r) \text{ dB}, & \text{if NLOS}, \end{cases} \tag{4.1}$$

where α_L and α_N represent the path loss exponent for LOS and NLOS links respectively, and β is the path loss at a close-in reference distance (i.e., 1 meter). For the rest of the chapter, the path loss function for LOS link and

NLOS link are denoted by $l_L(r)$ and $l_N(r)$ respectively.

The small scale fading effect is assumed to be Rayleigh fading, where each link is subject to an i.i.d. exponentially distributed fading power with unit mean. Compared to more realistic small-scale fading models such as Nakagami-m fading, Rayleigh fading leads to much more tractable results with very similar design insights [120, 125, 128].

4.3.3 Antenna Model and Beamforming Gains

BSs and users are equipped with an antenna array of M and N antennas respectively to support directional communications, where $M/N \in \mathbb{N}^+$. Both mmWave BSs and users have 1 RF chain, such that only one analog beam can be transmitted or received at a time[2]. For analytical tractability, we assume the actual antenna pattern is approximated by a sectorized beam pattern [110, 118,119,121–125,128,129], where the antenna has constant main-lobe gain over its half power beamwidth, and also a constant side-lobe gain otherwise. We adopt the beamforming gain model for sectorized beam pattern as [110, 123], whose accuracy has been validated in Fig. 8 of [123]. Specifically, if we denote by $G_u(\theta_u)$ the beamforming gain at user with beamwidth θ_u, then $G_u(\theta_u)$ is given by:

$$G_u(\theta_u) = \begin{cases} G(\theta_u) = \frac{2\pi}{\theta_u}\frac{\gamma}{\gamma+1}, & \text{in the main lobe,} \\ g(\theta_u) = \frac{2\pi}{2\pi-\theta_u}\frac{1}{\gamma+1}, & \text{in the side lobe,} \end{cases} \tag{4.2}$$

[2]Our analysis in the rest of the chapter based on analog beamforming directly applies to the scenario where cell sectorization with frequency reuse across sectors within the same cell is used. Hybrid beamforming is left to future work.

where γ mimics the front-back power ratio, which is given by $\gamma = \frac{2\pi}{C_0(2\pi-\theta_u)}$ for some constant C_0. A similar beamforming gain model is used at BS, but we assume 0 side lobe gain for BS (i.e. γ in (4.2) is extremely large), and thus the main lobe gain for BS with beamwidth θ_b is $G(\theta_b) = \frac{2\pi}{\theta_b}$. This assumption is important to ensure the analytical tractability in Section 4.5, which is also reasonable since mmWave BSs use large dimensional antenna array, and modern antenna design could enable a front-to-back ratio larger than 30 dB for mmWave BSs [130].

Similar to [109, 123], we assume each BS has a codebook of M possible beamforming vectors, which will correspond to M sectorized beam patterns that have non-overlapping main lobes with beamwidth $\frac{2\pi}{M}$. Specifically, the m-th BS beam ($1 \leq m \leq M$) covers a sector area centered at the BS, whose angle is within $[2\pi\frac{m-1}{M}, 2\pi\frac{m}{M})$. The spatial signature of any plane wave of the BS is given by the superposition of these M non-overlapping beam directions [109]. Similarly, each user has N possible sectorized-pattern beamforming vectors that correspond to N non-overlapping main lobes with beamwidth $\frac{2\pi}{N}$. Fig. 4.2 shows the first beam direction of the user and the fifth beam direction of the BSs with $M = 8$ and $N = 4$. For any BS and its associated users, their aligned beamforming vectors need to be learned through the initial access, which will be used for subsequent data transmissions.

Finally, Table 4.1 summarizes the definitions and simulation values of the important notation and system parameters that will be used in the rest of

this chapter. In particular, three special functions are defined as:

$$V(z,\Gamma,\lambda)=\exp\left\{-2\pi\lambda\left(\int_{l_L^{-1}(z)}^{+\infty}\frac{\Gamma z h(r)r\mathrm{d}r}{\Gamma z+l_L(r)}+\int_{l_N^{-1}(z)}^{+\infty}\frac{\Gamma z(1-h(r))r\mathrm{d}r}{\Gamma z+l_N(r)}\right)\right\},$$

$$U(z,\Gamma,\lambda)=\exp\left\{-2\pi\lambda\left(\int_{0}^{+\infty}\frac{\Gamma z h(r)r\mathrm{d}r}{\Gamma z+l_L(r)}+\int_{0}^{+\infty}\frac{\Gamma z(1-h(r))r\mathrm{d}r}{\Gamma z+l_N(r)}\right)\right\},$$

$$W(z,\Gamma_1,\Gamma_2,\lambda,M)=\exp\left\{-2\pi\lambda\left(\int_{l_L^{-1}(z)}^{+\infty}\left[1-(1-\frac{1}{M}\frac{\Gamma_1 z}{\Gamma_1 z+l_L(r)})\frac{1}{1+\Gamma_2 z/l_L(r)}\right]\right.\right.$$
$$\left.\left.\times\, r h(r)\mathrm{d}r+\int_{l_N^{-1}(z)}^{+\infty}\left[1-(1-\frac{1}{M}\frac{\Gamma_1 z}{\Gamma_1 z+l_N(r)})\frac{1}{1+\Gamma_2 z/l_N(r)}\right]r(1-h(r))\mathrm{d}r\right)\right\}. \tag{4.3}$$

It will be shown in the next section that V and U give the SIR coverage probability of the typical user with minimum path loss association rule and no specific association rule respectively, where z denotes the path loss from the typical user to its associated BS, T denotes the SIR threshold, and λ denotes the BS intensity.

4.4 Initial Access Design for MmWave Networks

In this section, we will briefly review initial access in LTE, then propose the beamforming structure and several initial access protocols for mmWave networks.

4.4.1 Initial Access in LTE

The main steps for initial access in LTE include cell search, reception of system information, and random access [8, 131]. Specifically, by detecting the synchronization signals broadcast by BSs during cell search, user can determine

the existence of its neighboring BSs, and it tries to camp on the BS that provides the strongest reference signal received power (RSRP). Then the user can extract some important system information from this BS such as system bandwidth and scheduling information. Finally, the user initiates the random access process to its desired serving BS by transmitting a RA preamble through the shared random access channel, and it is successfully connected to the network if the BS can decode the RA preamble without any collision. However, the initial access of LTE is performed omni-directionally, which cannot be directly applied by mmWave networks due to the high isotropic path loss in mmWave frequencies.

4.4.2 Cell Search and Random Access Procedure

Similar to [109], we investigate mmWave initial access protocols that are compliant with the basic procedures of LTE. We assume the BS and user will follow the beam patterns described in Section 4.3.3. The two main design objectives for initial access in mmWave cellular networks include: (1) connect the users to the network, and (2) enable both BS and its associated user to learn their aligned beamforming directions with beamwidth $\frac{2\pi}{M_{IA}}$ and $\frac{2\pi}{N}$ respectively. These objectives are achieved through the following directional cell search and random access procedures.

During CS phase, BSs sweep through M_{cs} transmit beamforming directions to broadcast the synchronization signals, while users sweep through N_{cs} receive beamforming directions to detect the synchronization signals. A syn-

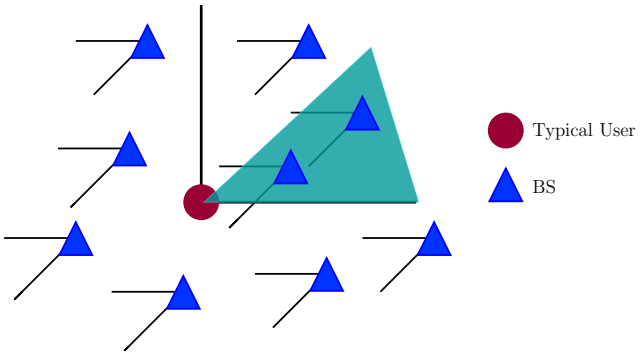

Figure 4.2: Illustration of the BF structure for BS and user beam pair $(5, 1)$ with $M = 8, N = 4$. Only the typical user is shown, where the shaded area represents its corresponding BS sector.

chronous beam sweeping pattern is used, such that during any synchronization signal period, all BSs/users will transmit/receive in the same direction, and one particular downlink beam pair is searched. We assume each user is able to detect a BS with sufficiently small miss detection probability (e.g., less than 1%), if the signal-to-interference-plus-noise ratio (SINR) of the synchronization signal from that BS exceeds Γ_{cs}. The beam reference signal is assumed to be transmitted along with the synchronization signal, such that the user is able to acquire BS beam direction upon successful cell search [102]. Among all the BSs that are detected during CS, the user selects the BS that provides the smallest path loss as its serving BS. If cell search fails, the user will not transmit in the random access phase, and it needs to repeat the initial access procedure in the next cycle. Therefore, the cell search phase leads to a total delay of $T_{cs} = M_{cs}N_{cs}\tau$, as shown in Fig. 4.1.

In the random access phase, the user initiates the connection to its de-

sired serving BS by transmitting a RA preamble sequence, which is uniformly selected from N_{pa} orthogonal preamble sequences. Users sweep through N_{ra} transmit beamforming directions synchronously, and BSs sweep through M_{ra} receive beamforming directions synchronously during random access. The user can be discovered by its serving BS if: 1) there is no RA preamble collision with other users transmitting simultaneously to the same BS; and 2) the SINR of the preamble sequence exceeds Γ_{ra}. Similar to cell search, we assume the probability of miss detection is sufficiently small (e.g., less than 1%) if the SINR of RA preamble exceeds Γ_{ra}. The user is connected to its serving BS upon successful random access, and both the user and BS are aware of their beamforming directions for data transmission. According to Fig. 4.1, the total random access delay is $T_{ra} = M_{ra}N_{ra}\tau$.

An optional beam refinement phase, or BRP, is initiated by BS to refine its beam direction to associated users after the initial access. Specifically, BSs sweep through $M = m \times M_{IA}$ refined beams to transmit the beam refinement reference signal (BRRS), where $M_{IA} = \max(M_{cs}, M_{ra})$ is the number BS beams searched during IA, and $m \geq 1$ is called the beam refinement factor. Each user tries to decode the beam refinement reference signal (BRRS) of its serving BS using the beam found in IA. The BRP is successful if when this user and its serving BS are beam aligned, the SINR of the BRRS exceeds Γ_B.

4.4.3 Initial Access Protocols

Different initial access protocols can be designed to enable the user and its serving BS to determine their aligned beamforming directions with beamwidth $\frac{2\pi}{N}$ and $\frac{2\pi}{M_{IA}}$ respectively. The protocols that are investigated in this chapter are as follows:

1) *Baseline*: BSs and users sweep through all possible beamforming directions during cell search (i.e., $M_{cs} = M_{IA}$, $N_{cs} = N$), so that the user can determine its beamforming direction after successful cell search. During random access, the user transmits in the beamforming direction it found during CS (i.e., $N_{ra} = 1$), while the BS sweeps through all its beamforming directions (i.e., $M_{ra} = M_{IA}$) to receive the RA preamble sequences from the users. BS beamforming direction to the user is determined as the receive direction of the RA preamble.

2) *Fast CS*: in order reduce the cell search overhead while maintaining reasonable synchronization signal strength, the BS applies a coarse beam-sweeping using relatively wide beams during CS (i.e., $M_{cs} = m_{cs}$ with $N \leq m_{cs} \leq M_{IA}$) [93]. Other procedures are the same as baseline.

3) *Omni RX*: Now $M_{cs} = M_{IA}$, $N_{cs} = 1$ (omni), $M_{ra} = 1$ (omni), $N_{ra} = N$, i.e., the user receives omni-directionally during cell search, and the BS receives omni-directionally during random access. The user determines the BS beamforming direction by decoding the beam reference signal during cell search, and it encodes that information into the RA preamble. The BS obtains

Table 4.2: Initial access protocols

Protocol	**BS during CS**	**User during CS**	**BS during RA**	**User during RA**
Baseline	Beam-sweeping ($M_{cs} = M_{IA}$)	Beam-sweeping ($N_{cs} = N$)	Beam-sweeping ($M_{ra} = M_{IA}$)	Fixed direction ($N_{ra} = 1$)
Fast CS	Omni-directional ($M_{cs} = m_{cs}$)	Beam-sweeping ($N_{cs} = N$)	Beam-sweeping ($M_{ra} = M_{IA}$)	Fixed direction ($N_{ra} = 1$)
Omni RX	Beam-sweeping ($M_{cs} = M_{IA}$)	Omni-directional ($N_{cs} = 1$)	Omni-directional ($M_{ra} = 1$)	Beam-sweeping ($N_{ra} = N$)

its beamforming direction by decoding the RA preamble. In addition, the user determines its beamforming direction by beam sweeping during random access.

A summary of these protocols is provided in Table 4.2.

4.4.4 Performance Metrics

The metrics that we use to evaluate the performance of the initial access protocols are defined as follows.

4.4.4.1 Success Probability of Initial Access

Initial access is successful if both cell search and random access are successful. For the typical user, we use e_0 and δ_0 to denote its success indicator for cell search and random access in a typical initial access cycle. Therefore, the initial access success probability is given by: $\eta_{IA} = \mathbb{E}(e_0 \times \delta_0)$.

4.4.4.2 Expected Initial Access Delay

If the user fails the initial access procedure in one initial access cycle, it will try to re-connect to the network in the next cycle. According to Fig. 4.1,

the total initial access delay for typical user to be connected is given by:

$$D_0 = (L_0 - 1)T + (M_{cs}N_{cs}\tau + M_{ra}N_{ra}\tau), \tag{4.4}$$

where $L_0 \in \mathbb{N}^+$ represents the number of cycles to discover the typical user, T represents the period of an initial access cycle, and $M_{cs}N_{cs}\tau + M_{ra}N_{ra}\tau$ represents the duration for initial access in each cycle. In this chapter, we focus on a high mobility scenario where the users or blockers (e.g., pedestrians and cars) are moving with a relatively high speed, such that the user and BS PPPs are independent across different initial access cycles. Therefore, the probability for the typical user to succeed the initial access procedure in different cycles becomes independent. Given the very high Doppler and sensitivity to blocking (such as human blocking) at mmWave, this may be reasonable. As a result, L_0 follows a geometric distribution with parameter η_{IA}, which means:

$$\mathbb{E}(D_0) = (\frac{1}{\eta_{IA}} - 1)T + (M_{cs}N_{cs}\tau + M_{ra}N_{ra}\tau). \tag{4.5}$$

4.4.4.3 Average User-Perceived Downlink Throughput

Although a TDD system is assumed, we will only focus on downlink and assume the entire data transmission period is occupied by the downlink. If the user succeeds the initial access, it is able to be scheduled by its serving BS for downlink transmission; otherwise, its data rate in the current cycle is 0 almost surely. In the data transmission phase, each BS randomly schedules one of its associated users to transmit downlink data. When the beam refinement

phase is used, the BS uses the refined beam with beamwidth $\frac{2\pi}{M}$ if BRP of its scheduled user is successful, otherwise the wide beam from IA phase with beamwidth $\frac{2\pi}{M_{IA}}$ is used.

Since the high mobility scenario is considered, the user needs to perform initial access every cycle. Therefore, the average user-perceived downlink throughput, or average UPT, which represents the expected downlink data rate a typical user achieves within one initial access cycle, is given by:

$$\bar{R} = (1 - \eta_{TO}) \times \eta_{IA} \times \mathbb{E}[\eta_s W \log_2(1 + \text{SINR}_{DL}) | e_0 \delta_0 = 1], \tag{4.6}$$

where η_{TO} represents the IA overhead, and $\eta_{TO} = \min(\frac{M_{cs}N_{cs}\tau + M_{ra}N_{ra}\tau}{T}, 1)$ if BRP is not used, otherwise $\eta_{TO} = \min(\frac{(M_{cs}N_{cs} + M_{ra}N_{ra} + M)\tau}{T}, 1)$. In addition, η_s denotes the average schedule probability of typical user; and SINR_{DL} denotes the downlink data SINR.

4.5 Success Probability for Cell Search and Random Access

In this section, the success probability for the initial access protocols are derived. Note for the same parameters of the initial access protocols in Table 4.2 (i.e., $M_{cs}, N_{cs}, M_{ra}, N_{ra}$), the initial access performance is the same for the single-stage beamforming approach and the two-stage beamforming approach.

4.5.1 Success Probability for Cell Search

4.5.1.1 Analytical Model for Cell Search

According to Section 4.4.2, BSs and users sweep through $M_{cs} \times N_{cs}$ transmit-receive beam pairs synchronously over the downlink during cell search. Since side lobe gains for BSs are assumed to be 0, the user can potentially detect a BS only when BS and user beams are aligned. For example, the typical user in Fig. 4.2 is only able to receive the synchronization signals from the BSs inside the shaded area, which is referred to as a "BS sector". Formally, we define an infinite sector area centered at $u \in \mathbb{R}^2$ as:

$$S(u, \theta_1, \theta_2) = \{x \in \mathbb{R}^2, \text{ s.t., } \angle(x-u) \in [\theta_1, \theta_2)\}. \tag{4.7}$$

If BS and user beam pair (m, n) $(1 \leq m \leq M_{cs},\ 1 \leq n \leq N_{cs})$ is aligned, the typical user can receive from the BSs inside the following area due to the synchronous beam sweeping pattern:

$$S(o, \frac{2\pi(n-1)}{N_{cs}}, \frac{2\pi n}{N_{cs}}) \cap S(o, \frac{2\pi(m-1)}{M_{cs}} + \pi, \frac{2\pi m}{M_{cs}} + \pi). \tag{4.8}$$

From the typical user's perspective, there are $K_{cs} \triangleq \max(M_{cs}, N_{cs})$ such non-overlapping BS sectors during cell search, with the j-th $(1 \leq j \leq K_{cs})$ BS sector being $S(o, \frac{2\pi(j-1)}{K_{cs}}, \frac{2\pi j}{K_{cs}})$.

For the rest of this chapter, when analyzing the typical user performance inside a BS sector, we implicitly assume the BS and user beams are aligned. In addition, we say a BS sector is detected during cell search if the typical user is able to detect the BS that provides the smallest path loss in this

sector, where path loss can be estimated from beam reference signals [102]. For simplicity, we neglect the scenario that the BS providing the smallest path loss inside a BS sector is in deep fade and unable to be detected, while some other BSs can be detected in the same sector. Such a scenario only provides marginal gains to the system, and we will incorporate that in our future work. After cell search, the typical user selects the BS with the smallest path loss across all the detected BS sectors as its desired serving BS, and initiates random access to this BS.

4.5.1.2 Success Probability of Cell Search

Since BSs are PPP and different BS sectors are non-overlapping, the event for BS sectors to be detected are i.i.d.. Without loss of generality, we consider the first BS sector as a "typical" BS sector, which is denoted by $S_1 \triangleq S(o, 0, \frac{2\pi}{K_{cs}})$. The minimum path loss distribution inside the typical BS sector is given by the following lemma.

Lemma 4.5.1. *Denote the minimum path loss from the typical user to BSs inside the typical BS sector by Z_1, then the probability density function (PDF) of Z_1 is given by:*

$$f_{Z_1}(z) = \left\{ \frac{2\pi\lambda}{K_{cs}} \frac{1}{\alpha_L} (\frac{1}{\beta})^{\frac{2}{\alpha_L}} z^{\frac{2}{\alpha_L}-1} h((\frac{z}{\beta})^{\frac{1}{\alpha_L}}) \exp\left(-\frac{2\pi\lambda}{K_{cs}} \int_0^{(\frac{z}{\beta})^{\frac{1}{\alpha_L}}} h(r) r \mathrm{d}r \right) \right\}$$
$$\exp\left(-\frac{2\pi\lambda}{K_{cs}} \int_0^{(\frac{z}{\beta})^{\frac{1}{\alpha_N}}} (1 - h(r)) r \mathrm{d}r \right) + \left\{ \frac{2\pi\lambda}{K_{cs}} \frac{1}{\alpha_N} (\frac{1}{\beta})^{\frac{2}{\alpha_N}} z^{\frac{2}{\alpha_N}-1} (1 - h((\frac{z}{\beta})^{\frac{1}{\alpha_N}})) \right.$$

$$\times \exp\left(-\frac{2\pi\lambda}{K_{cs}}\int_0^{(\frac{z}{\beta})^{\frac{1}{\alpha_N}}}(1-h(r))r\mathrm{d}r\right)\Bigg\}\exp\left(-\frac{2\pi\lambda}{K_{cs}}\int_0^{(\frac{z}{\beta})^{\frac{1}{\alpha_L}}}h(r)r\mathrm{d}r\right), \tag{4.9}$$

where $K_{cs}=\min(M_{cs},N_{cs})$.

Proof. The proof is provided in Appendix 4.10.1. □

The first term and second term in (4.9) refer to the PDF of Z_1 when the BS providing the minimum path loss is LOS and NLOS respectively.

Remark 4.5.1. The result in (4.9) is in integral form since it provides the path loss distribution under a general blockage model. It can be simplified for specific blockage models such as the LOS ball model and exponential blockage model. For example, for the LOS ball model with $p=1$, Lemma 4.9 simply becomes:

$$\begin{aligned} f_{Z_1}(z) =& \frac{2\pi\lambda}{K_{cs}}\frac{1}{\alpha_L}(\frac{1}{\beta})^{\frac{2}{\alpha_L}}z^{\frac{2}{\alpha_L}-1}\exp\left(-\frac{\pi\lambda}{K_{cs}}(\frac{z}{\beta})^{\frac{1}{\alpha_L}}\right)\mathbb{1}_{(\frac{z}{\beta})^{\frac{1}{\alpha_L}}\leq R_c} \\ &+\frac{2\pi\lambda}{K_{cs}}\frac{1}{\alpha_N}(\frac{1}{\beta})^{\frac{2}{\alpha_N}}z^{\frac{2}{\alpha_N}-1}\exp\left(-\frac{\pi\lambda}{K_{cs}}(\frac{z}{\beta})^{\frac{1}{\alpha_N}}\right)\mathbb{1}_{(\frac{z}{\beta})^{\frac{1}{\alpha_N}}\geq R_c}. \end{aligned}$$

Similarly, all the analytical results afterwards can be simplified under specific blockage models.

Conditionally on the minimum path loss inside the typical BS sector Z_1, the SINR of the synchronization signal from the BS providing the minimum path loss is given by:

$\mathrm{SINR}_{SS}(Z_1)$

$$= \frac{F_0/Z_1}{\sum\limits_{x_i^L \in \Phi_L \cap S_1 \cap B^c(o, l_L^{-1}(Z_1))} F_i^L / l_L(\|x_i^L\|) + \sum\limits_{x_j^N \in \Phi_N \cap S_1 \cap B^c(o, l_N^{-1}(Z_1))} F_j^N / l_N(\|x_j^N\|) + \frac{\sigma^2}{P_b M_{cs} G(2\pi/N_{cs})}}, \tag{4.10}$$

where F_0, F_i^L and F_j^N represent the Rayleigh fading channel from the typical user to the BS proving the minimum path loss, interfering LOS BS x_i^L and interfering NLOS BS x_j^N respectively. The last term in the denominator of (4.10) represents the "effective noise" at the typical user, which is the total noise power normalized by the transmit power and antenna gains. In particular, the user antenna gain is $G(\frac{2\pi}{N_{cs}})$, and the BS antenna gain is M_{cs} since it has 0 side lobe gain. We have applied the strong Markov property of PPPs [43, Proposition 1.5.3] for obtaining (4.10): conditionally on the minimum path loss Z_1, the interference only depends on the interfering LOS and NLOS BSs located inside $S_1 \cap B^c(0, l_L^{-1}(Z_1))$ and $S_1 \cap B^c(0, l_N^{-1}(Z_1))$ respectively. Since the typical user will detect a BS if the received SINR of the synchronization signal from that BS exceeds Γ_{cs}, the detection probability of the typical BS sector is as follows:

Lemma 4.5.2. *The probability for the typical user to detect the BS providing the smallest path loss inside the typical BS sector is given by:*

$$P_{M_{cs},N_{cs}}(\Gamma_{cs}) = \int_0^\infty \tilde{P}_{M_{cs},N_{cs}}(z, \Gamma_{cs}) f_{Z_1}(z) \mathrm{d}z, \tag{4.11}$$

where $\tilde{P}_{M_{cs},N_{cs}}(z, \Gamma_{cs})$ denotes the conditional detection probability when the minimum path loss inside the typical BS sector is z, which is given by:

$$\tilde{P}_{M_{cs},N_{cs}}(z, \Gamma_{cs}) = \exp\left(-\frac{\Gamma_{cs} z \sigma^2}{P_b M_{cs} G(2\pi/N_{cs})}\right) V\left(z, \Gamma_{cs}, \frac{\lambda}{K_{cs}}\right), \tag{4.12}$$

where function V is defined in (4.3), and other parameters are defined in Table 5.1.

Proof. The proof is provided in Appendix 4.10.2. □

Since the events for the typical user to detect the various BS sectors are i.i.d., we can easily derive the overall cell search success probability, i.e., the probability that the typical user is able to detect at least one BS sector, in the following theorem:

Theorem 4.5.3. *The probability for the typical user to succeed the cell search is given by:*

$$\hat{P}_{M_{cs},N_{cs}}(\Gamma_{cs}) = 1 - (1 - P_{M_{cs},N_{cs}}(\Gamma_{cs}))^{K_{cs}}, \tag{4.13}$$

where $P_{M_{cs},N_{cs}}(\Gamma_{cs})$ is derived in Lemma 4.5.2.

Remark 4.5.2. Intuitively, by increasing the number of beamforming directions to search (i.e., K_{cs}), the synchronization signal received at the typical user is subject to less effective noise as well as less interference on average, and therefore a higher cell search success probability is expected. This observation will be validated more rigorously in Section 4.8.

4.5.1.3 Serving Path Loss Distribution

Since the main objective of cell search is for the typical user to detect its neighboring BSs and make cell association decision, it is important to determine the path loss distribution from the typical user to its potential serving

BS. For the rest of this chapter, we call the potential serving BS of the typical user the "tagged BS".

Denote by Z_0 the path loss from the typical user to the tagged BS; it is the minimum path loss from the typical user to the BSs inside the detected BS sectors. If cell search fails, we assume the potential serving BS to the typical user is infinitely far away and therefore Z_0 is infinity. Based on Lemma 4.5.2, we are able to derive the distribution of Z_0 as follows:

Lemma 4.5.4. *The CCDF of the path loss from the typical user to the tagged BS is given by:*

$$\mathbb{P}(Z_0 \geq z_0) = \left(P_{M_{cs},N_{cs}}(z_0, \Gamma_{cs}) + 1 - P_{M_{cs},N_{cs}}(\Gamma_{cs}) \right)^{K_{cs}}, \tag{4.14}$$

where $P_{M_{cs},N_{cs}}(z_0, \Gamma_{cs}) \triangleq \int_{z_0}^{\infty} \tilde{P}_{M_{cs},N_{cs}}(z, \Gamma_{cs}) f_{Z_1}(z) \mathrm{d}z$. *In addition, the PDF of* Z_0 *is given by:*

$$f_{Z_0}(z_0) = K_{cs} \left(P_{M_{cs},N_{cs}}(z_0, \Gamma_{cs}) + 1 - P_{M_{cs},N_{cs}}(\Gamma_{cs}) \right)^{K_{cs}-1} \tilde{P}_{M_{cs},N_{cs}}(z_0, \Gamma_{cs}) f_{Z_1}(z_0),$$

where the notation and functions are defined in Table 5.1.

Proof. The proof is provided in Appendix 4.10.3. □

Remark 4.5.3. It is straightforward that $\lim_{z_0 \to \infty} \mathbb{P}(Z_0 \geq z_0) = 1 - \hat{P}_{M_{cs},N_{cs}}(\Gamma_{cs})$, which means the tail distribution of Z_0 will approach the probability that the typical user fails cell search. Since $\hat{P}_{M_{cs},N_{cs}}(\Gamma_{cs})$ is non-decreasing with respect to K_{cs}, Z_0 will have a lighter tail as K_{cs} increases.

4.5.2 Success Probability for Random Access

According to Section 4.4.2, users that succeed cell search will initiate the random access procedure, where BSs and users sweep through $M_{ra} \times N_{ra}$ transmit-receive beam pairs over the uplink synchronously. Since each user can initiate random access only upon successful cell search, the users that are involved in the random access process has intensity $\lambda_u \hat{P}_{M_{cs},N_{cs}}(\Gamma_{cs})$. For analytical tractability, we assume the user process during RA is approximated by a homogeneous PPP with intensity $\lambda_u \hat{P}_{M_{cs},N_{cs}}(\Gamma_{cs})$, and we will show in Remark 4.5.4 that this is a reasonable approximation. Note $\Phi_u^{'}$ does not include the typical user, which is assumed to be fixed at the origin by Slivnyak's theorem. Since random access is successful if the RA preamble of the typical user can be decoded by the tagged BS without any collision, the success probability for random access is derived in the following two parts.

4.5.2.1 No RA Preamble Collision Probability

The RA preamble collision happens at the typical user when there exists another user such that: (1) it tries to associate with the tagged BS; (2) it chooses the same RA preamble sequence as the typical user, and (3) the tagged BS receives the RA preamble from this user under the same receive beam as the typical user. Therefore, the probability that the typical user has no RA premable collision is as follows:

Lemma 4.5.5. *The probability that the typical user is not subject to RA*

preamble collision is approximated by:

$$P_{co} \approx \exp(-\frac{1.28\lambda_u \hat{P}_{M_{cs},N_{cs}}(\Gamma_{cs})}{\lambda N_{PA} M_{ra}}). \tag{4.15}$$

Proof. The proof is provided in Appendix 4.10.4. □

4.5.2.2 Successful Reception Probability of RA Preamble

The RA preamble sequence of the typical user is successfully decoded if its received SINR at the tagged BS is greater than or equal to Γ_{ra}. For simplicity, we assume perfect RA preamble sequences are used, such that they have delta function as their auto-correlation functions and zero as their cross-correlation functions. Thus, only the users choosing the same RA preamble sequence as the typical user can potentially interferer with it. Conditionally on the path loss from the typical user to the tagged BS, the successful reception probability of the RA preamble is as follows:

Lemma 4.5.6. *Denote by Z_0 the path loss from the typical user to the tagged BS, the probability that the RA preamble of the typical user can be successfully received by the tagged BS is:*

$$\begin{aligned} P_{ra}(Z_0, \Gamma_{ra}) = &\exp\left(-\frac{\Gamma_{ra} Z_0 \sigma^2}{P_u M_{ra} G(2\pi/N)}\right) U\left(Z_0, \Gamma_{ra}, \frac{\lambda_u \hat{P}_{M_{cs},N_{cs}}(\Gamma_{cs})}{N M_{ra} N_{PA}}\right) \\ &\times U\left(Z_0, \frac{g(2\pi/N)}{G(2\pi/N)}\Gamma_{ra}, (1-\frac{1}{N})\frac{\lambda_u \hat{P}_{M_{cs},N_{cs}}(\Gamma_{cs})}{M_{ra} N_{PA}}\right), \end{aligned} \tag{4.16}$$

where $N = \max(N_{cs}, N_{ra})$, and U is defined in (4.3).

Proof. The proof is provided in Appendix 4.10.5. □

Since $P_{ra}(Z_0, \Gamma_{ra}) = 0$ when $Z_0 = \infty$, the overall success probability of the initial access procedure can be obtained by combining Lemma 4.5.4, Lemma 4.5.5 and Lemma 4.5.6, which gives:

Theorem 4.5.7. *The initial access success probability for the typical user is given by:*

$$\eta_{IA} = \int_0^\infty K_{cs} \Big(P_{M_{cs},N_{cs}}(z_0, \Gamma_{cs}) + 1 - P_{M_{cs},N_{cs}}(\Gamma_{cs}) \Big)^{K_{cs}-1} \times \tilde{P}_{M_{cs},N_{cs}}(z_0, \Gamma_{cs}) \times P_{co} \times P_{ra}(z_0, \Gamma_{ra}) f_{Z_1}(z_0) \mathrm{d}z_0, \tag{4.17}$$

where the notation and functions are defined in Table 5.1.

Remark 4.5.4. Denote by $\Phi_u^{''}$ the users that succeed initial access, Theorem 4.5.7 shows the intensity of $\Phi_u^{''}$ is $\lambda_u \eta_{IA}$. Intuitively, $\Phi_u^{''}$ is expected to exhibit spatial clustering since the users in $\Phi_u^{''}$ should be centered around BSs and sparse at cell edges. In Fig. 4.3, we plot the empty space function (ESF) of $\Phi_u^{''}$ which is defined as $F(r) \triangleq \mathbb{P}_\Phi^0 \left(\min\{\|u\| : u \in \Phi_u^{''}\} \leq r \right)$, where $\mathbb{P}_\Phi^0$ denotes the Palm distribution of BS process Φ. Fig. 4.3 shows that $\Phi_u^{''}$ has a smaller ESF than its fitted PPP, which means $\Phi_u^{''}$ exhibits clustered pattern [10]. In fact, Fig. 4.3 also shows that for most range of r, the ESF of $\Phi_u^{''}$ falls within the 95% confidence interval created by its fitted PPP. Therefore, we still assume $\Phi_u^{''}$ is modeled by a PPP with intensity $\lambda_u \eta_{IA}$ for analytical simplicity. The accuracy of this assumption will be validated in Section 4.8.

Based on Theorem 4.5.7, the expected initial access delay defined in (4.5) can be easily evaluated, which will be discussed in more detail in Section 4.8.

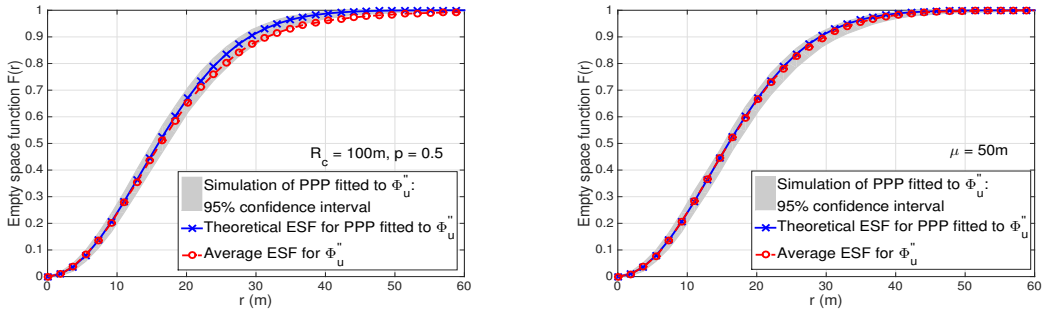

(a) Generalized LOS ball model (b) Exponential blockage model

Figure 4.3: Empty space function comparison of Φ_u'' and its fitted PPP ($M = 8$, $N = 4$).

4.6 Downlink SINR Distribution and UPT in Single-Stage BF Approach

In this section, we will focus on the performance of the data transmission phase for the single-stage beamforming approach, wherein the beam refinement phase is not utilized. As a result, each BS will determine the beam directions to its associated users only from the initial access phase, which will be used during the data transmission phase. Therefore, we assume $\max(M_{cs}, M_{ra}) = M_{IA} = M$ in this section.

During the data transmission phase in Fig. 4.1, each BS randomly schedules one of its associated users, and the beam directions of the BS and its scheduled user are aligned. In particular, the BS beamwidth and user beamwidth are $\frac{2\pi}{M}$ and $\frac{2\pi}{N}$ respectively. We assume the typical user has succeeded initial access and is scheduled by the tagged BS, such that the CCDF

of its conditional downlink data SINR is given by:

$$P_{DL}(\Gamma) = \mathbb{P}(\text{SINR}_{DL} \geq \Gamma | e_0 \delta_0 = 1), \tag{4.18}$$

where SINR_{DL} represents the SINR of the typical user, while e_0 and δ_0 represent the success indicator for cell search and random access respectively.

Since a random scheduler is used, the beam direction of all the interfering BSs to the typical user are assumed to be independent and uniformly distributed. Despite every interfering BS has positive probability to have zero associated users, we assume it is actively transmitting for analytical simplicity. Although this overestimates the interference at the typical user, we will show in Section 4.8 that the effect is negligible. Based on the assumptions above, the expression of $P_{DL}(\Gamma)$ is derived in the following lemma:

Lemma 4.6.1. *The CCDF of the SINR of the typical user given it succeeds the initial access is approximated by:*

$$\begin{aligned}
&P_{DL}(\Gamma) \\
=&\frac{1}{\eta_{IA}} \int_0^\infty \exp\left(-\frac{\Gamma z \sigma^2}{P_b M N}\right) K_{cs} \Bigg[V(z, \Gamma, \frac{\lambda}{M K_{cs}}) P_{M_{cs}, N_{cs}}(z, \Gamma_{cs}) + U(z, \Gamma, \frac{\lambda}{M K_{cs}}) \\
&\times (1 - P_{M_{cs}, N_{cs}}(\Gamma_{cs})) \Bigg]^{q-1} \Bigg[P_{M_{cs}, N_{cs}}(z, \Gamma_{cs}) V(z, \frac{g(2\pi/N)}{G(2\pi/N)} \Gamma, \frac{\lambda}{M K_{cs}}) \\
&+ (1 - P_{M_{cs}, N_{cs}}(\Gamma_{cs})) U(z, \frac{g(2\pi/N)}{G(2\pi/N)} \Gamma, \frac{\lambda}{M K_{cs}}) \Bigg]^{K_{cs}-q} V(z, \Gamma, \frac{\lambda}{M K_{cs}}) \\
&\times \tilde{P}_{M_{cs}, N_{cs}}(z, \Gamma_{cs}) P_{ra}(z, \Gamma_{ra}) P_{co} f_{Z_1}(z) \mathrm{d}z,
\end{aligned}$$

where $q = \frac{K_{cs}}{N}$, and other notation and functions are all defined in Table 5.1.

Proof. The proof is provided in Appendix 4.10.6. □

Given the data SINR distribution, we are able to derive the average user-perceived downlink throughput defined in (4.6). According to Remark 4.5.4, the users that succeed initial access are assumed to form a homogeneous PPP with intensity $\lambda_u \eta_{IA}$. As a result, the average number of users that are associated to the tagged BS is $1 + 1.28\frac{\lambda_u \eta_{IA}}{\lambda}$, which means the average scheduling probability for the typical user is $\eta_s = \frac{1}{1+1.28\lambda_u \eta_{IA}/\lambda}$. By substituting η_s into (4.6), we can derive the average user-perceived downlink throughput as follows:

Theorem 4.6.2. *When the beam refinement phase is not used, the average user-perceived downlink throughput is given by:*

$$\bar{R} = \max(0, 1 - \frac{M_{cs}N_{cs}\tau + M_{ra}N_{ra}\tau}{T}) \times \frac{\eta_{IA}}{1 + 1.28\lambda_u \eta_{IA}/\lambda} \times \int_0^\infty \frac{W}{\ln 2} \frac{P_{DL}(\Gamma)\mathrm{d}\Gamma}{1+\Gamma}, \tag{4.19}$$

where $P_{DL}(\Gamma)$ is derived in Lemma 4.6.1, and other notations are defined in Table 4.1.

4.7 Beam Refinement Phase Success Probability and UPT in Two-Stage BF Approach

In this section, we will investigate the performance of the two-stage beamforming phase. During the BRP, each BS transmits the BRRS to its associated users by sweeping through M refined beams with beamwidth $\frac{2\pi}{M}$. Denote by x_0 the location of the tagged BS, we assume x_0 satisfies that $x_0 \in S_1 \triangleq S(o, 0, \frac{2\pi}{K_{cs}})$ and $x_0 \in \tilde{S}_1 \triangleq S(o, \frac{2(q-1)\pi}{M}, \frac{2q\pi}{M})$ for some $q \in \mathbb{N}^+$, wherein S_1 and $\tilde{S}_1$ denote the area of potential BSs the typical user can receive, when it

is beam aligned with the tagged BS during cell search and BRP respectively. For analytical simplicity, the side lobe gain for user beam is assumed to be 0 in this section. The BRP success probability given the typical user succeeds IA is derived in the following theorem.

Lemma 4.7.1. *Denote by $H(\Gamma_B)$ probability that the typical user can detect BRRS from the tagged BS given it succeeds IA, then $H(\Gamma_B)$ is given by:*

$$H(\Gamma_B) = \frac{1}{\eta_{IA}} \int_0^\infty K_{cs} \exp(-\frac{\Gamma_B z_0 \sigma^2}{P_b MN}) \frac{W(z_0, \Gamma_B, \Gamma_{cs}, \frac{\lambda}{M}, 1)}{V(z_0, \Gamma_{cs}, \frac{\lambda}{M})} G_{M_{cs},N_{cs}}(z_0, \Gamma_{cs}) \times \bar{P}_{M_{cs},N_{cs}}(z_0, \Gamma_{cs})^{K_{cs}-1} P_{co} P_{ra}(z_0, \Gamma_{ra}) f_{Z_1}(z_0) \mathrm{d}z_0, \tag{4.20}$$

where $\bar{P}_{M_{cs},N_{cs}}(z_0, \Gamma_{cs}) = 1 - \int_0^{z_0} G_{M_{cs},N_{cs}}(z, \Gamma_{cs}) f_{Z_1}(z) \mathrm{d}z$, other special functions are defined in (4.3) and Theorem 4.5.7.

Proof. Please see Appendix 4.10.7. □

During the data transmission phase in Fig. 4.1, each BS randomly schedules one of its associated users. In particular, given the typical user succeeds the IA and is scheduled by the tagged BS, the tagged BS will transmit downlink data using a narrow beam of beam-width $\frac{2\pi}{M}$ if typical user succeeds the BRP, otherwise a wide beam of beam-width $\frac{2\pi}{M_{IA}}$ is used. For analytical simplicity, we assume every interfering BS is actively transmitting during the data transmission phase with beam-width $\frac{2\pi}{M}$. In addition, since a random scheduler is used, the beam direction of the interfering BS to the typical user is assumed to be independent and uniformly distributed. Based on the above assumptions, we can derive the following result:

Lemma 4.7.2. *Given the typical user succeeds IA and is scheduled by the tagged BS, the data SINR coverage probability when BRP is used, i.e.,* $\tilde{P}_{DL}(\Gamma) \triangleq \mathbb{P}(SINR_{DL} \geq \Gamma | IA)$*, is approximated by:*

$$\begin{aligned}\tilde{P}_{DL}(\Gamma) = &\frac{1}{\eta_{IA}} \int_0^\infty K_{cs} G_{M_{cs},N_{cs}}(z,\Gamma_{cs})(\bar{P}_{M_{cs},N_{cs}}(z,\Gamma_{cs}))^{K_{cs}-q} \\ &\times P_{co} P_{ra}(z,\Gamma_{ra}) \Bigg\{ \exp\left(-\frac{(\Gamma+\Gamma_B)z\sigma^2}{P_b M N}\right) V(z,\Gamma,\frac{\lambda(M-K_{cs})}{M^2 K_{cs}}) \\ &\times W(z,\Gamma,\Gamma_B,\frac{\lambda}{M},M)(\hat{P}_{M_{cs},N_{cs},M}(z,\Gamma,\Gamma_{cs}))^{q-1} + \exp(-\frac{\Gamma z\sigma^2}{P_b M_{IA} N}) \\ &\times V(z,m\Gamma,\frac{\lambda(M-K_{cs})}{M^2 K_{cs}}) \times \Bigg(V(z,m\Gamma,\frac{\lambda}{M^2}) - \exp(-\frac{\Gamma_B z\sigma^2}{P_b M N}) \\ &\times W(z,m\Gamma,\Gamma_B,\frac{\lambda}{M},M)\Bigg)(\hat{P}_{M_{cs},N_{cs},M}(z,m\Gamma,\Gamma_{cs}))^{q-1} \Bigg\} f_{Z_1}(z)\mathrm{d}z,\end{aligned}$$

where:

$$\begin{aligned}\hat{P}_{M_{cs},N_{cs},M}(z,\Gamma,\Gamma_{cs}) = &\Bigg[V(z,\Gamma,\frac{\lambda}{MK_{cs}}) \int_z^\infty G_{M_{cs},N_{cs}}(z,\Gamma_{cs}) \\ &\times f_{Z_1}(z)\mathrm{d}z + U(z,\Gamma,\frac{\lambda}{MK_{cs}})(1-\int_0^\infty G_{M_{cs},N_{cs}}(z,\Gamma_{cs}) f_{Z_1}(z)\mathrm{d}z)\Bigg],\end{aligned}$$

$q = \frac{\max(M_{cs},N_{cs})}{N}$*, and other special functions are defined in (4.3) and Theorem 4.5.7.*

Lemma 4.7.2 can be proved by following similar steps to the proof of Lemma 4.6.1. In particular, given $Z_1 = z$ and the typical user succeeds IA, the downlink coverage probability can be derived by adding up the coverage probability when the typical user succeeds BRP and when it fails the BRP. We omit the detailed proof here.

Given the data SINR distribution, we are able to derive the average UPT defined in (4.6). As shown earlier, the users involved in the data transmission phase can be accurately modeled by a homogeneous PPP with intensity $\lambda_u \eta_{IA}$, such that the average scheduling probability for the typical user is $\eta_s = \frac{1}{1+1.28\lambda_u \eta_{IA}/\lambda}$. By substituting η_s into (4.6), the average UPT is derived as follows:

Theorem 4.7.3. *When the beam refinement phase is used, the average user-perceived throughput is approximated by:*

$$\bar{R} = \max\left(0, 1 - \frac{(M_{cs}N_{cs} + M_{ra}N_{ra} + M)\tau}{T}\right) \frac{\eta_{IA}}{1 + 1.28\frac{\lambda_u \eta_{IA}}{\lambda}} \int_0^\infty \frac{W}{\ln 2} \frac{\tilde{P}_{DL}(\Gamma)\mathrm{d}\Gamma}{1+\Gamma}, \tag{4.21}$$

where $\tilde{P}_{DL}(\Gamma)$ is obtained in Lemma 4.7.2.

4.8 Numerical Evaluation

In this section, the initial access delay and user-perceived throughput performance are numerically evaluated for the proposed initial access protocols. Specifically, we first investigate the performance of the single-stage BF approach, then the performance of the two-stage BF approach.

We consider a mmWave cellular system with the same frame structure and synchronization signal configuration as the one specified in [102]. Specifically, the system operates at the 28 GHz carrier frequency with 100 MHz bandwidth, the sub-carrier spacing is 75 kHz, and the corresponding OFDM symbol length (including cyclic prefix) is 14.3 μs. Each synchronization sig-

nal/RA preamble sequence occupies only one OFDM symbol (i.e., $\tau = 14.3$ μs), and the beam reference signal is also transmitted in the same symbol to uniquely identify the beam index. The synchronization signal/beam reference signal transmission period is 20 ms, which means $T = 20$ ms. The default system parameter values are summarized in Table 4.1.

In order to simulate the initial access and data transmission procedures, we have generated 50 realizations of the BS PPP, and 50 realizations of the user PPP given every BS PPP, inside a 1.5 km $\times$ 1.5 km network area. For each pair of the BS and user PPPs, we first simulate the initial access procedure according to Section 4.4. Then the downlink data transmission phase (also the beam refinement phase if it is used) is simulated, where each BS either randomly schedules one of its associated users, or keeps silent if it has no user to serve. By averaging over all the 2500 combinations of BS and user PPPs, different performance metrics of this mmWave system are recorded. BS and user locations are simulated by PPPs since currently there is no location data for mmWave system, and PPPs have already been shown to be an accurate model for mmWave system design [118–121, 123, 124].

4.8.1 Performance of the Single-stage BF Approach

4.8.1.1 Baseline IA Protocol Performance

The cell search success probability is plotted in Fig. 4.4 for the generalized LOS ball model and the exponential blockage model. It can be observed from Fig. 4.4 that the analytical result in Theorem 4.5.3 is accurate. In ad-

dition, Fig. 4.4 shows that when BSs transmit omni-directionally and users receive omni-directionally, the cell search success probability is relatively low for various Γ_{cs}, which means the system is subject to significant coverage issues when cell search is performed omni-directionally as LTE. By contrast, when beam sweeping is applied, the cell search success probability can be significantly improved even with a small value of $\max(M_{cs}, N_{cs})$ such as 4. As M_{cs} or N_{cs} is increased, the cell search probability can be further improved, so beam sweeping needs to be applied to guarantee a reasonable cell search performance. In the remaining simulations, we use $\Gamma_{cs} = -4$ dB as the SINR threshold to detect the synchronization signals, above which a sufficiently small miss detection probability (e.g., 1%) can be achieved [109].

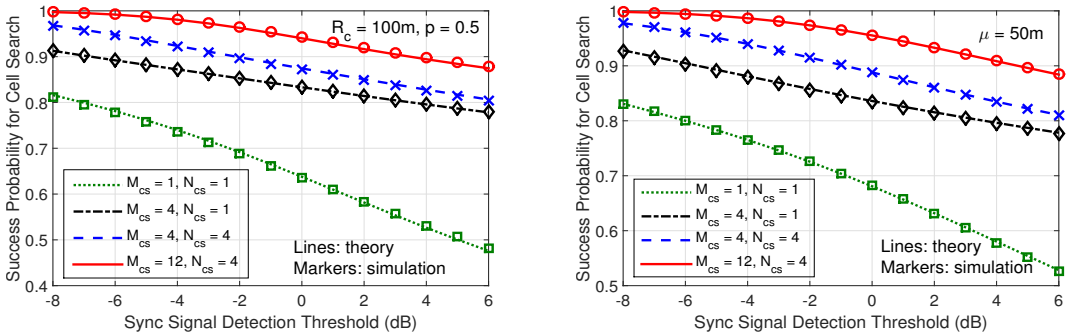

(a) Generalized LOS ball model (b) Exponential blockage model

Figure 4.4: Cell search success probability.

Fig. 4.5 shows the CCDF of the path loss from the typical user to the tagged BS, which is derived in Lemma 4.5.4. As we increase M_{cs} or N_{cs}, the CCDF of the path loss decreases, especially at the tail of the distribution. Note when $M_{cs} = N_{cs} = 1$, the tagged BS is the BS providing the minimum

path loss to the typical user, which coincides with the conventional minimum path loss association rule [2, 118, 119, 121, 123]. By contrast, if beam sweeping is implemented for cell search, the typical user can connect to other BSs even if the BS providing the minimum path loss is unable to be detected. As a result, the typical user will have a smaller path loss to the tagged BS almost surely as M_{cs} or N_{cs} increases. This fact further demonstrates the benefit of beam sweeping for cell search.

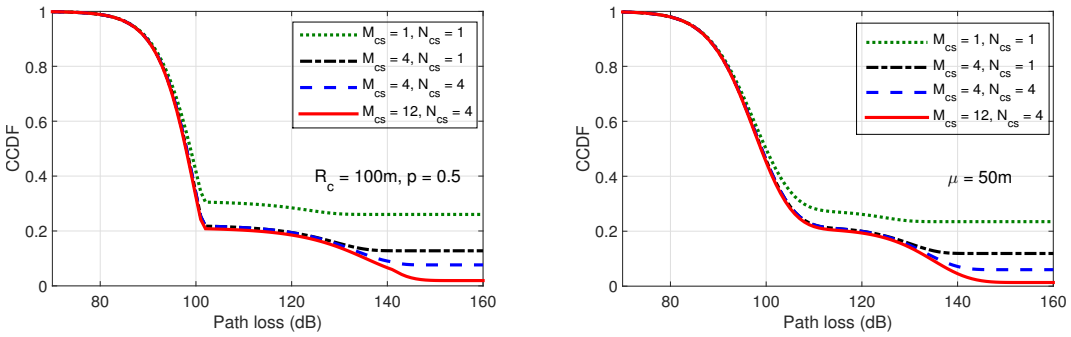

(a) Generalized LOS ball model (b) Exponential blockage model

Figure 4.5: Path loss distribution from the typical user to tagged BS.

Fig. 4.5 shows the CCDF of the path loss from the typical user to the tagged BS, which is derived in Lemma 4.5.4. As we increase M_{cs} or N_{cs}, the CCDF of the path loss decreases, especially at the tail of the distribution. Note when $M_{cs} = N_{cs} = 1$, the tagged BS is the BS providing the minimum path loss to the typical user, which coincides with the conventional minimum path loss association rule [2, 118, 119, 121, 123]. By contrast, if beam sweeping is implemented for cell search, the typical user can connect to other BSs even if the BS providing the minimum path loss is unable to be detected. As a result,

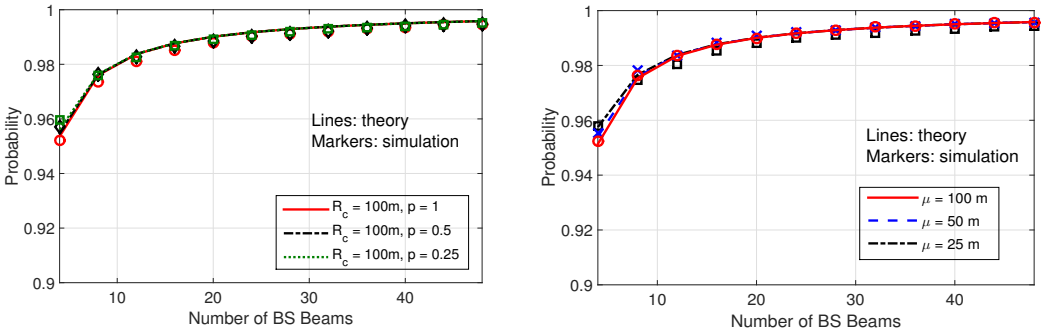

(a) Generalized LOS ball model (b) Exponential blockage model

Figure 4.6: Probability of no RA preamble collision.

the typical user will have a smaller path loss to the tagged BS almost surely as M_{cs} or N_{cs} increases. This fact further demonstrates the benefit of beam sweeping for cell search. Actually, all the CCDF curves in Fig. 4.5a have an inflection point at 101.4 dB. This is because for the LOS ball blockage model, the serving BS could be either LOS or NLOS when the path loss is smaller than 101.4 dB, while it is NLOS almost surely when the path loss is higher than 101.4 dB.

Fig. 4.6 plots the probability that the typical user is not subject to RA preamble collisions versus the number of BS beams $M = \max(M_{cs}, M_{ra})$. Different parameters for the two blockage models are considered, where blockage becomes more severe as p decreases in the generalized LOS ball model, or μ decreases in the exponential blockage model. It can be observed from Fig. 4.6 that Lemma 4.5.5 is an accurate approximation to the actual simulation results, which shows that it is accurate to approximate the users that succeed cell search by PPP. In addition, Fig. 4.6 shows that the probability of no RA

preamble collision P_{co} is relatively insensitive to the underlying blockage conditions, and P_{co} increases as the number of BS beams increases. Since P_{co} remains consistently high (greater than 95%) for different blockage conditions and various M values, RA preamble collision is therefore not the performance bottleneck for the baseline protocol. It is clear from Lemma 4.5.5 that this is a result of the 64 RA preamble sequences and beam sweeping at the BS during random access.

The initial access delay, which can be derived from Theorem 4.5.7, is plotted in Fig. 4.7 for both blockage models. Despite some approximations used in deriving Theorem 4.5.7, Fig. 4.7 validates the accuracy of the analytical results. In addition, Fig. 4.7 shows that as blockage becomes less severe, the expected initial access delay decreases as a result of the improved initial access success probability. Depending on the propagation environment, the optimal expected initial access delay in our simulations ranges from 2.2 ms to 4.1 ms for the generalized LOS ball model, and 1.2 ms to 5.0 ms for the exponential blockage model.

According to Fig. 4.7, the expected initial access delay is relatively high when the number of BS beams is small, which is because the typical user needs more initial access cycles until it can connect to the network. By increasing the number of BS beams, despite the typical user has higher probability to succeed within one initial access cycle, the overhead for initial access starts to become more dominant. As a result, there exists an optimal BS beam number (or BS beamwidth) in terms of the expected initial access delay. For example,

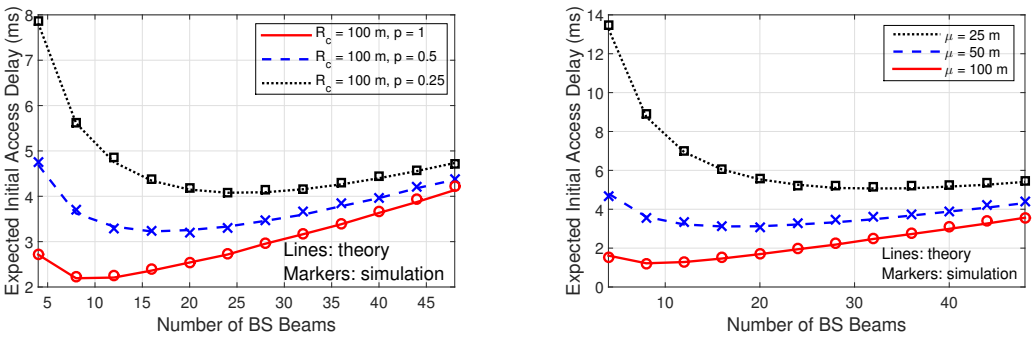

(a) Generalized LOS ball model (b) Exponential blockage model

Figure 4.7: Expected initial access delay performance.

given $R_c = 100$ m for the generalized LOS ball model, this optimal beamwidth is 45°, 22.5° and 15° when p is equal to 1, 0.5 and 0.25 respectively. In fact, as blockage becomes more severe, the optimal BS beamwidth is decreasing for both blockage models, which means a more robust link with higher antenna gain is needed in order to quickly establish the connection. In addition, we have also verified that the optimal BS beamwidth in terms of initial access delay is non-decreasing as user density increases, which is mainly because a narrower beam at the BS will reduce the collision of RA preambles among different users.

Fig. 4.8 plots the downlink data SINR coverage probability given the typical user succeeds the initial access, where the BS and user beamwidth are 30° and 90° respectively. Although all interfering BSs are assumed to be active in deriving Lemma 4.6.1, the difference between the analytical results and simulation results in Fig. 4.8 is negligible. The same trend has been observed for other BS and user beamwidth values as well, which validates the

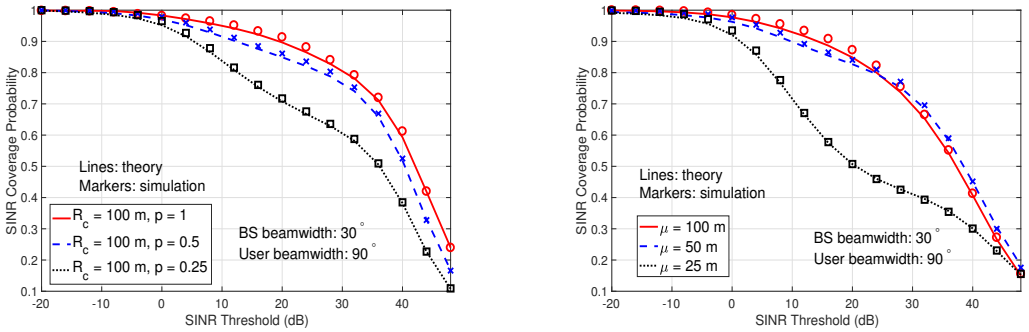

(a) Generalized LOS ball model (b) Exponential blockage model

Figure 4.8: CCDF of data SINR given successful initial access.

accuracy of Lemma 4.6.1. In addition, we can observe that the conditional downlink coverage probability improves as blockage becomes less severe. In fact, the conditional SINR CCDF in Fig. 4.8 is relatively high for most SINR thresholds, which is mainly because the typical user should reside in a location with favorable propagation conditions to succeed the initial access. Another reason for the improved CCDF is that unlike previous works that require the tagged BS to be the BS providing the minimum path loss, the typical user is actually able to connect to other BSs if the BS providing the minimum path loss is blocked or in deep fade.

The average user-perceived downlink throughput versus the number of BS beams is plotted in Fig. 4.9 for both blockage models. Fig. 4.9 shows the average UPT has a steep increase when the number of BS beams increases from a very small value to a medium value. This is mainly due to a much improved link quality and relatively low initial access overhead in this range. However, as the number of BS beams further increases, the initial access overhead starts

to become more dominant, which leads to a steady decrease of the average UPT. In terms of the average UPT, Fig. 4.9 shows the optimal BS beamwidth does not vary too much for different blockage conditions, which is typically between 10° to 18°. This is because the average UPT is affected by multiple counterbalancing factors such as the initial access overhead, success probability of initial access, and scheduling factors. For example, a high initial access success probability will lead to a heavily-loaded cell for the tagged BS, such that the typical user has smaller probability to be scheduled.

Therefore, for the baseline protocol, depending on the blockage condition and which metric is more important, the optimal BS beamwidth could vary. When blockage is not very significant, a wide BS beamwidth (e.g. 45°) is preferred to reduce the initial access delay, while a narrow BS beamwidth (e.g. 15°) is preferred to achieve higher UPT performance. By contrast, when blockage is severe, a narrow BS beamwidth (e.g. 15°) could achieve good performance for both initial access delay and average UPT.

4.8.1.2 Performance Comparison for Different IA Protocols

In this part, based on Theorem 4.5.7 and Theorem 4.6.2, we compare the expected initial access delay and average user-perceived downlink throughput[3] for the four initial access protocols in Table 4.2. In making the comparisons, we consider both a severely blocked condition (e.g., $R_c = 100$ m,

[3]The accuracy of the analytical results for the other three protocols can be validated similar to the baseline protocol, so only analytical results are shown in this section.

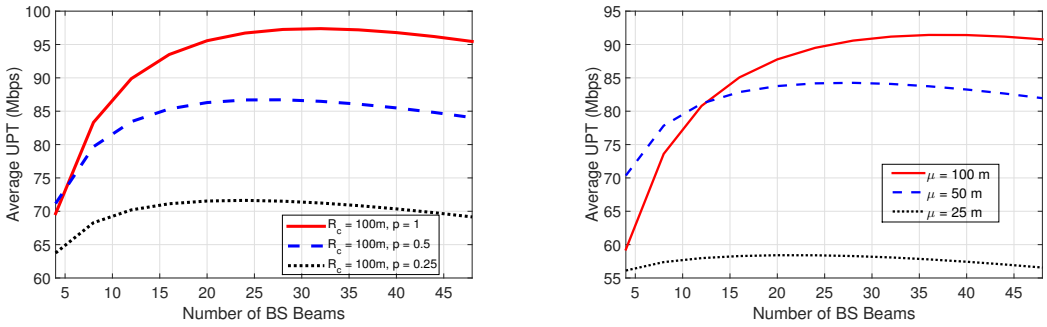

(a) Generalized LOS ball model (b) Exponential blockage model

Figure 4.9: Average user-perceived downlink throughput performance, where the rectangle area denotes the range for quasi-optimal BS beam number.

$p = 0.25$ for generalized LOS ball model; $\mu = 25$ m for exponential blockage model), and also a lightly blocked condition (e.g., $R_c = 100$ m, $p = 1$ for generalized LOS ball model; $\mu = 100$ m for exponential blockage model) for both blockage models. All the other system parameters remain the same as in Table 5.1. The expected initial access delay and average UPT comparisons for the three protocols are plotted in Fig. 4.10 and Fig. 4.11 respectively.

Comparison of Expected Initial Access Delay: Baseline and fast CS outperform omni RX in terms of the expected initial access delay. The expected initial access delay is plotted in Fig. 4.10, which shows that the omni RX protocols always have higher initial access delay than the baseline and fast CS protocols. The main reason is that omni RX protocol requires the BS to receive omni-directionally during random access, which leads to a high RA preamble collision probability according to Lemma 4.5.5. Specifically, in contrast to the baseline and fast CS protocols wherein P_{co} is consistently

higher than 0.95, P_{co} for the omni RX protocol is around 0.82 for all blockage conditions and various BS beamwidth values. In addition, the RA preamble decoding probability for the omni RX protocol is also lower (around 5%) compared to the other two protocols, which can be analytically shown from Lemma 4.5.6. Both factors make the expected initial access delay under omni RX protocol significantly higher than the other two protocols.

In terms of the expected initial access delay, Fig. 4.10 also shows whether or not the baseline protocol outperforms the fast CS protocol depends on the severity of blockage. Specifically, under a severely blocked condition, the baseline protocol has smaller initial access delay than the fast CS protocol. This is mainly because the baseline protocol has better link quality under both cell search and random access phases, which leads to significantly higher initial access success probability than the fast CS protocol. By contrast, under light blockage, the fast CS protocol is also able to achieve a sufficiently high initial access success probability. As a result, the fast CS protocol will outperform the baseline protocol due to a much lower initial access overhead.

Comparison of the Average User-perceived Downlink Throughput: In terms of the average UPT, the omni RX protocol and fast CS protocol generally outperform the baseline protocol. Despite having smaller initial access success probability than the baseline, the following reasons contribute to the high UPT for omni RX and fast CS protocols. First, both protocols have the lowest initial access overhead, which is significantly lower than the other two protocols, especially when the number of BS beams M is high. Second,

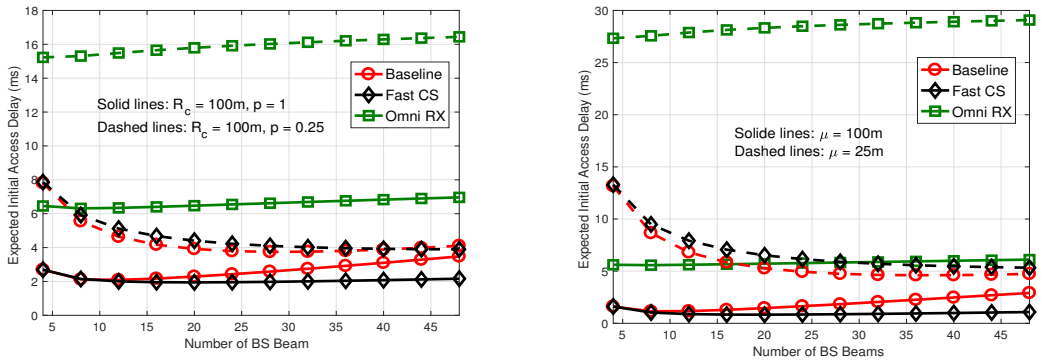

(a) Generalized LOS ball model (b) Exponential blockage model

Figure 4.10: Comparison of expected initial access delay.

despite both protocols having lower initial access success probability than the baseline, the typical user actually has higher scheduling probability since it will observe a lightly loaded cell once it succeeds at initial access. Third, under the omni RX and fast CS protocols, the typical user will have higher conditional downlink data SINR than the baseline, because it needs more favorable propagation in order to succeed at initial access. Despite the baseline protocol having the highest initial access success probability, the above factors render it inferior in terms of UPT versus the other protocols. Compares to the omni RX protocol, Fig. 4.11 shows that the fast CS protocol achieves a similar UPT performance under a lightly blocked condition, while it provides a much smaller UPT under a severely blocked condition. Another observation from Fig. 4.11 is that for omni RX and fast CS protocols, the average UPT increases as the number of BS beams increases, which means a narrow beam (e.g., 7.5°) is preferred. In fact, an optimal BS beamwidth still exists as we

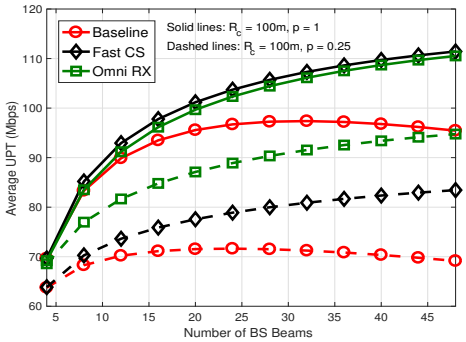

(a) Generalized LOS ball model

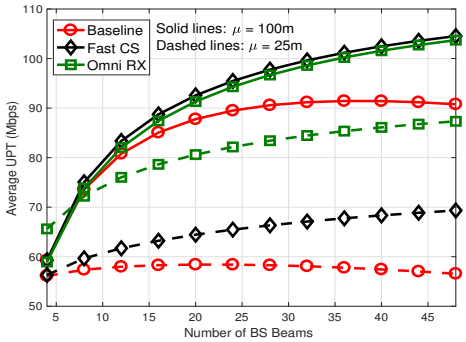

(b) Exponential blockage model

Figure 4.11: Comparison of average user-perceived downlink throughput.

continue to increase the number of BS beams, but such an optimal beamwidth could be too narrow to implement in a real system.

In summary, when the beam refinement phase is not adopted, the baseline protocol is mainly beneficial for delay-sensitive applications since it provides a small initial access delay, especially when blockage is severe. However, due to the high initial access overhead, the baseline protocol also has a poor user-perceived downlink throughput performance. The omni RX protocol provides the best user-perceived downlink throughput performance, but it is unlikely to be adopted unless the network is delay-tolerant. By contrast, the fast CS protocol wherein BS transmits omni-directionally and user applies beam sweeping during cell search, generally gives a good trade-off between the initial access delay and user-perceived throughput performance, especially under a lightly blocked condition.

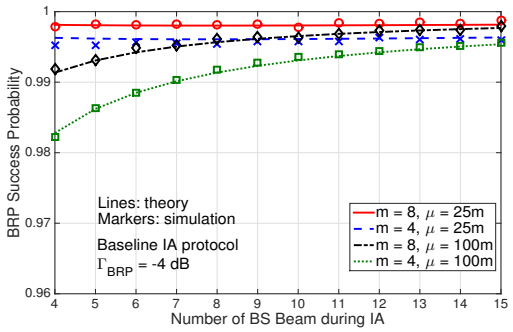

Figure 4.12: Conditional beam refinement phase success probability.

4.8.2 Performance of the Two-stage BF Approach

In this part, the performance of the two-stage beamforming approach is investigated under the exponential blockage model.

4.8.2.1 Beam Refinement Phase Success Probability

Fig. 4.12 plots the BRP success probability of the typical user given it succeeds the IA under the baseline protocol. Different beam refinement factor m and blockage conditions are considered. For all these scenarios, Fig. 4.12 shows the probability for the typical user to succeed the BRP is over 95%. Same observation also applies to the other IA protocols as well. This high conditional BRP success probability is because compared to the IA phase, the BSs have higher antenna gain and will observe fewer interferers in the BRP. As a result, given the typical user succeeds the IA, it should also succeed the BRP unless it is subject to a very deep fade.

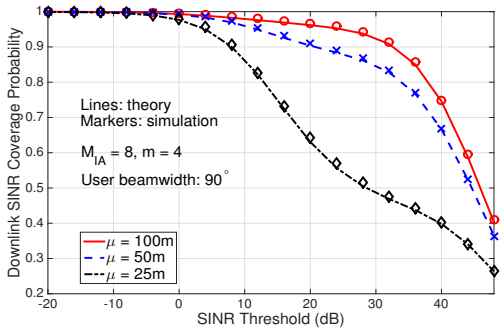

Figure 4.13: CCDF of data SINR given successful initial access with BRP.

4.8.2.2 Performance of Data Transmission Phase

Fig. 4.13 plots the downlink SINR coverage probability given the typical user succeeds initial access and is scheduled by the tagged BS. The BS beamwidth during the initial access is 45°, and the beam refinement factor $m = 4$ in Fig. 4.13. The difference between the analytical results and simulation results in Fig. 4.13 is negligible, which validates the accuracy of Lemma 4.6.1.

Given the accuracy of Theorem 4.5.7, Lemma 4.7.1 and Lemma 4.7.2, Fig. 4.14 shows the average UPT of the three IA protocols. It can be observed that given the total number of BS beams to search in BRP (i.e. M), the average UPT increases with beam refinement factor m for all three protocols. This is due to the fact that for a fixed M, there is less IA overhead (i.e., $M_{IA} = M/m$) as m increases. By considering both Fig. 4.7 and Fig. 4.14, we can find that the fast CS protocol generally gives the best trade-off between the IA delay and UPT.

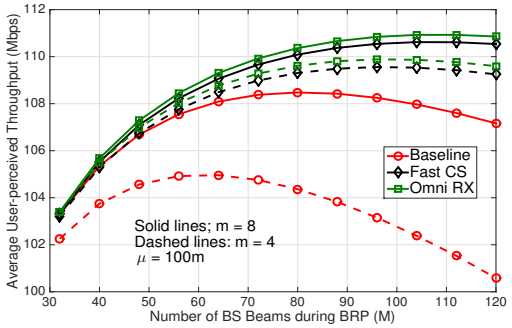

Figure 4.14: Comparison of average UPT with BRP.

4.8.3 Two-stage BF Approach v.s. Single-stage BF Approach

Fig. 4.15 plots the analytical average UPT under the proposed two-stage BF approach versus the single stage approach[4]. For the single-stage approach, BS will search all M beams during IA; for the two stage approach, the BS will search M_{IA} wide beams in IA, then apply the BRP to search $M = mM_{IA}$ refined beams. Fig. 4.15 shows that the baseline protocol has significant UPT gain under the two-stage approach. This is mainly because when $m > 1$, the total overhead for beam searching under the two stage approach, which is $NM_{IA} + M_{IA} + M$ symbols, is much smaller than that under the single stage approach, which is $MN + M$ symbols. However, the fast CS and the omni RX protocols have similar UPT as the single stage approach since the beam searching overhead under the two stage approach, which is $M_{IA} + N + M$ symbols, is larger than that under the single stage approach, which is $M + N$ symbols. Despite having slightly smaller average

[4]The side lobe gain for user is assumed to be 0 for both approaches in this comparison.

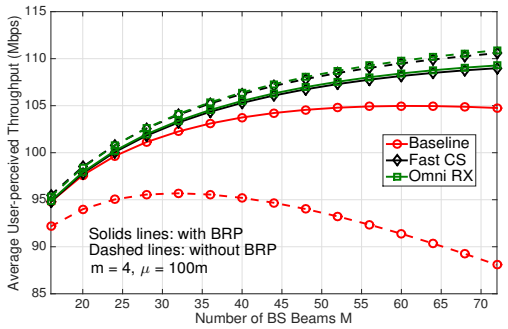

Figure 4.15: Average UPT with and without BRP.

UPT, the main benefit of the two stage approach for fast CS and omni RX is that we can adapt the beam refinement factor m to achieve good IA delay and UPT simultaneously. For example, when the LOS region size $\mu = 100$m and $m = 4$, the fast CS has near optimal expected IA delay when $M_{IA} \in [20, 24]$, and it also has optimal average UPT when $M \in [80, 96]$.

4.9 Summary

This chapter is the first work to propose a stochastic geometry based analytical framework to investigate the effects of initial access protocol design on the system level performance of mmWave cellular networks. We consider a high mobility scenario where the BS PPP and user PPP are independently re-shuffled across initial access cycles, which leads to i.i.d. performance for the typical user in different cycles. The proposed framework can derive the joint performance of the initial access phase, beam refinement phase, and data transmission phase, in a typical initial access cycle. In particular, the main

technical challenge is that temporal correlations exist for different phases in the same cycle due to common BS and user locations. Such correlations can be handled by equally dividing the plane into non-overlapping BS sectors, and deriving the typical user's performance under each sector in different phases. Several important metrics including the expected initial access delay and average user-perceived throughput can be analytically derived through the proposed methodology, which are given by unified expressions for various initial access protocols. We have shown through these expressions that the baseline exhaustive search protocol is able to achieve the smallest initial access delay when blockage is severe, while the best trade-off between the initial access delay and user-perceived downlink throughput can be achieved by a fast cell search protocol.

4.10 Appendix

4.10.1 Proof of Lemma 4.5.1

Inside the typical BS sector, since the minimum path loss to the typical user is either from the nearest LOS BS or the nearest NLOS BS, we have:

$$\begin{aligned}\mathbb{P}(Z_1 \geq z) &\overset{(a)}{=} \mathbb{P}\left(\min_{x\in\Phi_L\cap S_1} \|x\| \geq l_L^{-1}(z)\right)\times\mathbb{P}\left(\min_{x\in\Phi_N\cap S_1} \|x\| \geq l_N^{-1}(z)\right)\\ &\overset{(b)}{=} \exp\left(-\frac{2\pi\lambda}{K_{cs}}\int_0^{(\frac{z}{\beta_L})^{\frac{1}{\alpha_L}}} h(r)r\mathrm{d}r\right)\exp\left(-\frac{2\pi\lambda}{K_{cs}}\int_0^{(\frac{z}{\beta_N})^{\frac{1}{\alpha_N}}}\Big(1-h(r)\Big)r\mathrm{d}r\right),\end{aligned}$$

where (a) is because Φ_L and Φ_N are independent, and (b) is from void probability of PPP. The proof can be concluded by taking the derivative of $\mathbb{P}(Z_1 < z)$ with respect to z.

4.10.2 Proof of Lemma 4.5.2

Given the minimum path loss inside the typical BS sector is $Z_1 = z$, the conditional success probability to detect the BS providing the minimum path loss is:

$$\begin{aligned}
&\mathbb{P}(\mathrm{SINR}_{SS}(z) > \Gamma_{cs}) \\
&\overset{(a)}{=} \exp\left(-\frac{\Gamma_{cs} z \sigma^2}{P M_{cs} G(2\pi/N_{cs})}\right) \mathbb{E}\left[\exp(-\Gamma_{cs} z \sum_{x_i^L \in \Phi_L \cap S_1 \cap B^c(o, l_L^{-1}(z))} F_i^L / l_L(x_i^L))\right] \\
&\quad \times \mathbb{E}\left[\exp(-\Gamma_{cs} z \sum_{x_j^N \in \Phi_N \cap S_1 \cap B^c(o, l_N^{-1}(z))} F_j^N / l_N(x_j^N))\right] \\
&\overset{(b)}{=} \exp\left(-\frac{\Gamma_{cs} z \sigma^2}{P M_{cs} G(2\pi/N_{cs})}\right) \mathbb{E}\left[\prod_{x_i^L \in \Phi_L \cap S_1 \cap B^c(o, l_L^{-1}(z))} \frac{l_L(x_i^L)}{l_L(x_i^L) + \Gamma_{cs} z}\right] \\
&\quad \times \mathbb{E}\left[\prod_{x_j^N \in \Phi_N \cap S_1 \cap B^c(o, l_N^{-1}(z))} \frac{l_N(x_j^N)}{l_N(x_j^N) + \Gamma_{cs} z}\right],
\end{aligned}$$

where (a) is from the expression of $\mathrm{SINR}_{SS}(z)$ in (4.10), and (b) is because all the fadings variables are i.i.d. exponentially distributed with parameter 1. Therefore, $\tilde{P}_{M_{cs},N_{cs}}(z, \Gamma_{cs})$ can be obtained by applying the probability generating functional of the PPP [44]. Finally, the overall detection probability of the typical BS sector is obtained by de-conditioning on z.

4.10.3 Proof of Lemma 4.5.4

Note that if the typical user is unable to detect a certain BS sector, the BSs inside this sector can be seen as infinitely far away from the typical user, or equivalently having an infinite path loss. Therefore, $Z_0 \geq z_0$ is equivalent to the fact that for any BS sector, either this sector cannot be detected, or

this sector is detected and the minimum path loss from the typical user to BSs inside this sector is greater than or equal to z_0. For the typical BS sector, the above events happen with the following probability:

$$\begin{aligned}
&\mathbb{P}(Z_1 \geq z_0 | \mathrm{SINR}_{SS}(Z_1) \geq \Gamma_{cs}) \times \mathbb{P}(\mathrm{SINR}_{SS}(Z_1) \geq \Gamma_{cs}) + \mathbb{P}(\mathrm{SINR}_{SS}(Z_1) < \Gamma_{cs}) \\
=&\mathbb{P}(Z_1 \geq z_0 \cap \mathrm{SINR}_{SS}(Z_1) \geq \Gamma_{cs}) + 1 - \mathbb{P}(\mathrm{SINR}_{SS}(Z_1) \geq \Gamma_{cs})] \\
=&\int_0^{\infty} \mathbb{1}_{z_1 \geq z_0} \mathbb{P}(\mathrm{SINR}_{SS}(z_1) \geq \Gamma_{cs}) f_{Z_1}(z_1) \mathrm{d}z_1 + 1 - P_{M_{cs},N_{cs}}(\Gamma_{cs}) \\
=&P_{M_{cs},N_{cs}}(z_0, \Gamma_{cs}) + 1 - P_{M_{cs},N_{cs}}(\Gamma_{cs}),
\end{aligned} \tag{4.22}$$

where Z_1 denotes the minimum path loss from typical user to BSs inside the typical BS sector. Finally, we can obtain (4.14) since the detection events for the BS sectors are independent from each other, and $Z_0 \geq z_0$ is equivalent to (4.22) is satisfied by all BS sectors.

4.10.4 Proof of Lemma 4.5.5

Since the association from the typical user to the tagged BS is stationary [132], the mean associated cell size of the tagged BS is given by: $\frac{1.28}{\lambda}$. In particular, the factor of "1.28" is due to the fact that the association cell of the tagged BS is an area-biased version to that of a typical BS [132], whose accuracy has been verified in [133]. Since each user randomly chooses its RA preamble sequence out of N_{PA} total sequences, and the receive beamwidth of the tagged BS is $\frac{2\pi}{M_{ra}}$, the probability that a user associated with the tagged BS collides with the typical user for random access is $\frac{1}{N_{PA}M_{ra}}$. As will be demonstrated in Remark 4.5.4, the user process during random access can be

accurately modeled by a stationary PPP with intensity $\lambda_u \hat{P}_{M_{cs},N_{cs}(\Gamma_{cs})}$. Therefore, the proof can be concluded from the void probability of the PPP [44].

4.10.5 Proof of Lemma 4.5.6

Without loss of generality, denote the location of the tagged BS by x_0, and assume the first transmit beam of the typical user and the m-th ($1 \leq m \leq M_{ra}$) receive beam of the tagged BS are aligned. Since RA preamble sequences are randomly chosen, the users with the same RA preamble as the typical user form a PPP with intensity $\lambda_u \frac{\hat{P}_{M_{cs},N_{cs}}(\Gamma_{cs})}{N_{PA}}$, which is denoted by $\Phi_u^{'}$. Depending on whether the link to the tagged BS with distance r is LOS or not, the users in $\Phi_u^{'}$ are further divided into two non-homogeneous PPPs $\Phi_{u,L}^{'}$ and $\Phi_{u,N}^{'}$, with the intensities being $\lambda_u \frac{\hat{P}_{M_{cs},N_{cs}}(\Gamma_{cs})}{N_{PA}} h(r)$ and $\lambda_u \frac{\hat{P}_{M_{cs},N_{cs}}(\Gamma_{cs})}{N_{PA}} (1-h(r))$ respectively.

When the typical user and the tagged BS are beam aligned, the SINR of the typical user's RA preamble sequence at the tagged BS is given by:

$$\begin{aligned}
&\mathrm{SINR}_{PA}(Z_0) \\
=&\frac{F_0 M_{ra} G(\frac{2\pi}{N})/Z_0}{\sum\limits_{u_i^L \in \Phi_{u,L}^{'} \cap S(x_0, \frac{2(m-1)\pi}{M_{ra}}, \frac{2m\pi}{M_{ra}})} \frac{F_i^L (G(\frac{2\pi}{N})\delta_i^L + g(\frac{2\pi}{N})(1-\delta_i^L))}{l_L(\|u_i^L - x_0\|)} + \sum\limits_{u_j^N \in \Phi_{u,N}^{'} \cap S(x_0, \frac{2(m-1)\pi}{M_{ra}}, \frac{2m\pi}{M_{ra}})} \frac{F_j^N (G(\frac{2\pi}{N})\delta_j^N + g(\frac{2\pi}{N})(1-\delta_j^N))}{l_N(\|u_j^N - x_0\|)} + \frac{\sigma^2}{P_u}},
\end{aligned} \tag{4.23}$$

where F_0, F_i^L and F_j^N represent the Rayleigh fading channels from the users to the tagged BS. In addition, δ_i^L (δ_j^N) is equal to 1 if the main lobe of u_i^L (u_j^N) covers the tagged BS and 0 otherwise. For the first three initial access protocols in Table 4.2, the transmit beam directions for the users in $\Phi_u^{'}$ are

decided from the cell search phase, which are assumed to be independent and uniformly distributed with $\mathbb{E}[\delta_i^L] = \mathbb{E}[\delta_j^N] = \frac{1}{N}$ for $\forall i, j$. For the omni RX protocol, δ_i^L (δ_j^N) is 1 if the beam direction of $u_i^L(u_j^N)$ is the same as the typical user, which has beamwidth $\frac{2\pi}{N}$. Since all the fading variables are i.i.d. exponentially distributed, the PGFL of PPP can be applied to (4.23) similar to Lemma 4.5.2, which completes the proof.

4.10.6 Proof of Lemma 4.6.1

Since $\mathbb{P}(\text{SINR}_{DL} \geq T | e_0\delta_0 = 1) = \frac{\mathbb{P}(\text{SINR}_{DL} \geq T \cap e_0\delta_0 = 1)}{\eta_{IA}}$, we will focus on the derivation of $\mathbb{P}(\text{SINR}_{DL} \geq T \cap e_0\delta_0 = 1)$. Without loss of generality, we assume the n-th receive beam of the typical user and the m-th transmit beam of the tagged BS are aligned during data transmission. We denote by $S_i \triangleq S(o, \frac{2\pi(i-1)}{K_{cs}}, \frac{2\pi i}{K_{cs}})$ the i-th BS sector for $1 \leq i \leq K_{cs}$. Note that during data transmission, the typical user is able to receive from the BSs inside $S(o, \frac{2\pi(n-1)}{N}, \frac{2\pi n}{N})$ under its main lobe. Therefore, there are $q = \frac{K_{cs}}{N}$ BS sectors within $S(o, \frac{2\pi(n-1)}{N}, \frac{2\pi n}{N})$, which are denoted by $\tilde{S}_1, \tilde{S}_2, ..., \tilde{S}_q$, with $\tilde{S}_i = S(o, \frac{2\pi(n-1)}{N} + \frac{2\pi(i-1)}{K_{cs}}, \frac{2\pi(n-1)}{N} + \frac{2\pi i}{K_{cs}})$ for $1 \leq i \leq q$.

Among all the BS sectors, we denote by $S_{i_1}, S_{i_2}, ..., S_{i_k}$ the sectors that are detected during cell search, where $1 \leq k \leq K_{cs}$. In addition, we assume $S_{i_1}, S_{i_2}, ..., S_{i_s}$ are among $\tilde{S}_1, \tilde{S}_2, ..., \tilde{S}_q$, where $\max(1, k - K_{cs} + q) \leq s \leq \min(q, k)$. Given k and s, we can obtain that there are: (1) $\binom{N}{1}$ choices for receive beam direction of typical user; (2) $\binom{q}{1}$ choices for the BS sector containing the tagged BS among $\tilde{S}_1$ to $\tilde{S}_q$; (3) $\binom{q-1}{s-1}$ number of combinations for

the other $s-1$ detected BS sectors among $\tilde{S}_1$ to $\tilde{S}_q$; and (4) $\binom{K_{cs}-q}{k-s}$ number of combinations for the detected BS sectors that are not among $\tilde{S}_1$ to $\tilde{S}_q$. Thus we have the following relation:

$$\begin{aligned}
&\mathbb{P}(\mathrm{SINR}_{DL} \geq \Gamma \cap e_0\delta_0 = 1) \\
=&\int_0^\infty \sum_{k=1}^{K_{cs}} \sum_{s=\max(1,k-K_{cs}+q)}^{\min(q,k)} \binom{N}{1}\binom{K_{cs}-q}{k-s}\binom{q}{1}\binom{q-1}{s-1}\mathbb{P}(\mathrm{SINR}_{DL} \geq \Gamma \cap A) \\
&\times P^{k-s}_{M_{cs},N_{cs}}(z,\Gamma_{cs})(1-P_{M_{cs},N_{cs}}(\Gamma_{cs}))^{K_{cs}-q-k+s} f_{Z_1}(z)\mathrm{d}z, \qquad (4.24)
\end{aligned}$$

where z in the integration represents the path loss from the typical user to the tagged BS. In addition, A denotes the event that among $\tilde{S}_1$ to $\tilde{S}_q$, S_{i_1} contains the tagged BS which the typical user is successfully connected to, S_{i_2} to S_{i_s} are detected during cell search, while the rest are not detected. From the definition of A, it is easy to obtain that:

$$\begin{aligned}
\mathbb{P}(A) =&\tilde{P}_{M_{cs},N_{cs}}(z,\Gamma_{cs}) \times P_{co} \times P_{ra}(z,\Gamma_{ra}) \times P^{s-1}_{M_{cs},N_{cs}}(z,\Gamma_{cs}) \\
&\times (1-P_{M_{cs},N_{cs}}(\Gamma_{cs}))^{q-s}. \qquad (4.25)
\end{aligned}$$

Since random access is an uplink procedure which does not dependent on the BS process given z, SINR_{DL} can be expressed as follows given event A happens:

$$\mathrm{SINR}_{DL} = \frac{P_b M G(\frac{2\pi}{N}) F_0 / z}{I_1 + I_2 + I_3 + I_4 + \sigma^2}, \qquad (4.26)$$

where:

$$I_1 = \sum_{x_i^L \in \Phi_L \cap (\cup_{j=1}^{s} S_{i_j}) \cap B^c(o, l_L^{-1}(z))} P_b M G(\frac{2\pi}{N}) F_i^L \delta_i^L / l_L(\|x_i^L\|) + \sum_{x_i^N \in \Phi_N \cap (\cup_{j=1}^{s} S_{i_j}) \cap B^c(o, l_N^{-1}(z))} P_b M G(\frac{2\pi}{N}) F_i^N \delta_i^N / l_N(\|x_i^N\|),$$

$$I_2 = \sum_{x_i^L \in \Phi_L \cap (S(o,\frac{2\pi(i-1)}{K_{cs}},\frac{2\pi i}{K_{cs}}) \setminus (\cup_{j=1}^{s} S_{i_j}))} P_b MG(\frac{2\pi}{N}) F_i^L \delta_i^L / l_L(\|x_i^L\|) + \sum_{x_i^N \in \Phi_N \cap (S(o,\frac{2\pi(i-1)}{K_{cs}},\frac{2\pi i}{K_{cs}}) \setminus (\cup_{j=1}^{s} S_{i_j}))} P_b MG(\frac{2\pi}{N}) F_i^N \delta_i^N / l_N(\|x_i^N\|),$$

$$I_3 = \sum_{x_i^L \in \Phi_L \cap (\cup_{j=s+1}^{k} S_{i_j}) \cap B^c(o, l_L^{-1}(z))} P_b Mg(\frac{2\pi}{N}) F_i^L \delta_i^L / l_L(\|x_i^L\|) + \sum_{x_i^N \in \Phi_N \cap (\cup_{j=s+1}^{k} S_{i_j}) \cap B^c(o, l_N^{-1}(z))} P_b Mg(\frac{2\pi}{N}) F_i^N \delta_i^N / l_N(\|x_i^N\|),$$

$$I_4 = \sum_{x_i^L \in \Phi_L \setminus (S(o,\frac{2\pi(i-1)}{K_{cs}},\frac{2\pi i}{K_{cs}}) \cup (\cup_{j=s+1}^{k} S_{i_j}))} P_b Mg(\frac{2\pi}{N}) F_i^L \delta_i^L / l_L(\|x_i^L\|) + \sum_{x_i^N \in \Phi_N \setminus (S(o,\frac{2\pi(i-1)}{K_{cs}},\frac{2\pi i}{K_{cs}}) \cup (\cup_{j=s+1}^{k} S_{i_j}))} P_b Mg(\frac{2\pi}{N}) F_i^N \delta_i^N / l_N(\|x_i^N\|). \tag{4.27}$$

I_1 and I_2 (I_3 and I_4) represent the interference from BSs that user receives under its main lobe (side lobe), which come from the BS sectors that are detected and not detected during cell search respectively. In (4.27), F_0, F_i^L, and F_i^N represent the exponential fading variables. The indicators δ_i^L and δ_i^N in (4.27) represent whether the transmit beam direction of the interfering BS covers the typical user or not, which happens with probability $\frac{1}{M}$. Therefore, based on (4.26) and (4.27), as well as the PGFL of PPPs, we can derive the following result:

$$\begin{aligned}
&\mathbb{P}(\mathrm{SINR}_{DL} > \Gamma | A) \\
=&\exp\left(-\frac{\Gamma z \sigma^2}{P_b MG(\frac{2\pi}{N})}\right)\left(V(z,\Gamma,\frac{\lambda}{MK_{cs}})\right)^{s}\left(U(z,\Gamma,\frac{\lambda}{MK_{cs}})\right)^{q-s} \\
&\times\left(V(z,\frac{g(2\pi/N)}{G(2\pi/N)}\Gamma,\frac{\lambda}{MK_{cs}})\right)^{k-s}\left(U(z,\frac{g(2\pi/N)}{G(2\pi/N)}\Gamma,\frac{\lambda}{MK_{cs}})\right)^{K_{cs}-q-k+s}.
\end{aligned} \tag{4.28}$$

For $\forall a, b, c, d \in \mathbb{R}$, we have:

$$\begin{aligned}
&(a+b)^{q-1}(c+d)^{K_{cs}-q} \\
=&\sum_{m=0}^{K_{cs}-q}\sum_{l=0}^{q-1}\binom{K_{cs}-q}{m}\binom{q-1}{l}a^l b^{q-1-l} c^m d^{K_{cs}-q-m}
\end{aligned}$$

$$\overset{(a)}{=}\sum_{k=1}^{K_{cs}}\sum_{s=\max(1,k-K_{cs}+q)}^{\min(q,k)}\binom{K_{cs}-q}{k-s}\binom{q-1}{s-1}a^{s-1}b^{q-s}c^{k-s}d^{K_{cs}-k-q+s}, \quad (4.29)$$

where (a) is obtained by letting $k = m+l+1$ and $s = l+1$. Finally, the proof is concluded by substituting (4.25), (4.28) and (4.29) into (4.24).

4.10.7 Proof of Lemma 4.7.1

In order to succeed the BRP, the typical user needs to succeed IA and detect the BRRS from the tagged BS. Denote by Z_1 the path loss from the typical user to tagged BS, and A the event that for every BS sector other than S_1, it is either not detected during cell search, or the path loss from BSs inside this sector to the typical user is larger than Z_1. Given the path loss from the typical user to the tagged BS, BRP is independent of event A. Since $\eta_{IA} = \mathbb{P}(e_0\delta_0 = 1)$, we only need to derive the joint success probability of IA and BRP. When the typical user and tagged BS are beam aligned, the SINR of synchronization signal and BRRS are:

$$\mathrm{SINR}_{SS} = \frac{F_0/Z_1}{\sum\limits_{x_i^L\in\Phi_L\cap S_1}\frac{F_i^L\mathbb{1}_{\|x_i^L\|\geq l_L^{-1}(Z_1)}}{l_L(\|x_i^L\|)}+\sum\limits_{x_j^N\in\Phi_N\cap S_1}\frac{F_j^N\mathbb{1}_{\|x_j^N\|\geq l_N^{-1}(Z_1)}}{l_N(\|x_j^N\|)}+\frac{\sigma^2}{P_bM_{cs}N_{cs}}},$$

$$\mathrm{SINR}_{BRRS} = \frac{\tilde{F}_0/Z_1}{\sum\limits_{x_i^L\in\Phi_L\cap \tilde{S}_1}\frac{\tilde{F}_i^L\mathbb{1}_{\|x_i^L\|\geq l_L^{-1}(Z_1)}}{l_L(\|x_i^L\|)}+\sum\limits_{x_j^N\in\Phi_N\cap \tilde{S}_1}\frac{\tilde{F}_j^N\mathbb{1}_{\|x_j^N\|\geq l_N^{-1}(Z_1)}}{l_N(\|x_j^N\|)}+\frac{\sigma^2}{P_bMN}},$$

where F_0, F_i^L, F_j^N, $\tilde{F}_0$, $\tilde{F}_i^L$, and $\tilde{F}_j^N$ represent the independent Rayleigh fading channels. By applying the probability generating functional of PPP [2], we

can derive that the conditional BRP success probability is:

$$\begin{aligned} H(z_0, \Gamma_B) \triangleq & \mathbb{P}(\mathrm{SINR}_{BRRS} > \Gamma_B | \mathrm{SINR}_{SS} > \Gamma_{cs}, Z_1 = z_0) \\ = & \exp(-\frac{\Gamma_B z_0 \sigma^2}{P_b MN}) \times \frac{W(z_0, \Gamma_B, \Gamma_{cs}, \frac{\lambda}{M}, 1)}{V(z_0, \Gamma_{cs}, \frac{\lambda}{M})}. \end{aligned} \tag{4.30}$$

We know from Theorem 4.5.7 that $\mathbb{P}(\mathrm{SINR}_{SS} > \Gamma_{cs} | Z_1 = z_0) = G_{M_{cs},N_{cs}}(z, \Gamma_{cs})$, $\mathbb{P}(A | Z_1 = z_0) = \tilde{P}_{M_{cs},N_{cs}}(z_0, \Gamma_{cs})^{K_{cs}-1}$, and RA is successful with probability $\tilde{P}_{ra}(z_0, \Gamma_{ra})$. Since BRP is independent of A and RA given Z_1, this proof can be concluded by de-conditioning on the distribution of Z_1.

Chapter 5

Directional Cell Search Delay in Cellular Networks with Slow Mobility

The initial access performance for mmWave cellular networks has been investigated under a high mobility scenario in Chapter 4. In contrast to high mobility, a slow mobile network where the BS and user locations are relatively fixed through very long period of time, is also a common and important application scenario for cellular networks. The fixed BS and user locations under the slow mobility scenario will introduce strong temporal correlations for the SINR experienced by a user or BS at different time, as opposed to the high mobility scenario where SINR at user or BS is independent across time. This renders the performance of slow mobility networks fundamentally different from its high mobility counterpart. In this chapter, we will analyze the cell search delay performance for cellular network with slow mobility, where a directional initial access protocol similar to Chapter 4 is adopted.

5.1 Related Works

In the traditional LTE system, the transmissions and receptions during initial access are performed omni-directionally [8]. However, such conven-

tional omni-directional initial access scheme is not suitable for the emerging 5G cellular networks, including the the mmWave cellular networks [95–98,134], as well as the massive MIMO networks [135–139] or full-dimensional (FD) MIMO networks [140–142] that operates in the sub-6 GHz bands. By contrast, the directional initial access scheme which leverages beam-sweeping to achieve extra directive gain, has been recognized as a useful method to ensure reasonable initial access performance for these emerging network scenarios [4,128,139,143–145]. Specifically, the necessity for directional initial access in mmWave cellular networks has been well motivated in Section 4. For the massive MIMO system with M antennas at the BS, an effective array gain of M can be achieved when the channel state information (CSI) has been correctly estimated and is available at the BS [139]. However, since the CSI is unavailable when a new user initiates cell search and random access to the network, there is no such array gain for initial access operations [145]. As a result, the traditional omnidirectional transmissions/receptions for initial access will significantly shorten the coverage range of the BSs as opposed to when CSI is available, and the new users may be unable to join the system due to the lack of the array gain [139,144,145]. In order to overcome this issue, [145] has proposed to use beamsweeping for control channel operations including cell search, where M non-overlapping beams with an array gain of M are sweeped through to provide the complete spatial coverage. This design has been implemented and verified on a sub-6 GHz massive MIMO prototype [145], but the analytical directional cell search performance has not been investigated for

the slow mobility networks from a system level perspective.

The performance for slow mobile Poisson networks has typically been studied through the local delay metric [90, 146–149]. Specifically, local delay characterizes the number of time slots for the SINR of the typical user's packet to exceed certain SINR level. In [90, 146], the local delay for ad-hoc networks with slow mobility is found to have infinite mean delay under several standard scenarios such as Rayleigh fading with constant noise. A phase transition is identified for the interference limited case in terms of the mean local delay, such that it is finite when certain parameters are above a threshold, and infinite otherwise. The local delay for noise-limited and interference-limited Poisson networks is also investigated in [147], which shows power control is essential to keep the mean local delay finite. Several power control policies are proposed in [148] to minimize local delay in a static noise limited network. By adopting a nearest neighbor distance based power control policy, the expected local delay is also shown to be finite [149]. Despite local delay performance for slow mobile networks has been well understood, the previous works mainly focused on the omni-directional communications which cannot be applied to the directional cell search method for emerging 5G cellular networks.

5.2 Contributions

In this chapter, we will analyze the cell search delay performance in a slow mobile cellular networks where a synchronous beam sweeping pattern is applied at the BSs during cell search. Since the BS and user locations are

fixed over a relative long period of time, there exists a strong correlation of the SINR experienced by the user/BS across time, which is fundamentally different from the high mobility scenario considered in Chapter 4. The main contributions in this chapter are summarized as follows:

- For any arbitrary BS locations and fading distribution, the expected number of initial access cycles required to succeed in cell search is proved to be decreasing almost surely when the number of BS antennas/beams is multiplied by a factor of $m > 1$.

- For PPP distributed BSs and Rayleigh fading channels, a closed-form expression is derived for the expected number of initial access cycles required to succeed in cell search, and the corresponding expected cell search delay. Based on this result, the following observations are obtained:

  1. Under the noise limited scenario, we have proved that as long as the path loss exponent for NLOS path is larger than 2, the mean cell search delay is infinity, irrespective of the BS transmit power and BS antenna number.

  2. Under the interference limited scenario, there exists a phase transition for cell search delay in terms of the BS antenna number M. Specifically, the mean cell search delay is infinite when M is smaller than a critical value and finite otherwise, where this critical value depends on both path loss exponent and the SINR detection threshold for synchronization signal.

- The conditional mean cell search delay of a typical user given its nearest BS distance has been derived for PPP distributed BSs and Rayleigh fading

channels, based on which the cell search delay distribution can be evaluated numerically. For the noise limited scenario, we have shown through numerical results that increasing BS antenna number M significantly reduces the cell search delay for cell edge users. By contrast, the cell search delay of median users first decreases then increases as M increases.

Overall, this chapter has proved that the expected cell search delay could be infinite due to the temporal correlations under the slow mobility scenario. As a result, key system parameters including the number of BS antennas and/or BS intensity need to be carefully designed, such that reasonable cell search delay performance can be achieved for the slow mobile networks.

5.3 System Model

In this section, we describe the proposed directional initial access protocol, location models, propagation assumptions, and the performance metrics.

5.3.1 Directional Initial Access Protocol

We consider a time-division duplex (TDD) cellular system as shown in Fig. 5.1, where the system time is divided into different IA cycles with period T, and τ denotes the OFDM symbol period. Each IA cycle begins with a cell search phase, followed by the random access phase and the data transmission phase, similar to Chapter 4.

A large dimensional antenna array with M antennas is assumed at each

BS to support highly directional communications. For analytical tractability, we assume the actual antenna pattern is approximated by a sectorized beam pattern, where the antenna gain is constant within the main lobe. In addition, we assume a 0 side lobe gain for the BS, which is feasible because the BS uses large dimensional antenna array with narrow beams, and modern BS antenna design could enable a front-to-back ratio larger than 30 dB [130]. Each BS supports analog beamforming with a maximum of M possible BF vectors, where the m-th ($1 \leq m \leq M$) beamforming (BF) vector corresponds to the main-lobe, which has antenna gain M, and covers a sector area with angle $[2\pi\frac{m-1}{M}, 2\pi\frac{m}{M})$ [123]. Each user is assumed to have single omni-directional antenna with unit gain.

In the cell search phase, each BS sweeps through all the M transmit beamforming directions to broadcast the synchronization signals, and each user is able to detect a BS (with sufficiently small miss detection probability such as 1%) if the signal-to-interference-plus-noise ratio (SINR) of the synchronization signal from that BS exceeds Γ_{cs}. All BSs transmit synchronously using the same beam direction during every symbol, and the cell search delay within each IA cycle is therefore $T_{cs} = M \times \tau$. When every BS transmits using the m-th ($1 \leq m \leq M$) BF direction, the typical user can only receive from the BSs located inside the following "BS sector":

$$S(o, \frac{2\pi(m-1)}{M} + \pi, \frac{2\pi m}{M} + \pi), \tag{5.1}$$

where we define an infinite sector domain centered at $u \in \mathbb{R}^2$ as:

$$S(u, \theta_1, \theta_2) = \{x \in \mathbb{R}^2, \text{ s.t., } \angle(x - u) \in [\theta_1, \theta_2)\}. \tag{5.2}$$

There are M such non-overlapping BS sectors during cell search, with the j-th $(1 \leq j \leq M)$ sector being $S(o, \frac{2\pi(j-1)}{M}, \frac{2\pi j}{M})$. We say a BS sector is detected during cell search if the typical user is able to detect the BS that provides the smallest path loss inside this sector, where the path loss can be estimated from the beam reference signals [102]. After cell search, the typical user selects the BS with the smallest path loss among all the detected BS sectors as its serving BS.

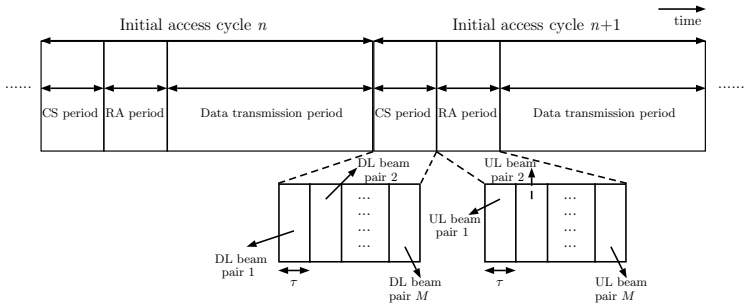

Figure 5.1: Illustration of two cycles for the timing structure.

In the random access phase, the user initiates the connection to its serving BS by transmitting a RA preamble sequence, which is uniformly selected from N_{pa} orthogonal preamble sequences. BSs will sweep through all M receive beamforming directions synchronously to detect users. A contention based random access process is adopted, and a user can be discovered by its serving BS if there is no RA preamble collision with other users, and the

Table 5.1: Notation and Simulation Parameters

Symbol	Definition	Simulation Value
Φ, λ	BS PPP and intensity	$\lambda = 100$ BS/km^2
Φ_u, λ_u	User PPP and intensity	$\lambda_u = 1000$ users/km^2
P_b, P_u	BS and user transmit power	30 dBm, 23 dBm
f_c, B	Carrier frequency and system bandwidth	$(f_c, B) = (73, 1)$ GHz, $(2, 0.2)$ GHz
W	Total thermal noise power	-174 dBm/Hz $+$ $10\log_{10}(B)$
M	Number of BS antennas and BF directions supported at each BS	
N_{pa}	Number of random access preamble sequences	64
α_L, α_N	Path loss exponents for dual-slope model	$(2.1, 3.3)$, $(4, 4)$
C_L, C_N	Path loss at close-in reference distance for dual-slope model	69.71 dB, 38.46 dB
R_c	Critical distance for dual-slope path loss model	50m
Γ_{cs}, Γ_{ra}	SINR threshold to detect synchronization signal and RA preamble	-4 dB, -4 dB
τ	OFDM symbol period	14.3 μs
T	Initial access cycle period	20 ms
$S_M(i)$	i-th BS sector, i.e., $S_M(i) = \{x \in \mathbb{R}^2, \text{ s.t., } \angle x \in [2\pi\frac{(i-1)}{M}, 2\pi\frac{i}{M})\}$	
$\{x_0^i\}_{i=1}^M$	BS providing the smallest path loss to the typical user inside $S_M(i)$	
$B(x,r)$ $(B^o(x,r))$	Closed (open) ball with center x and radius r	

SINR of its preamble sequence exceeds Γ_{ra}. A user is connected to its serving BS upon successful random access, and the BS beamforming direction is determined as the receive beamforming direction for the RA preamble of this user. According to Fig. 5.1, the random access delay within each IA cycle is $T_{ra} = M \times \tau$.

5.3.2 Spatial Locations and Propagation Models

The BS locations are assumed to form the realization of a stationary point process $\Phi = \{x_i\}_i$ with intensity λ. The user locations are modeled as the realization of a homogeneous PPP with intensity λ_u, which is denoted by $\Phi_u = \{u_i\}_i$. The slow mobility scenario is investigated in this chapter, where the BSs are static, and the users are either static or move with very slow speed such as the pedestrian speed. As a result, the BS and user locations

appear to be fixed across different initial access cycles. This is different from the high mobility scenario investigated in Chapter 4, which assumes the users and random blockers are moving with highway speeds, such that the BS and user locations are independently re-shuffled across every initial access cycles. We will prove later that the cell search delay under the slow mobility scenario is fundamentally different from the high mobility scenario.

The transmit power of BSs and users are denoted by P and P_u respectively. Without loss of generality, we can analyze the performance of a typical user u_0 located at the origin. This is guaranteed by Slivnyak's theorem, which states that the property observed by the typical point of a PPP Φ' is the same as that observed by an additional point located at origin in the process $\Phi' \cup \{o\}$ [43, 44].

A dual-slope, non-decreasing path loss function [150] is adopted, such that the path loss for a link with distance r is given by:

$$l(r) = \begin{cases} C_L r^{\alpha_L}, & \text{if } r < R_C, \\ C_N r^{\alpha_N}, & \text{if } r \geq R_C. \end{cases} \tag{5.3}$$

The dual slope path loss model is able to capture the dependency of the path loss exponent on the link distance for various network scenarios, including ultra-dense networks [150] and mmWave networks [121]. In particular, (5.3) is referred to as the LOS ball blockage model for mmWave networks [150], wherein α_L and α_N represent the LOS and NLOS path loss exponents, and C_L and C_N represent the path loss at a close-in reference distance (e.g., 1 meter). We focus on the scenario where $\alpha_N \geq \max(\alpha_L, 2)$. If $\alpha_L = \alpha_N = \alpha$

and $C_L = C_N = C$, the dual slope path loss model reverts to the standard single-slope path loss model.

Due to the adopted antenna pattern for BSs, the directivity gain between BS and user is M when BS beam is aligned with the user, and 0 otherwise. The fading effect for every BS-user link is modeled by an i.i.d. random variable, whose complementary cumulative distribution function (CCDF) is a decreasing function $G(\cdot)$ with support $[0, \infty)$. In addition, we assume the IA cycle length is such that the fading random variable for every link is also i.i.d. across different cycles.

5.3.3 Performance Metrics

The main performance metrics to investigate in this chapter is the cell search delay, which quantifies the delay for the typical user to discover its neighboring BSs and determine a potential serving BS.

Without loss of generality, IA cycle 1 in Fig. 5.1 represents the first IA cycle of the typical user. Denote by $e_M(n)$ and $\delta_M(n)$ the success indicator for cell search and random access of IA cycle n. The number of IA cycles for the typical user to succeed cell search and IA are therefore $L_{cs}(M, \lambda) = \inf\{n \geq 1 : e_M(n) = 1\}$ and $L_{IA}(M, \lambda, \lambda_u) = \inf\{n \geq 1 : e_M(n)\delta_M(n) = 1\}$ respectively. Since analog beamforming is adopted at each BS, the cell search delay and initial access delay can be defined as follows:

$$\begin{aligned} D_{cs}(M, \lambda) &= (L_{cs}(M, \lambda) - 1)T + M\tau, \\ D_{IA}(M, \lambda, \lambda_u) &= (L_{IA}(M, \lambda, \lambda_u) - 1)T + 2M\tau. \end{aligned} \tag{5.4}$$

5.4 Analysis for Cell Search Delay

In this section, we will present the analytical model for deriving cell search delay, and investigate the mean cell search delay under various network scenarios.

5.4.1 Cell Search Delay Under General BS Deployment and Fading Assumptions

In this part, we investigate the cell search delay under a general BS location model (not necessarily PPP) and fading distribution. According to Section 5.3, the BS and user locations are fixed, and the fading variables for every link are i.i.d. across IA cycles. Therefore, given the BS process Φ, the cell search success indicator $e_M(n)$ is an i.i.d. Bernoulli random variable for different IA cycles, and the cell search success probability is denoted by $\pi_M(\Phi) = \mathbb{E}\left[e_M(1)|\Phi\right]$.

Since each BS sector can be independently detected given Φ, and cell search is successful if at least one BS sector is detected, the cell search success probability for every IA cycle is:

$$\pi_M(\Phi) = 1 - \prod_{i=1}^{M} \left[1 - \mathbb{E}\left[\hat{e}_M(i)|\Phi\right]\right], \tag{5.5}$$

where $\hat{e}_M(i)$ denotes the indicator that the BS providing the smallest path loss inside BS sector i is detected. Specifically, if we denote by $S_M(i) \triangleq S(o, \frac{2\pi(i-1)}{M}, \frac{2\pi i}{M})$ the BS sector i, x_0^i the BS providing the smallest path loss to the typical user in $\Phi \cap S_M(i)$, and $\{F_j^i\}$ the fading random variables from BSs

in $S_M(i)$ to the typical user, we have:

$$\mathbb{E}\left[\hat{e}_M(i)|\Phi\right] = \mathbb{P}\Bigg(\frac{F_0^i/l(\|x_0^i\|)}{\sum\limits_{x_j^i\in\Phi\cap S_M(i)\setminus\{x_0^i\}} F_j^i/l(\|x_j^i\|)+W/PM} > \Gamma_{cs}\Bigg|\Phi\Bigg) \tag{5.6}$$

$$= \mathbb{E}\Bigg[G\Bigg(\Gamma_{cs}l(\|x_0^i\|)(\sum_{x_j^i\in\Phi\cap S_M(i)\setminus\{x_0^i\}} F_j^i/l(\|x_j^i\|)+W/PM)\Bigg)\Bigg|\Phi\Bigg], \tag{5.7}$$

where the expectation in (5.7) is taken with respect to the i.i.d. fading random variables $\{F_j^i\}$.

In the following theorem, we derive the mean number of IA cycles for the typical user to succeed the cell search under the Palm expectation of the user process, i.e., $\mathbb{E}^0_{\Phi_u}[L_{cs}(M,\lambda)|\Phi]$. Specifically, the Palm expectation of $L_{cs}(M,\lambda)$ is equal to the empirical average of $L_{cs}(M,\lambda)$ seen by a large number of users located within a large circular area. We will show later that since there will exist a certain fraction of cell edge users requiring a very large number of IA cycles to succeed in cell search, the mean of $L_{cs}(M,\lambda)$ could be infinity under the Palm expectation. For notational simplicity, we will use $\mathbb{E}$ to also denote the Palm expectation for the rest of this chapter.

Theorem 5.4.1. *The mean number of IA cycles needed for the typical user to succeed the cell search is given by:*

$$\mathbb{E}[L_{cs}(M,\lambda)|\Phi] = \frac{1}{1-\prod_{i=1}^{M}\left[1-\mathbb{E}\left[\hat{e}_M(i)|\Phi\right]\right]}, \tag{5.8}$$

$$\mathbb{E}[L_{cs}(M,\lambda)] = \mathbb{E}_\Phi\left[\frac{1}{1-\prod_{i=1}^{M}\left[1-\mathbb{E}\left[\hat{e}_M(i)|\Phi\right]\right]}\right]. \tag{5.9}$$

Proof. The first part can be proved by the fact that given Φ, $L_{cs}(M,\lambda)$ follows the geometric distribution with success probability $\pi_M(\Phi)$; while the second part follows by taking the expectation of (5.8) with respect to Φ. $\square$

A lower bound and upper bound to $\mathbb{E}[L_{cs}(M,\lambda)]$ can immediately be obtained from (5.9), which are provided in the following remarks.

Remark 5.4.1. By applying Jensen's inequality to a positive random variable X and function $f(x)=\frac{1}{x}$, we know that $\mathbb{E}[\frac{1}{X}] \geq \frac{1}{\mathbb{E}[X]}$. Thus a lower bound to $\mathbb{E}[L_{cs}(M,\lambda)]$ is given by:

$$\mathbb{E}[L_{cs}(M,\lambda)] \geq \frac{1}{1-\mathbb{E}\left[\prod_{i=1}^{M}\left[1-\mathbb{E}\left[\hat{e}_M(i)|\Phi\right]\right]\right]}, \tag{5.10}$$

where the equality holds when the BS locations are independent across different IA cycles from the typical user's perspective, i.e., the high mobility scenario considered in [143].

Since $\mathbb{E}\left[\hat{e}_M(i)|\Phi\right] > 0$ almost surely according to (5.7), $\mathbb{E}[L_{cs}(M,\lambda)]$ will be finite under the high mobility scenario. In fact, we will show in the rest of this section that $\mathbb{E}[L_{cs}(M,\lambda)]$ behaves differently under the slow mobility scenario, in that $\mathbb{E}[L_{cs}(M,\lambda)]$ could be infinite under certain network settings.

Remark 5.4.2. If we denote by x_0 the BS providing the smallest path loss to the typical user, and i^* the index for the BS sector that contains x_0, then $\prod_{j=1}^{M}\left[1-\mathbb{E}\left[\hat{e}_M(j)|\Phi\right]\right] \leq 1-\mathbb{E}\left[\hat{e}_M(i^*)|\Phi\right]$. Therefore, an upper bound to $\mathbb{E}[L_{cs}(M,\lambda)]$ is given by:

$$\mathbb{E}[L_{cs}(M,\lambda)] \leq \mathbb{E}\left[\frac{1}{\mathbb{E}\left[\hat{e}_M(i^*)|\Phi\right]}\right]. \tag{5.11}$$

Based on Theorem 5.4.1, we can prove the following relation between the BS antenna/beam number M and $\mathbb{E}[L_{cs}(M,\lambda)]$.

Lemma 5.4.2. *Given a realization of BS locations Φ, the mean number of IA cycles to succeed cell search satisfies that $\mathbb{E}[L_{cs}(M_2,\lambda)|\Phi] < \mathbb{E}[L_{cs}(M_1,\lambda)|\Phi]$, if $M_2 = mM_1$ with m being an integer larger than 1.*

Proof. The proof is provided in Appendix 5.7.1. □

Lemma 5.4.2 shows that for any BS location model and fading distribution, the conditional number of IA cycles for cell search to succeed decreases when the number of BS antenna/beams is multiplied by m, or equivalently when the BS beamwidth is divided by m. This result also implies that $\mathbb{E}[L_{cs}(M_2,\lambda)] \leq \mathbb{E}[L_{cs}(M_1,\lambda)]$ if $M_2 = mM_1$. However, besides the simple ordering relation in Lemma 5.4.2, Theorem 5.4.1 does not provide a general framework to compute the value of $\mathbb{E}[L_{cs}(M,\lambda)]$ in closed form. For the rest of this section, we will investigate the mean cell search delay under several specific network scenarios.

5.4.2 Mean Cell Search Delay in Poisson Networks with Rayleigh Fading

In this part, the BS locations are assumed to be the realization of a homogeneous PPP with intensity λ, and the fading random variables are assumed to be exponentially distributed with unit mean (i.e., $G(x) = \exp(-x)$). Due to its high analytical tractability, this network setting has been widely

adopted to obtain the fundamental design insights for conventional macro and heterogeneous cellular networks [2,22], ultra-dense cellular networks [150], and even mmWave cellular networks[1] [125, 143].

Due to the PPP assumption for BSs, and the fact that different BS sectors are non-overlapping, every BS sector can therefore be detected independently with the same probability. Since the path loss function $l(r)$ is non-decreasing, the BS that provides the minimum path loss to the typical user inside i-th BS sector $\Phi \cap S_M(i)$ (i.e., x_0^i) is the closest BS to the origin. The angle of x_0^i is uniformly distributed within $[2\pi(i-1)/M, 2\pi i/M)$, and the CCDF for the norm of x_0^i can be derived as follows:

$$\mathbb{P}(\|x_0^i\| \geq r) = \mathbb{P}\left(\min_{x \in \Phi \cap S_M(i)} \|x\| \geq r\right) = \exp(-\frac{\lambda \pi r^2}{M}), \tag{5.12}$$

where the second equality follows from the void probability for PPPs. Therefore, the probability distribution function (PDF) for $\|x_0^i\|$ is given by:

$$f_{\|x_0^i\|}(r) = \frac{2\lambda \pi r}{M} \exp(-\frac{\lambda \pi r^2}{M}). \tag{5.13}$$

By applying $\Phi \sim \text{PPP}(\lambda)$ and $G(x) = \exp(-x)$ into (5.7), the conditional detection probability for the i-th BS sector is given by:

$$\mathbb{E}\left[\hat{e}_M(i)|\Phi\right] = \mathbb{E}\left[\exp\left(-\Gamma_{cs} l(\|x_0^i\|)\left(\sum_{x_j^i \in \Phi \cap S_M(i) \setminus \{x_0^i\}} F_j^i / l(\|x_j^i\|) + W/PM\right)\right)\middle|\Phi\right]$$

[1]The SINR and rate trends for mmWave networks under Rayleigh fading and PPP configured BSs have been shown to be close to more realistic fading assumptions, such as the Nakagami fading or log-normal shadowing [125].

$$= \exp\left(-\frac{W\Gamma_{cs} l(\|x_0^i\|)}{PM}\right)\mathbb{E}\left[\prod_{x_j^i \in \Phi \cap S_M(i)\setminus\{x_0^i\}} \exp\left(-\Gamma_{cs} l(\|x_0^i\|)F_j^i / l(\|x_j^i\|)\right)\right]$$

$$\stackrel{(a)}{=} \exp\left(-\frac{W\Gamma_{cs} l(\|x_0^i\|)}{PM}\right) \prod_{x_j^i \in \Phi \cap S_M(i)\setminus\{x_0^i\}} \frac{1}{1+\Gamma_{cs} l(\|x_0^i\|)/l(\|x_j^i\|)} \triangleq F_M(i,\Phi), \tag{5.14}$$

where step (a) is obtained by taking the expectation w.r.t. the fading random variables.

Theorem 5.4.3. *If BS process $\Phi \sim PPP(\lambda)$, and the fading variable is exponentially distributed with unit mean, the mean number of cycles for cell search to succeed is:*

$$\mathbb{E}[L_{cs}(M,\lambda)] = \sum_{j=0}^{\infty} A_j^M, \tag{5.15}$$

where $A_j = \mathbb{E}[(1-F_M(1,\Phi))^j]$, which is given by:

$$A_j = \int_0^\infty \left\{ \sum_{k=0}^{j} (-1)^k \binom{j}{k} \exp\left(-\frac{Wk\Gamma_{cs} l(r_1)}{PM}\right) \exp\left(-\frac{2\pi\lambda}{M}\int_{r_1}^{\infty}\left(1- \frac{1}{(1+\Gamma_{cs} l(r_1)/l(r))^k}\right) r\mathrm{d}r\right)\right\} \frac{2\lambda\pi r_1}{M}\exp(-\frac{\lambda\pi r_1^2}{M})\mathrm{d}r_1. \tag{5.16}$$

Proof. The proof is provided in Appendix 5.7.2. □

Remark 5.4.3. Theorem 5.4.3 can be interpreted as:

$$\mathbb{E}[L_{cs}(M,\lambda)] = \sum_{j=0}^{\infty} \mathbb{P}(L_{cs}(M,\lambda) > j),$$

with A_j^M in (5.15) representing the probability that all the BS sectors are unable to be detected within j IA cycles, i.e., $\mathbb{P}(L_{cs}(M,\lambda) > j)$.

Theorem 5.4.3 provides a series-expansion form expression to compute the expected number of IA cycles to succeed cell search. However, it is unclear whether $\mathbb{E}[L_{cs}(M,\lambda)]$ is finite or not. Therefore, we will investigate the finiteness of $\mathbb{E}[L_{cs}(M,\lambda)]$ under two typical network scenarios, namely the noise limited scenario and the interference limited scenario.

5.4.2.1 Noise limited Scenario

In the noise limited scenario, we assume the noise power dominates the interference power (or interference power is perfectly canceled), such that only noise power needs to be taken into account. Compared to the conventional micro-wave cellular network, the mmWave network has much higher noise power due to the wider bandwidth, and the interference power is much smaller due to the high isotropic path loss in mmWave. As a result, the mmWave cellular network is typically noise limited, especially when the carrier frequency and system bandwidth are high enough (e.g. 73 GHz carrier frequency with 500 MHz bandwidth) [119, 121].

Since the interference power is zero under the noise limited scenario, Theorem 5.4.3 becomes:

$$\mathbb{E}[L_{cs}(M,\lambda)] = \sum_{j=0}^{\infty}\left\{\int_0^{\infty}\left(1-\exp\left(-\frac{W\Gamma_{cs}l(r_1)}{PM}\right)\right)^j \frac{2\lambda\pi r_1}{M}\exp(-\frac{\lambda\pi r_1^2}{M})\mathrm{d}r_1\right\}^M. \tag{5.17}$$

Through change of variable ($v = \lambda r^2$), (5.17) becomes

$$\mathbb{E}[L_{cs}(M,\lambda)] = \sum_{j=0}^{\infty}\left\{\int_0^{\infty}\left(1-\exp\left(-\frac{W\Gamma_{cs}l(\sqrt{(v/\lambda)})}{PM}\right)\right)^j \frac{2\pi}{M}\exp(-\frac{\pi v}{M})\mathrm{d}v\right\}^M, \tag{5.18}$$

which shows that $\mathbb{E}[L_{cs}(M,\lambda)]$ is non-increasing as the BS intensity λ increases. In the next two lemmas, we will prove that the finiteness for $\mathbb{E}[L_{cs}(M,\lambda)]$ depends on the NLOS path loss exponent α_N, and a phase transition for $\mathbb{E}[L_{cs}(M,\lambda)]$ happens when $\alpha_N = 2$.

Lemma 5.4.4. *Under the noise limited scenario, for any finite number of BS antennas M and BS intensity λ, $\mathbb{E}[L_{cs}(M,\lambda)] = \infty$ whenever the NLOS path loss exponent $\alpha_N > 2$.*

Proof. The proof is provided in Appendix 5.7.3. □

According to Lemma 5.4.4, the expected cell search delay is infinity whenever $\alpha_N > 2$, which cannot be alleviated by BS densification (i.e., increase λ), or using higher number of BS antennas (i.e., increase M). The reason can be explained from (5.29), which shows that due to the PPP-configured BS deployment, the typical user could locate at the "cell edge" with its closest BS inside every BS sector farther than some arbitrarily large distance v. There is $\exp(-\lambda\pi v^2)$ fraction of such cell edge users, and the corresponding number of IA cycles required for them to succeed cell search is at least $\exp(Cv^{\alpha_N})$ for some $C > 0$. Therefore, the expected cell search delay averaged over all the users will ultimately be infinite since $\alpha_N > 2$. From a system level perspective,

this indicates that for noise limited network with $\alpha_N > 2$, there will always be a significant fraction of cell edge users requiring very large number of IA cycle to succeed cell search, such that the average cell search delay perceived by all users will be crushed by these cell edge users, i.e., an infinite average cell search delay is observed.

Lemma 5.4.5. *Under the noise limited scenario with NLOS path loss exponent $\alpha_N = 2$, the expected number of IA cycles to succeed cell in search $\mathbb{E}[L_{cs}(M,\lambda)] = \infty$ if BS density λ and BS antenna number M satisfy that $\lambda M < \frac{\Gamma_{cs} C_N W}{P\pi}$, and $\mathbb{E}[L_{cs}(M,\lambda)] < \infty$ if $\lambda M > \frac{\Gamma_{cs} C_N W}{P\pi}$, i.e., the phase transition for $\mathbb{E}[L_{cs}(M,\lambda)]$ happens at (λ^*, M^*) with $\lambda^* M^* = \frac{\Gamma_{cs} C_N W}{P\pi}$.*

Proof. The proof is provided in Appendix 5.7.4. □

We can observe from the proof to Lemma 5.4.5 that for any arbitrarily large distance r_0, there is $\exp(-\lambda\pi r_0^2)$ fraction of cell edge users whose nearest BSs are farther than r_0, and the number of IA cycles for these edge users to succeed cell search scales as $\exp(\frac{W\Gamma_{cs} C_N r_0^2}{PM})$. As a result, if the BS deployment is too sparse or the number of BS antennas/beams is too small such that $\lambda M < \frac{\Gamma_{cs} C_N W}{P\pi}$, the average cell search delay perceived by all the users becomes infinity due to the cell edge users. By contrast, under network densification, the fraction of cell edge users with bad conditions is reduced, and the average cell search delay can be reduced to a finite value whenever $\lambda M > \frac{\Gamma_{cs} C_N W}{P\pi}$. Similar behavior happens when the BSs are using more antennas to increase the SNR for the cell edge users.

To summarize, for the noise limited scenario such as mmWave networks, the cell search delay distribution is heavy-tailed due to the common BS locations across different IA cycles. In particular, the mean cell search delay is infinite whenever the NLOS path loss exponent $\alpha_N > 2$, which is typically the case for mmWave. However, the mean cell search delay when $\alpha_N = 2$ could switch from infinity to a finite value through careful network design, such as BS densification or adopting more BS antennas.

5.4.2.2 Interference limited Scenario

In the interference limited scenario, the noise power is dominated by the interference power, or the noise power is perfectly canceled, such that we can assume $W = 0$. In particular, conventional micro-wave cellular networks which communicate below 6 GHz, are typically interference limited. In this part, we investigate the cell search delay in sub 6 GHz network with standard single slope path loss function $l(r) = Cr^{\alpha}$, which is suitable for networks with sparsely deployed BSs as opposed to the ultra-dense networks [150].

First, we prove that Theorem 5.4.3 can be greatly simplified under the interference limited scenario.

Lemma 5.4.6. *The expected number of initial access cycles required for cell search to succeed under the interference limited scenario is given by:*

$$\mathbb{E}[L_{cs}(M)] = \sum_{j=0}^{\infty} \left(\sum_{k=0}^{j} \frac{(-1)^k \binom{j}{k}}{1 + 2\int_1^{+\infty} (1 - (1 + \Gamma_{cs}/r^{\alpha})^{-k}) r \mathrm{d}r} \right)^M. \tag{5.19}$$

Proof. The proof is provided in Appendix 5.7.5. □

We can observe from Lemma 5.4.6 that $\mathbb{E}[L_{cs}(M)]$ does not depend on the BS intensity under the interference limited scenario. This is because the increase/decrease of signal power can be perfectly counter-effected by the increase/decrease of interference power in the interference limited network [2]. Another immediate observation from Lemma 5.4.6 is that A_j is independent of the number of the BS antennas M for $\forall j$. As a result, $\mathbb{E}[L_{cs}(M)]$ is monotonically non-increasing with respect to M, which is a stronger observation than Lemma 5.4.2.

Remark 5.4.4. If $\alpha = 2$, Lemma 5.4.6 directly shows that $\mathbb{E}[L_{cs}(M)] = \infty$ for $\forall M$. This is mainly because the interference power will dominate the signal power when $\alpha = 2$, such that the coverage probability is 0 for any SINR threshold Γ_{cs}.

In fact, we can prove that, for the interference limited scenario with $\alpha > 2$, there may exist a phase transition for $\mathbb{E}[L_{cs}(M)]$ in terms of the BS beam number M. In order to show that, we will first apply Remark 5.4.2 and obtain a sufficient condition to guarantee the finiteness for $\mathbb{E}[L_{cs}(M)]$.

Lemma 5.4.7. *Under the interference limited scenario with path loss exponent $\alpha > 2$, the expected number of IA cycles to succeed cell search $\mathbb{E}[L_{cs}(M)] < \infty$ whenever the number of BS beams $M > \frac{2\Gamma_{cs}}{\alpha-2}$, where Γ_{cs} denotes the detection threshold for a BS. In particular, when $M = 1$, i.e., the BS is omni-directional, $\mathbb{E}[L_{cs}(1)]$ is finite if and only if $\alpha > 2\Gamma_{cs} + 2$.*

Proof. The proof is provided in Appendix 5.7.6. □

Remark 5.4.5. According to Remark 5.4.4, Lemma 5.4.6 and Lemma 5.4.7, the number of IA cycles to succeed in cell search (i.e., $\mathbb{E}[L_{cs}(M)]$) may have a phase transition in terms of the number of BS beams M, depending on the relation between the path loss exponent α and detection threshold Γ_{cs}.

- If $\alpha > 2 + 2\Gamma_{cs}$, $\mathbb{E}[L_{cs}(M)] < \infty$ for the omni-directional BS antenna case, i.e., $M = 1$. By the monotonicity of $\mathbb{E}[L_{cs}(M)]$ with respect to M, $\mathbb{E}[L_{cs}(M)]$ is guaranteed to be finite for any $M \geq 1$.

- If $\alpha \leq 2 + 2\Gamma_{cs}$, we know that $\mathbb{E}[L_{cs}(M)] = \infty$ for $M = 1$, and $\mathbb{E}[L_{cs}(M)] < \infty$ if $M > \frac{2\Gamma_{cs}}{\alpha - 2}$. Therefore, according to the monotonicity of $\mathbb{E}[L_{cs}(M)]$, there exists a phase transition of $M^* \in [2, \frac{2\Gamma_{cs}}{\alpha-2}]$, such that $\mathbb{E}[L_{cs}(M)] = \infty$ for $M \leq M^*$, and $\mathbb{E}[L_{cs}(M)] < \infty$ for $M > M^*$. In particular, $\mathbb{E}[L_{cs}(M)] = \infty$ for $\forall M$ if $\alpha = 2$, which means $M^* = \infty$.

The path loss exponent α depends on the propagation environment, and $\alpha = 2$ corresponds to a free space LOS scenario; while α increases as the environment becomes relatively more lossy and scatter-rich, such as urban and suburban areas. In addition, the SINR detection threshold Γ_{cs} depends on the receiver decoding capability, which is typically within -10 dB and 0 dB [109].

Remark 5.4.5 shows that in a lossy environment with $\alpha > 2 + 2\Gamma_{cs}$, the typical user can detect a nearby BS in a finite number of IA cycles on average. This is because the relative strength of the useful signal with respect to the interfering signals is strong enough. However, when $\alpha \leq 2 + 2\Gamma_{cs}$, $\mathbb{E}[L_{cs}(M)]$ could be exploded due to the cell edge users that require very high number

of IA cycles to succeed cell search. Specifically, the cell edge user has poor coverage and SIR performance because it is located at a position where there exist other BSs, at a distance similar to that of its potential serving BS. When M is very small (e.g., $M = 1$), there is a significant fraction of such cell edge users, so the corresponding cell search delay averaged over all users becomes infinity. However, as M increases, the BS beam sweeping will create enough angular separation so that the nearby BSs to the edge user could locate in different BS sectors. As a result, $L_{cs}(M)$ is significantly decreased for the cell edge users as M increases, and therefore the phase transition for $\mathbb{E}[L_{cs}(M)]$ happens.

In summary, for interference limited networks, we can always ensure the network to be in a desirable condition with finite mean cell search delay, by tuning the number of BS beams/antennas M appropriately.

5.4.3 Cell Search Delay Distribution in Poisson Networks with Rayleigh Fading

The previous part is mainly focused on the expected number of IA cycles to succeed cell search $\mathbb{E}[L_{cs}(M, \lambda)]$, or the cell search delay equivalently through (5.4). However, due to the large fraction of cell edge users requiring significantly high number of IA cycles for cell search, $\mathbb{E}[L_{cs}(M, \lambda)]$ is infinity under several settings. In this section, we will focus on obtaining the cell search delay distribution, and investigate the cell search delay performance for the 95^{th} percentile, 50^{th} percentile, and 10^{th} percentile users, which correspond to

the cell center, median, and cell edge users respectively.

We investigate the cell search delay distribution through deriving the expected number of IA cycles to succeed in cell search, given the distance from the typical user to its closest BS R_0, i.e., $\mathbb{E}[L_{cs}(M,\lambda)|R_0]$. In fact, $\mathbb{E}[L_{cs}(M,\lambda)|R_0]$ is a random variable with mean $\mathbb{E}[L_{cs}(M,\lambda)]$. According to (5.4), we will evaluate the empirical distribution of the following conditional expected cell search delay in this section:

$$D_{cs}(R_0,M,\lambda) \triangleq (\mathbb{E}[L_{cs}(M,\lambda)|R_0]-1)T + M\tau. \tag{5.20}$$

The main reason to instigate the cell search delay conditional on R_0 is because R_0 measures the location and therefore the signal quality of the typical user. In particular, $R_0 \ll \frac{1}{2\sqrt{\lambda}}$ corresponds to the cell center user, while $R_0 \gg \frac{1}{2\sqrt{\lambda}}$ corresponds to the cell edge user.

In order to derive $\mathbb{E}[L_{cs}(M,\lambda)|R_0]$ in (5.20), we will first derive the following quantity: $\mathbb{E}[L_{cs}(M,\lambda)|R_1,R_2,...,R_M]$, where R_i denotes the distance from the typical user to its closest BS in the i-th BS sector (i.e., $R_i = \|x_0^i\|$) for $1 \le i \le M$.

Lemma 5.4.8. *Given the distances from the typical user to its nearest BSs inside every BS sector $R_1,...,R_M$, the mean number of IA cycles for cell search is:*

$$\mathbb{E}[L_{cs}(M,\lambda)|R_1,R_2,...,R_M] = \sum_{j=0}^{\infty}\prod_{i=1}^{M} f_j(R_i,M,\lambda), \tag{5.21}$$

where $f_j(R_i)$ denotes the probability that x_0^i is detected in at least j IA cycles, which is:

$$f_j(R_i, M, \lambda) = \sum_{k=0}^{j} (-1)^k \binom{j}{k} \exp\left(-\frac{Wk\Gamma_{cs} l(R_i)}{PM}\right) \times \exp\left(-\frac{2\lambda\pi}{M} \int_{R_i}^{\infty} (1 - \frac{1}{(1+\Gamma_{cs} l(R_i)/l(r))^k}) r \mathrm{d}r\right).$$

We can first use the tower property for conditional expectations to prove $\mathbb{E}[L_{cs}(M,\lambda)|R_1, R_2, ..., R_M] = \mathbb{E}[\mathbb{E}[L_{cs}(M,\lambda)|\Phi]|R_1, R_2, ..., R_M]$. The rest of the proof follows similar steps to Theorem 5.4.3, and therefore we omit the details.

We will need the following corollary to derive $\mathbb{E}[L_{cs}(M,\lambda)|R_0]$ from $\mathbb{E}[L_{cs}(M,\lambda)|R_1, R_2, ..., R_M]$.

Corollary 5.4.9. *For all i.i.d. non-negative random variables R_1, R_2,...,R_M with CCDF $G(r)$, and all functions $F : [0,\infty)^M \to [0,\infty)$ which are symmetric, the following relation is true:*

$$\mathbb{E}[F(R_1, R_2, ..., R_M)| \min(R_1, R_2, ..., R_M) = r] = \frac{\mathbb{E}[F(r, R_2, ..., R_M)\mathbb{1}_{\{R_j > r, \forall j \neq 1\}}]}{(G(r))^{M-1}}. \tag{5.22}$$

Proof. The proof is provided in Appendix 5.7.7. □

By taking $F(R_1, R_2, ..., R_M) = \mathbb{E}[L_{cs}(M,\lambda)|R_1, R_2, ..., R_M]$ in Corollary 5.4.9, $\mathbb{E}[L_{cs}(M,\lambda)|R_0]$ can directly obtained as follows.

Lemma 5.4.10. *Given the distance from the typical user to the nearest BS R_0, the mean number of IA cycles to succeed cell search is:*

$$\mathbb{E}[L_{cs}(M,\lambda)|R_0] = \sum_{j=0}^{\infty} f_j(R_0,M,\lambda)\left\{\int_{R_0}^{\infty} f_j(r,M,\lambda)\frac{\lambda 2\pi r}{M}\exp(-\frac{\lambda\pi r^2}{M})\mathrm{d}r\right\}^{M-1} \times \exp\left(\frac{\lambda\pi(M-1)R_0^2}{M}\right),$$

where the function $f_j(r,M,\lambda)$ is defined in Lemma 5.4.8.

Lemma 5.4.10 provides a method to evaluate the cell search delay distribution under a general setting, which cannot be further simplified. However, for the noise limited networks and interference limited networks, we can obtain the following simple result.

Corollary 5.4.11. *For a noise limited scenario, $\mathbb{E}[L_{cs}(M,\lambda)|R_0]$ is given by:*

$$\begin{aligned}&\mathbb{E}[L_{cs}(M,\lambda)|R_0]\\ &= \begin{cases} \sum_{j=0}^{\infty}(1-\exp(-\frac{\Gamma_{cs}WC_N R_0^{\alpha_N}}{PM}))^j\{\int_{R_0}^{\infty}(1-\exp(-\frac{\Gamma_{cs}WC_N r^{\alpha_N}}{PM}))^j \\ \times\frac{\lambda 2\pi r}{M}\exp(-\frac{\lambda\pi r^2}{M})\mathrm{d}r\}^{M-1}\exp(\lambda\pi\frac{M-1}{M}R_0^2), & \text{if } R_0 \geq R_c, \\ \sum_{j=0}^{\infty}(1-\exp(-\frac{\Gamma_{cs}WC_L R_0^{\alpha_L}}{PM}))^j\{\int_{R_C}^{\infty}(1-\exp(-\frac{\Gamma_{cs}WC_N r^{\alpha_N}}{PM}))^j \\ \times\frac{\lambda 2\pi r}{M}\exp(-\frac{\lambda\pi r^2}{M})\mathrm{d}r + \int_{R_0}^{R_C}(1-\exp(-\frac{\Gamma_{cs}WC_L r^{\alpha_L}}{PM}))^j \\ \times\frac{\lambda 2\pi r}{M}\exp(-\frac{\lambda\pi r^2}{M})\mathrm{d}r\}^{M-1}\exp(\lambda\pi\frac{M-1}{M}R_0^2), & \text{if } R_0 < R_c. \end{cases}\end{aligned} \tag{5.23}$$

Corollary 5.4.11 can be easily proved from Lemma 5.4.10 and the fact that interference power is 0.

Corollary 5.4.12. *Under the interference limited scenario and the standard single-slope path loss model with path loss exponent $\alpha > 2$, $\mathbb{E}[L_{cs}(M)|R_0]$ is*

given by:

$$\mathbb{E}[L_{cs}(M)|R_0] = \sum_{j=0}^{\infty}\left\{\sum_{k=0}^{j}(-1)^k\binom{j}{k}\exp\left(-\frac{2\pi\lambda R_0^2 H(k,\alpha,\Gamma_{cs})}{M}\right)\right\} \times\left\{\sum_{k=0}^{j}\frac{(-1)^k\binom{j}{k}\exp\left(-\frac{2\pi\lambda R_0^2 H(k,\alpha,\Gamma_{cs})}{M}\right)}{1+2H(k,\alpha,\Gamma_{cs})}\right\}^{M-1}, \quad (5.24)$$

where $H(k,\alpha,\Gamma_{cs}) = \int_1^{\infty}(1-\frac{1}{(1+\Gamma/r^{\alpha})^k})r\mathrm{d}r$.

Proof. The proof is provided in Appendix 5.7.8. □

5.5 Numerical Evaluations for Cell Search Delay Distribution in Noise Limited Networks

For the noise limited networks, we have proven that the expected cell search delay is infinite whenever the NLOS path loss exponent is greater than 2. Therefore, the cell search delay distribution is numerically evaluated in this section. Specifically, we consider a mmWave cellular network operating at $f_c = 73$ GHz with bandwidth $B = 2$ GHz, and the BS intensity is $\lambda = 100$ BS/km^2. The path loss exponents for LOS and NLOS links are 2.1 and 3.3 respectively, and the critical distance $R_c = 50$m. In addition, the IA cycle length is chosen as $T = 20$ ms, and the OFDM symbol period $\tau = 14.3$ μs [102, 143].

Fig. 5.2 plots the empirical CCDF of the cell search delay $D_{cs}(R_0, M, \lambda)$, which is obtained by generating 10^5 realizations of R_0 and computing the corresponding cell search delay through Corollary 5.4.11. We can observe

from Fig. 5.2 that under the log-log scale, the tail distribution function of $D_{cs}(R_0, M, \lambda)$, i.e., $\mathbb{P}(D_{cs}(R_0, M, \lambda) \geq t)$, decreases almost linearly with respect to t. This validates the fact that the cell search delay is indeed heavy-tailed. It can also be observed from Fig. 5.2 that the decrease rate for the tail distribution function satisfies $\lim_{t\to\infty} \frac{-\log \mathbb{P}(D_{cs}(R_0,M,\lambda)\geq t)}{\log t} < 1$ for $M = 4, 8, 18, 36$, which validates Lemma 5.4.4.

In addition, Fig. 5.2 shows that as the number of BS antennas M increases, the tail of $D_{cs}(R_0, M, \lambda)$ becomes lighter and thus the cell search delay for edge users is significantly reduced. For example, the cell search delay for the 10^{th} percentile user is almost 10 times smaller when M increases from 18 to 36. In fact, increasing M will increase the SNR of cell edge users, such that the number of IA cycles required for the edge users to succeed in cell search (i.e., $\mathbb{E}[L_{cs}(M, \lambda)|R_0]$) can be shortened. Since $D_{cs}(R_0, M, \lambda) \triangleq T(\mathbb{E}[L_{cs}(M, \lambda)|R_0] - 1) + M\tau$, and the IA cycle length T is much larger than the OFDM symbol period τ, the tail distribution of $D_{cs}(R_0, M, \lambda)$ therefore becomes lighter as M increases, despite having a higher beam-sweeping overhead within every IA cycle.

Due to the heavy-tail nature for the cell search delay distribution, Fig. 5.2 shows there exists an extremely large variation of the cell search delay performance from cell center users to cell edge users. Fig. 5.3 plots the cell search delay for the 95^{th} percentile users, as the number of BS antennas M increase. Since the 95^{th} percentile users are located at the cell center, they are typically LOS to their serving BSs with sufficiently high isotropic SNR,

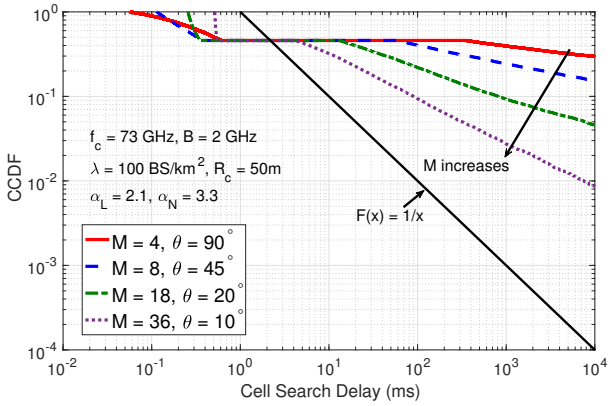

Figure 5.2: Cell search delay distribution for noise limited networks.

and thus they can succeed cell search in the first cycle that they initiates IA. Therefore, as M increases, Fig. 5.3 shows that the cell search delay for the 95$^{\text{th}}$ percentile users increases almost linearly due to the increase of the beam-sweeping overhead.

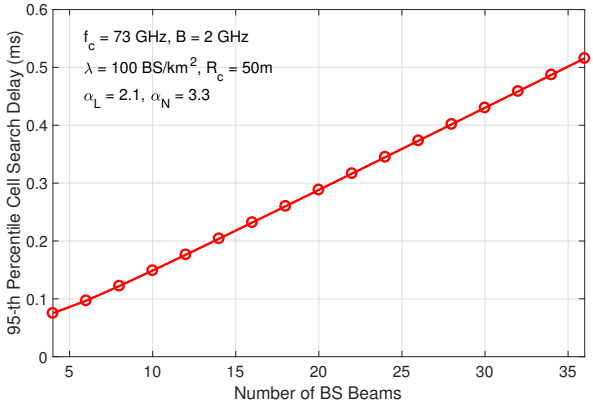

Figure 5.3: 95$^{\text{th}}$ percentile cell search delay for noise limited networks.

The cell search delay performance for the 50$^{\text{th}}$ percentile users, or the median users, is plotted in Fig. 5.4. We can observe that in contrast to the

mean cell search delay which is infinity, the median delay is less than 1 ms for various BS antenna number M. When M is small, median users do not have high enough SNR and thus they will need more than 1 IA cycles to succeed in cell search. As M increases, the cell search delay for median users first decreases due to the improved SNR and cell search success probability, until the median users could succeed cell search in the first cycle that they initiates IA. Then the cell search delay will increase as M is further increased, which is because of the higher beam sweeping overhead within every IA cycle. The optimal BS antenna number M is 12 in Fig. 5.4, which corresponds to a cell search delay of 0.31 ms.

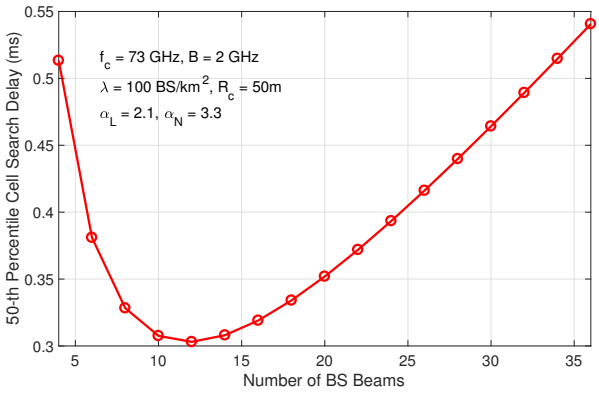

Figure 5.4: 50^{th} percentile cell search delay for noise limited networks.

5.6 Summary

This chapter has proposed a stochastic geometry framework to derive the directional cell search delay for slow mobile cellular networks, where the BS and user locations are fixed for long period of time. Different from the local

delay metric which quantifies the number of cycles for the typical user's SINR from the entire plane to exceed a threshold [90,146], the directional cell search delay is the number of cycles for the maximum SINR that the typical user experiences from non-overlapping BS sectors to exceed a threshold. Given the BS locations, we have first derived the conditional expected cell search delay under the Palm distribution of the user process. By utilizing the Taylor series expansion, we have further derived the exact expression for the overall expected cell search delay in a Poisson cellular network. Base on this expression, the expected cell search delay under noise-limited scenario is shown to be infinite as long as the NLOS path loss exponent is larger than 2. By contrast, a new type of phase transition for the expected cell search delay in interference-limited scenario is proved to exist, such that it is finite when the number of BS beams/antennas is greater than a threshold, and infinite otherwise.

The framework developed in this chapter provides an analytical tool for investigating the spatial-temporal performance of cellular networks. The overall initial access delay, as well as the downlink throughput performance for the slow mobile networks, can be further derived based on this framework.

5.7 Appendix

5.7.1 Proof of Lemma 5.4.2

Since $M_2 = mM_1$, we know that $S_{M_1}(i) = \bigcup_{j=1}^{m} S_{M_2}((i-1)m+j)$ for $1 \leq i \leq M_1$. Denote by x_0^i the BS providing the smallest path loss to the typical user inside $\Phi \cap S_{M_1}(i)$, and assume $x_0^i \in \Phi \cap S_{M_2}((i-1)m+j_0)$ for some

$j_0 \in [1, m]$. Due to the facts that $M_2 > M_1$, $S_{M_2}((i-1)m + j_0) \subsetneq S_{M_1}(i)$, and $G(\cdot)$ is a decreasing function, we can observe from (5.7) that $\mathbb{E}\left[\hat{e}_{M_1}(i)|\Phi\right] < \mathbb{E}\left[\hat{e}_{M_2}((i-1)m + j_0)|\Phi\right]$. Also note that $\mathbb{E}\left[\hat{e}_{M_2}((i-1)m + j)|\Phi\right] > 0$ for $\forall j \neq j_0$ according to (5.7), we have:

$$\prod_{j=1}^{m} \left[1 - \mathbb{E}\left[\hat{e}_{M_2}\left((i-1)m + j\right)|\Phi\right]\right] < 1 - \mathbb{E}\left[\hat{e}_{M_2}(i)|\Phi\right]. \tag{5.25}$$

Thus the cell search success probability for the typical IA cycle will satisfy:

$$\begin{aligned}
\pi_{M_2}(\Phi) &= 1 - \prod_{i=1}^{M_2} \left[1 - \mathbb{E}\left[\hat{e}_{M_2}(i)|\Phi\right]\right] \\
&= 1 - \prod_{i=1}^{M_1} \left(\prod_{j=1}^{m} \left[1 - \mathbb{E}\left[\hat{e}_{M_2}\left((i-1)m + j\right) \middle| \Phi\right]\right]\right) \\
&> 1 - \prod_{i=1}^{M_1} \left[1 - \mathbb{E}\left[\hat{e}_{M_1}(i)|\Phi\right]\right] = \pi_{M_1}(\Phi).
\end{aligned} \tag{5.26}$$

Finally the proof is concluded by applying Theorem 5.4.1.

5.7.2 Proof of Theorem 5.4.3

By substituting (5.14) into Theorem 5.4.1, we can obtain:

$$\begin{aligned}
\mathbb{E}[L_{cs}(M, \lambda)] &= \mathbb{E}\left[\frac{1}{1 - \prod_{i=1}^{M}\left[1 - F_M(i, \Phi)\right]}\right] \\
&\overset{(a)}{=} \mathbb{E}\left[\sum_{j=0}^{\infty}\left(\prod_{i=1}^{M}\left[1 - F_M(i, \Phi)\right]\right)^j\right] \\
&\overset{(b)}{=} \sum_{j=0}^{\infty}\mathbb{E}\left[\left(\prod_{i=1}^{M}\left[1 - F_M(i, \Phi)\right]\right)^j\right] \\
&\overset{(c)}{=} \sum_{j=0}^{\infty}\left\{\mathbb{E}\left[\left(1 - F_M(1, \Phi)\right)^j\right]\right\}^M,
\end{aligned} \tag{5.27}$$

where step (a) is derived from the fact that $\frac{1}{1-x} = \sum_{j=0}^{\infty} x^j$ for $0 \leq x < 1$, step (b) follows from the monotone convergence theorem, and step (c) is because the event for every BS sector to be detected is i.i.d.. Furthermore, we can compute A_j as follows:

$$
\begin{aligned}
&\mathbb{E}\left[\left(1 - F_M(1,\Phi)\right)^j\right] \\
&= \int_0^{\infty} \mathbb{E}\left[\left(1 - F_M(1,\Phi)\right)^j \middle| x_0^1 = (r_1, 0)\right] \frac{2\lambda\pi r_1}{M} \exp(-\frac{\lambda\pi r_1^2}{M}) \mathrm{d}r \\
&\overset{(a)}{=} \int_0^{\infty} \sum_{k=0}^{j} (-1)^k \binom{j}{k} \mathbb{E}_{\Phi}^{x_0^1}\left[\left(F_M(1,\Phi)\right)^k \middle| \Phi \cap S_M(1) \cap B(o, r_1) = 0\right] \\
&\quad \times \frac{2\lambda\pi r_1}{M} \exp(-\frac{\lambda\pi r_1^2}{M}) \mathrm{d}r \\
&\overset{(b)}{=} \int_0^{\infty} \sum_{k=0}^{j} (-1)^k \binom{j}{k} \mathbb{E}\left[\exp\left(-\frac{Wk\Gamma_{cs} l(r_1)}{PM}\right) \prod_{x_j^i \in \Phi \cap S_M(i) \cap B^c(o,r_1)} \frac{1}{(1 + \Gamma_{cs} l(r_1)/l(\|x_j^i\|))^k}\right] \\
&\quad \times \frac{2\lambda\pi r_1}{M} \exp(-\frac{\lambda\pi r_1^2}{M}) \mathrm{d}r, \qquad (5.28)
\end{aligned}
$$

where $\mathbb{E}_{\Phi}^{x_0^1}[\cdot]$ in (a) denotes the expectation under the Palm distribution at x_0^1; and step (b) is derived from the Slivnyak's theorem. Finally the proof can be concluded by applying the probability generating functional (PGFL) of PPP [44] to (5.28).

5.7.3 Proof of Lemma 5.4.4

Given the number of BS sectors M and for any arbitrarily large value $v_0 > 0$ with $v_0 > R_c$, we can re-write (5.17) to obtain the lower upper of

$\mathbb{E}[L_{cs}(M)]$ as follows:

$$\begin{aligned}
&\sum_{j=0}^{\infty}\left\{\int_0^{\infty}\left(1-\exp\left(-\frac{W\Gamma_{cs}l(r_1)}{PM}\right)\right)^j\frac{2\lambda\pi r_1}{M}\exp(-\frac{\lambda\pi r_1^2}{M})\mathrm{d}r_1\right\}^M\\
\overset{(a)}{\geq}&\sum_{j=0}^{\infty}\left\{\int_{v_0}^{\infty}\left(1-\exp\left(-\frac{W\Gamma_{cs}C_Nr_1^{\alpha_N}}{PM}\right)\right)^j\frac{2\lambda\pi r_1}{M}\exp(-\frac{\lambda\pi r_1^2}{M})\mathrm{d}r_1\right\}^M\\
>&\sum_{j=0}^{\infty}\left\{\left(1-\exp\left(-\frac{W\Gamma_{cs}C_Nv_0^{\alpha_N}}{PM}\right)\right)^j\int_{v_0}^{\infty}\frac{2\lambda\pi r_1}{M}\exp(-\frac{\lambda\pi r_1^2}{M})\mathrm{d}r_1\right\}^M\\
=&\sum_{j=0}^{\infty}\left(1-\exp\left(-\frac{W\Gamma_{cs}C_Nv_0^{\alpha_N}}{PM}\right)\right)^{jM}\exp(-\lambda\pi v_0^2)\\
=&\frac{\exp(-\lambda\pi v_0^2)}{1-(1-\exp(-W\Gamma_{cs}C_Nv_0^{\alpha_N}/PM))^M}\\
\overset{(b)}{\geq}&\frac{1}{M}\exp\left(W\Gamma_{cs}C_Nv_0^{\alpha_N}/PM-\lambda\pi v_0^2\right)\overset{v_0\to\infty}{\longrightarrow}\infty,
\end{aligned}\tag{5.29}$$

where $l(r_1)=C_Nr_1^{\alpha_N}$ in step (a) because $r_1\geq v_0>R_c$. Step (b) follows from the fact that for any $0\leq x\leq 1$ and $M\in\mathbb{N}^+$, we have: $(1-x)^M+xM\geq 1$, thus $\frac{1}{1-(1-x)^M}\geq\frac{1}{xM}$. Note that since $\alpha_N>2$, (5.29) goes to infinity when v_0 goes to infinity, which completes the proof.

5.7.4 Proof of Lemma 5.4.5

If $\alpha_N=2$, it is clear from (5.29) that $\mathbb{E}[L_{cs}(M,\lambda)]=\infty$ if $\lambda M<\frac{\Gamma_{cs}C_NW}{P\pi}$. In addition, we can simplify the upper bound to $\mathbb{E}[L_{cs}(M,\lambda)]$ from Remark 5.4.2 under the noise limited scenario, which is given as follows:

$$\begin{aligned}
&\mathbb{E}[L_{cs}(M,\lambda)]\\
\overset{(a)}{\leq}&\int_0^{\infty}\exp\left(\frac{W\Gamma_{cs}l(r_0)}{PM}\right)\lambda 2\pi r_0\exp(-\lambda\pi r_0^2)\mathrm{d}r_0
\end{aligned}$$

$$
\begin{aligned}
&= \int_0^{R_c} \exp\left(\frac{W\Gamma_{cs}C_L r_0^{\alpha_L}}{PM}\right)\lambda 2\pi r_0 \exp(-\lambda\pi r_0^2)\mathrm{d}r_0 + \int_{R_c}^{\infty} \exp\left(\frac{W\Gamma_{cs}C_N r_0^{\alpha_N}}{PM}\right) \\
&\quad \times \lambda 2\pi r_0 \exp(-\lambda\pi r_0^2)\mathrm{d}r_0 \\
&< \exp\left(\frac{W\Gamma_{cs}C_L R_c^{\alpha_L}}{PM}\right)\left(1-\exp(-\lambda\pi R_c^2)\right) + \int_{R_c}^{\infty} \exp\left(\frac{W\Gamma_{cs}C_N r_0^{\alpha_N}}{PM}\right) \\
&\quad \times \lambda 2\pi r_0 \exp(-\lambda\pi r_0^2)\mathrm{d}r_0, \qquad (5.30)
\end{aligned}
$$

where (a) is obtained by applying the noise limited assumption to (5.14), and noting that the BS providing the smallest path loss is the closest BS of Φ to the origin. Since $\alpha_N = 2$, it can be observed from (5.30) that $\mathbb{E}[L_{cs}(M)]$ is guaranteed to have finite mean if $\lambda M > \frac{\Gamma_{cs}C_N W}{P\pi}$.

5.7.5 Proof of Lemma 5.4.6

By substituting $W = 0$ and $l(r) = Cr^{\alpha}$ into (5.16), then A_j defined in (5.16) can be further simplified as follows:

$$
\begin{aligned}
A_j &= \int_0^{\infty} \left\{ \sum_{k=0}^{j} (-1)^k \binom{j}{k} \exp\left(-\frac{2\pi\lambda}{M}\int_{r_1}^{\infty}\left(1-\frac{1}{(1+\Gamma_{cs}r_1^{\alpha}/r^{\alpha})^k}\right)r\mathrm{d}r\right)\right\} \\
&\quad \times \frac{2\lambda\pi r_1}{M}\exp(-\frac{\lambda\pi r_1^2}{M})\mathrm{d}r_1 \\
&= \sum_{k=0}^{j} (-1)^k \binom{j}{k} \left\{ \int_0^{\infty} \exp\left(-\frac{2\pi\lambda r_1^2}{M}\int_{1}^{\infty}\left(1-\frac{1}{(1+\Gamma_{cs}/r^{\alpha})^k}\right)r\mathrm{d}r\right)\right. \\
&\quad \left. \times \frac{2\lambda\pi r_1}{M}\exp(-\frac{\lambda\pi r_1^2}{M})\mathrm{d}r_1 \right\} \\
&= \sum_{k=0}^{j} \frac{(-1)^k \binom{j}{k}}{1+2\int_1^{+\infty}(1-(1+\Gamma_{cs}/r^{\alpha})^{-k})r\mathrm{d}r},
\end{aligned}
$$

which completes the proof.

5.7.6 Proof of Lemma 5.4.7

Denote by x_0 the BS closest to the origin, and $S_M(i^*)$ the BS sector containing x_0, we can obtain an upper bound to $\mathbb{E}[L_{cs}(M)]$ by substituting (5.14) and $W = 0$ into Remark 5.4.2 as follows:

$$\begin{aligned}
\mathbb{E}[L_{cs}(M)] &\leq \mathbb{E}\Bigg[\prod_{x_j \in \Phi \cap S_M(i^*)\setminus\{x_0\}} \Big(1 + \Gamma_{cs} l(\|x_0\|)/l(\|x_j\|)\Big)\Bigg] \\
&\overset{(a)}{=} \int_0^\infty \mathbb{E}\Bigg[\prod_{x_j \in \Phi \cap S_M(i^*) \cap B^c(o,r_0)} \Big(1 + \Gamma_{cs} l(r_0)/l(\|x_j\|)\Big)\Bigg] 2\lambda\pi r_0 \exp(-\lambda\pi r_0^2) \mathrm{d}r_0 \\
&\overset{(b)}{=} \int_0^\infty \exp\left(\frac{2\pi\lambda\Gamma_{cs}}{M} \int_{r_0}^\infty \frac{l(r_0) r}{l(r)} \mathrm{d}r\right) 2\lambda\pi r_0 \exp(-\lambda\pi r_0^2) \mathrm{d}r_0 \\
&\overset{(c)}{=} \int_0^\infty \exp\left(-\left(1 - \frac{2\Gamma_{cs}}{M(\alpha-2)}\right) v\right) \mathrm{d}v \\
&= \begin{cases} \infty, & \text{if } M \leq \frac{2\Gamma_{cs}}{\alpha-2}, \\ \frac{M(\alpha-2)}{M(\alpha-2)-2\Gamma_{cs}}, & \text{if } M > \frac{2\Gamma_{cs}}{\alpha-2}, \end{cases}
\end{aligned} \tag{5.31}$$

where (a) is obtained by noting that x_0 is the closest BS to the origin, (b) follows from the PGFL for the PPP[2], and (c) is derived through change of variables (i.e. $v = \lambda\pi r_0^2$). It can be observed that (5.31) is finite whenever $M > \frac{2\Gamma_{cs}}{\alpha-2}$, which is a sufficient condition for the finiteness of $\mathbb{E}[L_{cs}(M)]$. In particular, the equality holds in the first step of (5.31) when $M = 1$. As a result, $\mathbb{E}[L_{cs}(1)]$ is finite if and only if $\alpha > 2\Gamma_{cs} + 2$.

[2]Note that [45, Theorem 4.9] does not directly apply to the PGFL calculation here since $f(x) = 1 + \Gamma_{cs} l(r_0)/l(x)$ is larger than 1. However, we can use dominated convergence theorem to prove that for PPP Φ with intensity measure $\Lambda(\cdot)$, the PGFL result still holds if function $f(x)$ satisfies $f(x) \geq 1$ and $\int_{\mathbb{R}^2}(f(x) - 1)\Lambda(\mathrm{d}x) < \infty$, i.e. $\mathbb{E}[\prod_{x_i \in \Phi} f(x_i)] = \exp(\int_{\mathbb{R}^2}(f(x) - 1)\Lambda(\mathrm{d}x)$.

5.7.7 Proof of Corollary 5.4.9

Denote by $R_0 = \min(R_1, R_2, ..., R_M)$, then we can obtain (5.22) as follows:

$$\begin{aligned}
&\mathbb{E}[F(R_1, R_2, ..., R_M)|R_0 = r] \\
=&\lim_{\epsilon\to 0} \frac{\mathbb{E}[F(R_1, R_2, ..., R_M) \times \mathbb{1}_{|R_0-r|<\epsilon}]}{\mathbb{P}(|R_0 - r| < \epsilon)} \\
=&\lim_{\epsilon\to 0} \frac{\sum_{i=1}^{M} \mathbb{E}[F(R_1, R_2, ..., R_M) \times \mathbb{1}_{(\{|R_i-r|<\epsilon\}\cap\{R_j>R_i,\forall j\neq i\})}]}{\sum_{k=1}^{M} \mathbb{P}(\{|R_k - r| < \epsilon\} \cap \{R_j > R_k, \forall j \neq k\})} \\
=&\lim_{\epsilon\to 0} \frac{\sum_{i=1}^{M} \mathbb{E}[F(R_1, R_2, ..., R_M)\mathbb{1}_{(\{R_j>R_i,\forall j\neq i\})}||R_i - r| < \epsilon]}{\sum_{k=1}^{M} \mathbb{P}(\{R_j > R_k, \forall j \neq k\}||R_k - r| < \epsilon)} \\
=&\frac{\sum_{i=1}^{M} \mathbb{E}[F(R_1, R_2, ..., R_M)\mathbb{1}_{(\{R_j>R_i,\forall j\neq i\})}|R_i = r]}{\sum_{k=1}^{M} \mathbb{P}(\{R_j > R_k, \forall j \neq k\}|R_k = r)},
\end{aligned}$$

the proof is completed by noting F is symmetric.

5.7.8 Proof of Corollary 5.4.12

Since $W = 0$ and $l(r) = Cr^{\alpha}$, $f_j(R_i, M, \lambda)$ in Lemma 5.4.10 can be simplified as:

$$f_j(R_i, M, \lambda) = \sum_{k=0}^{j} (-1)^k \binom{j}{k} \exp\left(-\frac{2\pi\lambda R_0^2 H(k, \alpha, \Gamma_{cs})}{M}\right). \tag{5.32}$$

Therefore, we can further obtain that:

$$\int_{R_0}^{\infty} f_j(r, M, \lambda) \frac{\lambda 2\pi r}{M} \exp(-\frac{\lambda\pi r^2}{M}) \mathrm{d}r = \sum_{k=0}^{j} (-1)^k \binom{j}{k} \frac{\exp(-\frac{\lambda\pi}{M}(1 + 2H(k, \alpha, \Gamma_{cs}))R_0^2)}{1 + 2H(k, \alpha, \Gamma_{cs})}. \tag{5.33}$$

The proof can be completed by substituting (5.32) and (5.33) into Lemma 5.4.10.

Chapter 6

Conclusions

This dissertation has utilized stochastic geometry to address several challenges in modeling and analyzing the evolution of cellular networks. A first contribution of this dissertation is the development of several new methodologies for the stochastic geometry analysis of cellular networks, including a new tractable analytical framework for determinantal point process based macro cellular network, a new probabilistic framework for the MAC layer analysis of the coexisting cellular network and Wi-Fi network, and new frameworks to analyze the spatial and temporal dynamics of the cellular networks with high mobility and slow mobility respectively. The second contribution, which leverages these new methodologies, is the new system design insights into several practical challenges during the evolution of cellular networks. In the rest of this chapter, we summarize the system design insights obtained from each contribution, and discuss the prospective future works.

6.1 Summary

In Chapter 2, we have proposed to use the soft-core repulsive determinantal point processes as an accurate yet also tractable model for macro

BS locations. The empty space function, the nearest neighbor function, the mean interference, and the SIR distribution for DPP configured macro cellular networks are derived. Based on the Quasi-Monte Carlo integration method, these metrics are numerically evaluated for the Gauss DPP model. By using hypothesis testing methods, DPPs fitted to real macro BS deployments are demonstrated to be accurate in terms of the K function and the coverage probability. Finally, we demonstrate that DPPs have better accuracy than the Poisson point process and the deterministic grid model for macro cellular networks.

In Chapter 3, we have developed a stochastic geometry framework for analyzing the coexistence performance of Wi-Fi network and cellular network, when cellular network operates in the 5 GHz unlicensed spectrum. Three coexistence scenarios are investigated, including cellular with no protocol change, cellular with discontinuous transmission, and cellular with listen-before-talk and random back-off. The medium access probability, SINR coverage probability, density of successful transmission and rate coverage probability have been analytically derived and numerically evaluated for these coexistence scenarios. We have shown that Wi-Fi performance will be significantly degraded when cellular network operates in the unlicensed spectrum with no protocol changes. In order to guarantee a fair coexistence with Wi-Fi, cellular network needs to adopt a short transmission duty cycle, lower channel access priority than Wi-Fi, or more sensitive CCA threshold.

In Chapter 4, we have utilized stochastic geometry to design and ana-

lyze initial access protocol for mmWave cellular networks under the high mobility scenario. For both both the single stage beamforming approach and two stage beamforming approach, unified analytical expressions for the expected initial access delay and average perceived throughput have been derived for three initial access protocols. Among the initial access protocols that are investigated, the baseline exhaustive search protocol is shown to achieve the smallest initial access delay when blockage is severe. The best trade-off between the initial access delay and user-perceived downlink throughput can be achieved by the fast CS protocol, which has low beam-sweeping overhead in cell search. Finally, the two stage beamforming approach is shown to increase the average user-perceived throughput for the baseline protocol over the single stage approach, and it is able to achieve good initial access delay and user-perceived throughput simultaneously by adapting the beam refinement factor.

In Chapter 5, the directional cell search delay performance for slow mobile cellular networks is analyzed using stochastic geometry. In particular, the proposed framework can handle the spatial and temporal correlations of user's SINR process, which is created by the fixed BS an user locations of slow mobile networks. For Poisson network with Rayleigh fading, closed-form expression for the expected cell search delay have be derived. Based on this expression, the expected delay is proved to be infinite for noise limited network (e.g., mmWave network) whenever the NLOS path loss exponent is larger than 2. In addition, the interference limited network is proved to exhibit a phase

transition for the expected cell search delay, such that it is finite when the number of BS antennas is greater than a threshold, and infinite otherwise.

6.2 Future Directions

Based on the stochastic geometry frameworks that have been developed in this dissertation, various performance metrics of the traditional macro cellular networks and emerging 5G cellular networks can be analyzed through a fundamental approach. As cellular networks continue to evolve with more advanced features, stochastic geometry still serves as an important system level analysis tool. However, the advanced network features could also lead to much more challenging stochastic geometry analysis, especially when homogeneous PPP is not the most accurate model for BS/user locations. Motivated by these facts, this dissertation is concluded with two prospective research directions that extends the derived stochastic geometry frameworks.

6.2.1 Multi-point Connectivity Performance in MmWave Cellular Networks

The initial access protocols proposed in Chapter 4 only allow the user to associate with one mmWave BS. However, when the users or blockers are moving, the users will be subject to frequent outages and re-associations if served by only one BS. By enabling the user to associate with multiple mmWave BSs (i.e., multi-point connectivity), better robustness to blockage and faster re-association/handover can be achieved.

Motivated by these observations, we will investigate the performance of multi-point connectivity in mmWave cellular networks from space-time aspects. Specifically, we consider a scenario where BSs and users are fixed, while the mmWave links are subject to random moving obstacles such as cars and pedestrians. During the initial access, each user tries to associate with multiple BSs, among which only one BS serves the user, and others are back-up BSs. In order to model the effects of moving obstacles, a simple Gilbert two-state Markov model for each BS-user link can be used. By leveraging both stochastic geometry and stochastic processes, we propose to investigate the following problems: (1) initial access protocol design to enable multi-point connectivity; (2) stationary distribution of the serving BS for the typical user; (3) duration of coverage for a user in given period with multi-point connectivity; and (4) optimal system parameters such as the number of associated BSs.

6.2.2 Exploration of Analytical Methods with Good Balance Between Accuracy and Simplicity for Non-Poisson Networks

Leveraging stochastic geometry to analyze the SINR distribution in cellular networks can be largely facilitated by modeling the node locations using homogeneous PPP, which is equivalent to assuming complete spatial randomness (CSR) for node locations. However, the CSR assumption neglects the dependencies among node locations in various network scenarios, including the conventional macro cellular networks discussed in Chapter 2, and the CSMA networks discussed in Chapter 3. In fact, an accurate spatial point process to model the dependencies among node locations could lead to very

complicated closed-form SINR coverage expressions, which generally require high computational complexity (e.g., DPPs or Ginibre point process for macro BSs [10,37]). In many scenarios including the modified Matérn hard-core process for CSMA/CA networks [53, 81], such closed-form SINR distribution is even unavailable. From a practical system design perspective, a method that can provide good balance between modeling accuracy and analytical simplicity is desirable.

One promising approach to achieve such balance is through the non-homogeneous PPP approximation, which approximates the interferers by a non-homogeneous PPP, whose intensity function is equal to the conditional intensity of the original point process given the serving transmitter location. This technique has been applied to various scenarios, including the macro cellular networks with DPP distributed BSs [10], the transmitting access points in CSMA/CA networks [53,81], and uplink transmitters in cellular networks [151,152]. The corresponding SINR coverage expressions can be efficiently evaluated as opposed to its closed-form counterparts. However, most of the existing works validate the accuracy of non-homogeneous PPP approximation through simulating limited set of scenarios, while its accuracy in general is still largely unknown. Therefore, a valuable future direction is to investigate the general applicability of non-homogeneous PPP approximation. For example, the accuracy of estimating SINR using non-homogeneous PPP can be validated through comprehensive numerical evaluations for parameterized point processes, such as the Gauss DPP, the Ginibre DPP, the modified Matern hard

core process for CSMA/CA, and the Poisson clustered processes. In summary, a good understanding of when and why non-homogeneous PPP approximation is accurate for certain network scenarios is important for efficient performance evaluation and optimization of practical wireless networks.

Bibliography

[1] S. Mukherjee, *Analytical Modeling of Heterogeneous Cellular Networks*. Cambridge University Press, 2014.

[2] J. Andrews, F. Baccelli, and R. Ganti, "A tractable approach to coverage and rate in cellular networks," *IEEE Transactions on Communications*, vol. 59, no. 11, pp. 3122–3134, Nov. 2011.

[3] Cisco, "Global mobile data traffic forecast update 2014–2019," *White Paper*, Feb. 2015.

[4] J. G. Andrews, S. Buzzi, W. Choi, S. V. Hanly, A. Lozano, A. C. Soong, and J. C. Zhang, "What will 5G be?" *IEEE Journal on Selected Areas in Communications*, vol. 32, no. 6, pp. 1065–1082, Jun. 2014.

[5] F. Boccardi, R. W. Heath, A. Lozano, T. L. Marzetta, and P. Popovski, "Five disruptive technology directions for 5G," *IEEE Communications Magazine*, vol. 52, no. 2, pp. 74–80, Feb. 2014.

[6] Y. Li, F. Baccelli, H. S. Dhillon, and J. G. Andrews, "Fitting determinantal point processes to macro base station deployments," in *2014 IEEE Global Communications Conference (GLOBECOM)*, Dec. 2014, pp. 3641–3646.

[7] T. S. Rappaport, R. W. Heath Jr, R. C. Daniels, and J. N. Murdock, *Millimeter wave wireless communications*. Pearson Education, 2014.

[8] E. Dahlman, S. Parkvall, and J. Skold, *4G: LTE/LTE-advanced for mobile broadband*. Elsevier Science, 2011.

[9] IEEE Std 802.11-2012, "IEEE standard for information technology telecommunications and information exchange between systems local and metropolitan area networks specific requirements part 11: Wireless lan medium access control (MAC) and physical layer (PHY) specifications," Mar. 2012.

[10] Y. Li, F. Baccelli, H. Dhillon, and J. Andrews, "Statistical modeling and probabilistic analysis of cellular networks with determinantal point processes," *IEEE Transactions on Communications*, vol. 63, no. 9, pp. 3405–3422, Sept. 2015.

[11] H. Dhillon, R. Ganti, F. Baccelli, and J. Andrews, "Modeling and analysis of K-tier downlink heterogeneous cellular networks," *IEEE Journal on Selected Areas in Communications*, vol. 30, no. 3, pp. 550–560, Apr. 2012.

[12] H. Dhillon, R. Ganti, and J. Andrews, "Load-aware modeling and analysis of heterogeneous cellular networks," *IEEE Transactions on Wireless Communications*, vol. 12, no. 4, pp. 1666–1677, Apr. 2013.

[13] S. Mukherjee, "Distribution of downlink SINR in heterogeneous cellular networks," *IEEE Journal on Selected Areas in Communications*, vol. 30, no. 3, pp. 575–585, Apr. 2012.

[14] P. Madhusudhanan, J. G. Restrepo, Y. Liu, T. X. Brown, and K. R. Baker, "Multi-tier network performance analysis using a shotgun cellular system," in *IEEE Global Communications Conference*, Dec. 2011, pp. 1–6.

[15] H. ElSawy, E. Hossain, and M. Haenggi, "Stochastic geometry for modeling, analysis, and design of multi-tier and cognitive cellular wireless networks: A survey," *IEEE Communications Surveys and Tutorials*, vol. 15, no. 3, pp. 996–1019, Jun. 2013.

[16] S. Singh, H. S. Dhillon, and J. G. Andrews, "Offloading in heterogeneous networks: Modeling, analysis, and design insights," *IEEE Transactions on Wireless Communications*, vol. 12, no. 5, pp. 2484–2497, May 2013.

[17] S. Singh and J. G. Andrews, "Joint resource partitioning and offloading in heterogeneous cellular networks," *IEEE Transactions on Wireless Communications*, vol. 13, no. 2, pp. 888–901, Feb. 2014.

[18] H. S. Jo, Y. J. Sang, P. Xia, and J. G. Andrews, "Heterogeneous cellular networks with flexible cell association: A comprehensive downlink SINR analysis," *IEEE Transactions on Wireless Communications*, vol. 11, no. 10, pp. 3484–3495, Oct. 2012.

[19] R. Heath, M. Kountouris, and T. Bai, "Modeling heterogeneous network interference using Poisson point processes," *IEEE Transactions on Signal Processing*, vol. 61, no. 16, pp. 4114–4126, Aug. 2013.

[20] P. Madhusudhanan, X. Li, Y. Liu, and T. Brown, "Stochastic geometric modeling and interference analysis for massive MIMO systems," in *International Symposium on Modeling Optimization in Mobile, Ad Hoc Wireless Networks (WiOpt)*, May 2013, pp. 15–22.

[21] A. K. Gupta, H. S. Dhillon, S. Vishwanath, and J. G. Andrews, "Downlink multi-antenna heterogeneous cellular network with load balancing," *IEEE Transactions on Communications*, vol. 62, no. 11, pp. 4052–4067, Nov. 2014.

[22] H. Dhillon, M. Kountouris, and J. Andrews, "Downlink MIMO HetNets: modeling, ordering results and performance analysis," *IEEE Transactions on Wireless Communications*, vol. 12, no. 10, pp. 5208–5222, Oct. 2013.

[23] M. Kountouris and N. Pappas, "HetNets and massive MIMO: modeling, potential gains, and performance analysis," in *IEEE-APS Topical Conference on Antennas and Propagation in Wireless Communications (APWC)*, Sept. 2013, pp. 1319–1322.

[24] T. D. Novlan, H. S. Dhillon, and J. G. Andrews, "Analytical modeling of uplink cellular networks," *IEEE Transactions on Wireless Communications*, vol. 12, no. 6, pp. 2669–2679, June 2013.

[25] H. ElSawy and E. Hossain, "On stochastic geometry modeling of cellular uplink transmission with truncated channel inversion power control," *IEEE Transactions on Wireless Communications*, vol. 13, no. 8, pp. 4454–4469, Aug. 2014.

[26] D. Taylor, H. Dhillon, T. Novlan, and J. Andrews, "Pairwise interaction processes for modeling cellular network topology," in *IEEE Global Communications Conference*, Dec. 2012, pp. 4524–4529.

[27] A. Guo and M. Haenggi, "Spatial stochastic models and metrics for the structure of base stations in cellular networks," *IEEE Transactions on Wireless Communications*, vol. 12, no. 11, pp. 5800–5812, Nov. 2013.

[28] J. Riihijarvi and P. Mahonen, "Modeling spatial structure of wireless communication networks," in *IEEE Conference on Computer Communications Workshops*, Mar. 2010, pp. 1–6.

[29] O. Macchi, "The coincidence approach to stochastic point processes," *Advances in Applied Probability*, pp. 83–122, Mar. 1975.

[30] R. Ganti, F. Baccelli, and J. Andrews, "Series expansion for interference in wireless networks," *IEEE Transactions on Information Theory*, vol. 58, no. 4, pp. 2194–2205, Apr. 2012.

[31] J. B. Hough, M. Krishnapur, Y. Peres, and B. Virág, *Zeros of Gaussian analytic functions and determinantal point processes*, ser. University Lecture Series. American Mathematical Society, 2009,

vol. 51. [Online]. Available: http://research.microsoft.com/en-us/um/people/peres/gaf_book.pdf

[32] F. Lavancier, J. Møller, and E. Rubak, "Determinantal point process models and statistical inference," *Journal of the Royal Statistical Society: Series B (Statistical Methodology)*, vol. 77, no. 4, pp. 853–877, 2015.

[33] L. Decreusefond, I. Flint, and K. C. Low, "Perfect simulation of determinantal point processes," *arXiv preprint arXiv:1311.1027*, 2013.

[34] L. Decreusefond, I. Flint, and A. Vergne, "A note on the simulation of the ginibre point process," *Journal of Applied Probability*, vol. 52, no. 04, pp. 1003–1012, 2015.

[35] T. Shirai and Y. Takahashi, "Random point fields associated with certain fredholm determinants i: fermion, poisson and boson point processes," *Journal of Functional Analysis*, vol. 205, no. 2, pp. 414–463, 2003.

[36] ——, "Random point fields associated with certain fredholm determinants ii: fermion shifts and their ergodic and Gibbs properties," *Annals of probability*, pp. 1533–1564, 2003.

[37] N. Miyoshi and T. Shirai, "A cellular network model with Ginibre configurated base stations," *Research Rep. on Math. and Comp. Sciences (Tokyo Inst. of Tech.)*, Oct. 2012.

[38] ——, "Spatial modeling and analysis of cellular networks using the Ginibre point process: A tutorial," *IEICE Transactions on Communications*, vol. 99, no. 11, pp. 2247–2255, 2016.

[39] I. Nakata and N. Miyoshi, "Spatial stochastic models for analysis of heterogeneous cellular networks with repulsively deployed base stations," *Research Rep. on Math. and Comp. Sciences, B-473 (Tokyo Inst. of Tech.)*, 2013.

[40] T. Kobayashi and N. Miyoshi, "Downlink coverage probability in Ginibre-poisson overlaid mimo cellular networks," in *2016 14th International Symposium on Modeling and Optimization in Mobile, Ad Hoc, and Wireless Networks (WiOpt)*, May 2016, pp. 1–8.

[41] N. Deng, W. Zhou, and M. Haenggi, "The Ginibre point process as a model for wireless networks with repulsion," *IEEE Transactions on Wireless Communications*, vol. 14, no. 1, pp. 107–121, Jan. 2015.

[42] A. Goldman *et al.*, "The Palm measure and the Voronoi tessellation for the Ginibre process," *The Annals of Applied Probability*, vol. 20, no. 1, pp. 90–128, 2010.

[43] F. Baccelli and B. Blaszczyszyn, *Stochastic Geometry and Wireless Networks: Volume 1: THEORY*. Now Publishers Inc, 2010.

[44] S. N. Chiu, D. Stoyan, W. S. Kendall, and J. Mecke, *Stochastic geometry and its applications*. John Wiley & Sons, 2013.

[45] M. Haenggi, *Stochastic geometry for wireless networks*. Cambridge University Press, 2013.

[46] F. Y. Kuo and I. H. Sloan, "Lifting the curse of dimensionality," *Notices of the AMS*, vol. 52, no. 11, pp. 1320–1328, 2005.

[47] B. Blaszczyszyn and H. P. Keeler, "Studying the sinr process of the typical user in poisson networks using its factorial moment measures," *IEEE Transactions on Information Theory*, vol. 61, no. 12, pp. 6774–6794, Dec. 2015.

[48] A. Jeffrey and D. Zwillinger, *Table of integrals, series, and products*. Academic Press, 2007.

[49] I. C. Ipsen and D. J. Lee, "Determinant approximations," *arXiv preprint arXiv:1105.0437*, 2011.

[50] A. Baddeley and R. Turner, "Spatstat: an R package for analyzing spatial point patterns," *Journal of Statistical Software*, vol. 12, no. 6, pp. 1–42, 2005.

[51] W. Rvudin, *Principles of mathematical analysis, 3rd edition*. McGraw-Hill New York, 1976.

[52] Y. Li, F. Baccelli, J. Andrews, T. Novlan, and J. Zhang, "Modeling and analyzing the coexistence of licensed-assisted access LTE and Wi-Fi," in *IEEE GLOBECOM Workshop on Heterogeneous and Small Cell Networks*, Dec. 2015.

[53] Y. Li, F. Baccelli, J. G. Andrews, T. D. Novlan, and J. C. Zhang, "Modeling and analyzing the coexistence of wi-fi and lte in unlicensed spectrum," *IEEE Transactions on Wireless Communications*, vol. 15, no. 9, pp. 6310–6326, Sept. 2016.

[54] Qualcomm, "Extending LTE Advanced to unlicensed spectrum," *white paper*, Dec 2013.

[55] R. Ratasuk, M. Uusitalo, N. Mangalvedhe, A. Sorri, S. Iraji, C. Wijting, and A. Ghosh, "License-exempt LTE deployment in heterogeneous network," in *International Symposium on Wireless Communication Systems (ISWCS)*, Aug. 2012, pp. 246–250.

[56] 3GPP TR 36.889, "Study on licensed-assisted access to unlicensed spectrum," 2015.

[57] F. M. Abinader, E. P. Almeida, F. S. Chaves, A. M. Cavalcante, R. D. Vieira, R. C. Paiva, A. M. Sobrinho, S. Choudhury, E. Tuomaala, K. Doppler *et al.*, "Enabling the coexistence of LTE and Wi-Fi in unlicensed bands," *IEEE Communications Magazine*, vol. 52, no. 11, pp. 54–61, Nov. 2014.

[58] R. Zhang, M. Wang, L. X. Cai, Z. Zheng, X. Shen, and L.-L. Xie, "LTE-unlicensed: the future of spectrum aggregation for cellular networks," *IEEE Wireless Communications*, vol. 22, no. 3, pp. 150–159, July 2015.

[59] H. Zhang, X. Chu, W. Guo, and S. Wang, "Coexistence of Wi-Fi and heterogeneous small cell networks sharing unlicensed spectrum," *IEEE*

Communications Magazine, vol. 53, no. 3, pp. 158–164, Mar. 2015.

[60] A. Al-Dulaimi, S. Al-Rubaye, Q. Ni, and E. Sousa, "5G communications race: Pursuit of more capacity triggers LTE in unlicensed band," *IEEE Vehicular Technology Magazine*, vol. 10, no. 1, pp. 43–51, Mar. 2015.

[61] S.-Y. Lien, C.-C. Chien, H.-L. Tsai, Y.-C. Liang, and D. I. Kim, "Configurable 3GPP licensed assisted access to unlicensed spectrum," *IEEE Wireless Communications*, vol. 23, no. 6, pp. 32–39, Jan. 2017.

[62] A. M. Cavalcante, E. Almeida, R. D. Vieira, F. Chaves, R. C. Paiva, F. Abinader, S. Choudhury, E. Tuomaala, and K. Doppler, "Performance evaluation of LTE and Wi-Fi coexistence in unlicensed bands," in *IEEE 77th Vehicular Technology Conference (VTC Spring)*, Jun. 2013, pp. 1–6.

[63] T. Nihtila, V. Tykhomyrov, O. Alanen, M. Uusitalo, A. Sorri, M. Moisio, S. Iraji, R. Ratasuk, N. Mangalvedhe *et al.*, "System performance of LTE and IEEE 802.11 coexisting on a shared frequency band," in *IEEE Wireless Communications and Networking Conference (WCNC)*, Jun. 2013, pp. 1038–1043.

[64] F. Liu, E. Bala, E. Erkip, and R. Yang, "A framework for femtocells to access both licensed and unlicensed bands," in *2011 International Symposium of Modeling and Optimization of Mobile, Ad Hoc, and Wireless Networks*, May 2011, pp. 407–411.

[65] E. Almeida, A. M. Cavalcante, R. C. Paiva, F. S. Chaves, F. M. Abinader, R. D. Vieira, S. Choudhury, E. Tuomaala, and K. Doppler, "Enabling LTE/WiFi coexistence by LTE blank subframe allocation," in *IEEE International Conference on Communications (ICC)*, Jun. 2013, pp. 5083–5088.

[66] J. Jeon, H. Niu, Q. C. Li, A. Papathanassiou, and G. Wu, "LTE in the unlicensed spectrum: Evaluating coexistence mechanisms," in *IEEE Globecom Workshops (GC Wkshps)*, Dec. 2014, pp. 740–745.

[67] R. Ratasuk, N. Mangalvedhe, and A. Ghosh, "LTE in unlicensed spectrum using licensed-assisted access," in *2014 IEEE Globecom Workshops (GC Wkshps)*, Dec. 2014, pp. 746–751.

[68] N. Rupasinghe and I. Guvenc, "Licensed-assisted access for WiFi-LTE coexistence in the unlicensed spectrum," in *2014 IEEE Globecom Workshops (GC Wkshps)*, Dec 2014, pp. 894–899.

[69] Q. C. Li, H. Niu, A. T. Papathanassiou, and G. Wu, "5G network capacity: Key elements and technologies," *IEEE Vehicular Technology Magazine*, vol. 9, no. 1, pp. 71–78, Mar. 2014.

[70] A. Mukherjee, J.-F. Cheng, S. Falahati, L. Falconetti, A. Furuskär, and B. Godana, "System architecture and coexistence evaluation of licensed-assisted access LTE with IEEE 802.11," in *IEEE ICC Workshop on LTE in Unlicensed Bands: Potentials and Challenges*, Jun. 2015.

[71] T. Novlan, B. L. Ng, H. Si, and J. C. Zhang, "Overview and evaluation of licensed assisted access for LTE-advanced," in *2015 49th Asilomar Conference on Signals, Systems and Computers*, Nov. 2015, pp. 1031–1035.

[72] H. J. Kwon, J. Jeon, A. Bhorkar, Q. Ye, H. Harada, Y. Jiang, L. Liu, S. Nagata, B. L. Ng, T. Novlan, J. Oh, and W. Yi, "Licensed-assisted access to unlicensed spectrum in LTE release 13," *IEEE Communications Magazine*, vol. 55, no. 2, pp. 201–207, Feb. 2017.

[73] Qualcomm, "LTE in unlicensed spectrum: Harmonious coexistence with Wi-Fi," *white paper*, Jun. 2014.

[74] N. Jindal and D. Breslin, "LTE and Wi-Fi in unlicensed spectrum: A coexistence study," *Google white paper*, Jun. 2015.

[75] S. Yun and L. Qiu, "Supporting WiFi and LTE co-existence," in *2015 IEEE Conference on Computer Communications (INFOCOM)*, April 2015, pp. 810–818.

[76] J. Jeon, Q. C. Li, H. Niu, A. Papathanassiou, and G. Wu, "LTE in the unlicensed spectrum: A novel coexistence analysis with WLAN systems," in *IEEE Global Communications Conference (GLOBECOM)*, Dec. 2014, pp. 3459–3464.

[77] S. Sagari, S. Baysting, D. Saha, I. Seskar, W. Trappe, and D. Raychaudhuri, "Coordinated dynamic spectrum management of LTE-U and

Wi-Fi networks," in *2015 IEEE International Symposium on Dynamic Spectrum Access Networks (DySPAN)*, Sept. 2015, pp. 209–220.

[78] G. Bianchi, "Performance analysis of the IEEE 802.11 distributed coordination function," *IEEE Journal on Selected Areas in Communications*, vol. 18, no. 3, pp. 535–547, Mar. 2000.

[79] H. Yu, G. Iosifidis, J. Huang, and L. Tassiulas, "Auction-based coopetition between LTE Unlicensed and Wi-Fi," *IEEE Journal on Selected Areas in Communications*, vol. 35, no. 1, pp. 79–90, Jan. 2017.

[80] F. Teng, D. Guo, and M. L. Honig, "Sharing of unlicensed spectrum by strategic operators," in *2014 IEEE Global Conference on Signal and Information Processing (GlobalSIP)*. IEEE, Dec. 2014, pp. 288–292.

[81] H. Nguyen, F. Baccelli, and D. Kofman, "A stochastic geometry analysis of dense IEEE 802.11 networks," in *IEEE INFOCOM 2007*, May 2007, pp. 1199–1207.

[82] F. Baccelli, J. Li, T. Richardson, S. Subramanian, X. Wu, and S. Shakkottai, "On optimizing csma for wide area ad-hoc networks," in *2011 International Symposium of Modeling and Optimization of Mobile, Ad Hoc, and Wireless Networks*, May 2011, pp. 354–359.

[83] Y. Kim, F. Baccelli, and G. de Veciana, "Spatial reuse and fairness of ad hoc networks with channel-aware CSMA protocols," *IEEE Transactions on Information Theory*, vol. 60, no. 7, pp. 4139–4157, Jul. 2014.

[84] G. Alfano, M. Garetto, and E. Leonardi, "New insights into the stochastic geometry analysis of dense CSMA networks," in *IEEE INFOCOM 2011*, April 2011, pp. 2642–2650.

[85] T. V. Nguyen and F. Baccelli, "A stochastic geometry model for cognitive radio networks," *The Computer Journal*, vol. 55, no. 5, pp. 534–552, Apr. 2012.

[86] A. Bhorkar, C. Ibars, and P. Zong, "On the throughput analysis of LTE and WiFi in unlicensed band," in *Asilomar Conference on Signals, Systems and Computers*, Nov. 2014, pp. 1309–1313.

[87] LTE-U Forum, "LTE-U technical report: coexistence study for LTE-U SDL v1.0," *Technical Report*, Feb. 2015.

[88] V. Chandrasekhar, J. G. Andrews, and A. Gatherer, "Femtocell networks: a survey," *IEEE Communications Magazine*, vol. 46, no. 9, pp. 59–67, Sept. 2008.

[89] A. Busson, G. Chelius, and J.-M. Gorce, "Interference modeling in CSMA multi-hop wireless networks," INRIA, Research Report RR-6624, Feb. 2009. [Online]. Available: https://hal.inria.fr/inria-00316029

[90] F. Baccelli and B. Blaszczyszyn, *Stochastic Geometry and Wireless Networks: Volume II-Applications*. Now Publishers Inc, 2010.

[91] M. Haenggi and R. K. Ganti, *Interference in large wireless networks*. Now Publishers Inc, 2009.

[92] Y. Li, J. G. Andrews, F. Baccelli, T. D. Novlan, and J. Zhang, "On the initial access design in millimeter wave cellular networks," in *2016 IEEE Globecom Workshops (GC Wkshps)*, Dec. 2016, pp. 1–6.

[93] Y. Li, J. G. Andrews, F. Baccelli, T. D. Novlan, and J. C. Zhang, "Performance analysis of millimeter-wave cellular networks with two-stage beamforming initial access protocols," in *2016 50th Asilomar Conference on Signals, Systems and Computers*, Nov. 2016, pp. 1171–1175.

[94] A. Khandekar, N. Bhushan, J. Tingfang, and V. Vanghi, "LTE-advanced: Heterogeneous networks," in *2010 European Wireless Conference (EW)*, 2010, pp. 978–982.

[95] Z. Pi and F. Khan, "An introduction to millimeter-wave mobile broadband systems," *IEEE Communications Magazine*, vol. 49, no. 6, pp. 101–107, Jun. 2011.

[96] T. S. Rappaport, S. Sun, R. Mayzus, H. Zhao, Y. Azar, K. Wang, G. N. Wong, J. K. Schulz, M. Samimi, and F. Gutierrez, "Millimeter wave mobile communications for 5G cellular: It will work!" *IEEE Access*, vol. 1, pp. 335–349, May 2013.

[97] W. Roh, J.-Y. Seol, J. Park, B. Lee, J. Lee, Y. Kim, J. Cho, K. Cheun, and F. Aryanfar, "Millimeter-wave beamforming as an enabling technology for 5G cellular communications: theoretical feasibility and prototype results," *IEEE Communications Magazine*, vol. 52, no. 2, pp. 106–113, Feb. 2014.

[98] A. Ghosh, T. Thomas, M. C. Cudak, R. Ratasuk, P. Moorut, F. W. Vook, T. S. Rappaport, G. R. MacCartney, S. Sun, S. Nie *et al.*, "Millimeter-wave enhanced local area systems: A high-data-rate approach for future wireless networks," *IEEE Journal on Selected Areas in Communications*, vol. 32, no. 6, pp. 1152–1163, Jul. 2014.

[99] M. Haenggi, J. Andrews, F. Baccelli, O. Dousse, and M. Franceschetti, "Stochastic geometry and random graphs for the analysis and design of wireless networks," *IEEE Journal on Selected Areas in Communications*, vol. 27, no. 7, pp. 1029–1046, Sept. 2009.

[100] IEEE Std 802.11ad-2012, "Part 11: Wireless LAN medium access control (MAC) and physical layer (PHY) specifications," Dec. 2012.

[101] T. Nitsche, C. Cordeiro, A. B. Flores, E. W. Knightly, E. Perahia, and J. C. Widmer, "IEEE 802.11ad: directional 60 GHz communication for multi-gigabit-per-second Wi-Fi," *IEEE Communications Magazine*, vol. 52, no. 12, pp. 132–141, Dec. 2014.

[102] TS V5G.213, "Verizon 5G radio access (V5G RA); physical layer procedures," Jun. 2016.

[103] R. W. Heath, N. Gonzalez-Prelcic, S. Rangan, W. Roh, and A. M. Sayeed, "An overview of signal processing techniques for millimeter wave MIMO systems," *IEEE Journal of Selected Topics in Signal Processing*, vol. 10, no. 3, pp. 436–453, Apr. 2016.

[104] C. Jeong, J. Park, and H. Yu, "Random access in millimeter-wave beamforming cellular networks: issues and approaches," *IEEE Communications Magazine*, vol. 53, no. 1, pp. 180–185, Jan. 2015.

[105] V. Desai, L. Krzymien, P. Sartori, W. Xiao, A. Soong, and A. Alkhateeb, "Initial beamforming for mmWave communications," in *2014 48th Asilomar Conference on Signals, Systems and Computers*, Nov. 2014, pp. 1926–1930.

[106] M. Giordani, M. Mezzavilla, C. Barati, S. Rangan, and M. Zorzi, "Comparative analysis of initial access techniques in 5G mmWave cellular networks," in *2016 Annual Conference on Information Science and Systems*, Mar. 2016, pp. 268–273.

[107] M. Giordani, M. Mezzavilla, and M. Zorzi, "Initial access in 5G mmwave cellular networks," *IEEE Communications Magazine*, vol. 54, no. 11, pp. 40–47, Nov. 2016.

[108] V. Raghavan, J. Cezanne, S. Subramanian, A. Sampath, and O. Koymen, "Beamforming tradeoffs for initial UE discovery in millimeter-wave MIMO systems," *IEEE Journal of Selected Topics in Signal Processing*, vol. 10, no. 3, pp. 543–559, Apr. 2016.

[109] C. N. Barati, S. A. Hosseini, M. Mezzavilla, T. Korakis, S. S. Panwar, S. Rangan, and M. Zorzi, "Initial access in millimeter wave cellular systems," *IEEE Transactions on Wireless Communications*, vol. 15, no. 12, pp. 7926–7940, Dec. 2016.

[110] H. Shokri-Ghadikolaei, C. Fischione, G. Fodor, P. Popovski, and M. Zorzi, "Millimeter wave cellular networks: A MAC layer perspective," *IEEE Transactions on Communications*, vol. 63, no. 10, pp. 3437–3458, Oct. 2015.

[111] S. Hur, T. Kim, D. J. Love, J. V. Krogmeier, T. A. Thomas, and A. Ghosh, "Millimeter wave beamforming for wireless backhaul and access in small cell networks," *IEEE Transactions on Communications*, vol. 61, no. 10, pp. 4391–4403, Oct. 2013.

[112] D. Zhu, J. Choi, and R. W. Heath, "Auxiliary beam pair enabled AoD and AoA estimation in mmWave FD-MIMO systems," in *2016 IEEE Global Communications Conference (GLOBECOM)*, Dec. 2016, pp. 1–6.

[113] D. Zhu, J. Choi, and R. W. Heath Jr, "Auxiliary beam pair enabled AoD and AoA estimation in closed-loop large-scale mmWave MIMO system," *arXiv preprint arXiv:1610.05587*, Dec. 2016.

[114] A. Ali, N. González-Prelcic, and R. W. Heath Jr, "Millimeter wave beam-selection using out-of-band spatial information," *arXiv preprint arXiv:1702.08574*, Feb. 2017.

[115] V. Va and R. W. Heath, "Performance analysis of beam sweeping in millimeter wave assuming noise and imperfect antenna patterns," in *2016 IEEE 84th Vehicular Technology Conference (VTC-Fall)*, Sept. 2016, pp. 1–5.

[116] M. Hussain and N. Michelusi, "Throughput optimal beam alignment in millimeter wave networks," *arXiv preprint arXiv:1702.06152*, Feb. 2017.

[117] R. K. Ganti and M. Haenggi, "Interference and outage in clustered wireless ad hoc networks," *IEEE Transactions on Information Theory*, vol. 55, no. 9, pp. 4067–4086, Sept. 2009.

[118] S. Akoum, O. El Ayach, and R. Heath, "Coverage and capacity in mmwave cellular systems," in *Asilomar Conference on Signals, Systems and Computers (ASILOMAR)*, Nov. 2012, pp. 688–692.

[119] S. Singh, M. Kulkarni, A. Ghosh, and J. Andrews, "Tractable model for rate in self-backhauled millimeter wave cellular networks," *IEEE Journal on Selected Areas in Communications*, vol. 33, no. 10, pp. 2196–2211, Oct. 2015.

[120] J. Park, S. L. Kim, and J. Zander, "Tractable resource management with uplink decoupled millimeter-wave overlay in ultra-dense cellular networks," *IEEE Transactions on Wireless Communications*, vol. 15, no. 6, pp. 4362–4379, Jun. 2016.

[121] T. Bai and R. Heath, "Coverage and rate analysis for millimeter-wave cellular networks," *IEEE Transactions on Wireless Communications*, vol. 14, no. 2, pp. 1100–1114, Feb. 2015.

[122] T. Bai, A. Alkhateeb, and R. Heath, "Coverage and capacity of millimeter-wave cellular networks," *IEEE Communications Magazine*, vol. 52, no. 9,

pp. 70–77, Sept. 2014.

[123] A. Alkhateeb, Y. H. Nam, M. S. Rahman, C. Zhang, and R. Heath, "Initial beam association in millimeter wave cellular systems: Analysis and design insights," *IEEE Transactions on Wireless Communications*, vol. PP, no. 99, pp. 1–1, 2017.

[124] M. D. Renzo, "Stochastic geometry modeling and analysis of multi-tier millimeter wave cellular networks," *IEEE Transactions on Wireless Communications*, vol. 14, no. 9, pp. 5038–5057, Sept. 2015.

[125] A. K. Gupta, J. G. Andrews, and R. W. Heath, "On the feasibility of sharing spectrum licenses in mmwave cellular systems," *IEEE Transactions on Communications*, vol. 64, no. 9, pp. 3981–3995, Sept. 2016.

[126] A. Guo and M. Haenggi, "Asymptotic deployment gain: A simple approach to characterize the sinr distribution in general cellular networks," *IEEE Transactions on Communications*, vol. 63, no. 3, pp. 962–976, Mar. 2015.

[127] B. Błaszczyszyn, M. K. Karray, and H. P. Keeler, "Wireless networks appear Poissonian due to strong shadowing," *IEEE Transactions on Wireless Communications*, vol. 14, no. 8, pp. 4379–4390, Apr. 2015.

[128] J. G. Andrews, T. Bai, M. Kulkarni, A. Alkhateeb, A. Gupta, and R. W. Heath, "Modeling and analyzing millimeter wave cellular sys-

tems," *IEEE Transactions on Communications*, vol. 65, no. 1, pp. 403–430, Jan. 2017.

[129] M. N. Kulkarni, S. Singh, and J. G. Andrews, "Coverage and rate trends in dense urban mmwave cellular networks," in *IEEE Global Communications Conference (GLOBECOM)*, Dec. 2014, pp. 3809–3814.

[130] R. B. Waterhouse, D. Novak, A. Nirmalathas, and C. Lim, "Broadband printed sectorized coverage antennas for millimeter-wave wireless applications," *IEEE Transactions on Antennas and Propagation*, vol. 50, no. 1, pp. 12–16, Aug. 2002.

[131] Y. Shen, T. Luo, and M. Z. Win, "Neighboring cell search for LTE systems," *IEEE Transactions on Wireless Communications*, vol. 11, no. 3, pp. 908–9198, Mar. 2012.

[132] S. Singh, F. Baccelli, and J. G. Andrews, "On association cells in random heterogeneous networks," *IEEE Wireless Communications Letters*, vol. 3, no. 1, pp. 70–73, Feb. 2014.

[133] S. Singh, H. S. Dhillon, and J. G. Andrews, "Offloading in heterogeneous networks: Modeling, analysis, and design insights," *IEEE Transactions on Wireless Communications*, vol. 12, no. 5, pp. 2484–2497, May 2013.

[134] T. S. Rappaport, F. Gutierrez, E. Ben-Dor, J. N. Murdock, Y. Qiao, J. Tamir *et al.*, "Broadband millimeter-wave propagation measurements and models using adaptive-beam antennas for outdoor urban cellular

communications," *IEEE Transactions on Antennas and Propagation*, vol. 61, no. 4, pp. 1850–1859, Apr. 2013.

[135] T. L. Marzetta, "Noncooperative cellular wireless with unlimited numbers of base station antennas," *IEEE Transactions on Wireless Communications*, vol. 9, no. 11, pp. 3590–3600, Nov. 2010.

[136] E. G. Larsson, O. Edfors, F. Tufvesson, and T. L. Marzetta, "Massive MIMO for next generation wireless systems," *IEEE Communications Magazine*, vol. 52, no. 2, pp. 186–195, Feb. 2014.

[137] F. Rusek, D. Persson, B. K. Lau, E. G. Larsson, T. L. Marzetta, O. Edfors, and F. Tufvesson, "Scaling up MIMO: Opportunities and challenges with very large arrays," *IEEE Signal Processing Magazine*, vol. 30, no. 1, pp. 40–60, Jan 2013.

[138] J. Hoydis, S. ten Brink, and M. Debbah, "Massive MIMO in the UL/DL of cellular networks: How many antennas do we need?" *IEEE Journal on Selected Areas in Communications*, vol. 31, no. 2, pp. 160–171, Feb. 2013.

[139] E. Bjornson, E. G. Larsson, and T. L. Marzetta, "Massive MIMO: ten myths and one critical question," *IEEE Communications Magazine*, vol. 54, no. 2, pp. 114–123, Feb. 2016.

[140] Y. Kim, H. Ji, J. Lee, Y. H. Nam, B. L. Ng, I. Tzanidis, Y. Li, and J. Zhang, "Full dimension mimo (FD-MIMO): the next evolution of

MIMO in LTE systems," *IEEE Wireless Communications*, vol. 21, no. 2, pp. 26–33, Apr. 2014.

[141] Y. Kim, H. Ji, H. Lee, J. Lee, B. L. Ng, and J. Zhang, "Evolution beyond LTE-advanced with full dimension MIMO," in *2013 IEEE International Conference on Communications Workshops (ICC)*, Jun. 2013, pp. 111–115.

[142] Y. Li, Y. Xm, M. Dong, G. Xu, J. C. Zhang, Y. Kim, and J. Lee, "Implementation of full-dimensional MIMO (FD-MIMO) in LTE," in *2013 Asilomar Conference on Signals, Systems and Computers*, Nov 2013, pp. 998–1003.

[143] Y. Li, J. G. Andrews, F. Baccelli, T. D. Novlan, and C. Zhang, "Design and analysis of initial access in millimeter wave cellular networks," *arXiv preprint arXiv:1609.05582*, Sept. 2016.

[144] M. Karlsson and E. G. Larsson, "On the operation of massive MIMO with and without transmitter CSI," in *2014 IEEE 15th International Workshop on Signal Processing Advances in Wireless Communications (SPAWC)*, Jun. 2014, pp. 1–5.

[145] C. Shepard, A. Javed, and L. Zhong, "Control channel design for many-antenna MU-MIMO," in *Proceedings of the 21st Annual International Conference on Mobile Computing and Networking*, Sept. 2015, pp. 578–591.

[146] F. Baccelli and B. Blaszczyszyn, "A new phase transitions for local delays in manets," in *INFOCOM, 2010 Proceedings IEEE*, Apr. 2010, pp. 1–9.

[147] M. Haenggi, "The local delay in Poisson networks," *IEEE Transactions on Information Theory*, vol. 59, no. 3, pp. 1788–1802, Mar. 2013.

[148] X. Zhang and M. Haenggi, "Delay-optimal power control policies," *IEEE Transactions on Wireless Communications*, vol. 11, no. 10, pp. 3518–3527, Oct. 2012.

[149] S. K. Iyer and R. Vaze, "Achieving non-zero information velocity in wireless networks," in *2015 13th International Symposium on Modeling and Optimization in Mobile, Ad Hoc, and Wireless Networks (WiOpt)*, May 2015, pp. 584–590.

[150] X. Zhang and J. G. Andrews, "Downlink cellular network analysis with multi-slope path loss models," *IEEE Transactions on Communications*, vol. 63, no. 5, pp. 1881–1894, Mar. 2015.

[151] S. Singh, X. Zhang, and J. G. Andrews, "Joint rate and SINR coverage analysis for decoupled uplink-downlink biased cell associations in HetNets," *IEEE Transactions on Wireless Communications*, vol. 14, no. 10, pp. 5360–5373, Oct. 2015.

[152] M. Haenggi, "User point processes in cellular networks," *arXiv preprint arXiv:1611.08560*, Nov. 2016.

Vita

Yingzhe Li received the B.S. degree in electronic engineering from Shanghai Jiao Tong University, Shanghai, China, in 2012 and the M.S. degree in electrical engineering from The University of Texas at Austin, Austin, TX, USA, in 2014. His research interests include communication theory, analysis of wireless networks using stochastic geometry, mmWave communications, and asymptotic analysis of ad hoc networks. He has held summer internships at Samsung Research America in Richardson, TX, USA; Qualcomm Inc. in San Diego, CA, USA; and Nokia Siemens Networks in Arlington Heights, IL, USA. He was among the 12 graduate student finalists to present at the Broadcom foundation university research competition in 2015. He was a recipient for the best paper award of the IEEE GLOBECOM Workshop on Heterogeneous and Small Cell Network in 2015. He was an exemplary reviewer for the IEEE Transactions on Communications in 2017.

Permanent email: yzli@utexas.edu

This dissertation was typeset with LaTeX[†] by the author.

[†]LaTeX is a document preparation system developed by Leslie Lamport as a special version of Donald Knuth's TeX Program.